Molecular Mechanism of *E. coli* ATP Synthase:

Structural Analysis of the Proton Channel.

A Thesis Submitted to the
College of Graduate Studies and Research
In Partial Fulfillment of the Requirements
For the Degree of Doctor of Philosophy
In the Department of Biochemistry
University of Saskatchewan
Saskatoon

By Hannah Elizabeth Pierson

PERMISSION TO USE

In presenting this thesis in partial fulfillment of the requirements for a Postgraduate degree from the University of Saskatchewan, I agree that the Libraries of the University may make it freely available for inspection. I further agree that permission for copying of thesis thesis in any manner, in whole or in part, for scholarly purposes may be granted by the professor of professors who supervised my thesis work or, in their absence, by the Head of the Department or Dean of the College in which my thesis work was done. It is understood that any copying or publication or use of this thesis or parts thereof for financial gain shall not be allowed without my written permission. It is also understood that due recognition shall be given to me and to the University of Saskatchewan in any scholarly use, which may be made of any material in my thesis.

Requests for permission to copy or to make use of the material in this thesis in whole or in part should be addressed to:

Head of the Department of Biochemistry
University of Saskatchewan
Saskatoon, Saskatchewan, S7N 5E5

COPYRIGHT NOTE

ABSTRACT

Adenosine triphosphate (ATP) is the energy currency of all living cells and its production is a key reaction in the energy metabolism of living organisms. Cells produce most of the ATP they require through ATP synthase, a unique molecular rotary motor driven by the movement of protons across the lipid membrane. In *E.coli*, ATP synthase is composed of a soluble domain called F_1, which houses the catalytic sites, and a transmembrane domain called F_0 that shuttles protons across the membrane to drive ATP production in the F_1 sector. The F_0 domain is built of three subunit types: subunit *a* and a dimer of subunit *b* form the stator of the motor, while a decameric *c* ring forms the rotor. The dynamic interface between *a* and c_{10} forms the proton channel. The ultimate goal of this work is to determine the structure of the proton transport machinery and understand the molecular mechanism of proton translocation in ATP synthase. We have characterized some of the key events in the stepwise assembly of the F_0-complex. We have designed and validated a model protein, consisting of genetically fused subunits *a* and *c*, for structural studies. We have made progress towards determining the structure of the proton channel, including the development of a novel procedure for purification of subunit *a* and the *a/c* fusion protein, and crystallization of subunit *a*. Medical applications of this work include the potential development of novel antibiotic compounds, as well as the characterization and potential treatment of three human diseases caused by disruptions in proton transport through F_0.

ACKNOWLEDGEMENTS

I extend my deepest gratitude to Professor Oleg Dmitriev for his guidance and support over the course of my studies. It is my pleasure to thank the outstanding technical staff in the Dmitriev lab, Christopher O'Grady and Eva-Maria Uhlemann, for their hands-on support. I also wish to thank the current and past members of the Dmitriev lab for their encouragement: Adam Wiebe, Ben Rempel, Corey Yu, Igor Moshynskyy, Natasha Dolgova, Sergiy Nokhrin and Tahereh Haji.

I would like to thank the present and past members of my academic advisory committee: Bill Roesler, Mary Pato, Peter Howard, Ramji Khandelwal, Rob Warrington, and Stan Moore. I appreciate the encouragement and constructive criticism you have all provided me with over the years.

DEDICATION

I would like to dedicate this thesis to my fiancé, Nathan, and my family, all of whom supported me unconditionally through my Ph.D. program.

"Love many, trust few, always tie down your own canoe"

- Grandpa Pierson

TABLE OF CONTENTS

LIST OF TABLES

LIST OF FIGURES

LIST OF ABBREVIATIONS

3-D	Three dimensional
ACMA	9-amino-6-chloro-2methoxyacridine
ADP	Adenosine diphosphate
AMS	4-acetamido-4'-maleimidylstilbene-2 2'-disulfonic acid
ATP	Adenosine triphosphate
BSA	Bovine serum albumin
B_0	Bulk magnetic field
LCP	Lipidic cubic phase
CLS	Canadian Light Source
Cryo-EM	Cryo-electron microscopy
DCCD	N,N'-dicyclohexylcarbodiimide
DHPC	1,2-diheptanoyl-*sn*-glycero-3-phosphocholine
DLS	Dynamic light scattering
DMPC	1,2-dimyristoyl-*sn*-glycero-3-phosphocholine
DNA	Deoxyribonucleic acid
DPC	*n*-dodecylphosphocholine
DTT	Dithiolthreitol
E. coli	*Escherichia coli*
EDTA	Ethylenediaminetetraacetic acid
$FADH_2$	Flavin adenine dinucleotide
FBSN	Familial bilateral striatal necrosis
FCCP	Carbonylcyanide-4-(trifluoromethoxy)- phenylhydrazone
GPCR	G-protein coupled receptor
His_6	Hexahistidine tag
HRP	Horseradish peroxidase
HSQC	Heteronuclear single quantum coherence
HWI-HTS	Hauptman Woodward Institute – high throughput screen
LB	Luria broth
LDAO	N,N-dimethyldodecylamine-N-oxide
LHON	Leber's hereditary optic neuropathy

LMPG	1-myristoyl-2-hydroxy-*sn*-glycero-3-[phospho-*rac*-(1- glycerol)]
LPPG	palmitoyl-2-hydroxy-*sn*-glycero-3-[phospho-*rac*-(1-glycerol)]
MES	2-(N-morpholino)ethanesulfonic acid
MILS	Maternally inhereted Leigh's syndrome
MOPS	3-(N-morpholino)propanesulfonic acid
MBP	3-(*N*-maleimidylpropionyl)-biocytin
MSC4	Membrane protein crystallization screen – 4
NADH	Nicotinamide adenine dinucleotide
NARP	Neuropathy, ataxia and retinitis pigmentosa
NMR	Nuclear magnetic resonance
NOE	Nuclear Overhauser Effect
OD	Optical density
OxPhos	Oxidative phosphorylation
PCR	Polymerase chain reaction
PEG	Polyethylene glycol
P_i	Inorganic phosphate
PMF	Proton motive force
PMSF	Phenylmethylsulfonyl fluoride
PVDF	Polyvinylidene fluoride
RecA/*recA*	Recombinase-A protein / gene encoding recombinase-A
RF	Radio Frequency
Rh	Hydrodynamic radius
SDS-PAGE	Sodium dodecyl sulfate polyacrylamide gel electrophoresis
SSRL	Stanford Synchrotron Radiation Lightsource
SRII	Sensory rhodopsin II
SER	Surface entropy reduction
Tet^R	Tetracycline resistance
TMH	Transmembrane helix
Tris	Tris(hydroxymethyl)aminomethane
TROSY	Transverse relaxation optimized spectroscopy
UV	Ultraviolet

1 Introduction

Living systems cannot survive without energy input. Energy is transformed from environmental sources to forms that can sustain life by respiration and photosynthesis. Two forms of energy that serve the needs of living cells are ion gradients and ATP. Ion gradients require membrane compartments to work, while ATP can act as a chemical carrier to distribute energy anywhere in the aqueous phase of the cell. In bacterial cells and mitochondria, energy can be generated through oxidative phosphorylation (OxPhos). Various exergonic processes feed into the OxPhos pathway. ATP synthase (also known as F_1F_0-ATPase), is the final step in OxPhos and facilitates transformation between the two universal forms of energy. ATP synthase can harnesses the power of ion gradients to produce ATP and it can consume ATP to restore the ion gradient if necessary.

ATP synthase is a molecular rotary motor powered by the proton motive force, or, in some cases, by a sodium motive force. It is composed of a soluble catalytic domain (F_1) which converts adenosine diphosphate (ADP) and inorganic phosphate (P_i) to ATP, and a transmembranous domain (F_0) which facilitates the movement of protons across biological membranes to drive catalytic activity in the F_1 domain. Proton transport though F_1F_0 catalyzes ATP synthesis by a unique rotational mechanism: the F_0 domain contains a molecular turbine, which spins as protons flow across the membrane along their gradient. The rotational force is then converted to chemical energy in the F_1 catalytic sites. ATP synthase is among a class of enzymes which couple the transit of ions across membranes with chemical catalysis. A detailed understanding of how proton transit drives ATP synthesis is desirable because of the central metabolic role of ATP synthase. High resolution structures and detailed mechanisms of ATP synthesis and hydrolysis in the F_1 domain are known. However, three key questions in the field of F_1F_0-ATPase research remain. First, what is the detailed molecular structure of the F_0 domain? Second, how is torque generated within the F_0 domain? Finally, what is the stepwise mechanism of assembly of the F_1 and F_0 components?

Our work aims to address these questions by taking a unique approach to understanding the steps involved in F_0 domain assembly, and to determining the high resolution structure of the proton channel. The proton transport machinery of F_1F_0-ATPase is highly dynamic, which

makes structural analysis of the proton channel challenging. We have designed and generated two model proteins, which contain the components of the proton transport machinery, to facilitate crystallographic structure studies. The model proteins also provide a convenient tool for studying the stepwise assembly mechanism of the F_0 domain. A high-resolution structure of the proton channel of ATP synthase has the potential to advance our understanding of a fundamental metabolic process in all living organisms, facilitate the characterization of human illness, and allow for the rational design of novel antibiotic compounds.

2 Review of the literature.

2.1 Bioenergetics and ATP production.

ATP is the energy currency of living cells. Decades of research have gone into understanding how cells produce and consume the energy that fuels life as we know it. In 1929, a German chemist named Karl Lohmann discovered the energy rich ATP molecule. Cells generate the bulk of the ATP they require by oxidative phosphorylation, a process which was discovered in the 1930s (Engelhardt, 1932). Initially the OxPhos research community believed that substrate level phosphorylation, through a high energy intermediate, was pivotal to the synthesis of ATP (Boyer *et al.*, 1954; Slater, 1953). Extensive efforts were made to identify the intermediate. Several candidate compounds were proposed, but none withstood experimental scrutiny (Allchin, 1997). In 1961, Boyer famously identified phosphohistidine as the elusive intermediate in oxidative phosphorylation (Boyer, 1963). However, his success was short-lived. It was later discovered that contamination with enzymes from the citric acid cycle gave a false indication that led Boyer to erroneously claim phosphohistidine as an intermediate in OxPhos (Kreil and Boyer, 1964; Mitchell *et al.*, 1964).

It was noted that OxPhos could only take place in intact membrane compartments (Penefsky *et al.*, 1960; Ziegler *et al.*, 1958), which was puzzling to the research community at the time because disruption of the membrane should not have affected the stability of a chemical intermediate. The chemisomotic theory, introduced by Peter Mitchell 1961, offered an entirely new concept of energy transformation through OxPhos. Mitchell linked OxPhos to energy stored in the form of a transmembrane proton gradient, rather than a chemical intermediate (Mitchell, 1961). The chemiosmotic hypothesis outlines how the accumulation of protons on one side of a membrane generates a gradient, which powers ATP synthesis as thermodynamic forces drive protons across the membrane along their electrochemical gradient. Peter Mitchell's chemiosmotic model revolutionized the field, and he is credited as the father of bioenergetics. However, a detailed understanding of how the energy of proton shuttling powered ATP synthesis was still decades away.

In 1945, Lardy and Elvehjem proposed that OxPhos may be linked to the ATPase activity of mitochondria (Lardy and Elvehjem, 1945). Efraim Racker's research group set out

to identify the source of this activity. By 1958 the membrane associated ATPase, termed soluble protein factor 1 (F_1), was isolated (Pullman *et al.*, 1958) although its central role in metabolism was not yet understood. The membrane associated oligomycin sensitive factor (F_0) of the ATPase was later identified and is now known to facilitate the translocation of protons across the membrane (Kagawa and Racker, 1966). Racker's group also demonstrated that F_1F_0 ATPase could catalyze ATP synthesis using the energy of the transmembrane proton gradient, which was consistent with Mitchell's chemiosmotic hypothesis (Racker and Kandrach, 1973; Ragan and Racker, 1973).

The ion gradient that drives ATP synthesis is referred to as the proton motive force (PMF). The PMF is generated by a series of enzymatic complexes embedded in the inner membrane, called the electron transport chain. The oxidation of nicotinamide adenine dinucleotide (NADH) and flavin adenine dinucleotide ($FADH_2$), and transfer of electrons through the chain creates the electrochemical proton gradient (Figure 2.1). In *E. coli*, oxidation of a single NADH molecule causes ten protons to shuttle from the cytosolic side of the membrane to the periplasm (Lehninger *et al.*, 2008) to build the gradient. Complexes I and III both shuttle four protons for each NADH oxidized, while complex IV shuttles two protons. The flow of protons through ATP synthase along their gradient, from the periplasm to the cytosol, drives the synthesis of ATP at a ratio of approximately 3 ATP per NADH oxidized.

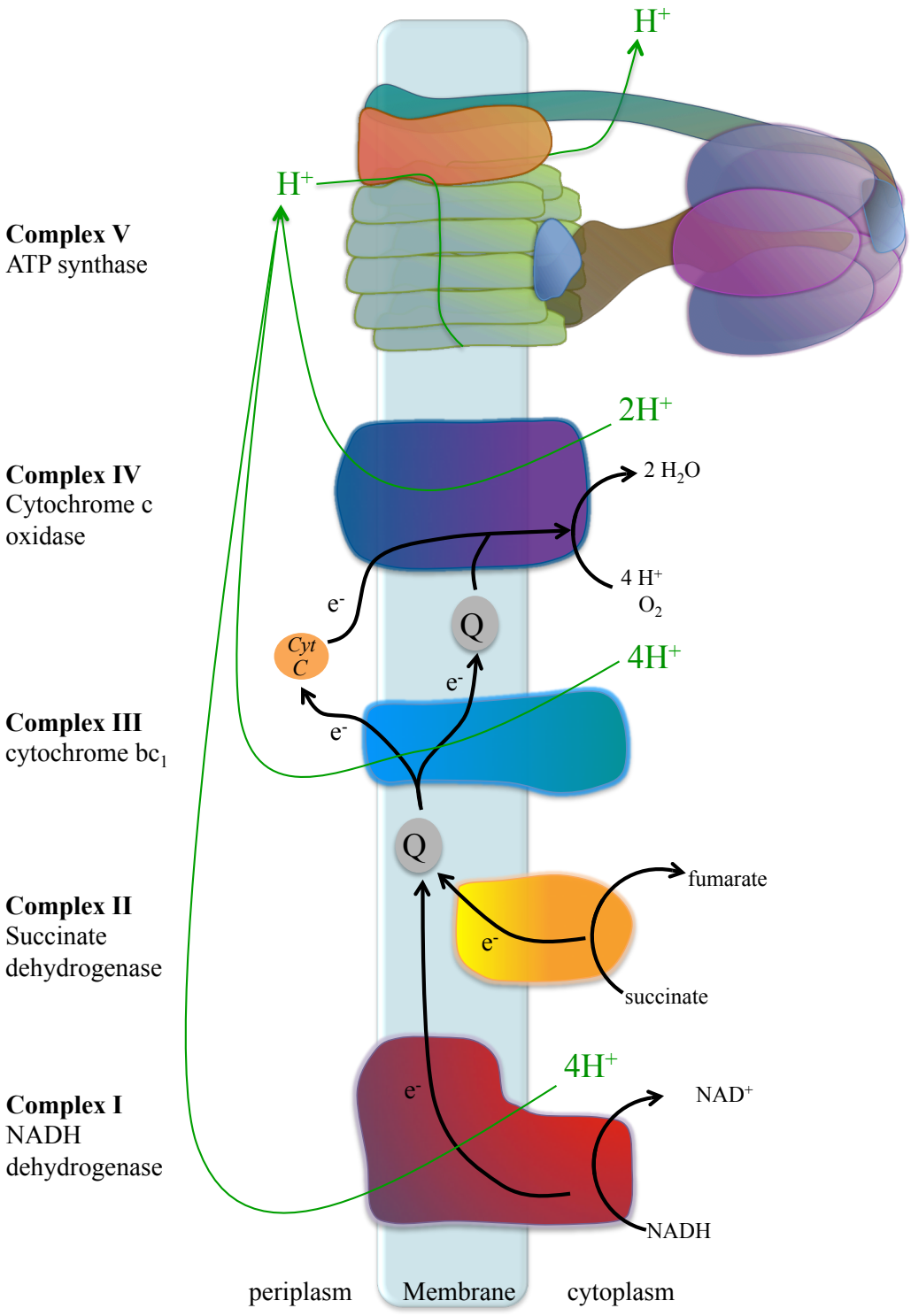

Figure 2.1: Oxidative phosphorylation and the electron transport chain. Each complex in the electron transport chain is labeled on the left. The orientation of each complex in the membrane is shown and the path of electrons through each complex is indicated with black arrows labeled e^-. The transport of protons through each complex is shown with a green arrow. 'Q' denotes ubiquinone and 'cyt c' denotes cytochrome c.

The free energy associated with the PMF describes the gradient's capacity to do work and is defined by Formula 2.1.

$$\Delta G = 2.303RT(\Delta pH) + ZF(\Delta \Psi) \quad \text{(Formula 2.1)}$$

Where, R – the universal gas constant – is 8.31 $J\,K^{-1}\,mol^{-1}$, T is temperature in Kelvin, F – the Faraday constant – is $9.64x10^4$ J/V*mol, ΔpH is the difference in pH between the cytoplasm and periplasm (in *E. coli*), and Z – proton charge – is +1. The PMF describes the electrochemical potential difference between the aqueous compartments on opposite sides of the membrane and has units of mV. The PMF has two major components, an electrical term (ΔΨ) and a concentration term (ΔpH). These terms are related by Formula 2.2.

$$PMF = \Delta \Psi - (2.303RT/F)\Delta pH \quad \text{(Formula 2.2)}$$

Where, ΔΨ is the electrical potential difference between the cytoplasmic space and the periplasm and R, T, F and ΔpH are the same as described for formula 2.1. At room temperature (25 ^oC) 2.303RT/F is equal to 59 mV. The PMF of growing *Escherichia coli* (*E. coli*) cells is usually between -140 mV and -180 mV (Foster, 2004) and is mostly in the form of ΔΨ.

F_1F_0 ATPase has a dual role as an ATP synthase and an ATPase. Under aerobic growth conditions cellular respiration maintains the proton gradient and F_1F_0 produces ATP at a high rate, as described above. However, in bacterial cells growing under anaerobic conditions, equilibrium shifts toward the reverse reaction and ATP is hydrolyzed to actively pump protons from the cytosol to the periplasm. The ATPase function allows bacterial cells to maintain the proton gradient and keep cellular processes such as flagella rotation and nutrient transport running during anaerobic growth. The ATP used to restore the proton gradient during anaerobic growth comes from substrate level phosphorylation. A diagram of proton cycling is shown in Figure 2.2.

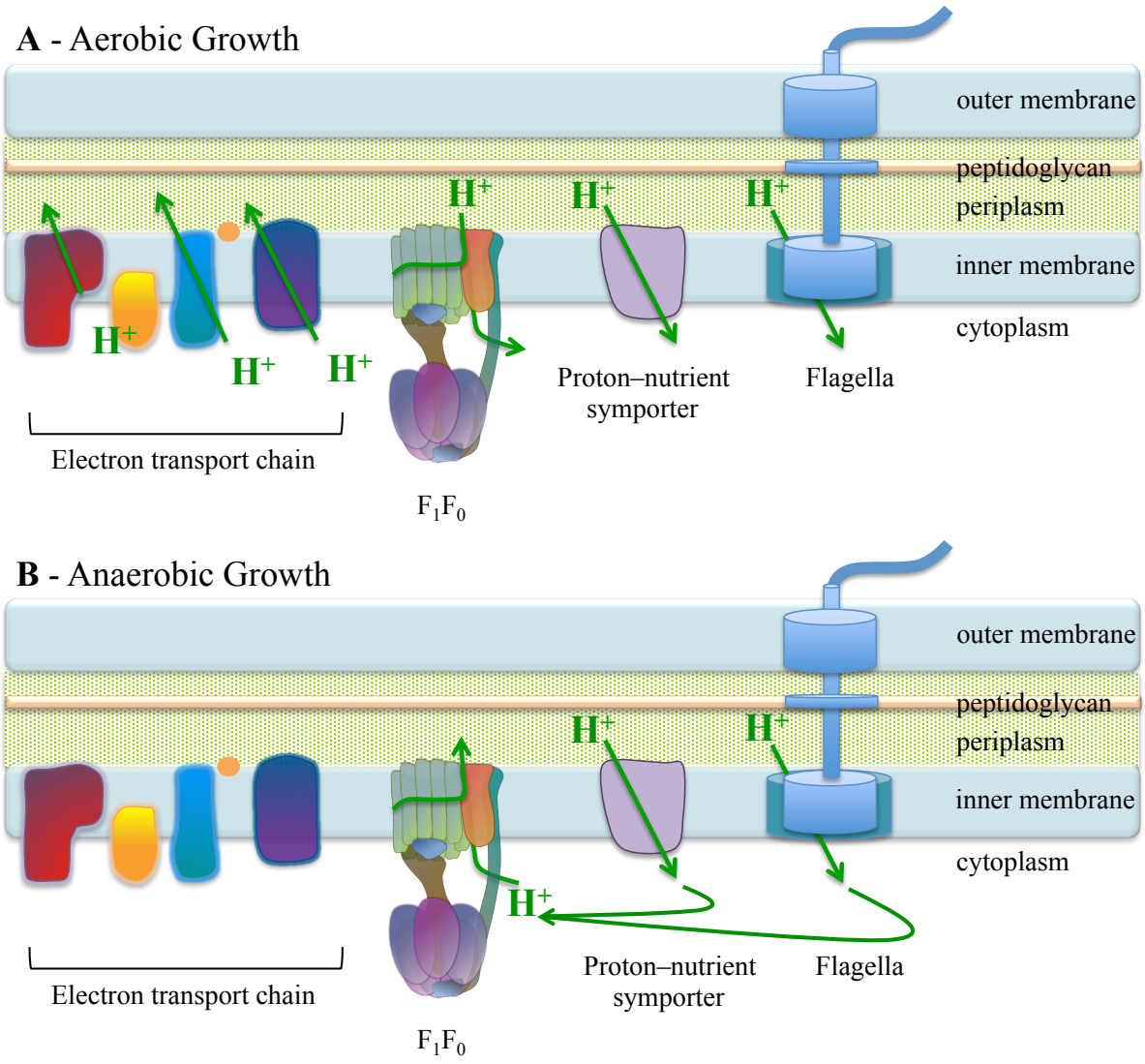

Figure 2.2: Proton cycling in *E. coli* cells. Under aerobic growth conditions (A) the electron transport chain maintains the proton gradient, which drives the synthesis of ATP through F_1F_0, and supports proton-nutrient symporters and flagellar movement. Under anaerobic conditions (B) the electron transport chain is silent and F_1F_0 hydrolyzes ATP to actively pump protons into the periplasmic space. Proton-nutrient symporters and flagella use the gradient generated by F_1F_0 to maintain activity.

2.2 F_1F_0-ATPase: form and function.

ATP synthase is a molecular rotary motor (Yoshida *et al.*, 2001) that catalyzes synthesis and hydrolysis of ATP coupled with the movement of protons across lipid membranes. ATP synthase is responsible for producing the bulk of ATP required by cells. It is a ubiquitous enzyme that has a similar structure in plants, animals and bacteria. ATP synthase is found in

the inner mitochondrial membrane of eukaryotic cells, the inner cellular membrane of bacteria, and in the thylakoid membrane of plant chloroplasts.

All forms of F_1F_0 ATPase contain an extramembranous F_1 complex which catalyzes synthesis or hydrolysis of ATP, and a transmembrane F_0 complex which facilitates transport of protons across the lipid membrane. The complete primary sequence of the ATP synthase subunits from *E. coli* was first determined in 1984 (Walker *et al.*, 1984). In *E. coli,* the F_1 complex is composed of five subunits, named α,β,γ,δ, and ε, that have molecular weights of 55.3 kDa, 50.3 kDa, 31.6 kDa, 19.3 kDa and 14.9 kDa respectively. The F_1 subunits are present in a ratio of $\alpha_3\beta_3\gamma\delta\varepsilon$ (Yoshida *et al.*, 1979). The F_0 complex is made up of three subunits, *a, b* and *c,* that have molecular weights of 30.3 kDa, 17.3 kDa and 8.3 kDa, respectively; and are present in a stoichiometry of $a_1b_2c_{10}$ (Jiang *et al.*, 2001). Figure 2.3 illustrates the interactions between the complexes of the enzyme.

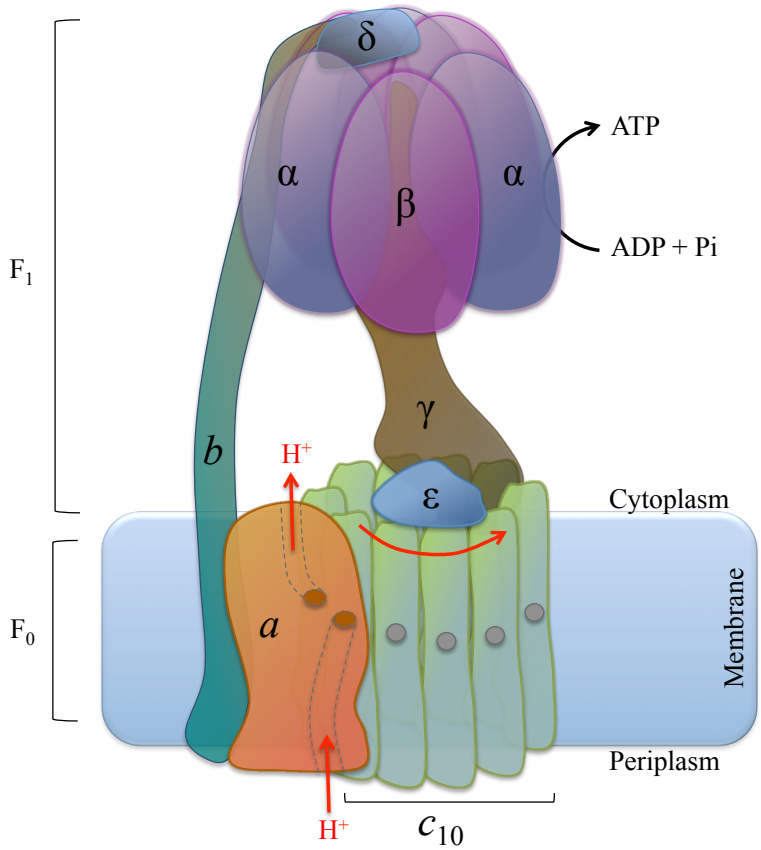

Figure 2.3: *E. coli* ATP synthase and its orientation in the lipid bilayer. The direction of proton flow is shown for ATP synthesis. The proton channel is shown at the interface of subunit *a* and the c_{10} ring.

ATP synthase contains three catalytically active sites, located within the $\alpha_3\beta_3$ hexamer, which work in a sequential cooperative mechanism to produce ATP. The stator of the ATP synthase motor is composed of subunits *a* and *b*. The *b* subunit also functions to hold the $\alpha_3\beta_3\delta$ components of F_1 stationary. The rotor of ATP synthase is made up of the *c*-ring, subunit γ, and subunit ε. One end of the γ shaft is accommodated in the hollow core of the $\alpha_3\beta_3$ hexamer and the other rests on top of the *c*-ring. During ATP synthesis, protons flow through the F_0 sector from the periplasmic side of the membrane to the cytoplasm. Subunit *a* and the *c*-ring are both components of the proton channel. Subunit *a* contributes two-half channels which shuttle protons to and from the *c*-ring. Protons bind to the individual *c* monomers and induce the stepwise rotation of the $c_{10}\gamma\varepsilon$ rotor. The γ subunit is asymmetrical and interacts with each of the three β subunits differently; rotation of γ causes conformational changes in the β active sites which allow for the binding of ADP and inorganic phosphate (P_i), catalysis, and release of synthesized ATP. The catalytic cycle is reversible and ATP can be actively hydrolyzed in the F_1 portion of the enzyme to drive proton transit across the membrane.

2.3 Molecular structure of ATP synthase.

The complete structure of ATP synthase from *T. thermophilus* was recently solved by cryo-electron microscopy (cryo-EM) (Lau and Rubinstein, 2011). The 9.7 Å resolution structure of the intact enzyme is the first of its kind and provides a comprehensive structural picture of ATP synthase (Figure 2.4). There is also large body of high resolution structural work on ATP synthase. The cryo-EM structure of intact ATP synthase converged well with available high resolution structures of individual subunits from *T. thermophilus* and provides a detailed understanding of how the individual subunits interact to form the mature enzyme. Unlike *E. coli* ATP synthase, *T. thermophilus* ATP synthase has two peripheral stalks, which are equivalent to the single b_2 stalk in *E. coli.* The peripheral stalks interact directly with the I subunit (equivalent to subunit *a* in *E. coli*) and function to hold the catalytic head of the enzyme in position above the rotational components.

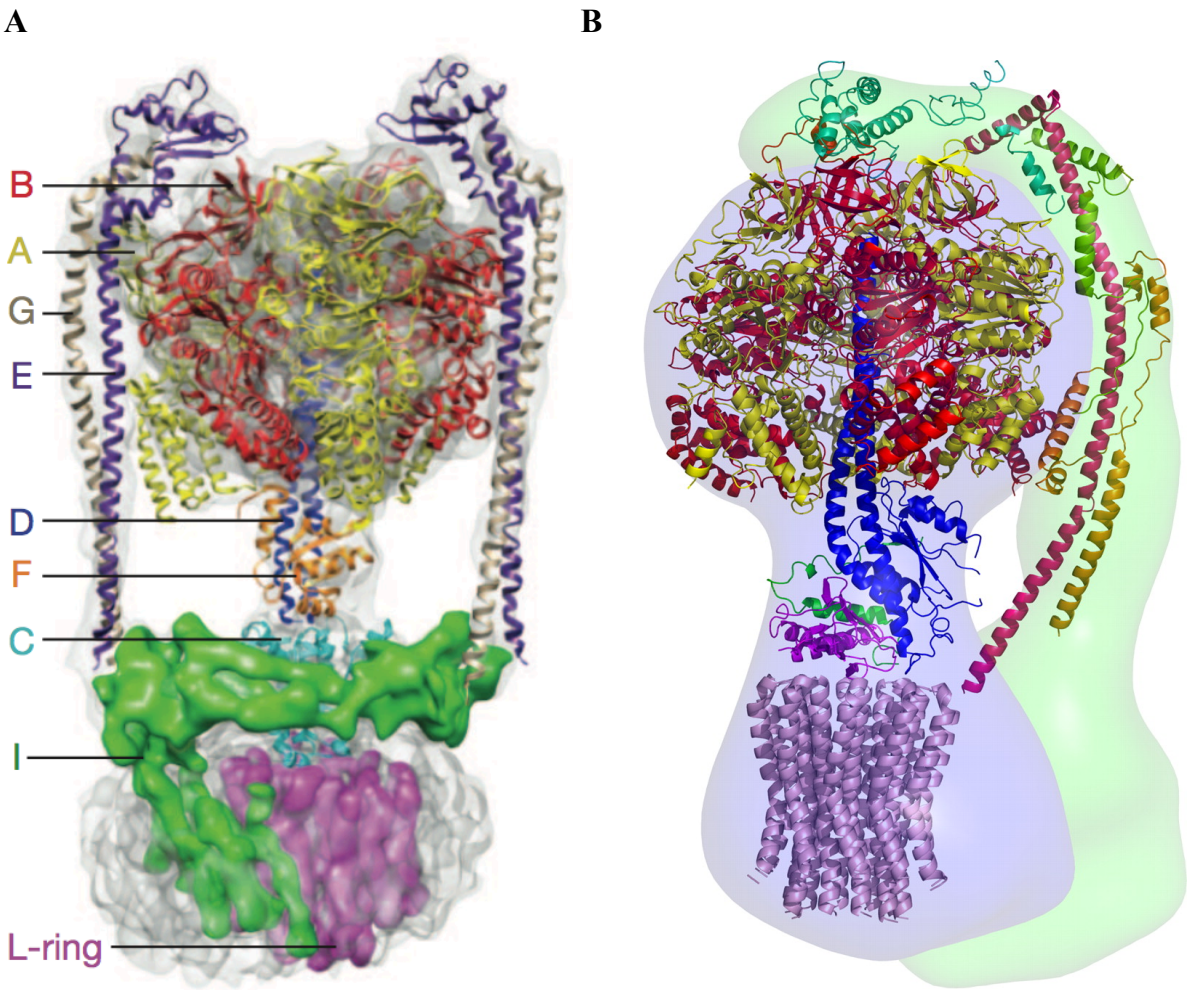

Figure 2.4: Mosaic diagrams of ATP synthase from *T. thermophilus* (A) and bovine mitochondrial ATP synthase (B). The cryo-EM shells are shown as transparent grey for the *T. thermophilus* structure and purple / green for the mitochondrial ATP synthase structure. Ribbon diagrams of high resolution crystal structures from individual subunits were fitted into the cryo-EM maps and are shown in a variety of colors. The 9.7 Å resolution cryo-EM structure from *T. thermophilus* provides the first structural view of subunit I (equivalent to subunit *a* in *E. coli*) and its interaction with subunit L (equivalent to subunit *c* in *E. coli*); subunits I and L are shown in green and purple respectively (Panel A). [Images taken from (Lau and Rubinstein, 2011; Rees *et al*., 2009)]. Images reprinted with permission from Nature and PNAS.

High resolution structural data is available for nearly all F_1 subunits, in a variety of species. The first detailed structural picture of the catalytic machinery came from John Walker's group in 1994 (Abrahams *et al*., 1994). Abrahams and co-authors solved the 2.8 Å resolution crystal structure of the $\alpha_3\beta_3$ hexamer along with the γ subunit from bovine

mitochondrial ATP synthase (Figure 2.5). The high resolution structure from Walker's group gave detailed insight into the catalytic cycle of ATP synthase. The structure showed that three active sites are present at the interface of each αβ pair and that the bulk of the binding site is located in the β subunit. The structure also showed the central location of the γ subunit in the core of the $\alpha_3\beta_3$ hexamer. The intrinsic asymmetry of the γ subunit allows it to interact with each of the β subunits differently, creating the conditions necessary to drive the catalytic cycle in the three active sites in a sequential fashion.

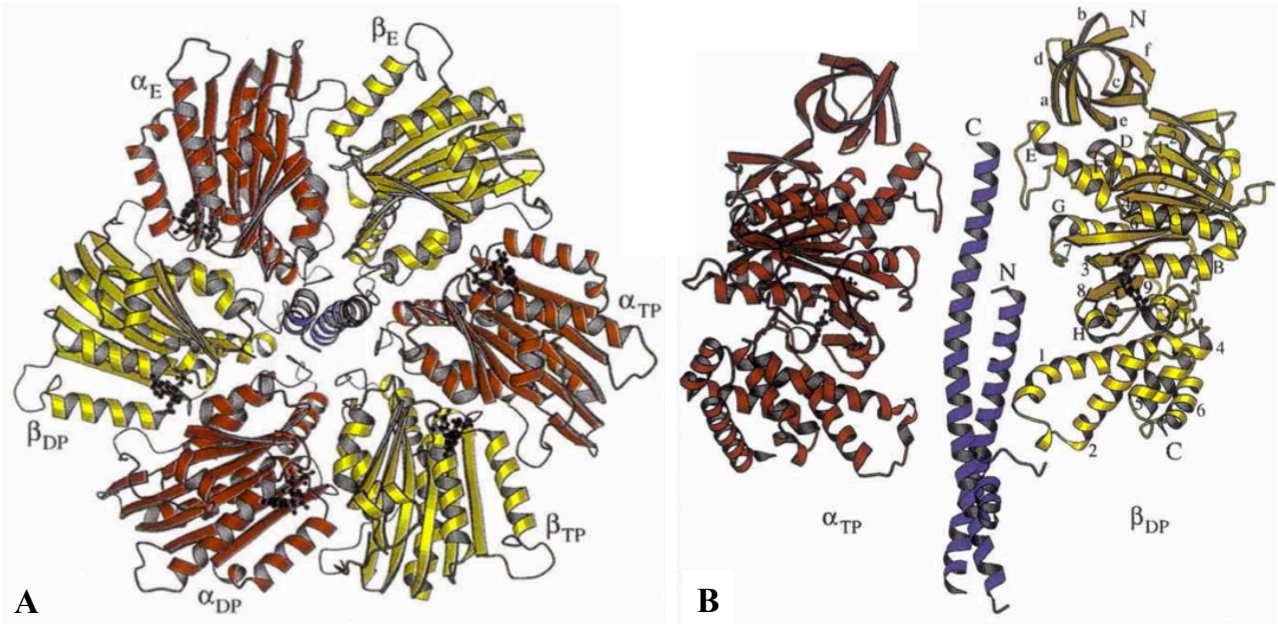

Figure 2.5: Crystallographically determined structure of F_1 ATPase. The γ subunit is shown in purple and the α and β subunits are shown in red and yellow respectively. A) Top down view of the $\alpha_3\beta_3$ hexamer. The empty, loose, and tight binding sites are labeled $\alpha\beta_E$, $\alpha\beta_{DP}$, and $\alpha\beta_{TP}$ respectively. B) Cross section of F_1 viewed from the side. Alpha helices are labeled with letters A – I and beta sheets are labeled with numbers 1 – 9. [Images taken from (Abrahams *et al.*, 1994) and modified; PDB-ID 1C0W]. Reprinted with permission from Nature.

Both the δ and ε subunits of the F_1 domain have been extensively characterized and high resolution structures are available for each (Uhlin *et al.*, 1997; Wilkens *et al.*, 1997; Wilkens and Capaldi, 1998). The δ subunit of *E. coli* ATP synthase is believed to facilitate the tight binding of the F_1 and F_0 sectors through interactions with both subunit α of F_1 and subunit *b* of F_0 (Rodgers *et al.*, 1997; Wilkens *et al.*, 2005). The ε subunit of *E. coli* ATP synthase stably interacts with both the γ shaft (Rodgers and Wilce, 2000) and the cytoplasmic loops of the *c*-

ring (Gibbons *et al.*, 2000). Several groups have conclusively demonstrated that the conformational state of ε plays an important role in regulating the ATPase activity of the F_1 domain. The ε subunit may either adopt an inhibitory 'upward' conformation in which C-terminal domain interacts with the αβ subunits of the catalytic head, or an un-inhibitory 'downward' conformation which does not make contact with $\alpha_3\beta_3$ (Hasurath *et al.*, 2001; Tsunoda *et al.*, 2001; Wilkens and Capaldi, 1998).

In contrast to the detailed structural models for F_1 from various species, the structural features of the F_0 domain are less well known. The general structure of the F_0 domain has been determined by atomic force microscopy (Singh *et al.*, 1996; Takeyasu *et al.*, 1996) and electron microscope scanning (Birkenhager *et al.*, 1995). These techniques have shown that subunit *a* and the *b* dimer lie at the periphery of the c_{10} ring. Subunit *b* has been shown to preferentially interact with subunit *a* (Stalz *et al.*, 2003), but direct interactions with subunit *c* have also been observed (Jones *et al.*, 2000). Furthermore, subunit *a* has been shown to lie counterclockwise of subunit *b* when the ATP synthase complex is viewed from the cytoplasm (Duser *et al.*, 2008).

Subunit *b* functions as a peripheral stalk that holds F_1 and F_0 together; it is a 156 amino acid helical protein (Walker *et al.*, 1984) that is composed of two distinct domains. The N-terminal domain, which is a single transmembrane alpha helix, anchors the elongated soluble C-terminal domain to the lipid bilayer (Walker *et al.*, 1984). In *E. coli*, two *b* subunits form a dimer that protrudes ~110 Å into the cytoplasm where it forms strong interactions with the α and δ subunits of F_1 (Dunn and Chandler, 1998; McLachlin and Dunn, 2000; Rodgers and Capaldi, 1998). The structures of the soluble C-terminal domain and transmembranous N-terminal domain of subunit *b* have been solved separately (Dmitriev *et al.*, 1999a; Del Rizzo *et al.*, 2002). The transmembrane segments of the *b* dimer appear to cross the membrane in a nearly parallel orientation (approximately 23^o) with a close association between the monomers. Crosslinking between the dimers at positions 2, 6, and 10 indicates that they are 4 – 8 Å apart.

Several independent studies have demonstrated that subunits *a* and *b* interact closely. Staltz and co-authors successfully co-purified subunit *b* with hexahistidine tagged subunit *a* in stoichiometric amounts (Stalz *et al.*, 2003). The first cytoplasmic loop of subunit *a* has been

implicated in interactions with subunit *b* (Long *et al.*, 2002). The central region of cytoplasmic loop 1 (residues 75-90) was found to be inaccessible to site specific labeling. Long *et al.* postulated that this region was likely involved in protein – protein interactions with subunit *b* and was therefore shielded from labeling. They also demonstrated that *a*K74C forms crosslinks with an unknown partner in subunit *b*, supporting the involvement of subunit *a*'s first cytoplasmic loop in the ab_2 interaction. Other crosslinking studies have also been conducted to assess the interactions between subunits *a* and *b*. Residue 2 of subunit *b* has been shown to be in close proximity to *a*G227 and *a*L228 through double cysteine substitution and crosslinking analysis (Fillingame *et al.*, 2000). Hermolin and co-authors as well as Aris and co-authors independently observed crosslinking between subunits *a* and *b*, although the actual contact points were not named (Aris and Simoni, 1983; Hermolin *et al.*, 1983). *b*R36C and *b*A32C were shown to form crosslinks to unidentified residues in subunit *a* (Greie *et al.*, 2000; McLachlin *et al.*, 2000). *a*P240 has also been shown to interact directly with *b*G9 by mutation studies (Kumamoto and Simoni, 1986).

Double cysteine replacement studies have shown that the amino acid at position 2 of subunit *b* forms strong crosslinks with positions 74, 75 and 78 of subunit *c* (Jones *et al.*, 2000). These interactions occur in the periplasmic space. To date, no crosslinking residues between subunit *b* and subunit *c* have been found within the transmembrane segments. The lack of direct contact in the transmembranous regions suggests that subunits *b* and *c* are not involved in close structural interactions. Jones and co-authors demonstrated that only one *c* subunit interacts directly with subunit *b* (Jones *et al.*, 2000). Whether both *b* subunits interact with a single *c*, or if one *b* subunit is involved in the interaction and the other is displaced farther to the periphery remains unknown.

The *c* subunit of F_0 spans the lipid membrane twice and has an alpha-helical hairpin arrangement (Girvin *et al.*, 1998). Each *c* promoter contains a highly conserved aspartic acid or glutamic acid residue, located centrally in the membrane slab, which functions to transport protons. In *E. coli,* ten copies of the *c* subunit form a ring structure in the complete enzyme (Jiang *et al.*, 2001) and aspartic acid 61 is the proton carrier. The high resolution structure of the *c*-ring from the sodium transporting ATP synthase of *I. tartaricus* was first solved in 2005

(Meier *et al.*, 2005). Atomic level resolution structures are also available for the *c* rings of the proton transporting ATP synthases from *P. sativum* (Saroussi *et al.*, 2012), *S. cerevisiae* (Symersky *et al.*, 2012), *B. pseudofirmus* (Preiss *et al.*, 2010), *S. oleracea* (Vollmar *et al.*, 2009), and *S. platensis* (Pogoryelov *et al.*, 2009). Figure 2.6 shows the structure of the proton transporting *S. cerevisiae c*-ring.

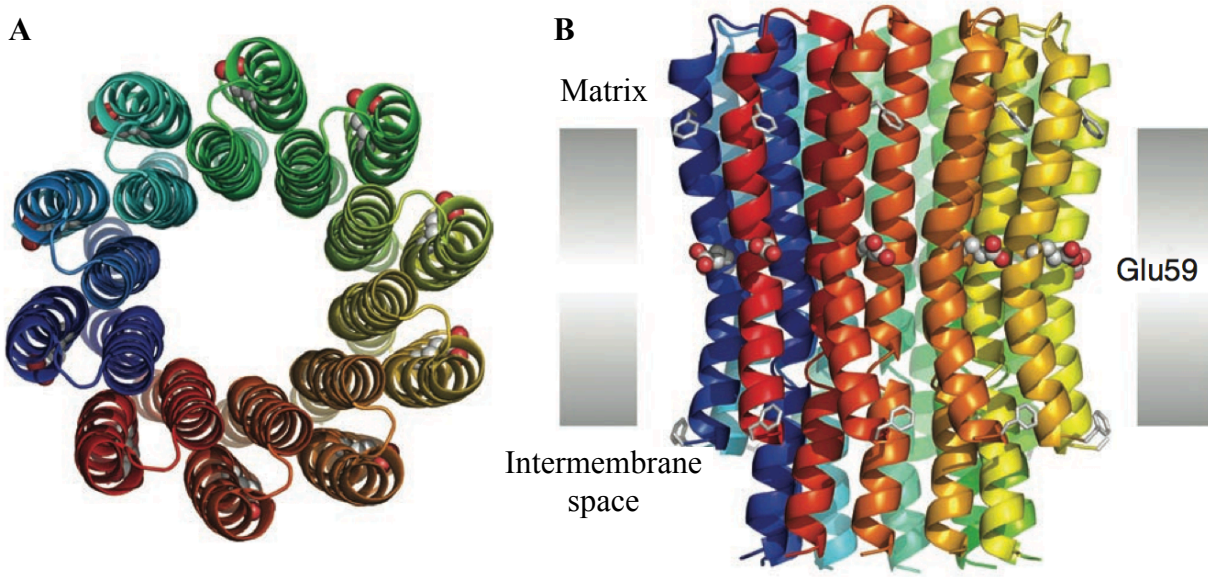

Figure 2.6: Crystallographically determined structure of the *S. cerevisiae* mitochondrial *c*-ring. A) Top down view. B) Side view. The position of the E59 (D61 in *E. coli*) is shown as a space filling model. In both panels each monomer is a different color for ease of distinction. [Image taken from (Symersky *et al.*, 2012), PDB-ID 3U2F]. Reprinted with permission from Nature.

The structure of *E. coli* monomeric subunit *c* has been solved by NMR (Girvin *et al.*, 1998) and the oligomeric ring has been modeled (Dmitriev *et al.*, 1999b; Rastogi and Girvin, 1999). The oligomeric models are based on extensive cross linking analyses between the transmembrane helix (TMH) segments of neighboring *c* subunits (Jones *et al.*, 1998). The cross linking studies that allowed positioning of the *c* subunits relative to one another have recently been further supported by solid state NMR investigations which placed I55, A62 and G69 and F76 on the outer surface of the oligomer (Todokoro *et al.*, 2010). In these models the *c*-ring contains twelve monomers, which was based on the expression of functional *c*-rings built of genetically fused *c* dimers and trimers that produced rings containing the equivalent of a

maximum of twelve *c* monomers (Jones and Fillingame, 1998). However, the *c*-ring is now known to be composed of ten individual *c* monomers (Jiang *et al.*, 2001) rather than twelve. The decameric *c*-ring has also been modeled and agrees well with the constraints used for the model presented by Rastogi and Girvin (Fillingame and Dmitriev, 2002).

The cryo-EM structure of the intact proton translocating ATP synthase from *T. thermophilus* (Lau and Rubinstein, 2011) gives the first true images of how subunit *a* and c_{10} ring interact. This work shows that subunit I, equivalent to subunit *a* in *E. coli*, is made up of two four-helix bundles and each bundle makes physical contact with two adjacent L subunits (*c* subunits in *E. coli*). Hakulinen and co-authors also used cryo-EM to solve the 7.0 Å structure of crystallized F_0 from *I. Tartaricus* (Hakulinen *et al.*, 2012). Their findings supported the work presented by Lau and Rubinstein and showed that subunit *a* forms a four-helix bundle and two individual helices interact directly with two *c* subunits. Taken together with the work of Lau and Rubnistein, Hakulinen and co-authors postulated that the four helix bundle is a conserved feature of subunit *a*. However, the electron density maps showed that three helices from the stator were in contact with the *c*-ring; the authors were not able to distinguish if the third *c*-helix was involved in interaction of subunit *a* or *b.*

2.3.1 Structural investigations into subunit *a*.

Transmembrane topology.

The transmembrane topology of *E. coli* subunit *a* has been established independently by three different groups of authors. Currently, subunit *a* is believed to contain five TMH segments with the amino terminus located in the periplasmic space and the carboxyl terminus located in the cytoplasm. Subunit *a* does not contain cysteine in its native form and cysteine substitution mutagenesis has been used extensively to investigate its structural elements. Fillingame's group conducted cysteine replacement studies where individual residues in the extramembranous regions of subunit *a* were systematically mutated to cysteine, and probed using sulfhydryl reagents (Valiyaveetil and Fillingame, 1998). Reciprocal labeling patterns were observed when inside-out and right-side-out membrane preparations were probed; indicating the cytoplasmic or periplasmic location of each residue tested. Residues placed on the cytoplasmic side of the membrane in this study were V71, M266, K169, and E196; and

residues placed on the periplasmic side of the membrane were S3, E131, P230. The findings of this study were supported by the work of Long and co-authors, who used the reciprocal reaction of 3-(*N*-maleimidylpropionyl)-biocytin (MBP), a cysteine binding probe, and 4-acetamido-4′-maleimidylstilbene-2,2′-disulfonic acid (AMS), a compound that blocks reaction of MBP, to probe single cysteine substitution mutants (Long *et al.*, 1998). Positions S69, G172, K176 and H271 were placed on the cytoplasmic side of the membrane, and P8, R24, S27 and E131 were placed on the periplasmic side of the membrane in these studies. The five helix model was further supported by Wada and co-authors, who used an in-cell method to label the periplasmic loops of subunit *a* (Wada, 1999). Whole cells were treated with polymyxin B nanopeptide to permeabilize the outer membrane and make the periplasmic space accessible to MPB labeling. The cytoplasmic loops remained inaccessible to labeling. In this study, residues A2, S27, T37, E131, P230, W231 and W232 were placed in the periplasmic space. Figure 2.7 summarizes the residues placed in the cytoplasmic and periplasmic loops of subunit *a*.

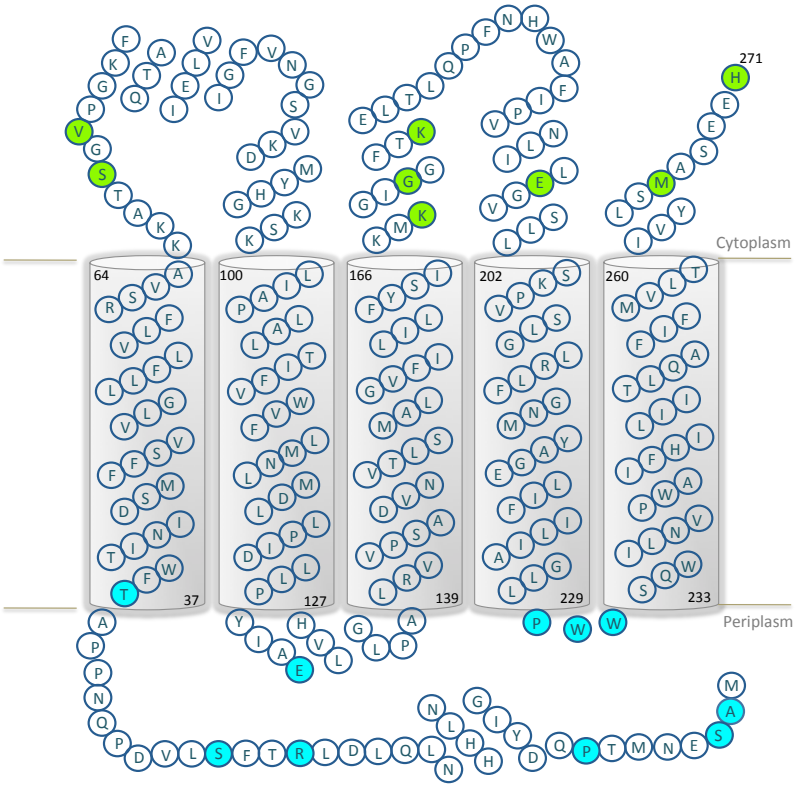

Figure 2.7: Residues of the *a* subunit probed for cytoplasmic and periplasmic accessibility. The TMH segments of subunit *a* are shown in grey. The residue number at membrane entrance and exit of each TMH is indicated. Residues identified as cytoplasmic are shown in green and residues identified as periplasmic are shown in blue. [The subunit *a* model in this Figure was adapted from (Vik *et al.*, 2000)]. Reprinted with permission from BBA.

Assembling the helix bundle.

Extensive biochemical analyses have been conducted to determine the interactions between the TMH segments of subunit *a*. They include: 1) second site suppressor mutation studies, 2) double cysteine substitutions and cross-linking analysis, 3) chemical labeling combined with proteolysis, 4) spin label difference nuclear magnetic resonance (NMR), and 5) site-directed mutagenesis.

Second site suppressors are point mutations that partially or completely restore loss of enzymatic function that is caused by a primary mutation at a different locus. Second site suppressor mutations are indicators of close spatial proximity between the residues involved and can be used to elucidate tertiary structural elements. Six suppressor mutant pairs have been identified in subunit *a* of *E. coli* ATP synthase. They are, G213N – L251V (Kuo and Nakamoto, 2000), E219C – A145E, H245C – D119H (Valiyaveetil, 1998), R210Q – Q252R (Hatch *et al.*, 1995), H245G – G218D/K (Hartzog and Cain, 1994), and E219H – H245E (Cain and Simoni, 1988). Although these suppressor pairs provide a rough approximation of how helices II, III, IV and V align with one another, they do not offer a clear representation of how the helical faces interact (Figure 2.8-A).

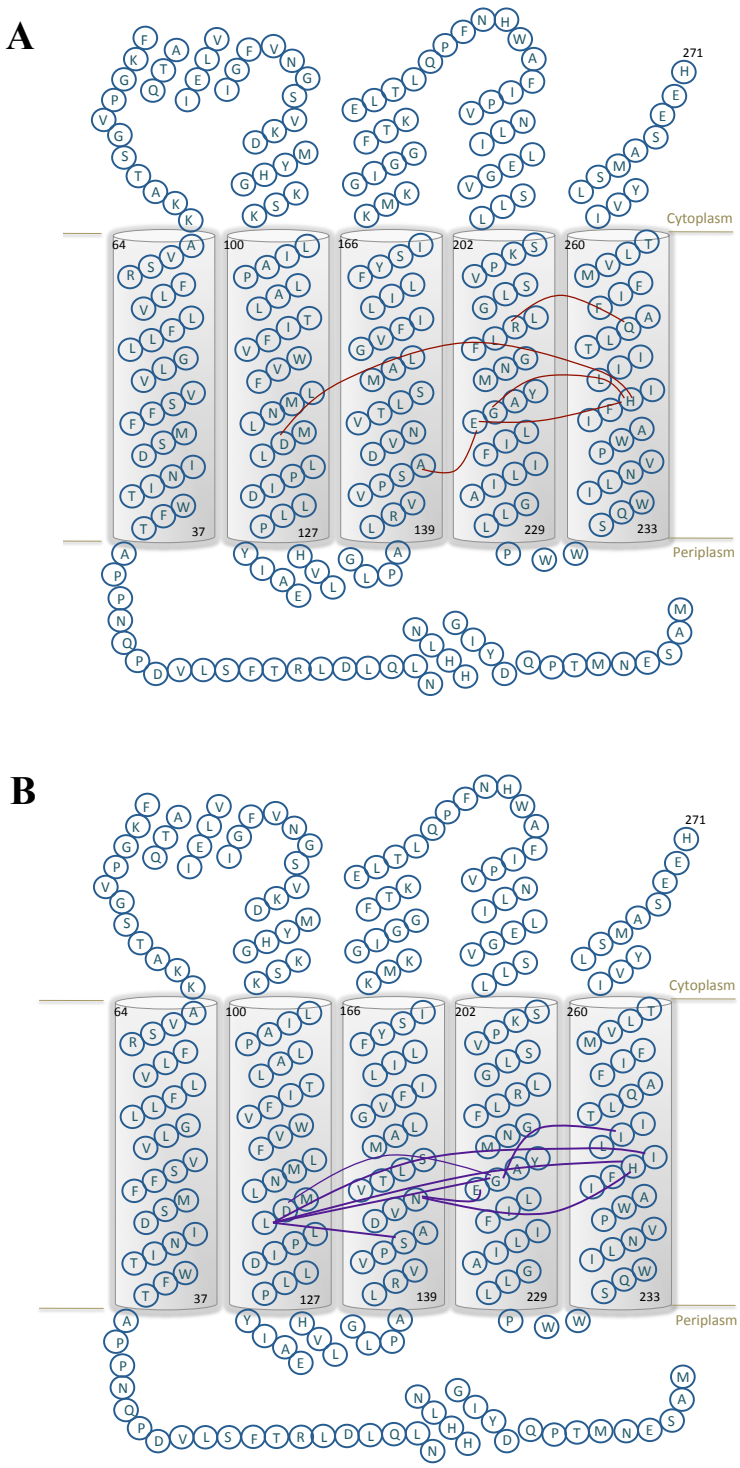

Figure 2.8: Subunit *a* residue pairs involved in second site suppression and zero distance crosslinking. A) Second site suppressor mutants. Residues involved in each suppressor pair are connected by red lines. B) Cross links between transmembrane helical segments. Residue pairs, substituted for cysteine, found to form zero distance disulfide bonds are connected with purple lines. [The subunit *a* model in this figure was adapted from (Vik *et al.*, 2000)]. See text for references. Reprinted with permission from BBA.

The helical packing arrangement determined by the second site suppressor data was supported and further defined by a series of crosslinking experiments (Schwem and Fillingame, 2006). Schwem and Fillingame introduced pairs of cysteine substitutions in different regions of subunit *a* and analyzed the proximity of the sulfhydryl group pairs that formed disulfide bonds in the presence of oxidizing reagents. Nine pairs of cysteine substitutions were demonstrated to be in close spatial proximity through the formation of zero-distance crosslinks: L210 – H144, L120 – G218, L120 – H245, L120 – I246, N148 – E219, N148 – H245, G218 – I248, D119 – G218 (Figure 2.8 B).

The work of Zhang and Vik supports the placement of suppressor pair 119 – 245. They demonstrated that W241 of TMH-V faces TMH-II using a chemical proteolysis approach that cleaves peptide bonds in close proximity to the locus of a covalently bound proteolytic probe (Zhang and Vik, 2003b). This work also provided the first evidence on the spatial orientation of TMH-I in relation to the rest of the helix bundle; D44 of helix I was shown to be oriented toward TMH-II using the same proteolytic approach.

PROXYL is a paramagnetic spin label that is commonly used in conjunction with NMR techniques to investigate membrane protein topography and inter-residue distances across space (Hubbell *et al.*, 1998). The presence of an unpaired electron on the spin label causes rapid relaxation of the neighboring nuclei. Residues within 15 – 20 Å of the spin label can be identified on HSQC or TROSY spectra. The interactions between TMH-IV and TMH-V were investigated using spin label difference NMR in a mixed organic solvent (Dmitriev *et al.*, 2008). Dmitriev and co-authors introduced the PROXYL spin label at positions 222 and 223, and observed broadening of tryptophan signals at positions 231, 232, 235 and 241. The spin label difference data was converted into distance constraints and residues 213, 232, 235 and 241 were calculated to lie with in 21.5 Å of residues 222/223. These experiments indicated that TMH-V and TMH-IV fold back on one another via a hairpin loop that stretches from residue 234 to 239. They also showed that the periplasmic ends of transmembrane spans IV and V lie adjacent to one another and the distance between the helical faces widens at an approximate thirty degree angle as the TMHs approach the cytoplasmic side of the membrane.

Howitt and co-authors used site directed mutagenesis to probe a cluster of charged residues on the periplasmic ends of TMHs I, II and III for structural interactions (Howitt *et al.*, 1990). They demonstrated that D44, D124 and R140 are not directly involved in proton transport and are more likely involved in structural stability of the *a* subunit. Individual mutations at positions 44, 124 and 140 partially disrupted proton transport. Mutation of D44 to asparagine in conjunction with either D124N or R140Q abolished oxidative phosphorylation. However, when the D124N and R140Q mutations were combined, proton transport was restored to the level seen in the individual mutants, suggesting that D124 and R140 likely form a salt bridge that stabilizes the structure of subunit *a*. Howitt and co-authors also suggest that the salt bridge between D124 and R140 is not an obligatory requirement for subunit *a* stability. The 124 – 140 salt bridge only becomes essential when D44 is also mutated; suggesting that D44 is involved in a second stabilizing salt bridge pair with another unknown residue. It appears that stability of subunit *a* is dependent on at least one of these salt bridge interactions remaining intact.

The TMH segments of subunit *a* can be treated as rigid bodies that conform to standard helical torsion angles and hydrogen bonding constraints. Residues involved in zero distance crosslinks, salt bridges, and second site suppression on adjacent helices are expected to face one another. Interaction of subunit *a*'s R210 with subunit *c*'s D61 is well established and pivitol to functionality of the F_0 domain (Cain, 2000; Valiyaveetil, 1997). TMH-IV is assumed to be oriented outward to allow the critical R210 residue to interact with D61 of subunit *c*.

The loops between the transmembrane segments of subunit *a* have been shown to be structurally important for the functionality of ATP synthase (Moore *et al.*, 2008). Moore and co-authors demonstrated that cytoplasmic loops one and two directly interact with one another using crosslinking experiments; specific interactions between residues V86C – E195C and M93C – E195C were identified. TMHs III and IV are believed to have ordered helical extensions that protrude beyond the 30 Å lipid bilayer and into the cytoplasm (Moore *et al.*, 2008; Zhang and Vik, 2003a). Moore and co-authors also used crosslinking analysis to characterize the interactions between the cytoplasmic helical extensions of TMH III and IV. They found crosslinks between double cysteine substituted mutants at positions, V157 – L203, I161 – S202, I161 – L203, I161 – S205, L160 – L203, L160 – S205, and K165 – S202. A

computational model of TMH-II – TMH-V of subunit *a*, based on the biochemical data described above, is shown in Figure 2.9.

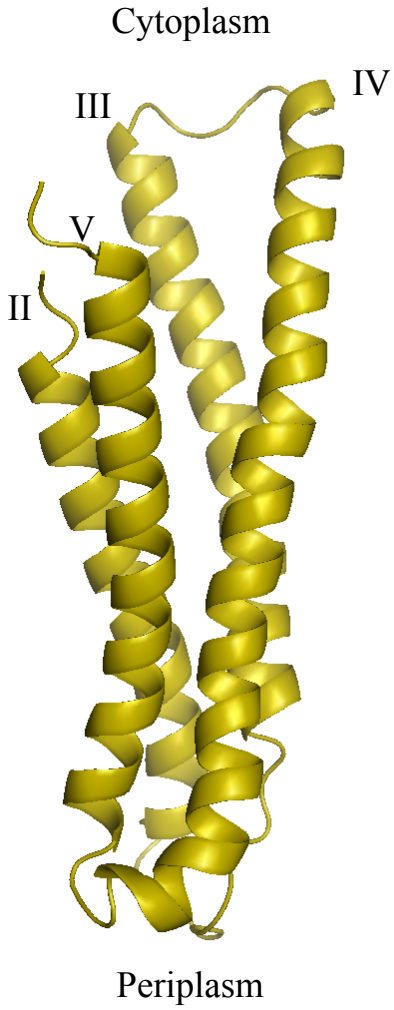

Figure 2.9: Computational model of subunit *a* based on the available biochemical data (Dmitriev, unpublished data). Helices II-V of subunit *a* are shown. The position of TMH-I of subunit *a* is still unclear as only limited biochemical evidence of its position relative to the other TMH segments is available. The periplasmic and cytoplasmic locations of the loops are indicated.

Structural interactions at the a/c interface.

Subunits *a* and *c* are known to interact closely; in *E. coli* ATP synthase the R210 of subunit *a* and the D61 of subunit *c* are known to interact directly and are both critical to proton transport through F_0 (Cain, 2000; Valiyaveetil and Fillingame, 1997). However, the detailed

molecular architecture of the *a*-c_{10} interface remains largely unknown. Similarly to the structural investigations into subunit *a,* the interactions between *a* and *c* have been examined using second site suppressor mutation studies and crosslinking analysis.

Subunit *c* contains a second site suppressor pair for the critical D61 residue. The *c*D61G mutation can be partially rescued by *c*A24D. Third site suppressor mutants to the *c*D61G/*c*A24D mutation have been found in subunit *a*. Fraga and co-authors demonstrated that point mutations at positions A217, I221 and L224 in subunit *a* can restore activity when co-expressed with the *c*D61G/*c*A24D mutation (Fraga *et al.*, 1994). These findings suggest that A217, I221 and L224 lie on one face of TMH-IV of subunit *a* and interact directly with TMH-II of subunit *c*.

Two different studies have identified residues in both TMH-IV and TMH-V of subunit *a* that interact with TMH-II of subunit *c*. The interactions between subunits *a* and *c* have been extensively mapped using site directed mutagenesis to introduce pairs of cysteine residues at key positions in both subunits *a* and *c*. F_0 complexes containing cysteine substitutions in both subunits *a* and *c* were treated with oxidizing agents and examined for dimer formation. The interactions between *a*THM-IV and *c*TMH-II were first described by Jiang and Fillingame (Jiang and Fillingame, 1998). The interaction points between *a* and *c* identified in this study were *a*207 – *c*I55, *a*N214 – *c*A62, *a*N214 – *c*M65, *a*I221 – *c*G69, *a*I223 – *c*L72, *a*L224 – *c*Y73, and *a*I225 – *c*Y73. The distance between the interacting residues is assumed to be approximately 4 – 8 Å, as calculated by zero distance crosslink geometry. In 2008 Moore and Fillingame described the packing interactions between helix five of subunit *a* and TMH-II of subunit *c* (Moore and Fillingame, 2008b). The crosslinking pairs identified in this study were *a*248 – *c*62, *a*248 – *c*63, *a*248 – *c*65, *a*251 – *c*59, *a*251 – *c*62, *a*252 – *c*62, *a*252 – *c*65, *a*262 – *c*53, *a*262 – *c*54, *a*262 – *c*55, and *a*263 – *c*54 (Moore, 2008; Moore and Fillingame, 2008a). TMH-IV and TMH-V of subunit *a* were demonstrated to crosslink to two separate, presumably adjacent, *c* monomers. Figure 2.10 summarizes the crosslinking data that defines the interactions between subunit *a*'s TMH-V and TMH-IV with subunit *c*'s TMH-II.

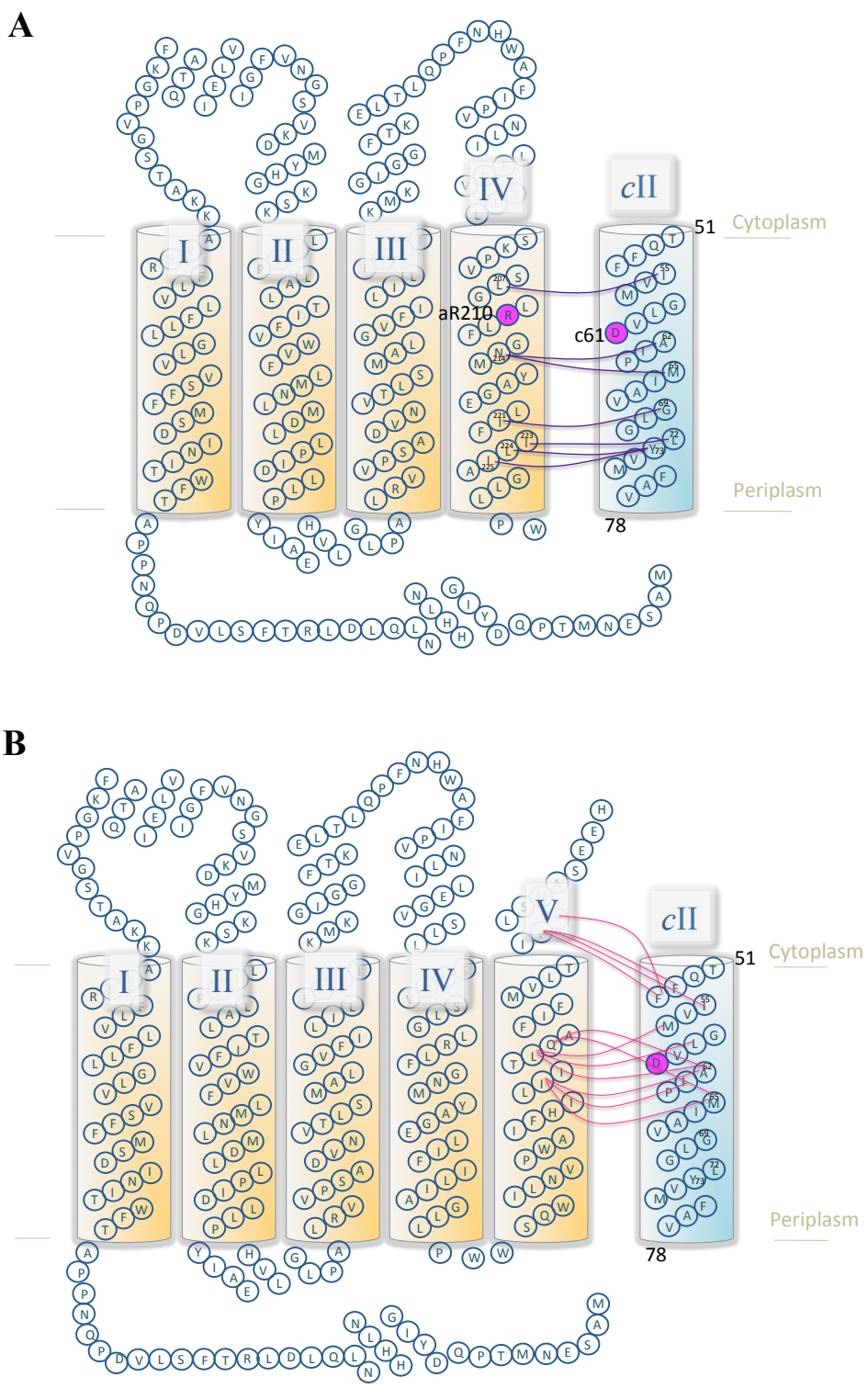

Figure 2.10: Interactions between subunit *a* and subunit *c* determined by crosslinking studies. TMH segments from subunit *a* are colored orange and TMH segments from subunit *c* are colored blue. A) Interactions between TMH-IV of subunit *a* and TMH-II of subunit *c*. B) Interactions between TMH-V of subunit *a* and TMH-II of subunit *c*. See text for references.

The cytoplasmic loops of subunit *a* have also been shown to be involved in direct interactions with subunit *c* through cysteine replacement studies. The loop between transmembrane segments III and IV is known to span approximately 34 amino acids starting at position 168 and ending at 202 (Long, 1998; Vik *et al.*, 1998). N-(3-Maleimidopropionyl) biocytin (MPB) is commonly used to define the extramembranous portions of integral membrane proteins because it reacts with the ionized thiol group on cysteine in the aqueous phase. The loop segment between residues 185 – 202 was shown to be resistant to labeling with MPB (Zhang and Vik, 2003a). Zhang and co-authors postulated that the amino terminal half of the loop was highly aqueous accessible and therefore readily labeled, and that the lack of labeling between positions 185 – 202 was consistent with shielding from MPB by protein – protein interactions. This 185 – 202 region is conserved between species (Appendix-I contains a multiple sequence alignment of subunit *a* from various species), also pointing to specific structural interactions (Vik *et al.*, 1990). Treatment with a photo-activated crosslinking agent caused single cysteine substitutions in the carboxyl terminal part of the loop to crosslink with subunit *c*, demonstrating direct interaction between cytoplasmic loop 2 of subunit *a* and subunit *c*. Although the crosslinking partner residues in subunit *c* are unknown, these results show that residues 165, 169, 173, 174, 177, 178, 182, 183 and 184 of subunit *a* fold within 10 -15 angstroms of subunit *c*. The model of subunit *a* and its interaction with two *c* subunits, based on the biochemical evidence discussed above, is presented in Figure 2.11.

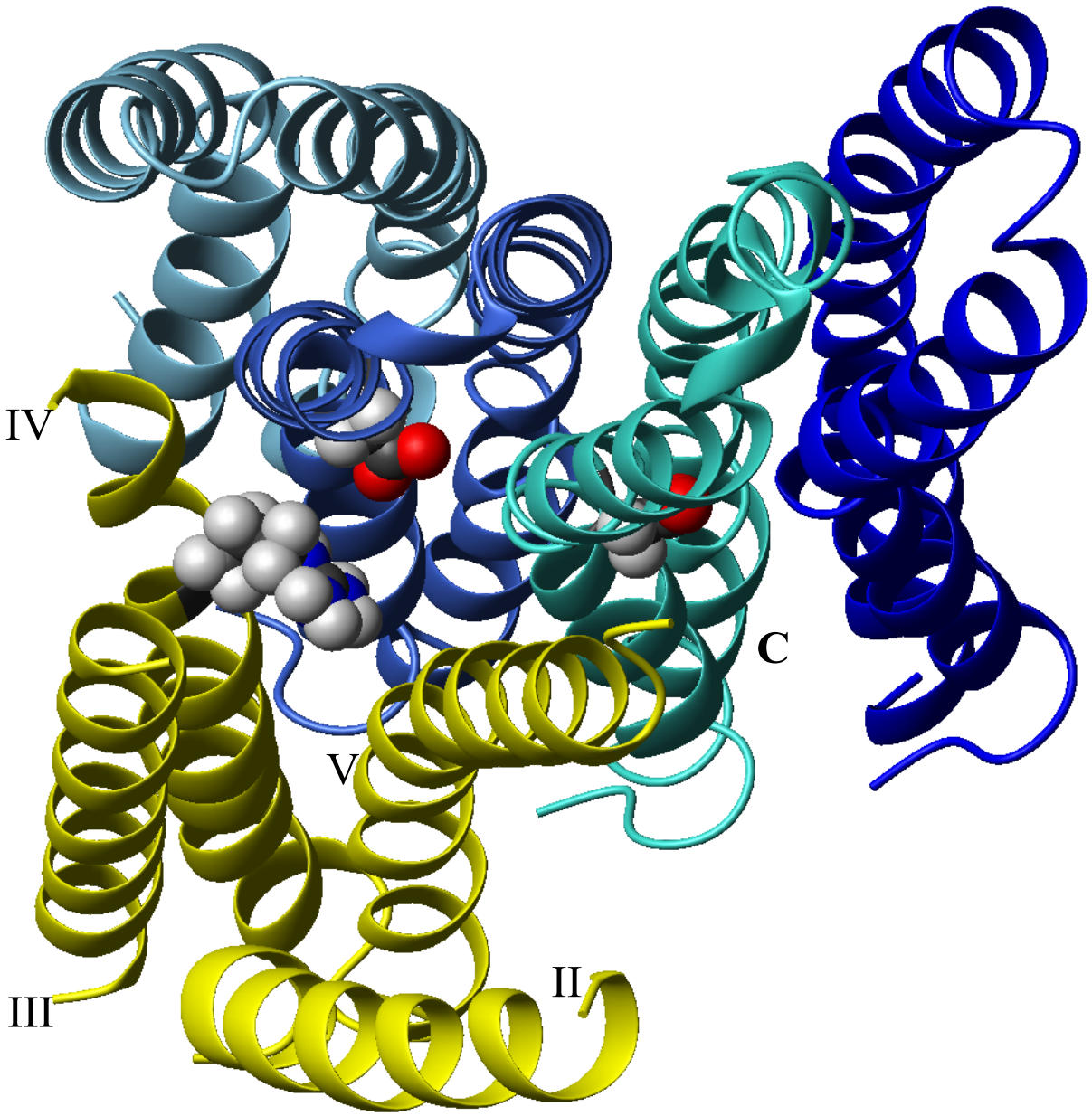

Figure 2.11: Computational model of subunit *a* and its interaction with the *c-ring*. The model is oriented looking downward from the cytoplasm. Helices II - V of subunit *a* are labeled and shown in yellow. The C-terminus of subunit *a* is labeled 'C'. Four copies of subunit *c* are shown in shades of blue. Arginine 210 of subunit *a* and aspartic acid 61 of the two *c* subunits in direct interaction with subunit *a* are shown as spacefilling diagrams.

2.4 The binding change mechanism and rotational catalysis.

Paul Boyer's binding change mechanism describes the process by which ATP synthase produces ATP from ADP and P_i (Boyer, 1993; Boyer, 1979). Two avenues of experimental evidence lead to the introduction of the binding change mechanism. First, the rapid and reversible synthesis and hydrolysis of ATP, measured by O^{18} exchange, continued within the catalytic sites of ATP synthase even after the submitochondrial particles under study were de-energized (Boyer *et al.*, 1973). This suggested that the equilibrium between ATP and ADP / P_i was close to unity, leading Boyer to believe that the energetic barrier to ATP synthesis was release of bound ATP from the active site, rather than formation of ATP itself. Supporting evidence came from Harris and co-authors who conclusively demonstrated the tight binding of ATP to the αβ catalytic sites (Harris *et al.*, 1973). Second, the research groups of Moundrianakis and Boyer independently demonstrated that multiple active sites on ATP synthase worked together sequentially (Adolfsen and Moudrianakis, 1976; Kayalar *et al.*, 1977). Boyer realized that participation of alternating sites and conformational changes between binding states may overcome the energy barrier to allow release of ATP from the binding site, prompting him to propose the binding change mechanism.

The binding change mechanism states that three nonequivalent active sites on F_1 work cooperatively to synthesize ATP (Figure 2.12). At any given time one site adopts the 'tight' conformation, the second site adopts the 'loose' conformation, and the third site adopts the 'empty' conformation. The rotation of the gamma subunit, along with the *c*-ring, relative to the $\alpha_3\beta_3$ hexamer induces conformational changes that allow each heterodimer to cycle through each conformational state. Therefore, the binding of ADP and P_i, formation of ATP, and release of ATP is accomplished in all three active sites with each rotation of gamma. The rotation of γ causing transitions between active site states was termed 'rotational catalysis' (Boyer, 1993). John Walker's F_1 structure supported the basis for the binding change mechanism and rotational catalysis (Abrahams *et al.*, 1994). Paul Boyer and John Walker shared a Nobel prize for their contributions to the field of bioenergetics in 1997.

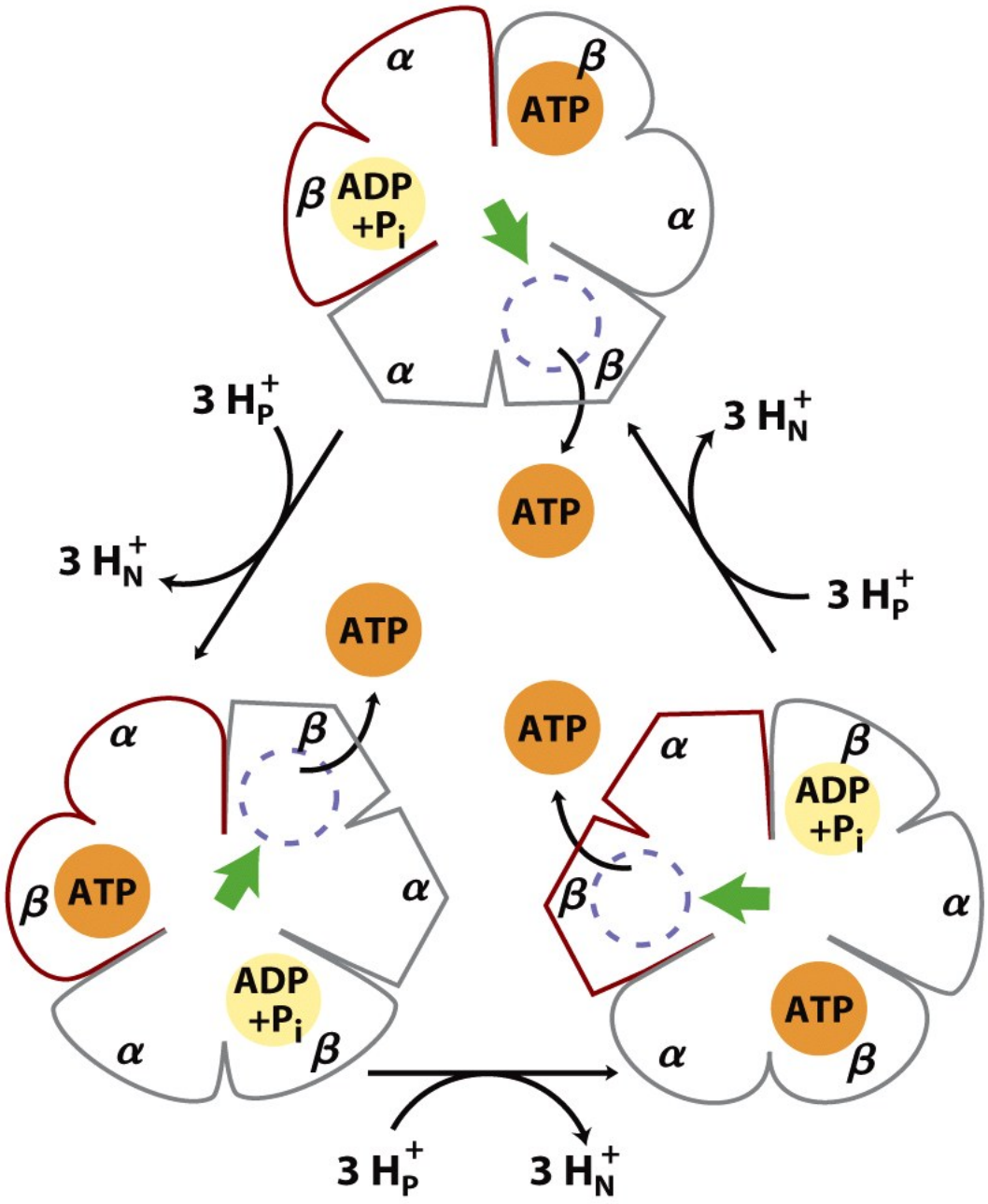

Figure 2.12: Schematic diagram of the binding change mechanism. The $\alpha_3\beta_3$ hexamer is shown in three different binding states (one in each panel). The green arrow in the center of each $\alpha_3\beta_3$ hexamer represents the relative position of subunit γ. The αβ pair bound to ATP is in the 'tight' conformation. The binding site transitions to the 'open' conformation upon ATP release. The αβ pair bound to ADP and P_i is in the 'loose' conformational state. The translocation of protons across the membrane with each successive movement through the conformational states is indicated with black arrows. [Image taken from (Lehninger *et al.*, 2008)]. Reprinted with permission from Freeman & Company / Worth Publishers.

Although Walker's structure confirmed the binding change mechanism, it did not provide direct evidence for rotational catalysis. The first evidence supporting rotational catalysis was provided by Duncan and co-authors (Duncan *et al.*, 1995). Duncan and co-authors used Walker's bovine F_1 structure to identify interacting residues on the γ and β subunits of the *E. coli* homolog; they then introduced the D380C point mutation on subunit β. Crosslinking between γC87 and a particular β subunit containing the D380C mutation immobilized the γ subunit and abolished activity. Reduction of the disulfide bond restored activity and subsequent oxidation caused the γ subunit to crosslink to a different β subunit. Duncan and co-authors demonstrated that γC87 interacted directly with all three β subunits throughout the catalytic cycle using this method. When the disulfide bond was reduced and ATP synthase was left inactive, i.e., in the absence of ATP, the same γβ pair re-formed upon oxidation. The rotational catalysis hypothesis was also supported by (Noji and Yoshida, 2001). Yoshida's group fixed F_1 of ATP synthase to glass slides, using affinity tags on the α subunits, and linked single fluorescent actin filaments to individual γ subunits. Rotation of single filaments was observed by microscopy upon the addition of ATP.

2.5 Molecular mechanisms of torque generation in the F_0 domain.

The mechanism of proton transit through F_0 is not well defined. Arginine 210 of subunit *a* and aspartic acid 61 of subunit *c* are located centrally in the membrane and are both critical to proton transport through F_0 (Cain, 2000; Valiyaveetil and Fillingame, 1997). Mutagenesis studies showed that no tested amino acid substitution at position 210 could sustain ATP synthase function, however, R210A was able to facilitate passive proton transport (Hatch et al., 1995; Valyaveetil and Fillingame, 1997) indicating that R210 is not obligatorily protonated during proton transit. The positive charge of R210 is believed to stabilize the *c*D61 proton carrier through salt bridge interactions (Fillingame *et al.*, 2002; Ishmukhametov *et al.*, 2008) (Figure 2.13).

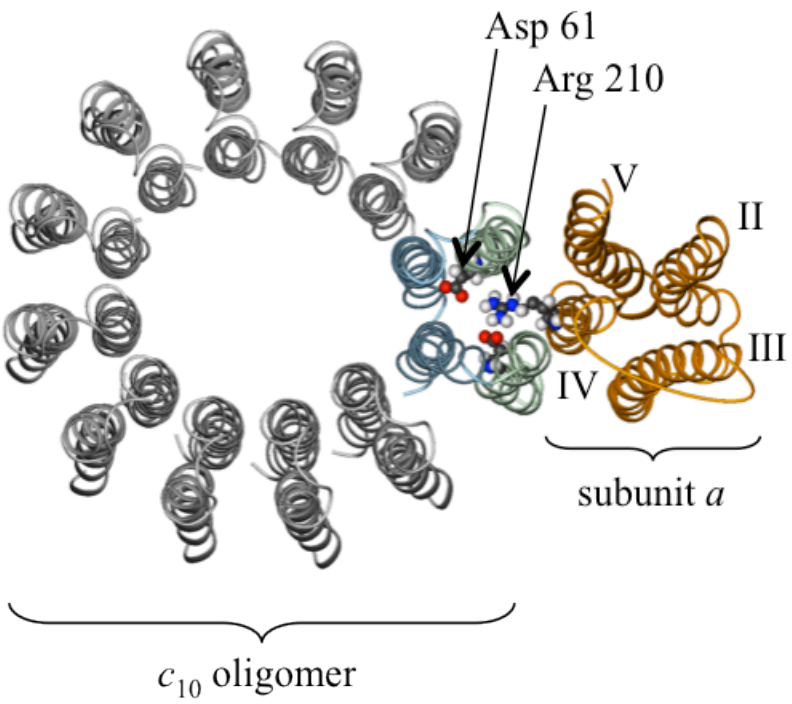

A

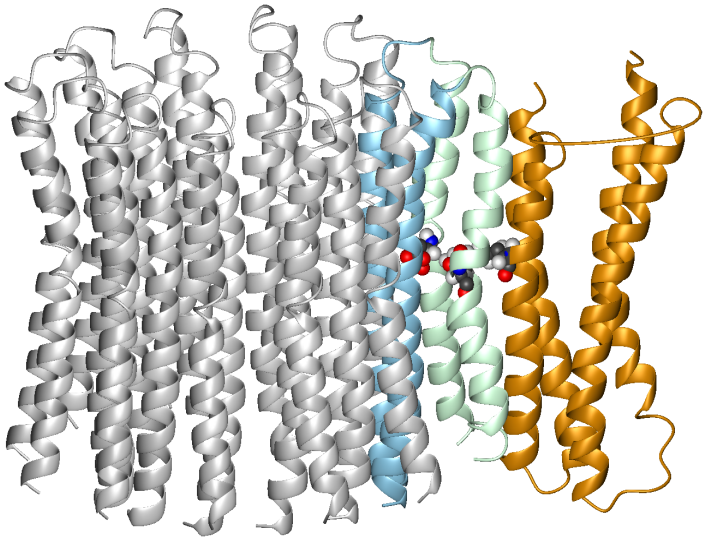

B

Figure 2.13: Computational models of the F_0 complex – Panels 'A' and 'B' show the top and side views of subunit *a* and the c_{10} oligomer, respectively. Twelve *c* subunits are shown but the presently accepted stoichiometry is 10 (Jiang *et al.*, 2001). Subunit *a* is shown in orange (TMHs II – V are numbered with roman numerals). *a*TMH-I is not shown in the models. The two *c* subunits involved in direct interaction with subunit *a* are shown in green and blue, the rest of the c_{10} oligomer is shown in grey. Arginine 210 of subunit *a* and D61 of subunit *c* are both critical for proton transport and their interaction is indicated with arrows. [Image taken from (Rastogi and Girvin, 1999), and modified; PDB-ID 1C17]. Reprinted with permission from Nature.

Junge and co-authors proposed a model in which subunit *a* contains two-half channels that facilitate proton transport through F_0 by shuttling protons to and from the D61 residue of subunit *c* (Junge *et al.,* 1997). Three bodies of experimental evidence support the two-half channel hypothesis: 1) crosslinking studies between subunit *a* and the *c*-ring, 2) structural evidence provided by cryo-EM, and 3) definition of the aqueous access channels by cysteine reactivity with silver ions.

Crosslinking studies aimed at understanding the structural interactions between subunit *a* and the *c*-ring (Kyle J. Moore, 2008; Moore and Fillingame, 2008a; Moore and Fillingame, 2008b), previously discussed in section 2.3.1, demonstrated that TMH-IV and TMH-V of subunit *a* interact with two adjacent *c* monomers. This work was strongly supported by the findings of Lau and co-authors as well as Hakulinen and co-authors. The work of Lau and co-authors showed that subunit I from *T. thermophilus* (equivalent to subunit *a* in *E. coli*) is made up of two four-helix bundles and each bundle makes physical contact with two adjacent L subunits (*c* subunits in *E. coli*) (Lau and Rubinstein, 2011). Hakulinen and co-authors solved the 7.0 Å structure of crystallized F_0 from *I. Tartaricus* (Hakulinen *et al.*, 2012) and found that subunit *a* forms a four-helix bundle and two individual helices interact directly with two *c* subunits. The differential contact points with the *c*-ring, observed in *E. coli*, *T. thermophilus*, and *I. tartaricus*, create distinct chemical environments on the respective *c* subunits and therefore create the required conditions for the two half channel hypothesis; one *c* subunit with periplasmic access and the other with access to the cytoplasm.

Cysteine mutagenesis has been used extensively to probe the aqueous accessible channels of subunit *a.* Silver ions and N-ethylmaleimide (NEM) are good probes for determining the aqueous accessibility of particular residues (Lu and Miller, 1995; Tamura *et al.*, 2001). Both silver and NEM react with the ionized thiol group on cysteine, which generally requires water. NEM is used to determine the boundaries of individual transmembrane segments because it is bulky and likely will not enter narrow aqueous channels. Silver ions have a small hydrodynamic radius and may enter constricted aqueous access channels within transmembrane proteins. Therefore, if a residue, which is embedded in the lipid membrane, is highly reactive with silver there is an aqueous channel that allows solvent access to the

particular residue under study. Agenvine and co-authors as well as Moore and co-authors demonstrated that several residues in transmembrane segments II, IV and V (extending from the cytoplasmic side of the membrane to the periplasmic side) were accessible to solvent using this method (Angevine and Fillingame, 2003; Angevine *et al.*, 2003; Angevine *et al.*, 2007; Moore *et al.*, 2008; Moore and Fillingame, 2008a). Aqueous accessible residues are assumed to line the proton channels. The data collected from these studies indicates that the periplasmic half channel is located at the interface of *a*TMH-II and *a*TMH-III, while the cytoplasmic half channel is located at the interface of *a*TMH-IV and *a*TMH-V. Figure 2.14 summarizes the aqueous accessible residues identified in these studies.

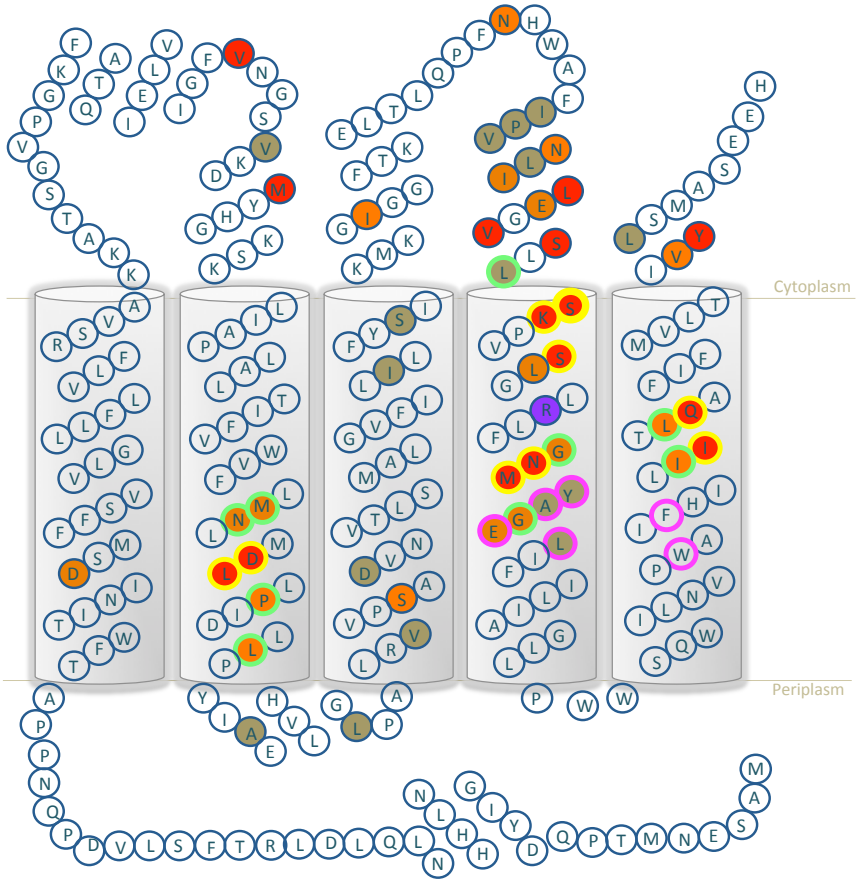

Figure 2.14: Aqueous accessible residues of subunit *a*. The sensitivity of specific residues to cysteine labeling with silver varies. The aqueous accessible residues identified by Moore and co-authors are categorized by > 85 % sensitivity (red filled circle), 66 – 85 % sensitivity (orange filled circle), and 46 – 65 % sensitivity (tan filled circle). The aqueous accessible residues identified by Angevine and co-authors are categorized by > 90 % sensitivity (yellow circle), 79 – 90 % sensitivity (green circle), and 50 – 75 % sensitivity (pink circle). The critical R210 residue is shown in purple. [The subunit *a* model in this Figure was adapted from (Vik *et al.*, 2000)].

The mechanistic mode of proton shuttling through the half channels in subunit *a* is still poorly understood. There are three theoretical forms that the half channels may adopt: 1) A channel of sufficient width to allow convection of water molecules; 2) a narrow channel containing ordered water molecules; and 3) a channel that excludes water altogether and relies on hydrogen bonding networks to provide the hydrophilic environment required for proton transport (Nagle and Morowitz, 1978). Several cysteine substitution experiments have shown that residues buried deep within the membrane are susceptible to silver ion inhibition, suggesting that the channels are either open to water or contain ordered waters. However, gating of proton transit through the channel is poorly understood and it is reasonable to speculate that protons move through both aqueous accessible regions as well as hydrogen bonding networks within the half channels.

Multiple models for proton transport through F_0 have been proposed. The commonalities between the current models are as follows: protons enter through the periplasmic half channel of subunit *a* and bind to *c*D61, in its carboxylate form. Each protonation event causes the *c*-ring to rotate 36^0 relative to subunit *a*. After making a complete turn about the rotor each protonated *c*D61 comes into close proximity with *a*R210. It has been proposed that the positive charge of R210 is necessary for controlling the pKa of *c*D61, which facilitates proton binding and release from subunit *c* (Fillingame *et al.*, 2002). Although the model shown in Figure 2.15 generally describes the currently accepted mechanism of proton transport, the detailed mechanism of torque generation has been under some debate.

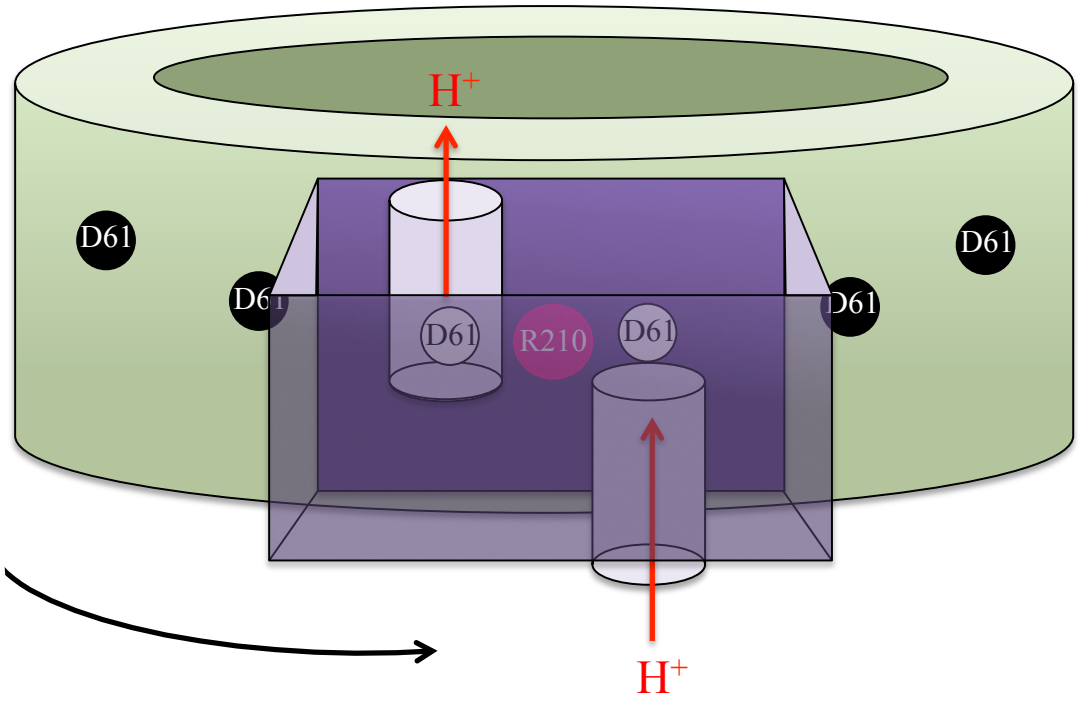

Figure 2.15: Schematic diagram of the proton channel. The *c*-ring is shown in green and subunit *a* is shown in purple. The path of proton flow is indicated with red arrows. Protonated D61 residues are shown as black circles. The D61 residues of each *c* protomer involved in active proton binding or release are shown as white circles. The direction of *c*-ring rotation is indicated with a black arrow. [Figure adapted from (Dimroth *et al.*, 2000)]. Reprinted with permission from BBA.

One model for torque generation involves swiveling of individual helices within both subunits *a* and *c* (Aksimentiev *et al.*, 2004; Elston *et al.*, 1998; Fillingame *et al.*, 2002; Rastogi and Girvin, 1999; Vik and Antonio, 1994; Xing *et al.*, 2004). Atomic level resolution structures are available for the *c*-rings of a number of proton transporting ATP synthases. In each case, the essential carboxylic acid (D61 in *E. coli*) is located near the middle of the second TMH of the hairpin. The structure of *E. coli* monomeric *c* was solved by NMR at pH 8.0 (Rastogi and Girvin, 1999) and pH 5.0 (Girvin *et al.*, 1998) and showed that the protonation state of D61 impacts the structural conformation of the *c* monomers. Protonation of D61 was proposed to cause *c*TMH-II to swivel 140^{o} relative to TMH-I, and drive rotation of the ring (Rastogi and Girvin, 1999). Figure 2.16 illustrates the proton transport mechanism proposed by Rastogi and Girvin. However, the protonation state of *c*E56 (equivalent to D61 of *E.coli*) from

thermophillic bacillus PS3 does not have significant impact on the structure, and raises debate over the applicability of the swiveling mechanism (Nakano *et al.*, 2006)

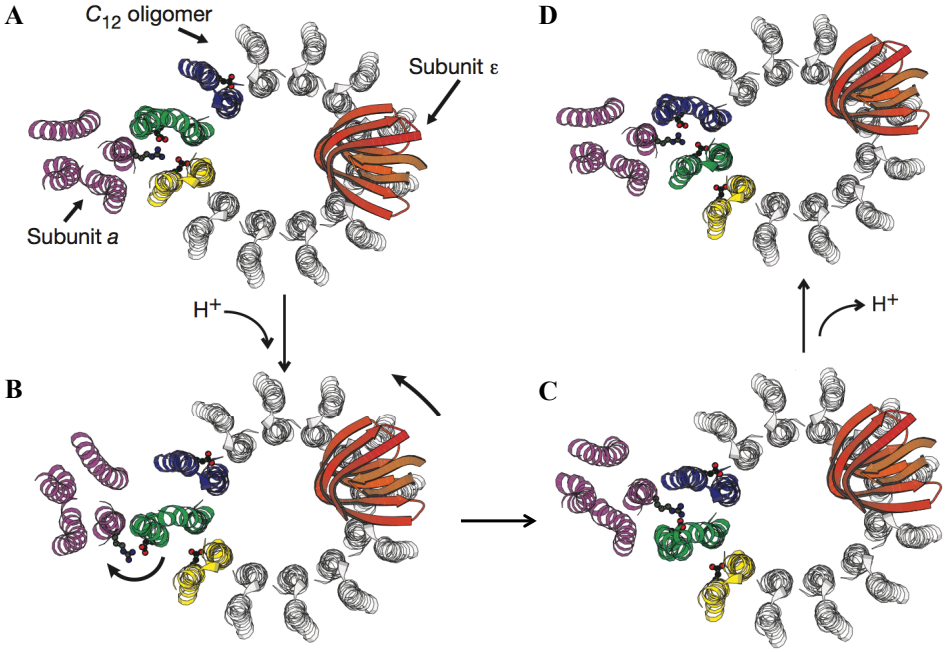

Figure 2.16: The theoretical model of proton translocation posited by Rastogi and Girvin. A) Resting state of R210. The D61 on the yellow *c* subunit is protonated and the D61 on the green *c* subunit is deprotonated. B) Protonation of the D61 on the green *c* subunit causes the swiveling of *c*TMH-II into the stable proton bound conformation. C) Fully protonated intermediate state, both the green and purple *c* subunits are in the proton bound form. D) Release of the proton from the purple *c* subunit to facilitate adoption of the resting state at the next position in the *c*-ring. [Image taken from (Rastogi and Girvin, 1999) and modified]. Reprinted with permission from Nature.

Helical swiveling has also been proposed within subunit *a*. Fillingame and co-authors posited that swiveling of TMH-IV of subunit *a* may gate access to the half channels and facilitate deprotonation and re-protonation of *c*D61 (Fillingame *et al.*, 2003). This model differed from the model presented by Rastogi and Girvin by showing that *c*TMH-II swiveling occurs when D61 is deprotonated, rather than as a result of protonation. The coordinated swiveling of *c*TMH-II and *a*TMH-IV was implicated as the mechanism of torque generation.

Aksimentiev and co-authors conducted extensive computational modeling studies based on the models proposed by the research groups of Girvin and Fillingame (Aksimentiev et al., 2004). Their modeling indicates that two adjacent *c* subunits are involved in a cooperative

mechanism where they are both in the deprotonated state for a brief period of time. The presence of two deprotonated D61 residues significantly reduces dissociation energy of the *a*R210-*c*D61 salt bridge and facilitates transfer of the salt bridge from one *c*-monomer to the next.

A second, and currently more accepted model of torque generation involves the Brownian ratchet mechanism (Junge et al., 1997). The Brownian ratchet mechanism states that the *c*-ring experiences small thermal oscillations relative to subunit *a* governed by Brownian motion. These thermal oscillations provide the initial force required to facilitate rotation of the *c*-ring in response to protonation and deprotonation of individual *c* subunits. The Brownian ratchet mechanism also assumes that the carboxyl groups on the *c*-ring must be protonated and neutral when facing in the lipid phase; but may be deprotonated and charged when facing subunit *a*. Electrostatic dynamics prevent the ring from slipping through the *a/c* interface when D61 is not protonated.

The high resolution crystal structure of the *c*-ring of *S. platensis* ATP synthase supports the Brownian ratchet mechanism posited by Junge and co-authors (Pogoryelov *et al.*, 2009). In this model, the *c*-ring is thought to oscillate back and forth relative to subunit *a* in a Brownian fashion. When a given *c*-subunit, in its proton locked conformation, interacts with the *a* subunit's critical arginine residue, the E62 (equivalent to *E. coli* D61) assumes an open conformation which allows the proton to be released. While E62 is deprotonated it is thought to be stabilized by a salt bridge with subunit *a*'s critical arginine. Brownian movement of the rotor is regulated by the deprotonated *c* subunit, which cannot exit the *a*-*c* interface. An incoming proton may then bind E62, allowing the neutralized glutamic acid to re-enter the hydrophobic membrane in its proton locked conformation under Brownian motion.

The Brownian ratchet mechanism is also supported by high resolution crystal structure of the *c*-ring from *S. cerevisiae*, which was solved in the open conformation (Symersky *et al.*, 2012). Symersky and co-authors showed that the introduction of a hydrophilic environment around the binding sites causes them to open, rather than concerted helical movements (as with the model proposed by Girvin and co-authors) or interaction with subunit *a*'s critical arginine

(as proposed by Pogoryelov and co-authors). A diagram of the Brownian ratchet model for proton transport through F_0 is shown in Figure 2.17.

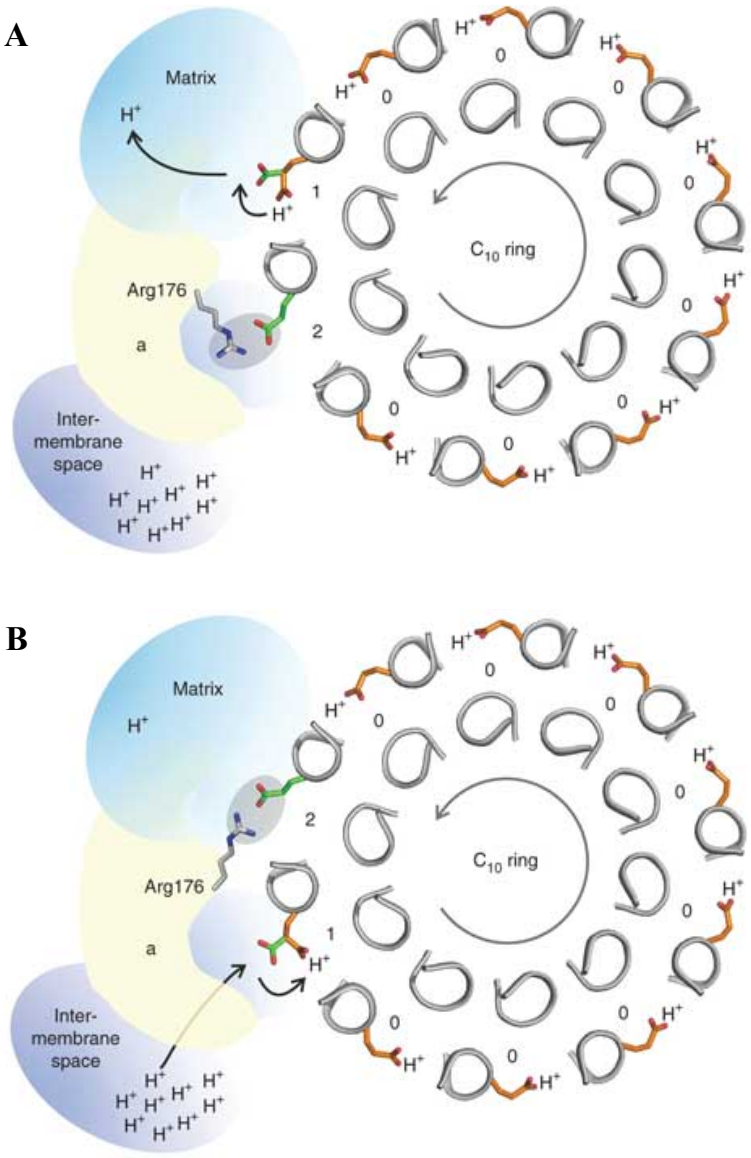

Figure 2.17: The mechanism of proton transport based on the high resolution structure of the *c*-ring from *S. cerevisiae*. The proton channel leading to the mitochondrial matrix is shown in light blue and the channel entering from the intermembrane space is shown in dark blue. A) The hydrophilic environment of the matrix channel facilitates opening of the proton binding site and proton release (1). R176 (equivalent to R210 in *E. coli*) is paired with the de-protonated E59 (equivalent to D61 in *E. coli*) (2). B) R176 releases the de-protonated E59 (1) to stabilize the upcoming E59 facing the matrix (2). Release of E59 from R176 allows the deprotonated E59 to bind an uncoming proton from the intermembrane space, and exit the *a/c* interface. [Image taken from (Symerkey et al., 2012)]. Reprinted with permission from Nature.

In the models discussed above, the conserved D61 residue is assumed to undergo protonation and deprotonation to facilitate proton transport across the membrane. However, Boyer postulated that protons may be transported as hydronium ions (Boyer, 1988). In order for this to occur the binding sites within the *c*-ring must have capacity to accept three hydrogen bonds, which is theoretically plausible based on the high resolution structure of the *c*-ring from *B. pseudofirmus* (Preiss *et al.*, 2010). However, extensive computational modeling has shown that the ion coordination in *B. pseudofirmus* is more likely to occur through protonation of the critical carboxylate group (Leone *et al.*, 2010). Several structures of other proton transporting *c*-rings have supported the assumption that proton transport occurs through obligatory protonation of the D61 (or equivalent) residue by demonstrating that the critical carboxylic acid group is directly involved in hydrogen bonding as a donor (Pogoryelov *et al.*, 2009; Vollmar *et al.*, 2009) (Figure 2.18).

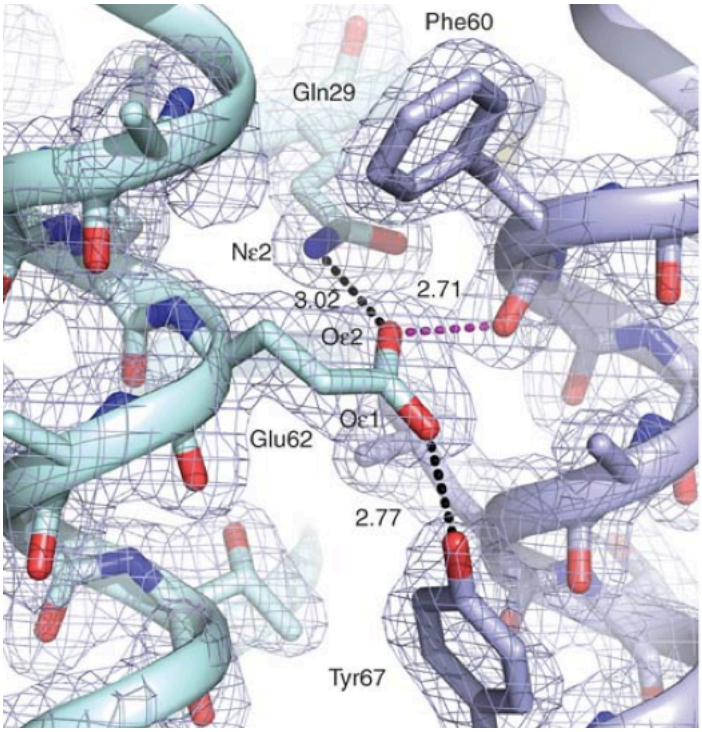

Figure 2.18: Crystallographically determined structure of the proton binding site of the *S. platensis* c-ring. Glu62 is the critical proton carrier in *S. platensis.* In this structure oxygen Oε1 serves as a hydrogen bond acceptor for the hydroxyl group of Tyr67. Oxygen Oε2 acts as a hydrogen bond acceptor from the Nε2 group of Gln29 and a hydrogen bond donor for the backbone oxygen of Phe60 (purple dashed line). Pogoryelov and co-authors state that hydrogen bond donation by the Oε2 oxygen conclusively identifies Glu62 as the obligatorily protonated proton carrier. [Image taken from (Pogoryelov *et al.*, 2009); PDB-ID 2WIE]. Reprinted with permission from Nature.

Sodium dependent F-type ATPases have been shown to facilitate sodium transport in a similar fashion to the proton transporting F_1F_0. The *c*-ring structures of two sodium transporting F-type ATPases have been solved by X-ray crystallography and provide detailed perspective on ion shuttling through the F_0 domain (Meier *et al.*, 2005; Murata *et al.*, 2005; Vonck *et al.*, 2002). In the *I. tartarticus* structure sodium atoms are coordinated by the side chain oxygens of Q32 and E65 on one *c* subunit, and the hydroxyl oxygen on S66 and carbonyl oxygen of V63 on the adjacent *c* subunit (Figure 2.19). The coordination network is also stabilized by several hydrogen bonds. Researchers have hypothesized that the hydrogen bond network serves to keep E65 deprotonated at physiological pH to facilitate sodium binding. Although the structure of the *a* subunit is unknown, they postulate that interaction with subunit *a* shifts the hydrogen bonding network and protonation state of E65 to release sodium ions from the binding site.

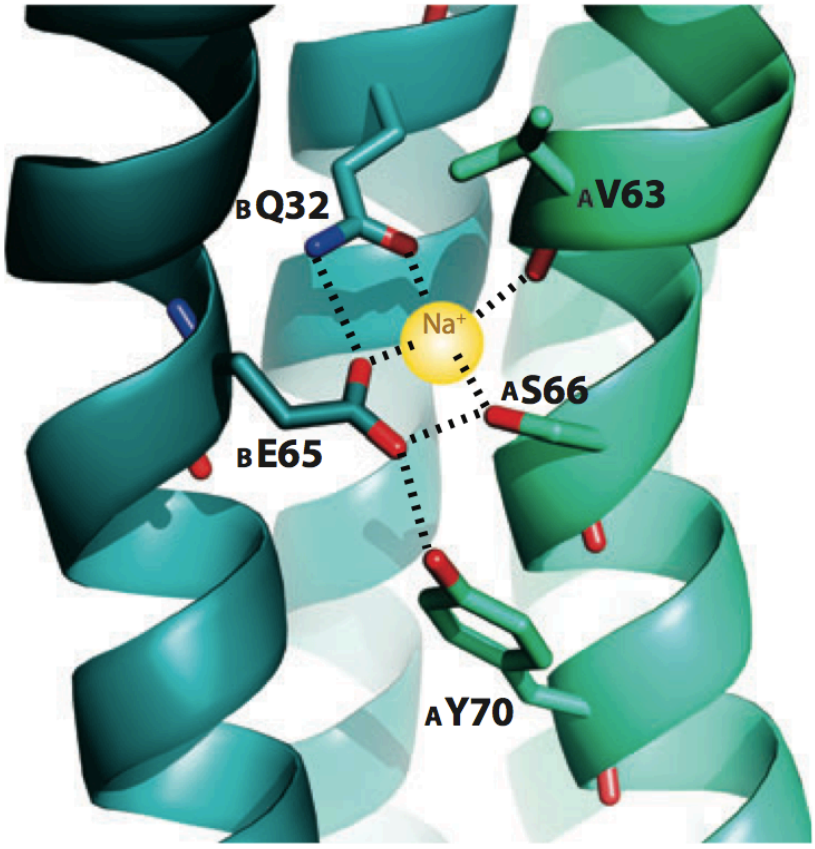

Figure 2.19: The sodium coordination site of the *c*-ring structure from *I. tartaricus*. The sodium atom (yellow) is coordinated by E65 and Q32 on one *c* subunit (dark green) and C63 and S66 on the adjacent *c* subunit (light green). [Image taken from von Ballmoos *et al.*, 2009; PDB-ID 2WGM]. Reprinted with permission from Annu. Rev. Biochem.

2.6 Membrane insertion and assembly of the F_0-complex.

The membrane incorporation requirements of the F_0 subunits have been characterized. Subunit *c* is inserted into the membrane via a novel pathway that is independent of Sec-translocase and requires only the YidC chaperone protein (Kol *et al.*, 2006). Insertion of subunit *c* is dependent on positively charged residues in the cytoplasmic loop (Kol *et al.*, 2008). Subunit *a* has a membrane targeting signal in its amino terminus that facilitates its incorporation into the membrane (Vik *et al.*, 2000) via the signal recognition particle and Sec-translocase pathway (Yi *et al.*, 2004). The YidC chaperone also plays a role in subunit *a* integration into the membrane in conjunction with the Sec-translocase machinery (Yi *et al.*, 2003). Insertion of subunit *a* into the membrane is known to be dependent on the presence of subunits *b* and *c* as well as the PMF (Hermolin and Fillingame, 1995; Yi *et al.*, 2003). The *b* subunit is inserted into the membrane via the Sec-translocase pathway.

In yeast cells, OxaI is the functional equivalent of YidC in *E. coli*. ATP synthase assembly is severely impaired in the absence of OxaI / YidC. Saint-Georges and co-authors identified a point mutation in one of the subunits of yeast cytochrome-bc_1, Qcr9p, which facilitates membrane insertion of the ATP synthase F_0 domain subunits in the absence of OxaI (Saint-Georges *et al.*, 2001). These authors proposed that introduction of a positively charged residue in the transmembrane portion of Qcr9p allowed interactions with negatively charged residues in the transmembrane segments of other respiratory chain complexes (i.e., the D61 or equivalent proton carrier of the ATP synthase subunit *c*) to facilitate co-insertion. Subunit *a* that is not associated with subunits *b* and *c* is highly toxic to cells and is rapidly degraded by FtsH protease (Akiyama, 2002; Akiyama *et al.*, 1996). It is interesting to speculate that this mechanism of co-insertion of *a* and *c* through charge-charge interactions may occur to prohibit the toxic *a* subunit from entering the membrane unpaired.

The assembly mechanism of the F_0 domain is largely unknown. Subunit *c* purified from *E. coli* has the capacity to self-assemble into ring structures (Arechaga *et al.*, 2002). However, in this study spontaneous ring assembly was shown to be a slow process. Self-assembly of the c_{10} ring is not likely to occur in live bacteria because the high energy demands of rapid cell division may not be met if ATP synthase cannot assemble quickly. The *uncI* is a 14 kDa

protein encoded on the *atp* operon that is not a component of the mature F_1F_0. *uncI* has been demonstrated to chaperone the assembly of the *c*-ring in *P. modestum*, and this functionality is likely conserved across species (Ozaki *et al.*, 2008; Suzuki *et al.*, 2007).

2.7 Membrane protein structure determination.

Structure and function are closely related in biological systems. Therefore, elucidation of complex tertiary structural elements can yield detailed information about how proteins and enzymes function in a living system. In addition to basic research efforts, protein structure determination is quickly becoming a cornerstone in human health research. Structural perturbations brought on by disease-causing mutations may be identified and evaluated for structure-based drug design. Also, enzymes from pathogens have been targeted using structure-based drug design to successfully combat human illness (Chintakrindi *et al.*, 2012; Martucci *et al.*, 2009; Roberts *et al.*, 1990; Traxler *et al.*, 1997). Membrane proteins are particularly attractive targets for structure-based drug design because many of them are involved in essential physiological processes, signal transducation for example, which contribute to disease.

Membrane proteins constitute approximately one-third of all gene expression products in humans (Fagerberg *et al.*, 2010). Over 84,000 soluble protein structures have been solved, while only 308 unique membrane proteins structures have been determined to date (White, 2012). Of the 308 known membrane protein structures, only 13 unique alpha-helical membrane protein structures have been solved. NMR spectroscopy, X-ray crystallography, and cryo-EM are the major methods for analyzing the three dimensional (3-D) features of both soluble and membrane proteins. Limited success in membrane protein structure determination has been attributed to several challenges specific to membrane proteins such as difficulties with protein overexpression, purification, yield, stability, and crystallization.

2.7.1 NMR spectroscopy for structure determination of membrane proteins.

In visible spectroscopy photons cause the system to move from a ground state to an excited state, which is measurable. However, in NMR spectroscopy microwaves induce the transition between ground and excited spin states, which are split by an external magnetic

field. The properties of individual nuclei determine their compatibility with NMR techniques. Nuclei have a quantum property called spin, which is described by a spin quantum number '*I*'. Nuclei with non-zero values of *I* are NMR detectable, some examples that are relevant to protein structure determination are ^{1}H, ^{13}C, and ^{15}N. The natural abundance of ^{13}C and ^{15}N is low and uniform labeling of protein samples is required for high-resolution NMR studies.

The bulk magnetic field (B_0) aligns the nuclear magnetic dipoles along an axis in both 'up' and 'down' states, which are respectively parallel and antiparallel to the B_0 (Figure 2.20). The up and down states are referred to as $\mu_{+1/2}$ and $\mu_{-1/2}$. The $\mu_{+1/2}$ state is parallel to B_0 and therefore low energy, while $\mu_{-1/2}$ is antiparallel to B_0 and high energy. More spins align parallel than antiparallel. Transition between the μ states is induced by the application of a radio frequency (RF) pulse. The RF pulse changes the equilibrium of the spin states and causes a small fraction of dipoles to tip from the parallel to the antiparallel alignment. The movement of this small fraction of dipoles from the excited (antiparallel) state back to the ground state (parallel) is termed 'relaxation' and is the basis of NMR spectroscopic detection. Measurement of the minuscule fraction of spin states that move from antiparallel to parallel produces the NMR signal used to determine protein structures. The lifetime of the excited state determines the spectral resolution and is characterized by relaxation rate, i.e., the rate at which the excited system returns to the ground state. Systems with long life times have slow relaxation rates and produce narrow well resolved spectral lines; while systems with short lifetime and fast relaxation rate produce broadened poorly resolved spectral lines. The position of each spectral line corresponds to the chemical shift of a unique nucleus.

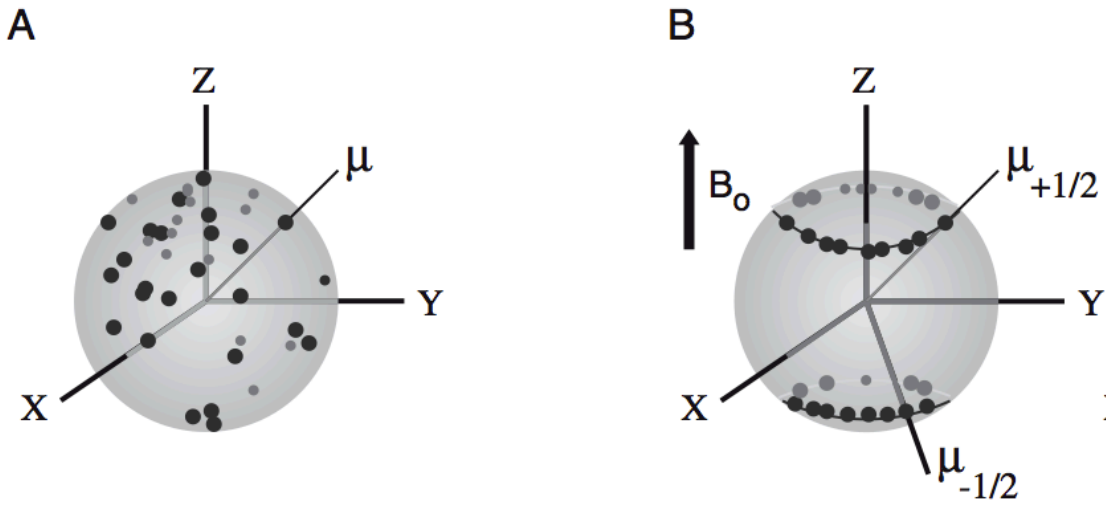

Figure 2.20: The effect of an external magnetic field on nuclear magnetic dipoles. A) Nuclear magnetic dipoles in the absence of a magnetic field. Black and grey dots represent the distribution of dipoles in space. B) Nuclear magnetic dipoles in the presence of an external magnetic field B_0. The dipoles may assume any position in the X-Y plane but may only be up or down on the Z axis. [Image taken from (Rule and Hitchens, 2006)]. Reprinted with permission from Springer.

Chemical shift is defined as the resonance frequency of a given nucleus relative to a standard. The chemical shifts of distinct carbon nuclei, nitrogen nuclei, and protons in a protein molecule can be identified and assigned on NMR spectra. Magnetization transfer through bonds (J-coupling) is used to connect chemical shifts of individual atoms in a single residue as well as to link the chemical shifts of neighboring amide backbone groups. A phenomenon called the nuclear Overhauser effect (NOE) is magnetization transfer through space. Measuring NOEs allows the calculation of distance constraints between assigned protons, and therefore, distances between larger structural elements. Compilation of multiple distance constraints, paired with the assumption that the protein molecule has regular chemical geometry, can be used to produce a high resolution 3D protein model.

NMR is a very sensitive technique for examining the local structural dynamics of proteins. Structural dynamics can be studied to determine which amino acid residues are involved in ligand binding and catalysis. Chemical shift changes can be monitored over a range of substrate concentrations and used to calculate binding and dissociation constants of ligands (Evans, 1995).

NMR does have some limitations, which are particularly relevant when working with membrane proteins. Relaxation rates are critical to spectral resolution and are significantly impacted by the size of the protein under study. Large proteins undergo rapid relaxation and tend to produce poor quality spectra. Currently, structure determination by NMR is limited to proteins with molecular weights less than 40 to 60 kDa (Rule and Hitchens, 2006). The highly hydrophobic nature of membrane proteins creates a need for membrane mimetics. Historically, NMR experiments with membrane proteins have been carried out using detergent micelles. Detergent micelles increase the effective size of the protein under study and fast relaxation of protein – detergent complexes can complicate acquisition of high quality NMR spectra. There are, however, several techniques used to study membrane proteins by NMR that aim to enhance spectral resolution.

Enhancement of NMR spectral resolution can be achieved both by the design of the NMR experiment itself and by sample preparation and handling. In heteronuclear single quantum coherence (HSQC) spectra each peak cooresponds to a single back bone or side chain amide group. HSQC spectra provide an NMR 'fingerprint' which is often a starting point for structure calculation. The two components of magnetization relaxation are T_1, longitudinal relaxation, and T_2, transverse relaxation. In HSQC spectra where decoupling has not been applied peaks appear as multiplets as a result of J-coupling. Each component of the multiplet has a different relaxation rate. Transverse relaxation optimized spectroscopy (TROSY) is an NMR spectroscopic method designed to select the multiplet component with the slowest relaxation rate and narrowest peak width, which effectively suppresses T_2 relaxation. The selection process dramatically reduces line width and enhances spectral resolution; the cost for enhanced resolution is an approximate 50 % decrease in sensitivity. Deuteration is also a commonly used method to improve spectral resolution of large and / or detergent bound proteins. Perdeuteration decreases the dipolar interactions between ^{13}C or ^{15}N and their bound protons, which decreases relaxation rates. Proton – proton coupling is also suppressed by deuteration which further improves resolution and reduces spectral complexity.

Sample handling techniques that reduce the size of the protein – detergent complex or reduce the viscosity of the sample can also improve spectral resolution. Relaxation rates can be

reduced by decreasing the size of the micellar complex, for instance, by using low molecular weight detergents. Mixed polarity solvents have also been used in membrane protein NMR to circumvent the use of detergent micelles and the complications they impart on high resolution data collection (Dmitriev, 2004b; Girvin *et al.*, 1998). Subjecting the samples to high temperatures during data collection may also enhance spectral resolution by reducing the effective viscosity of the sample.

Selective isotopic labeling and solid state NMR are emerging techniques which are useful for improving the resolution of membrane protein samples. Selective isotopic labeling involves specific labeling of individual residues by cell free protein synthesis or *in vivo* labeling (Hiroaki *et al.*, 2011; O'Grady *et al.*, 2012; Torizawa, 2004). In selectively labeled protein samples only specific backbone chemical shifts are observed, which simplifies the spectra and aids in residue assignment. Solid state NMR is useful for individual proteins as well as large protein complexes (Judge and Watts, 2011). Solid state NMR also offers a method to study the dynamic interactions between protein and lipid to give a more complete understanding of the functionalities of membrane proteins. Fourteen non-redundant membrane protein structures have been solved using solid state NMR (Warschawski, 2012).

Recently a group of researchers successfully determined the structure of a 247 amino acid membrane protein, sensory rhodopsin II (SRII), solubilized in detergent micelles using solution NMR (Gautier *et al.*, 2010) (Figure 2.21). The solution structure of SRII is the first of its kind and agrees well with the crystal structures of SRII (Luecke *et al.*, 2001; Royant *et al.*, 2001). Sensory rhodopsins appear to lend themselves to structural investigation and provide proof of principle for alphahelical membrane protein structure determination. Successful structure determination of sensory rhodopsins has been attributed to a unique combination of properties including their relatively small size, enhanced stability, and highly ordered internal structure. Gautier and co-authors were able to produce high quality NMR spectra from this integral membrane protein through the use of optimized detergents, monodispersed protein samples, and high temperatures during data acquisition.

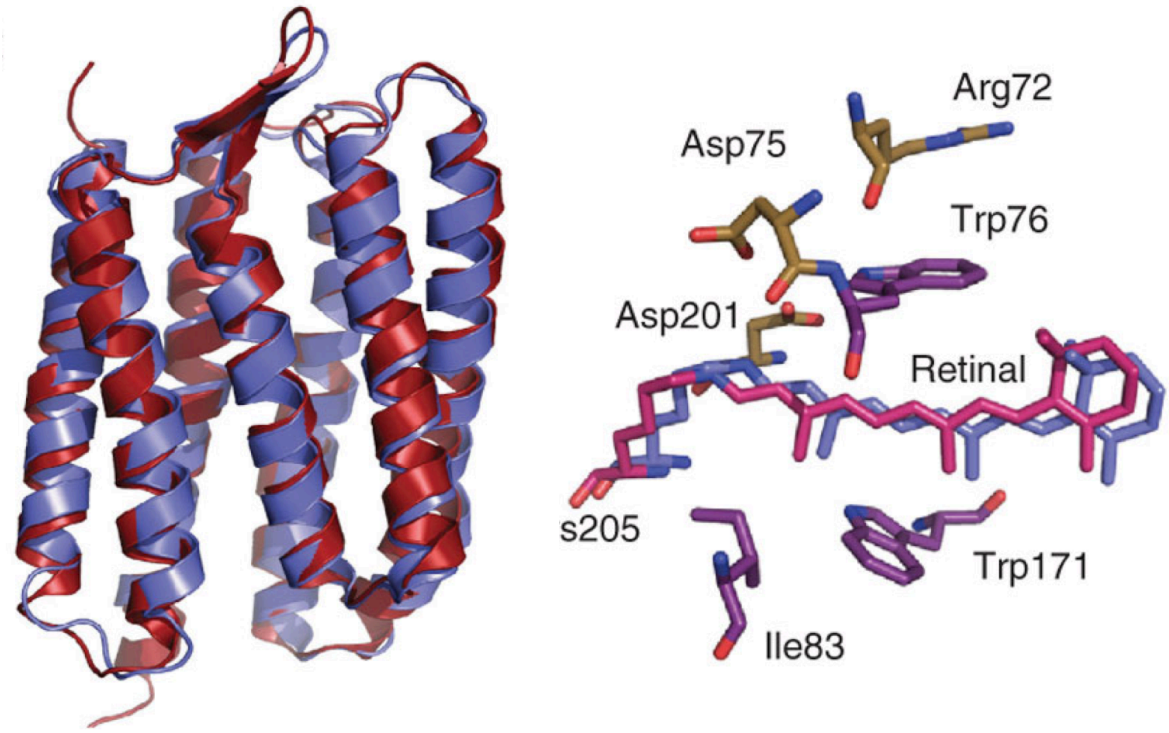

Figure 2.21: Solution structure of SRII. Left: ensemble NMR structure of receptor SRII. Right: retinal in the binding pocket from the NMR structure (pink) superimposed with the X-ray structure (blue) side chain residues in purple and brown are taken from the NMR structure [Image taken from (Gautier *et al.*, 2010); PDB-ID 2KSY]. Reprinted with permission from Nature.

2.7.2 X-ray crystallography of membrane proteins.

X-ray crystallography is widely used for protein structure determination. There are three main steps involved in protein X-ray crystallography. The first step, which is often the most difficult, is to produce high quality protein crystals. The crystals generated need to be larger than 0.001 mm^3 and ideally should be free of cracks and blemishes. After high quality crystals are obtained they must be subjected to X-ray diffraction. During diffraction, X-rays enter the crystal at a fixed angle and scatter off of electron dense regions to produce a diffraction pattern. The diffraction pattern contains the structural information of the crystallized protein. The third and final step in protein crystallography is the generation of an accurate protein model.

Crystallization of membrane proteins is particularly challenging because detergent solubilized membrane proteins are often unstable and have limited surfaces available for crystal

contacts (Bowie, 2001). Detergents are a relatively poor substitute for the lipid bilayer, and can often interfere with crystal lattice packing. In some cases, bicellar crystallization methods have been used to improve crystallization propensity of membrane proteins (Faham and Bowie, 2002; Katona *et al.*, 2003; Landau and Rosenbusch, 1996; Rosenbaum *et al.*, 2011; Wu *et al.*, 2010). Bicellar crystallization involves reconstitution of the target protein into bicelles, which are small lipid bilayer disks capped by detergent molecules (Figure 2.22). Bicelles are advantageous for membrane protein crystal trials because they closely mimic cellular membranes. They are relatively easy to work with, and keep the protein solubilized, which is ideal for crystallization by vapor diffusion and microbatch methods.

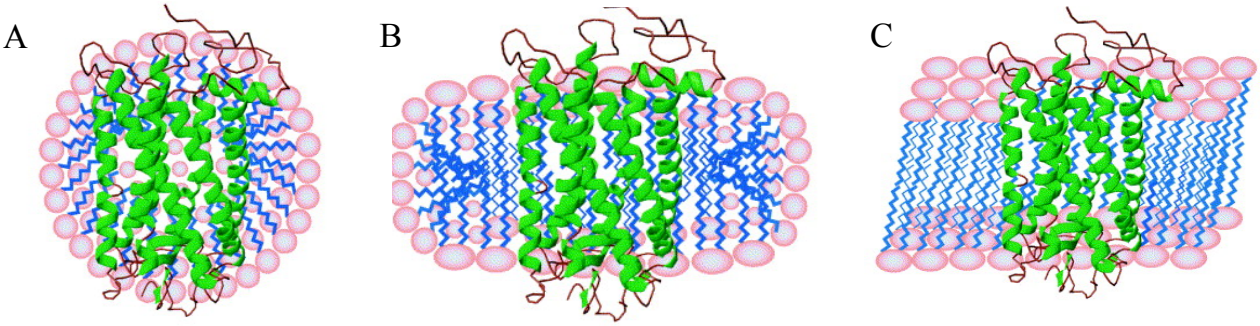

Figure 2.22: Graphical representations of membrane mimetics used in membrane protein crystallography. The green globular alpha helical membrane protein is shown in detergent micelles (A), bicelles (B), and lipid bilayer (C). [Image taken from (Arora and Tamm, 2001) and modified]. Reprinted with permission from Curr. Opin. Struct. Biol.

There are two main types of crystal growth: type I and type II. Membrane proteins crystallized in micelles or bicelles are typically type II crystals, where crystal contacts are limited to the polar regions. Type II crystals are often fragile and difficult to work with. Figure 2.22 illustrates how micelles and bicelles select for type II crystal growth, because the detergent molecules shield the core of the protein from making crystal contacts. For membrane proteins, crystal contacts within the polar regions as well as within the plane of the membrane are required for type I growth.

Crystallization of membrane proteins within lipid bilayers is a relatively new technique. Lipidic cubic phase (LCP) crystallization was developed by Landau and Rosenbusch; and

utilizes highly organized, incredibly viscous, three dimensional, and continuous lipid bilayers (Landau and Rosenbusch, 1996). LCP forms spontaneously upon mixing of monoolein and water at ideal ratios. The structure of the LCP changes when the water to monoolein ratio is adjusted. The target membrane protein can be re-constituted into LCP and stabilized in an environment that closely mimics the cellular membrane (Figure 2.23). After the protein is reconstituted into LCP it can be mixed with precipitant solution to enhance the probability of nucleation. Crystal growth in LCP systems occurs through re-arrangements in the lipid lattice that allow individual protein molecules to stack against one another within the plane of the membrane, as well as the ordered stacking of two-dimensional crystal sheets.

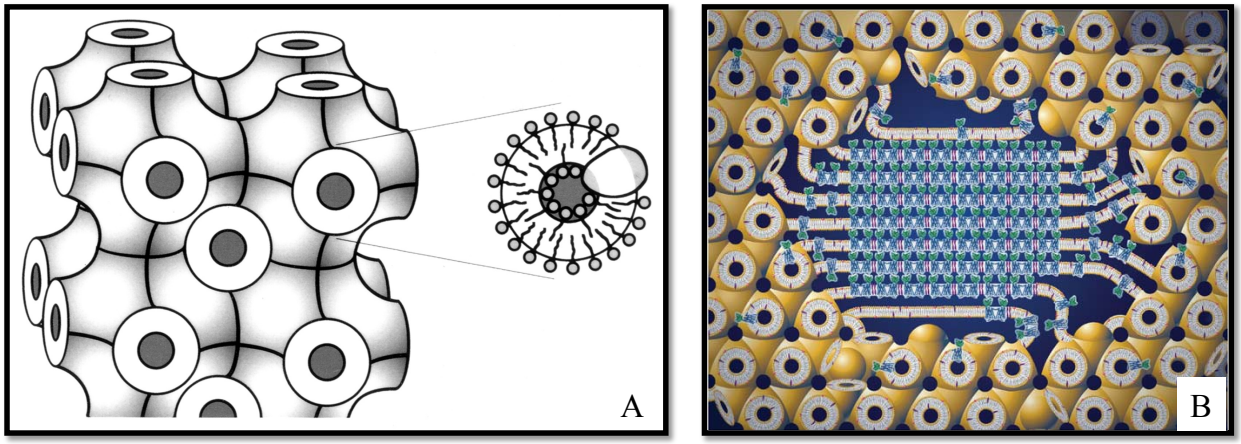

Figure 2.23: LCP facilitated membrane protein crystal formation and growth. A) A diagram of the LCP structure is shown on the left and an enhanced view of the edge of the LCP matrix (with a reconstituted membrane protein) is depicted on the right. [Image taken from: (Landau and Rosenbusch, 1996)]. Reprinted with permission from Elseiver Science. B) The protein molecules diffuse freely within the plane of the membrane to form crystal plates. The LCP matrix is also capable of remodeling to facilitate the stacking of crystal plates to form 3D crystals. LCP matrix is shown in yellow and white, protein molecules are blue [Image taken from (Caffrey and Cherezov, 2009)]. Reprinted with permission from Nature.

Optimal crystallization conditions are identified by trial and error, which often produces unwanted small molecule crystals consisting of salt, buffer or detergent. There are several techniques that help to determine whether a crystal is composed of protein or small molecules. Crystal staining with dyes such as methylene blue or ponceau red is one of the most common methods of assessing protein content. Protein crystals have relatively large pores and dye molecules can diffuse into the crystal to bind protein creating a dark blue or red appearance.

Salt crystals do not absorb dyes and remain colorless. Birefringence is generally a property of salt crystals and most protein crystals exhibit low levels of birefringence. However, proteins with a strong dipole moment may exhibit higher levels of birefringence and salt crystals with cubic internal ordering may exhibit none. Potential protein crystals can be tested for birefringence using a polarized light source. Finally, crystals of unknown composition can be diffracted with X-rays to determine protein content. Both salt and protein crystals give distinct diffraction patterns that can be readily identified.

Crystallization is a labor intensive process that requires testing thousands of combinations of experimental conditions. Precipitant types and concentrations, buffer types, pH values, protein concentrations, and detergents must all be optimized, and changes in one component may alter the effects of other components. High throughput screening methods are often necessary to identify initial conditions; laborious refined screening is required to optimize crystal quality. However, the propensity of any given protein to crystallize is also heavily dependent on the physicochemical properties of the protein. In some cases, favorable crystallization conditions can be predicted based on the properties of the protein (Chen *et al.*, 2007; Jia and Liu, 2006; Overton and Barton, 2006).

Among the 13 unique α-helical membrane protein structures are several crystal structures from different types of G-protein coupled receptors (GPCRs). GPCRs are a large family of integral membrane signaling proteins that are characteristically composed of seven transmembrane alpha helical segments and are responsible for cellular responses to hormones, neurotransmitters, olfaction, and light. GPCRs are involved in a wide spectrum of human diseases and are attractive targets for structure determination and rational drug design. Robert Lefkowitz and Brian Kobilka shared the 2012 Nobel prize for their crystallographic and mechanistic investigations on GPCRs. The GPCR success stories serve as a benchmark for structure studies on a wide variety of alpha helical membrane proteins. A structural diagram of the human β_2 adrenergic G-protein coupled receptor is shown in Figure 2.24.

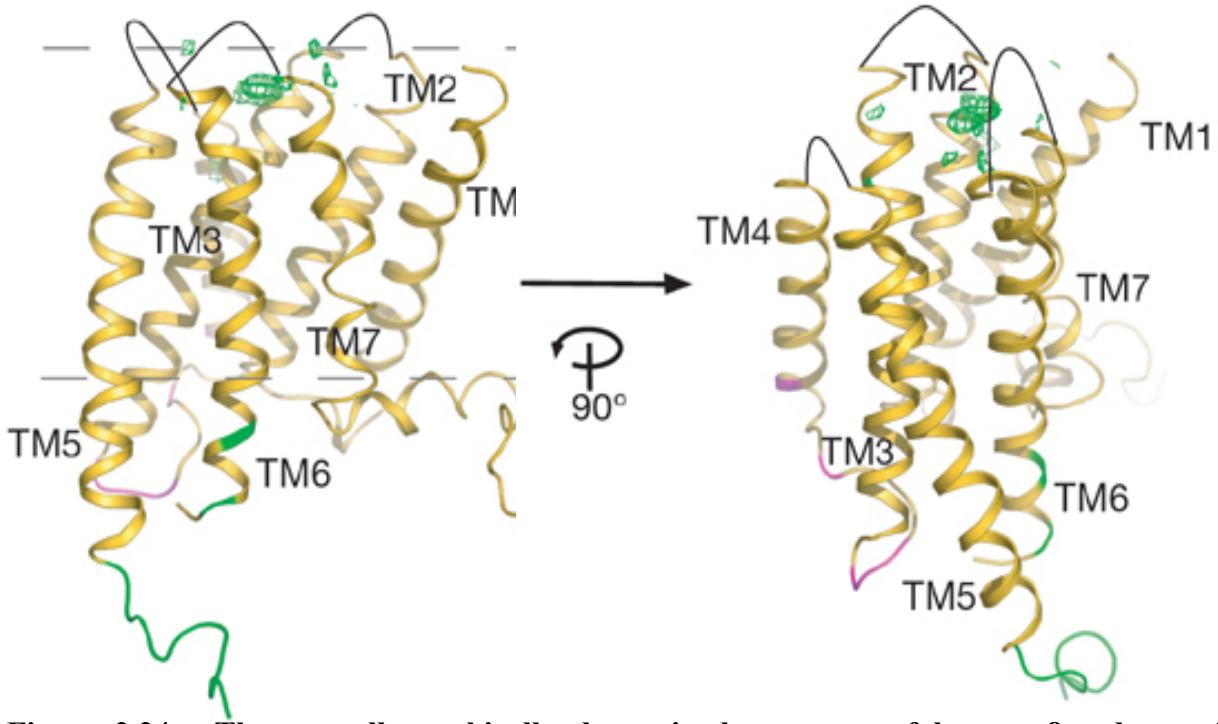

Figure 2.24: The crystallographically determined structure of human β_2 adrenergic GPCR. Two views of the protein are shown. Transmembrane alpha helical segments (marked TM) are shown in yellow and numbered. The green patches represent areas that form direct interaction with specific protein binding partners. [Image taken from (Rasmussen *et al.*, 2007); PDB-ID 2R4R]. Reprinted with permission from Nature.

Bacteriorhodopsin and the K2P1 potassium transporting protein are both examples of transmembrane alpha helical ion transporters; high resolution structures determined X-ray crystallographically are available for each. Bacteriorhodopsin is a well characterized proton pump that is composed of three identical monomers which form a trimeric structure in the membrane (Luecke et al., 1998). Bacteriorhodopsin functions to maintain the PMF in *H. salinarium* in response to light, which in turn drives ATP synthase. The human K2P1 potassium channel is highly selective for potassium ions and consists four pore forming domains that arrange in a cone shape within the membrane (Miller and Long, 2012). K2P1 and its homologues are heavily involved in cellular signaling, including regulating electrical signaling in excitable cells, hormone secretion, and maintenance of cell volume. Structural diagrams of both bacteriorhodopsin and K2P1 are shown in Figure 2.25.

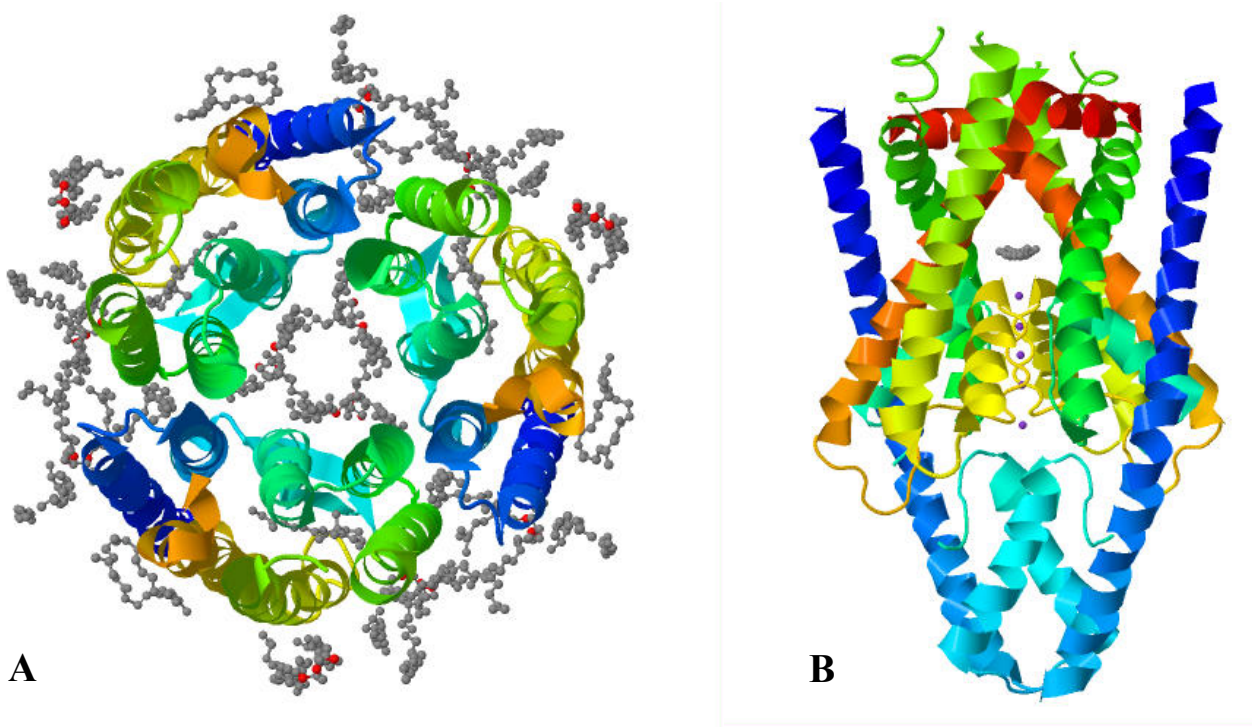

Figure 2.25: The crystallographically determined structures of bacteriorhodopsin and the human K1P2 potassium transporter. A) The trimeric biological complex of bacteriorhodopsin. The TMHs of bacteriorhodopsin monomers are shown in blue, yellow and green. Individual ordered lipid molecules are shown in grey and red. B) The tetrameric biological K2P1 potassium pore. Potassium ions are shown in purple. [Figures taken from (Luecke et al., 1998; Miller and Long, 2012)]. The PDB-IDs for bacteriorhodopsin and the K2P1 potassium pore are 1C3W and 3UKM respectively. Images reprinted with permission from Science.

Protein NMR and crystallography are complementary methods. Diffraction based methods have the potential to reveal larger structures in a shorter time, while NMR is time consuming and is not currently practical for proteins larger than 60-70 kDa. However, NMR can reveal more about molecular dynamics in solution. Also, NMR provides a means for determining the structure of proteins that will not readily crystallize. There are several examples of protein structures that have been solved by both NMR and X-ray crystallographic methods. Generally, solution and crystal structures of the same protein agree with each other which shows both methods can be used to explain the relationship between form and function (Garbuzynskiy *et al.*, 2005). NMR and X-ray diffraction based models are more meaningful taken together than either alone.

2.8 Proton transport through ATP synthase and human health implications.

Mitochondrial diseases are among the most common genetic disorders and are a growing concern for community health (DiMauro, 2007). Mitochondrial diseases, often referred to as mitochondrial myopathies, are caused by mutations in mitochondrial deoxyribonucleic acid (DNA) that affect the cell's ability to produce ATP. Over 150 pathogenic mutations have been identified on the mitochondrial genome (Figure 2.26).

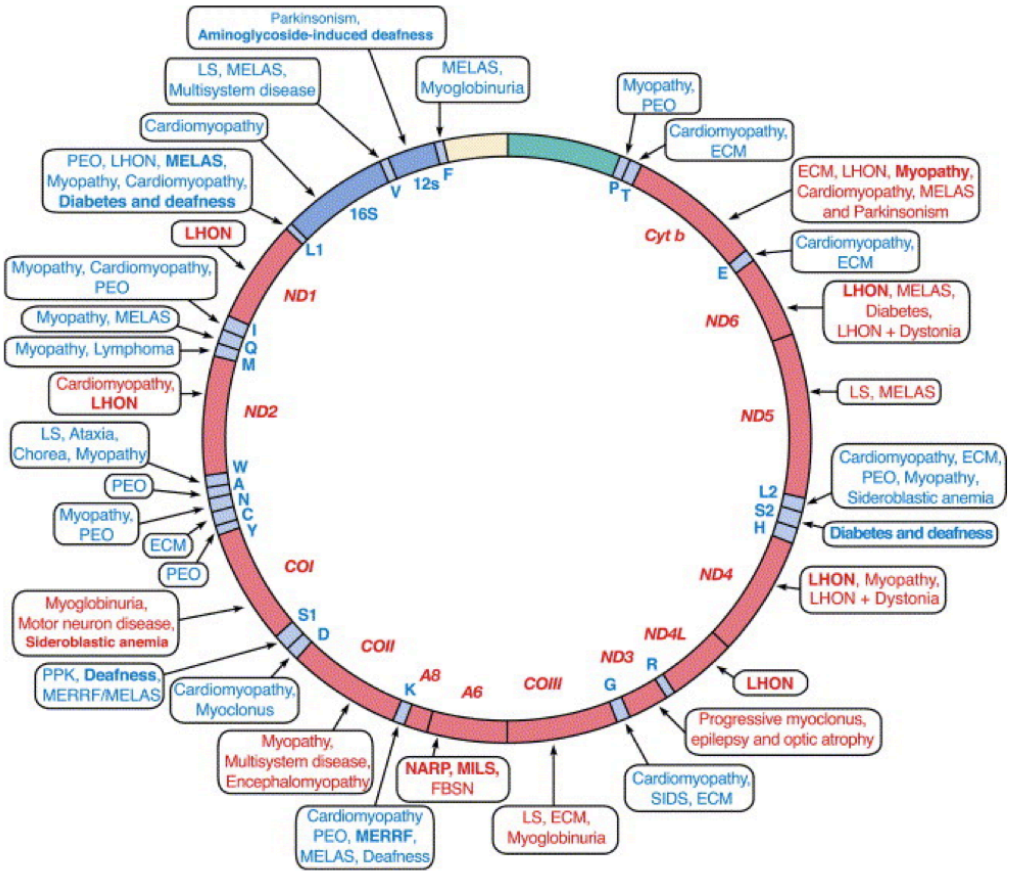

Figure 2.26: Morbidity map of the human mitochondrial genome. Genes labeled A8 and A6 correspond to the *c* and *a* subunits of human ATP synthase respectively. [Image taken from (DiMauro, 2004)]. Reprinted with permission from BBA.

There are three human diseases caused by mutations in the gene encoding subunit *a* of ATP synthase (Kucharczyk *et al.*, 2009). They are 1) neuropathy, ataxia and retinitis pigmentosa (NARP) syndrome (Tatuch and Robinson, 1993); 2) maternally inherited Leigh's syndrome (MILS) (de Vries *et al.*, 1993; Santorelli *et al.*, 1994); and 3) familial bilateral striatal necrosis (FBSN) (De Meirleir *et al.*, 1995). A fourth disease, Leber's hereditary optic

neuropathy (LHON), has also been shown to be associated a point mutation in subunit *a*. However, LHON is also associated with a number of mutations in several of the OxPhos complexes and appears to be caused when protons leak across the membrane (Lamminen *et al.*, 1995). LHON is characterized by bilateral optic nerve atrophy, pre-excitation syndrome, and a variety of neurological disorders. It has a prevalence of 1 in 8,500 individuals, although only a minority of cases are related to the ATP synthase mutation (Man *et al.*, 2003).

NARP and MILS syndromes are both caused by one of four point mutations within subunit *a* (Table 2.1). The mutations associated with NARP / MILS syndromes cause severe impairment of steady state ATP synthesis, likely due to partial blockage of proton passage through F_0 (Baracca *et al.*, 2000; Sgarbi *et al.*, 2006). ATP synthase containing the NARP / MILS mutations is correctly assembled and present at levels comparable to wild type (Rak *et al.*, 2007). In all known cases the T – G (Leucine to Arginine) mutations result in more aggressive forms of the diseases (Santorelli *et al.*, 1996). Researchers have speculated that the introduction of the positively charged arginine interferes with the proton channel (Vazquez-Memije *et al.*, 2009).

Table 2.1: Summary of the mutations, symptoms and prevalence of mitochondrial myopathies related to subunit *a*. *Note: The human equivalent of subunit a is expressed from the gene named "atp6".*

Disease	Mutation (*mt*DNA)	Amino acid (Human atp6)	Equivalent amino acid (*E. coli sub-a)*	Symptoms	Prevalence
NARP/MILS	T8993G	Leu156 → Arg	Leu207 → Arg	Dementia, seizures, neuropathy, neurogenic muscle weakness, ataxia, encephalopathy	NARP 1:12,000
	T8993C	Leu156 → Pro	Leu207 → Pro		MILS 1:36,000
	T9176G	Leu217 → Arg	Leu259→ Arg		
	T9176C	Leu217 → Pro	Leu259 → Pro		
LHON	T9101C	Ile192 → Arg	Ile242 → Thr	Optic nerve atrophy, pre-excitation syndrome	1:8500
FBSN	T8851C	Trp109 → Arg	Phe185→ Arg	dystonia, herkinesia, spasticity, seizures, mental deterioration	unknown

It seems counterintuitive that two distinct disorders are caused by the same mutations, however, in this case the distinguishing variable is mitochondrial heteroplasmy – also known as 'mutant load' (White *et al.*, 1999). The NARP / MILS causing mutations do not occur in all of the mitochondria in the body. Individuals with less than a 70 % mutant load are clinically asymptomatic, while individuals harboring between 70 – 90 % mutated mitochondria display NARP symptoms. People with a mitochondrial mutation rate greater than 90 % display symptoms of MILS. Although NARP and MILS are closely related disorders the clinical presentations are strikingly different. Several acute symptoms characterize NARP syndrome, including retinitis pigmentosa, ataxia, seizures, dementia, sensory neuropathy and developmental delay. The onset of MILS is typically 6 months of age and it is characterized by symptoms including brainstem dysfunction, progressive psychomotor decline and death within 2 years. NARP syndrome has a prevalence of 1 in 12,000 individuals and MILS has a prevalence of 1:36,000 (Santorelli and Tessa, 2004).

FBSN is not well characterized. It is an early onset disease characterized by brain lesions and neuronal cell death. Symptoms include dystonia, hyperkinesia, spasticity, seizures, mental deterioration and disturbed behavior. FBSN is caused by a mutation in the C-terminus of subunit *a*; specifically, T8851C which leads to substitution of tryptophan 109 for arginine (De Meirleir *et al.*, 1995). Reminiscent of the NARP / MILS mutations, the T109A FBSN mutation does not disrupt assembly of the F_1F_0 complex (Kucharczyk *et al.*, 2012). Although the T109A mutation is thought to be distant from the *a/c* interface it appears to exert long range structural perturbations that partially occlude proton translocation through subunit *a* (Kucharczyk *et al.*, 2012).

ATP synthase has also been the focus of infectious disease research. Tuberculosis is one of the leading causes of death due to infection world-wide. Recently, ATP synthase has been targeted in the design of novel antimycobacterial compounds called diarylquinolines (Andries *et al.*, 2005). Andries and co-authors demonstrated that Diarylquinoline – R207910 exerts a potent antibiotic effect against a variety of drug resistant *M. tuberculosis* strains. This compound was found to function by blocking proton transport through the F_0 channel of *M. tuberculosis* ATP synthase by binding to subunit *c* (Huitric *et al.*, 2010; Petrella *et al.*, 2006;

Segala *et al.*, 2012). Andries and co-authors also demonstrated that the Diarqunioline – R207910 does not have significant impact on the human form of ATP synthase and is tolerated well by patients. Diarlyquniolines are currently in use to fight tuberculosis infections (Andries *et al.*, 2005).

3 Materials and Methods.

3.1 Design of a model protein for structure studies.

Our goal was to generate a stable, single peptide model of the *a/c* interface that was more amenable to structural studies than the complete F_0 domain. We designed two fusion protein constructs consisting of subunits *a* and *c* to achieve this goal. The current model for subunit *a* places the C-terminus in the cytoplasm and the N-terminus in the periplasm (Valiyaveetil and Fillingame, 1998). Both the 'N' and 'C' termini of subunit *c* are on the periplasmic side of the inner membrane of *E. coli.* In the first fusion construct, the flexible connecting loop of subunit *c's* TMH-II was fused to the C-terminus of subunit *a* (*a-c/2* fusion). A second copy of the complete subunit *c* was fused to the C-terminal end of *a-c/2* in a head-to-tail fashion (Figure 3.1). This protein fusion construct will be referred to as '*a-c/2-c*' and is expected to have correct membrane topology. The second fusion construct was prepared by fusing the N-terminus of subunit *c* to the C-terminus of subunit *a* with a flexible linker. This construct does not have the additional connecting helix (*c/2*) present in the first construct. According to the current model of subunit *a,* the second construct, called '*a-c',* should have incorrect membrane topology. The *a-c* construct was made as a measure of completeness. If the C-terminus of subunit *a* is on the periplasmic side of the membrane, contrary to the current model, then the *a-c* fusion construct will be the one with correct transmembrane topology.

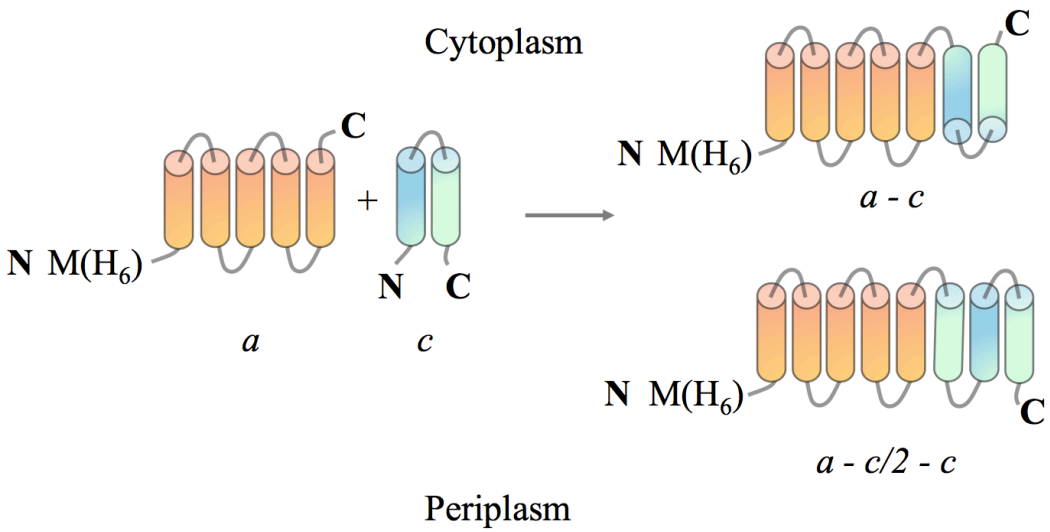

Figure 3.1. The *a/c* fusion constructs. Subunits *a* and *c* are shown as well as both fusion proteins. The *a-c* protein is shown at the top right and the *a-c/2-c* protein is shown on the bottom right. The cytoplasmic side of the membrane is on top and the periplasmic side is on the bottom. (H_6) represents the hexahistidine tag.

3.2 Plasmids and strains.

3.2.1 Description of bacterial strains used in cloning and expression.

C43(DE3)

C41(DE3) was derived from BL21(DE3) [*E. coli* F$^-$ *ompT hsdS*$_B$ (r_B^- m_B^-) *gal dcm* (DE3)] and contains an uncharacterized mutation or mutations that make the cells tolerant of overexpression of transmembrane proteins (Miroux and Walker, 1996). C43(DE3) was derived from C41(DE3) cells that grew robustly during expression of highly toxic membrane proteins (Miroux and Walker, 1996). C43(DE3) is commercially available (Invitrogen, Burlington ON).

OM202

The *E. coli* OM202 strain has a chromosomal deletion of the entire *atp* operon (Dmitriev, 2004a). This strain was a gift from Robert Fillingame and is not commercially available.

TOP10

E. coli TOP10 cells are ideal for cloning and plasmid amplification because they are capable of highly efficient and stable replication of plasmid DNA. The genotype of TOP10 is: F– *mcr*A Δ(*mrr-hsd*RMS-*mcr*BC) Φ80*lac*ZΔM15 Δ*lac*X74 *rec*A1 *ara*D139 Δ(*ara leu*) 7697 *gal*U *gal*K *rps*L (StrR) *end*A1 *nup*G. TOP10 *E. coli* are commercially available (Invitrogen, Burlington ON). TOP10 can also be used to express protein from the pBAD102 TOPO directional vector system.

DH5α

The DH5α strain is commercially available (Invitrogen, Burlington ON) and is ideal for cloning and storage of plasmids because of its ability to take up and retain plasmid DNA. DH5a cells have the genotype: F– Φ80*lac*ZΔM15 Δ(*lac*ZYA-*arg*F) U169 *rec*A1 *end*A1 *hsd*R17 (rK–, mK+) *pho*A *sup*E44 λ– *thi*-1 *gyr*A96 *rel*A1.

3.2.2 Generation of Recombinase-A deficient variants of OM202 and C43(DE3) *E. coli.*

OM202*recA* and C43*recA* strains were generated by P1 phage transduction, as previously described by Miller (Miller, 1972). *E. coli* BLR(DE3) was used as a donor strain for

deficient Recombinase-A (*recA*, recominase-A gene; RecA, recombinase-A protein). *E. coli* OM202 and C43(DE3) were the recipient strains. BLR(DE3) is convenient for *recA* transduction because of the close proximity of a tetracycline resistance selectable marker to the *recA* gene, (*recA*)::Tn10(tet^R), on the chromosome. Primary screens for Tn10 transductants were conducted on Luria broth (LB) plates containing 120 µg/mL tetracycline. Secondary screening for the *recA* deficient phenotype was done by ultraviolet (UV) irradiation at 254 nm. A single colony of each potential transductant was used to inoculate 5 ml of LB containing 120 µg/mL tetracycline. The cultures were grown at 37 ^{0}C, with shaking at 220 r.p.m., to an optical density (OD) of 0.3. A 10 µl droplet of cell culture from each potential transductant was spotted on a series of LB-tetracycline plates and subjected to UV radiation with variable UV doses up to 0.04 J/cm^2. Cell growth was assessed following 16 hours of incubation at 37 ^{o}C in complete darkness. Clones killed by a 0.02 J/cm^2 dose were selected as *recA* deficient.

3.2.3 Plasmids for expression of subunit *a* and the *a/c* constructs.

All plasmids were isolated from liquid *E. coli* cultures using miniprep spin kits (Qiagen, Mississauga, ON). A summary of the primers used in all cloning projects can be found in Table 3.1. A summary of the plasmids generated for overexpression and purification of wild type subunit *a* and the *a/c* fuion proteins can be found in Table 3.2. The complete DNA sequence of the native *E. coli atp* operon can be found at http://www.ncbi.nlm.nih.gov/nuccore/j01594.1 (accession number J01594.1). A summary of the *atp* operon nomenclature is presented in Table 3.3. All plasmids generated were verified by sequencing analysis. All sequencing analysis was conducted at the DNA sequencing and Gene Synthesis laboratory at the Plant Biotechnology Institute (National Research Council). Sequencing data was processed using the DNASTAR Lasergene 8 – SeqMan Pro software package.

Table 3.1: List of primers used in cloning.

Primer Name	Sequence
B966FNheI	5’ - TGGCGTCTGAAGAACATTAAGCTAGCAACACTAC - 3’
BSR320	5’ - AAAACCAGGAACAACAGACCCAGCACCACC - 3’
ESR1285	5’ - AGCAACGCTTACTACGCGACAGC - 3’
HP_ara_EcoRI_R	5’ - GGTGTTCCATGAATTCGTATATCTCCTTCTTAAAG - 3’
HP_ara_SacI_F	5’ - CGTAGTAAGAGCTCCTTAAACGGTCTCCAGC - 3’
HP_cG23Dr	5’ - ACCGATCGCAGCATCGATTG - 3’
HP_cL31Fr	5’ - GAATTTACCCCCGAAGATGCCGAT - 3’
HP_F0_EcoRI_F	5’ - CAGCTTATCAGAATTCAAGCTTTCAAAGTTC - 3’
HP_F0_SacI_R	5’ - TCAGCCCCTGAGCTCTTACAGTTCAG - 3’
HP_L31F_a2cR	5’ - CGGCATCTTCGGGGGTAAATTCC - 3’
HP_Nhe957	5’ - CTGAAGAACATTAAGCTAGCAACACTAC - 3’
HP_NheI_a2cR	5’ - ATAAAAGGCTAGCTTACTACGCGACA - 3’
HP_NheI_BROD6	5' - GGGTAAAAGCTAGCATGCATCACCATCAC - 3'
HP_pBAD_NheIR	5’ - GGTGTTCCATGCTAGCGTATATCTCCTTC - 3’
HP_pBAD_PmeIF	5’ - CGTAGTAAGTTTAAACTAAACGGTCTCCAGC - 3’
HP_PflMI224	5’ - CGTACATTCTCGCTGGTGGA - 3’
HP_PmeI_BROD6	5’ - CAGCCCGTTTAAACTTACAGTTCAGC - 3’
HP_Sph2547	5’ - CCATAACAACCGCACCTACAGAGTCGCGCTC - 3’
HPBA_RL1	5’ - TTGACGCGCTGCGCCTCCAGCTGATCCGGTACCATGTTCT TCA - 3’
HPBA_RL3	5’ - TTGACGCGCTGCGCCAGCATTTCCTGAAGCTGAA GCCGTTCCAGCTGATCCGGTACCATGTTCTTCA - 3’
pBADBFNcoI	5’ - GGTAAAAGGCACCATGGGACACCATCACC - 3’

Table 3.2: Summary of the plasmids generated for expression and purification.

Plasmid Name	Target expression product	Description
pBWU13	*a*	Encodes the native *atp* operon
pBWU13 derivative plasmids		
pBROD2	*a-c*	Encodes *atp I, a-c, E, F, H*
pBROD4	*a-c/2-c*	Encodes *atp I, a-c/2-c, E, F, H*
pHP2	*a-c*	Encodes the entire *atp* operon, except native *atpE* and *atpB*, which were replaced by the *a-c* gene.
pBROD6	*a-c/2-c*	Encodes the entire *atp* operon, except native *atpE* or *atpB,* which were replaced by *a-c/2-c* gene.
pHP7	*a-c*	Encodes the entire *atp* operon except native *atpB* which was replaced by *a-c* gene.
pHP808	*a-c/2-c*	Encodes the entire *atp* operon except native *atpB* replaced by *a-c/2-c*.
pHP9	*a*	Same as pBWU13 except *atpE* encodes the G23D point mutation.
pHP10	*a*	Same as pBWU13 except *atpE* encodes the L31F point mutation.
pHP11	*a-c*	Same as pHP7 except *atpE* encodes the G23D point mutation.
pHP8012	*a-c/2-c*	Same as pHP808 except *atpE* encodes the G23D point mutation.
pHP13	*a-c*	Same as pHP7 except *atpE* encodes the L31F point mutation.
pHP8014	*a-c/2-c*	Same as pHP808 except *atpE* encodes the L31F point mutation.
pHP8015	*a-c/2-c*	Same as pHP808 except the *a-c/2-c* fusion gene contains the L31F point mutation on *c*TMH-I.
pHP8016	*a-c/2-c*	Same as pHP808 except both the *a-c/2-c* fusion gene and native *atp E* contain the L31F mutation.
pHPa210Q	*a*	Same as pBWU13 except that *atpB* contains R210Q mutation.
pHPBA_1	*a-c/2-c-linker-1*	Same as pHP808 except that the GSAG sequence is inserted in the linker connecting subunits *a* and *c*.
pHPBA_3	*a-c/2-c-linker-3*	Same as pHP808 except that the GSAGTASANSGA sequence is inserted in the linker connecting subuntis *a* and *c*.
pBAD derivative plasmids		
pHP805	*a-c/2-c*	Encodes only the *a-c/2-c* fusion construct.
pHP80-102	*a-c/2-c*	Encodes the *a-c/2-c* and *atpF*.
pHP8024	*a-c/2-c*	Encodes *atpI, a-c/2-c, atpE*, and *atpF*.
pHP8025	*a*	Encodes *atpI,* atpB, *atpE* with the G23D mutation.

Table 3.3: The *atp* operon nomenclature.

atp operon gene name	Subunit expression product
atpI	*I*
atpB	*a*
atpE	*c*
atpF	*b*
atpH	δ
atpA	α
atpG	γ
atpD	β
atpC	ε

Cloning the a-c constructs into the atp operon.

The pBWU13 plasmid is derived from pBR322 and encodes the entire wild type *atp* operon. The *atpB* gene in pBWU13 was modified to insert a hexa-histidine tag (His_6) at the N-terminus of subunit *a*. The *a/c* and *a-c/2-c* fusion genes with the His_6-tag sequence were constructed previously (Rempel & Dmitriev, unpublished data) and cloned into pBWU13 derivatives pBROD2 and pBPROD4 respectively. The fusion genes were then cloned into the full *atp* operon in two different contexts. In one case, both the genes encoding subunits *a* and *c* (*atpB* and *atpE*) were replaced with the fusion constructs. In the second case the gene encoding subunit *a* (*atpB*) was replaced with the genes encoding the fusion proteins.

To replace the *atpB* and *atpE* genes with the *a-c* gene fusion, pBWU13 and pBROD2 were restricted with HindIII and SphI. The resultant fragments from pBWU13 were an 8408 base pair vector fragment and a 2352 base pair fragment containing *atpI'*, *atpB* (subunit *a*), *atpE* (subunit *c*), and *atpF* (subunit *b*). The fragments obtained from pBROD2 were a 3932 base pair vector fragment and a 2334 base pair fragment containing *atpI'*, the gene encoding the *a-c* construct and *atpF*. The 8408 base pair fragment from pBWU13 and the 2334 base pair fragment from pBROD2 were gel purified and ligated to produce the pHP2 plasmid. pBROD6 encodes the *a-c/2-c* construct in the context of the full *atp* operon, in the absence of native *c*,

and was constructed previously in a similar fashion to pHP2 (Rempel and Dmitriev, unpublished data). See Figure 3.2 for plasmid maps of pBWU13, pBROD2, pBROD6 and pHP2.

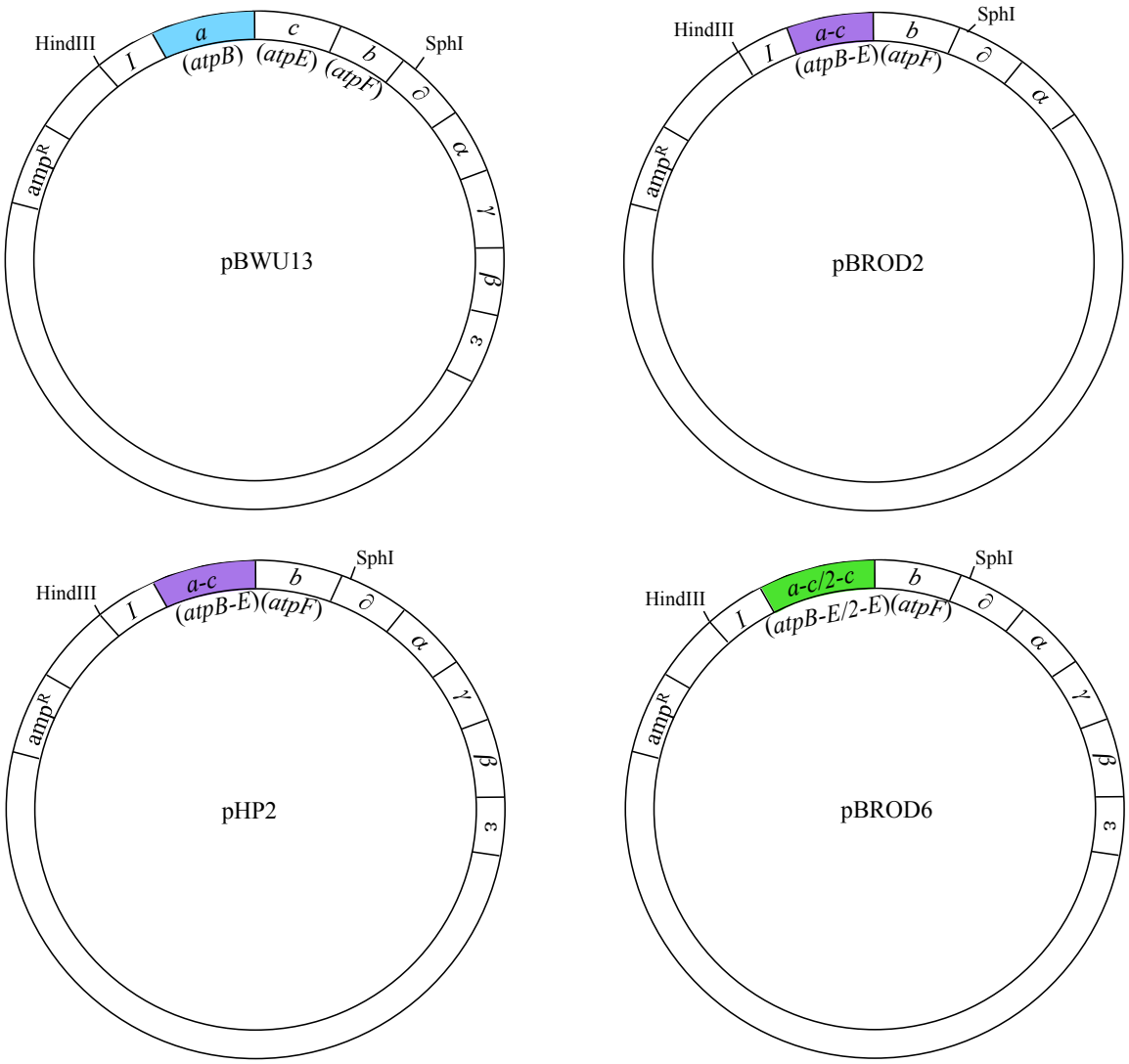

Figure 3.2: Plasmid diagrams of pBWU13, pBROD2, pHP2 and pBROD6. The gene encoding wild type subunit *a* is shown in blue. The genes encoding *a-c* and *a-c/2-c* are shown in purple and green respectively. The positions of the other *atp* operon expression products are indicated on each plasmid as well as the positions of the HindIII and SphI restriction sites.

The gene encoding subunit *a* (*atpB*) was replaced with the genes encoding the fusion proteins using the pHP3 and pHP4 vectors. pHP3 and pHP4 are pEXP1-DEST derivative vectors, designed for cell free synthesis, which encode the *a-c/2-c* and *a-c* constructs

respectively. pHP3 and pHP4 both contain an NheI site immediately 3' of the stop codon for each construct. Both pHP3 and pHP4 were digested with PflMI and NheI. The resulting 1150 base pair fragment of pHP3 and the 960 base pair fragment of pHP4 encoded the *a-c/2-c* and *a-c* fusion protein respectively. To generate a pBWU13 vector fragment lacking the *atpB* gene, pBWU13 was amplified by around-the-plasmid PCR (Figure 3.3). The reverse primer BSR320 was designed to anneal downstream of the PflMI site within the *atpB* gene and the forward primer B966FNheI was designed to introduce an NheI site immediately 3' of the *atpE* gene. PCR was conducted using Phusion DNA polymerase (Thermo Scientific – Finnzymes, Lafayette, CO). The 10,700 base pair PCR product was restricted with PflMI and NheI and gel purified. The 960 base pair fragment from pHP4 and the 1150 base pair fragment of pHP3 were individually ligated with the 10,700 base pair PCR fragment to generate pHP7* and pHP808* respectively. pHP7* and pHP808* were used to transform OM202*recA E. coli* cells. Several transformants were isolated and the pHP7* and pHP808* plasmid identity was verified by control restriction analysis.

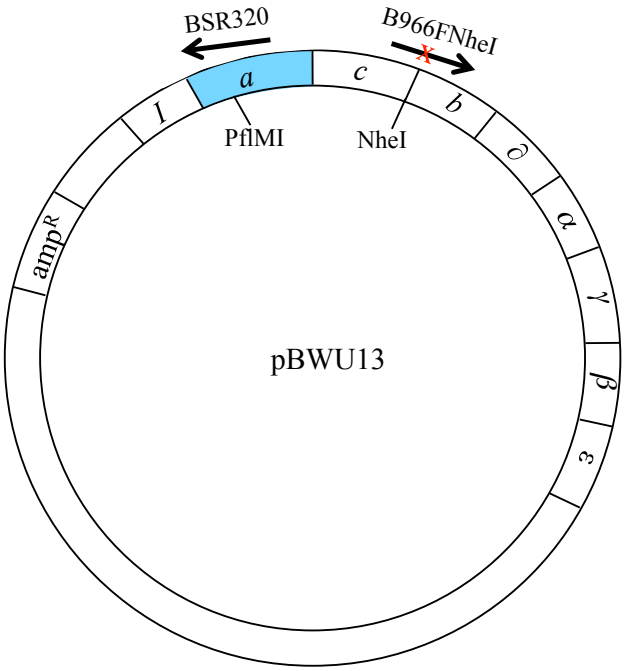

Figure 3.3: PCR strategy for the amplification of the pBWU13 vector fragment lacking *atpE* (subunit *c*). The positions of primers BSR320 (reverse) and B966FNheI (forward) are indicated with black arrows. The NheI restriction site was introduced by primer B966FNheI, the site directed mutagenesis is indicated with a red 'x'. The positions of PflMI and NheI are shown.

Once clones with the correct restriction pattern were identified, the fragment containing *atpI'* the *a/c* fusion gene, *atpE* and *atpF* were recloned from pHP7* and pHP808* into the original pBWU13 vector to eliminate possible errors introduced by PCR. Single clones of pHP7*, pHP808*, and pBWU13 were digested with HindIII and SphI. Digestion of pHP7* resulted a 2641 base pair fragment and an 8410 base pair fragment. Digestion of pHP808* resulted in a 2773 base pair fragment and an 8410 base pair fragment. Digestion of pBWU13 resulted in a 2360 base pair fragment and an 8410 base pair fragment. The 2641 base pair fragment of pHP7* and the 2773 base pair fragment of pHP808* were ligated into the 8410 base pair vector fragment of pBWU13 to generate pHP7 and pHP808 respectively (Figure 3.4).

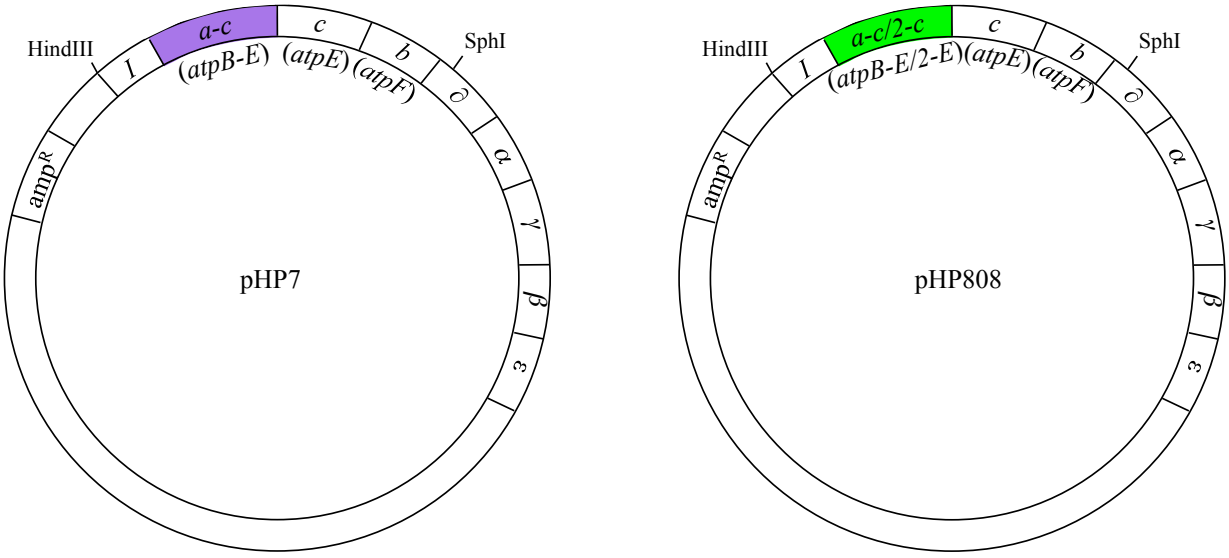

Figure 3.4: Plasmid maps of pHP7 and pHP808. pHP7 is shown on the left and pHP808 is shown on the right. The *a-c* construct is in purple and the *a-c/2-c* is in green. The relative positions of the other *atp* operon genes are shown. The approximate locations of the HindIII and SphI restriction sites are indicated.

Cloning and plasmid construction of the c_{10} assembly mutants.

The G23D and L31F mutations in subunit *c* prevent formation of the c_{10} ring within the membrane. These mutations were introduced into *atpE* using the mega-primer method (Ke and Madison, 1997) with pBWU13 as the template (Table 3.4 and Figure 3.5). The resulting PCR fragments containing *c*G23D and *c*L31F mutations were digested with NheI and SphI and purified. pHP7 and pHP808 were digested with NheI and SphI and the vector fragment was purified. The digested PCR products containing the subunit *c* mutants were ligated into the

pHP7 and pHP808 vector fragments to generate a set of vectors that encode each *a/c* construct in the presence of the c_{10} assembly mutations (Figure 3.6). The pHP7 (*a-c*) derivative plasmids containing *c*G23D and *c*L31F were named pHP11 and pHP13 respectively. The pHP808 (*a-c/2-c*) derivative plasmids containing *c*G23D and *c*L31F mutations were named pHP8012 and pHP8014.

Table 3.4: Primers used in generating the c_{10} assembly mutants. Primer sequences are listed in Table 3.1.

Final plasmid	Primer # (Figure 3.5)	Primer name
pHP9 & pHP10	1	HP_PflMI224
	2	HP_cG23Dr (for pHP9) or HP_cL31Fr (for pHP10)
	3	HP_Sph2547
pHP11 & pHP8012	1	HP_Nhe957
	2	HP_cG23Dr
	3	HP_Sph2574
pHP8013 & pHP8014	1	HP_Nhe957
	2	HP_cL31Fr
	3	HP_Sph2547

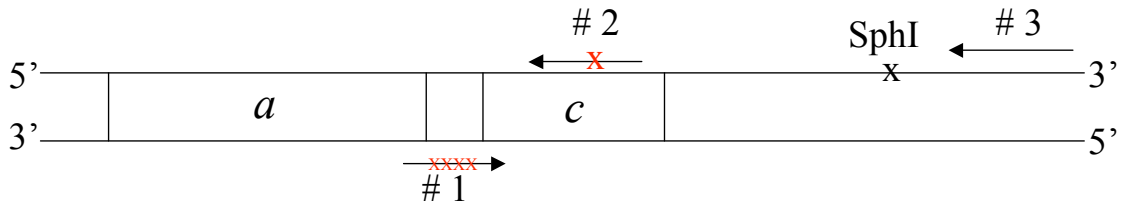

Figure 3.5: General cloning strategy for introducing the c_{10} assembly mutations into pHP7 and pHP808. Primer 1 was designed to introduce and NheI site immediately 3' of the gene encoding subunit *a* on pBWU13. Primer 2 was designed to introduce the GAU or UUC codons that encode the *c*G23D and *c*L31F mutations respectively. Primers 1 and 2 amplified the region between subunit *a* and the c_{10} assembly mutations. The resultant PCR products were used as mega-primers. Primer 3 and the mega-primers amplified the region between the NheI site and SphI site of pBWU13.

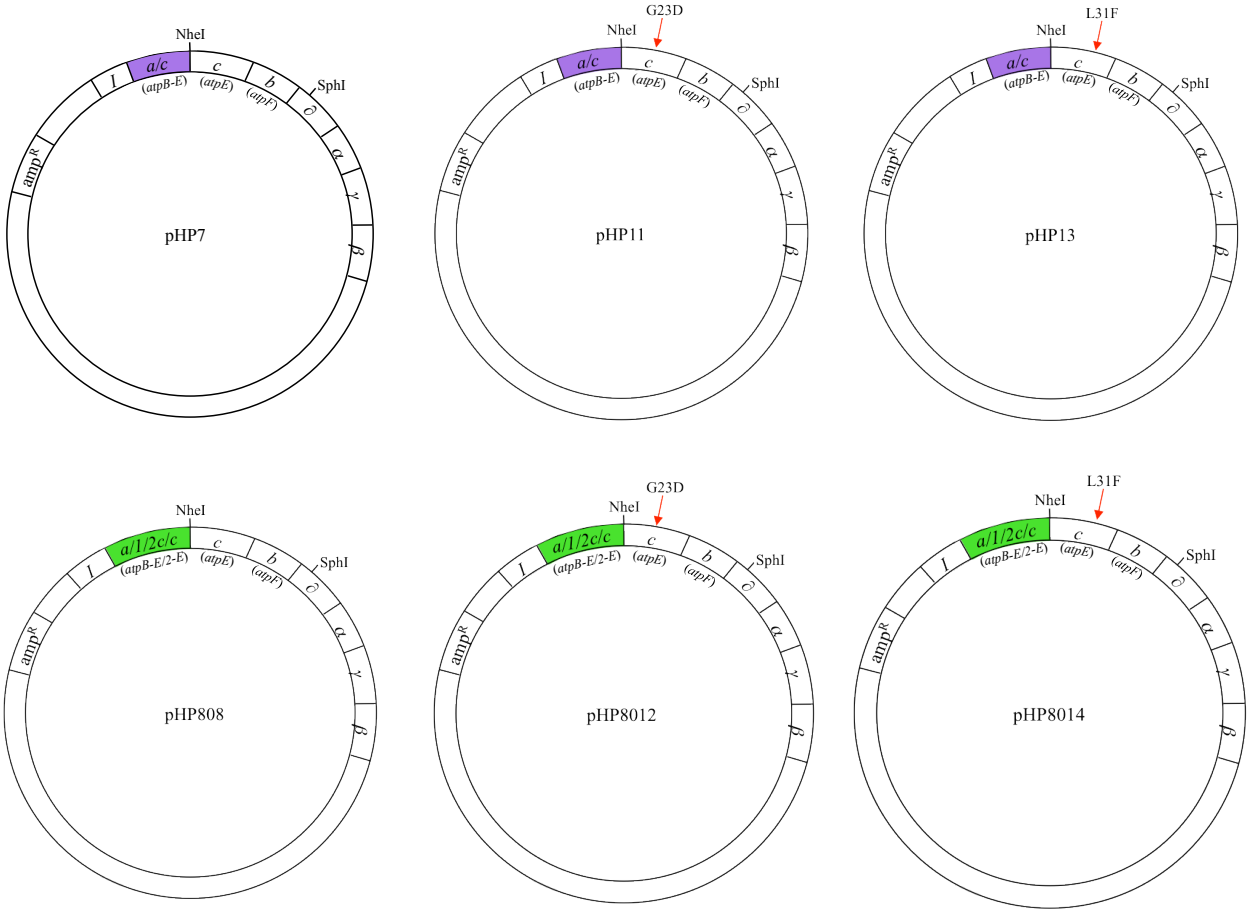

Figure 3.6: Plasmid maps of pHP7, pHP808, and their c_{10} assembly mutant derivatives. The gene encoding the *a-c* construct is shown in purple and the gene encoding the *a-c/2-c* construct is shown in green. The approximate positions of the c_{10} assembly mutations are indicated with red arrows. The relative positions of the other *atp* operon subunits are indicated. The NheI and SphI sites are also shown.

A similar strategy was used to generate plasmids pHP9 and pHP10, which express wild type subunit *a* in the presence of *c*G23D and *c*L31F respectively, in the context of the full *atp* operon.

Introducing the cL31F mutation into the a-c/2-c fusion gene.

The *c*L31F mutation was introduced into the fused *c* subunit of *a-c/2-c* by mega primer PCR (primers: HP_L31F_a2cF & HP_NheI_a2cR), using pBROD6 as a template. The mega primer PCR product spanned the region from the *c*L31F mutation site to approximately 20 bp downstream of the *a-c/2-c* stop codon including an NheI restriction site. The mega primer was

used in conjunction with a third primer (PlfMI224) that annealed over the PflMI site near the 3' end of the *a-c/2-c* gene. The resultant PCR product encoded the *a-c/2-c* fusion construct with the L31F mutation in the fused *c* subunit. The PCR fragment as well as pHP808 and pHP8014 were digested with PflMI and NheI. The PCR fragment was ligated into both pHP808 and pHP8014 vector fragments to produce pHP8015 and pHP8016 respectively (Figure 3.7).

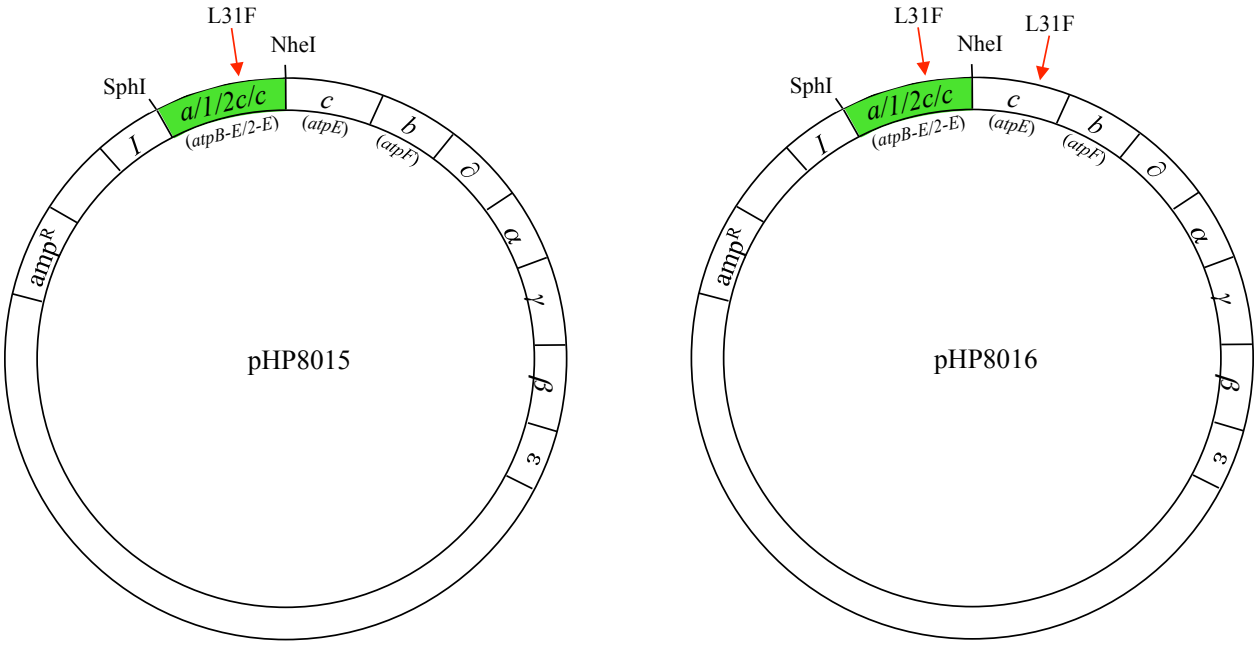

Figure 3.7: Plasmid maps of pHP8015 and pHP8016. The gene encoding the *a-c/2-c* fusion construct is shown in green. The positions of the *c*L31F point mutations are indicated with red arrows. The relative positions of the PflMI and NheI sites are shown.

Cloning the R210Q mutation into subunit a of pBWU13

The pVF2R210Q plasmid, which encodes the entire ATP operon with R210Q mutation in subunit *a* and is closely related to pBWU13 (Ishmukhametov *et al.*, 2008), was provided to us by Dr. Steven Vik (South Methodist University, Dallas, TX). pVF2R210Q and pBWU13 were digested with PflMI and PpuMI (Figure 3.8). The *a*R210Q fragment of pVF2R210Q and the vector fragment of pBWU13 were gel purified and ligated to produce pHP20Q, which is identical to pBWU13, except for the *a*R210Q mutation.

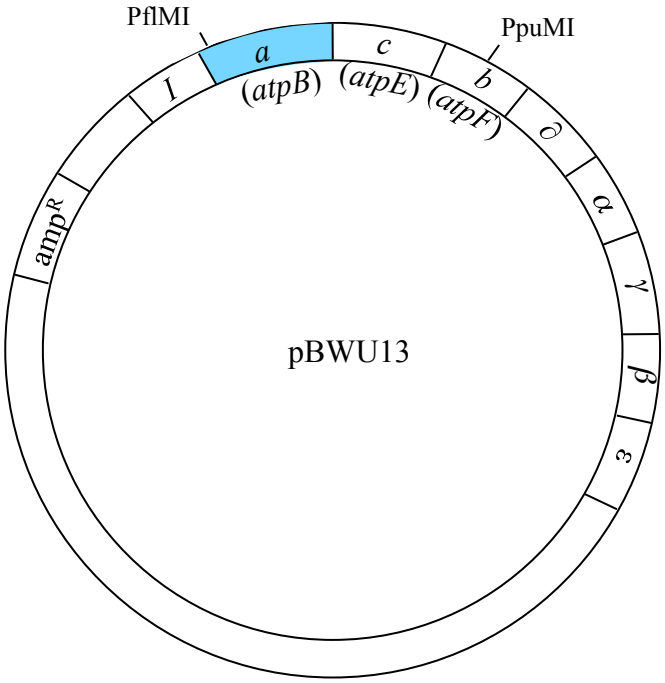

Figure 3.8: Plasmid map of pBWU13. The gene encoding subunit *a* is shown in blue. The other subunits of the *atp* operon are shown. Relative positions of the PflMI and PpuMI restriction sites used for cloning the R210Q mutation are indicated.

Introducing the spacers into a-c/2-c

Two linkers were designed to extend the loop between the fused *a* and *c/2-c* subunits; GSAG (linker 1) and GSAGTASANSGA (linker 2). DNA sequences encoding linkers 1 and 2 were introduced into the *a-c/2-c* fusion construct using the mega-primer method (Ke and Madison, 1997) with pHP808 as the template (Figure 3.9 and Table 3.5). The resultant PCR fragments containing the *a-c/2-c* fusion construct with the extended linkers and pHP808 were digested with PflMI and SphI. Following gel purification, the digested PCR products were ligated into the pHP808 vector fragment to generate plasmids pHPBA_1 and pHPBA_3, which encode the *a-c/2-c-linker-1* and *a-c/2-c-linker-2* proteins respectively. The pHPBA_1 and pHPBA_3 plasmid sequences were transformed into OM202*recA E. coli* cells.

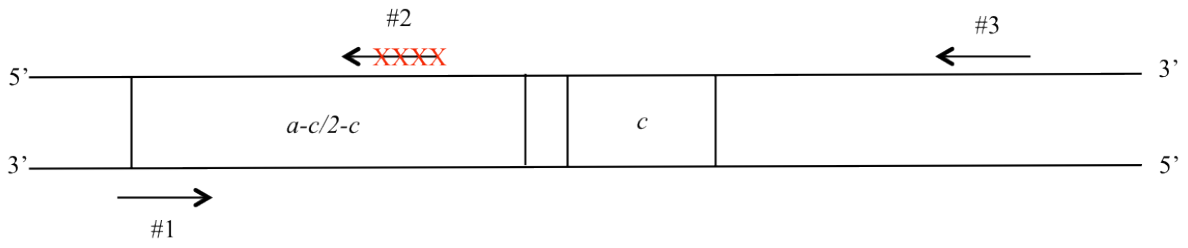

Figure 3.9: The megaprimer cloning strategy used to incorporate the linker extensions into *a-c/2-c*. Primer #1 annealed over the PflMI restriction site. Primer # 2 was designed to encode each linker sequence. Primers 1 and 2 amplified the region between the PflMI site and the linkers. The resultant PCR products were used as a mega primers. Primer 3 and the mega primers amplified the region between SphI and PflMI sites of pHP808.

Table 3.5: Primers used in cloning pHPBA1 and pHPBA3. Primer sequences are listed in Table 3.1.

Final plasmid	Primer # (Fig 3.9)	Primer name
pHPBA1	1	HP_PflMI224
	2	HPBA_RL1
	3	HP_Sph2547
pHPBA3	1	HP_PflMI224
	2	HPBA_RL3
	3	HP_Sph2547

Cloning the a-c/2-c fusion construct into pBAD-102

The *a-c/2-c* fusion protein was cloned into pBAD102, which contains an arabinose inducble promoter. pOD1016 is a pBAD102 derivative vector that expresses the multi-drug transport protein Mdfa (Dmitriev, unpublished data). The gene for Mdfa is flanked by two restriction sites; NcoI lies immediately 5' of the start codon and PmeI lies immediately 3' of the stop codon. pOD1016 was digested with NcoI and PmeI and the pBAD102 vector fragment was isolated. The gene encoding the *a-c/2-c* fusion protein was amplified from pBROD6 by PCR. The primers used to amplify the *a-c/2-c* fusion construct were designed to introduce an NcoI restriction site immediately 5' of the *a-c/2-c* start codon (pBADBFNcoI) and a PmeI site immediately 3' of the stop codon (ESR1285). The resultant PCR fragment was digested with

NcoI and PmeI. The gene for *a-c/2-c* contains an NcoI site, therefore, two fragments approximately 300 base pair and 900 base pair in length were obtained. The 900 base pair fragment was ligated into the pBAD102 vector fragment to yield plasmid pHP805*, which was transformed into TOP10 *E. coli* cells. pHP805* was digested with NcoI and then ligated with the 300 base pair fragment of the *a-c/2-c* gene. The resulting plasmid was named pHP805 (Figure 3.10).

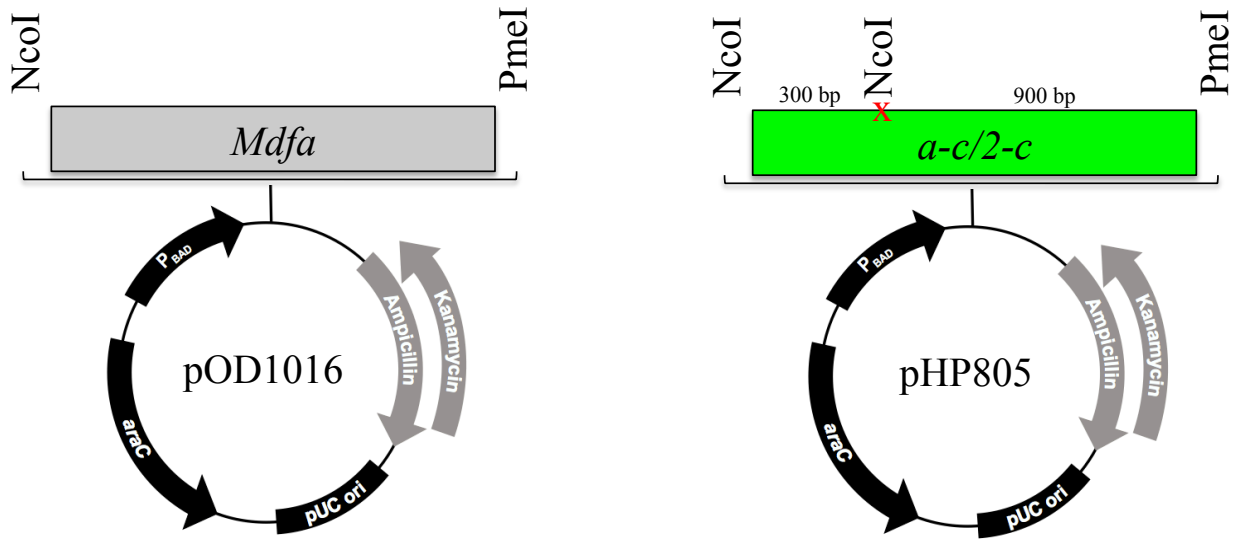

Figure 3.10: Plasmid maps of pOD1016 and pHP805. The positions of the PmeI and NcoI restriction sites are shown. The *a-c/2-c* fusion construct is shown in green and the position of the internal NcoI site is indicated with a red 'x'. The 300 and 900 base pair fragments from digestion of the *a-c/2-c* PCR fragment are labeled.

Cloning the a-c/2-c fusion construct and atpF into pBAD-102.

The *a-c/2-c* fusion protein, along with the gene encoding subunit *b*, were cloned into pBAD102. PCR was used to amplify the pBAD102 vector fragment from ODM1016. The primers used to amplify the pBAD102 vector were designed to introduce an NheI site at the 5' end of the multiple cloning site (HP_pBAD_NheIR) and a PmeI site (HP_pBAD_PmeIF) at the 3' end of the multiple cloning site. In pBROD6, the *a-c/2-c* fusion construct is followed by a noncoding sequence from the *atp* operon, and then by the *atpF* gene. This fragment was amplified by PCR using primers designed to introduce an NheI site immediately 5' of the *a-c/2-c* start codon (HP_PmeI_BROD6) and a PmeI site immediately 3' of the *atp F* stop codon (HP_NheI_BROD6). The PCR product and the pBAD102 vector fragment were digested with

NheI and PmeI, gel purified, and ligated. The resulting plasmid, pHP80-102, was transformed into TOP10 *E. coli* cells (Figure 3.11).

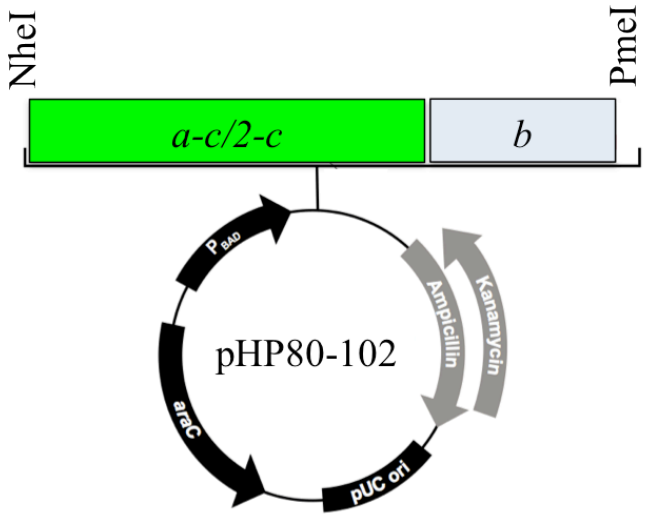

Figure 3.11: Plasmid map of pHP80-102. The positions of the PmeI and NheI restriction sites are shown. The gene encoding the *a-c/2-c* fusion construct is shown in green and the gene encoding subunit *b* is shown in light blue.

Cloning atpI' and the F_0 genes into pBAD-102

The pBAD102 vector fragment was amplified by PCR, using primers to introduce an EcoRI site 5' of the multiple cloning site (HP_ara_EcoRI_R) and a SacI site 3' of the multiple cloning site (HP_ara_SacI_F). The pBWU13 vector encodes a truncated version of the *atpI* gene, which is denoted as *atpI'*. The *atpI'* gene, and the genes encoding the *a-c/2-c* construct, subunit *c*, and subunit *b,* were amplified from pHP808 by PCR. The primers were designed to introduce an EcoRI site immediately 5' of *atpI'* (HP_F0_EcoRI_F) and a SacI site immediately 3' of the *atpF* stop codon (HP_F0_SacI_R). The 4024 base pair vector fragment and 2240 base pair fragment encoding the F_0 genes were restricted with EcoRI and SacI, gel purified, and ligated. The resultant plasmid, pHP8024, was used to transform TOP10 *E. coli* cells. A similar procedure was used to clone the F_0-encoding fragment of the *atp* operon with native *atpB* (subunit *a*) into pBAD. The *c*G23D point mutation disrupts formation of the *c*-ring in the membrane. pHP9 encodes the entire wild type *atp* operon, except *atpE* contains the *c*G23D mutation. We amplified the F_0 genes from pHP9 by PCR, digested the resultant fragment with

EcoRI and SacI, gel purified the restricted fragment, and ligated the fragment with the 4024 base pair pBAD-102 vector fragment. The pBAD-102 derivative plasmid encoding the genes for *atpI'*, native subunit *a*, subunit *c* with the G23D mutation, and subunit *b* was named pHP8025 (Figure 3.12).

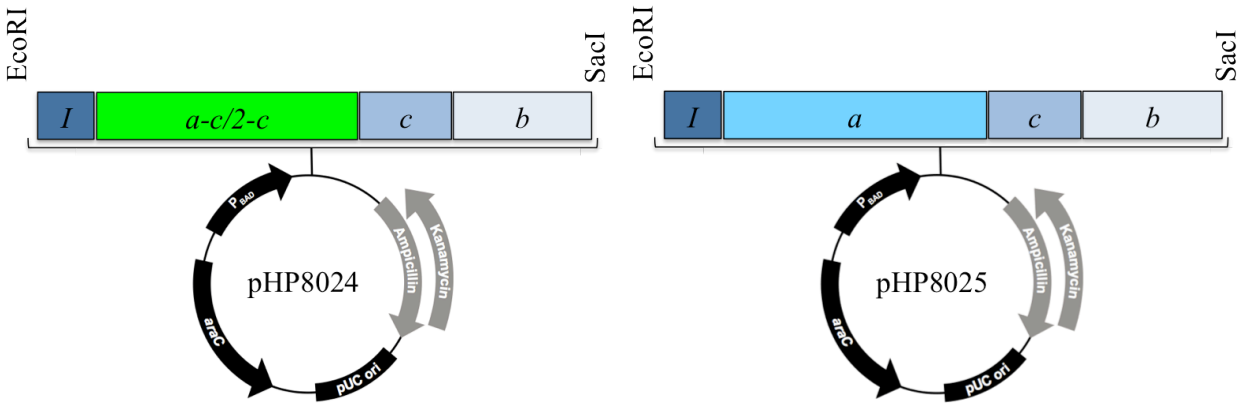

Figure 3.12: Plasmid maps of pHP8024 and pHP8025. The *a-c/2-c* gene is shown in green and native subunit *a* is shown in bright blue. The relative positions of the F_0 genes are shown. The positions of the EcoRI and SacI sites are indicated.

3.3 *E. coli* culture growth and protein expression.

Strains expressing wild type subunit *a* and the *a/c* constructs from vectors derived from pBWU13 were grown on M9 minimal media (40 mM $Na_2HPO_4*7H_2O$, 22 mM KH_2PO_4, 8 mM NaCl, 18 mM NH_4Cl, 2 mM $MgSO_4$, 0.4 % glucose, 0.1 mM $CaCl_2$) in the presence of 200 µg/ml ampicillin. Cells were grown at 37 ^{0}C, with shaking at 220 r.p.m., to late exponential phase and harvested by centrifugation at 6,000 x *g* for 15 minutes. Raw cell samples for SDS-PAGE were prepared in SDS sample buffer and incubated at 37 ^{o}C for 15 minutes. SDS-PAGE was carried out using 10 % polyacrylamide gels (Schagger and von Jagow, 1987). Expression was examined by Western blot analysis of whole cell samples.

Expression experiments with pBAD derivative vectors were conducted essentially as described in the pBAD-102 manual from Invitrogen (pBAD TOPO Expression Kit Manual, 2010). TOP10 cells containing either pHP805 or pHP80-102 were induced with a range of arabinose concentrations from 0.00002 % to 0.2 %. OM202*recA* cells containing pHP805,

pHP80-102, pHP8024, and pHP8025 were induced with a range of arabinose concentrations from 0.002 % to 0.8 %. Cells were grown for 4 hours at 37 ^{o}C with shaking at 220 r.p.m. after the addition of arabinose. Samples for SDS-PAGE and Western blot analysis were prepared as described in the preceding paragraph.

3.4 Purification of subunit *a* and the *a-c/2-c* fusion protein from isolated F_0 complex.

C43(DE3) and C43*recA E. coli* cells expressing subunit *a* or the *a-c/2-c* fusion protein respectively were grown as described in section 3.3. Membrane vesicle preparation for protein purification was done essentially as described by (Mosher *et al.*, 1985). The membranes were stripped of F_1 with EDTA. F_0 was then extracted from the membrane with octylglucopyranoside and sodium cholate, and enriched by ammonium sulfate precipitation, essentially as described by Schneider and Altendorf (Schneider and Altendorf, 1984). To dissociate F_0-complex into individual subunits, isolated F_0 was diluted to a final concentration of ~ 1 mg/mL in dissociation buffer (10 mM tris(hydroxymethyl)aminomethane (Tris) -HCl, pH 8.0, 1 mM EDTA, 1 mM dithiothreitol (DTT), 3 M LiBr, 1 % (w/v) deoxycholate, and 5 % Zwittergent 3-14) and incubated at room temperature for 20 hours with light stirring.

Dissociated F_0 samples were subjected to nickel-nitrilotriacetic acid (Ni-NTA) affinity chromatography. A column loaded with 3 ml Ni-NTA agarose was prewashed with ten bed volumes of equilibration buffer (10 mM Tris-HCl, pH 8.0, 1 mM DTT, 3 M LiBr, and 2 % sodium cholate). The dissociated F_0 samples were loaded onto the Ni-NTA column and allowed to flow through the resin at a rate of approximately 0.2 ml/min. The column was sequentially washed with 5 bed volumes of equilibration buffer, 5 bed volumes of equilibration buffer containing 20 mM imidazole, and 10 bed volumes of LMPG-0 buffer (10 mM Tris, pH 8.0, 1 mM DTT, and 0.01 % 1-myristoyl-2-hydroxy-sn-glycero-3-[phosphor-*rac* -(1-glycerol)] (LMPG)). Stepwise elution was carried out in three stages: 2 bed volumes of LMPG-0 buffer containing 50 mM imidazole, 2 bed volumes of LMPG-0 buffer containing 100 mM imidazole, and 2 bed volumes of LMPG-0 buffer containing 250 mM imidazole. Three milliliter fractions were collected and analyzed by SDS-PAGE. In protein purifications intended for NMR experiments 10 mM KH_2PO_4 was substituted for 10 mM Tris in the LMPG-0 buffer.

Vivaspin-20 centrifugal membrane concentration devices were used to concentrate purified subunit *a* and *a-c/2-c*. All washes and treatments were carried out for 3 minutes at 4,000 x *g*. The Vivaspin devices were washed with 5 ml ddH_2O to remove traces of azide. The membrane was then washed with equilibration buffer (10 mM Tris, pH 8.0, 1 mM DTT, and 0.01 % LMPG. The membrane was treated with equilibration buffer containing 1 mg/mL bovine serum albumin (BSA), which was removed by decanting. The membrane was then washed twice with equilibration buffer to remove residual BSA.

Fractions containing subunit *a* or *a-c/2-c* were pooled and concentrated to a final concentration between 5 – 12 mg/ml using the pre-treated Vivaspin concentration devices. Purified and concentrated protein was transferred into either NMR buffer (10 mM KH_2PO_4, pH 6.0, 0.01 % LMPG), or crystallization buffer (15 mM 2-(N-morpholino)ethanseulfonic acid (MES) buffer, pH 6.0, 0.01% LMPG), and stored at 4 ^oC.

3.5 Purification of subunit *a* and the *a-c/2-c* fusion protein from intact F_1F_0.

Intact ATP synthase was isolated using a modified version of the protocol developed by Laubinger and Dimroth (Haji and Dmitriev, unpublished data; Laubinger and Dimroth, 1988). Membrane vesicles were isolated as described in section 3.4. Membranes were suspended in 50 mM 4-morpholinepropanesulfonic acid (MOPS) - KOH, pH 7.0, at 5 mg/mL total membrane protein. ATP synthase was solubilized from the membranes by mixing with a final concentration of 0.2 % 1,2-diheptanoyl-*sn*-glycero-3-phosphocholine (DHPC) at room temperature for 30 minutes. Soluble protein was isolated by ultracentrifugation at 200,000 x *g* for 30 minutes. Final concentrations of 50 mM $MgCl_2$ and 2 % polyethylene glycol (PEG) 6000 were added to the protein solution and mixed for 20 minutes at room temperature. The solution was subjected to centrifugation at 39,000 x *g* for 15 minutes. The ATP synthase was precipitated from the supernatant with a final concentration of 10 % PEG-6000. Precipitated ATP synthase was isolated by centrifugation at 39,000 x *g* for 20 minutes. The protein pellet was resuspended in F_1F_0-Buffer (10 mM Tris-HCl, pH 8.0, 5 mM $MgCl_2$, 1 mM DTT, 1 mM phenylmethylsulfonyl fluoride (PMSF) and 0.2 % DHPC). Insoluble material was removed by centrifugation at 39,000 x *g* for 15 minutes. Purified ATP synthase was stored under liquid nitrogen. A flow diagram of the complete purification procedure is shown in Figure 3.13.

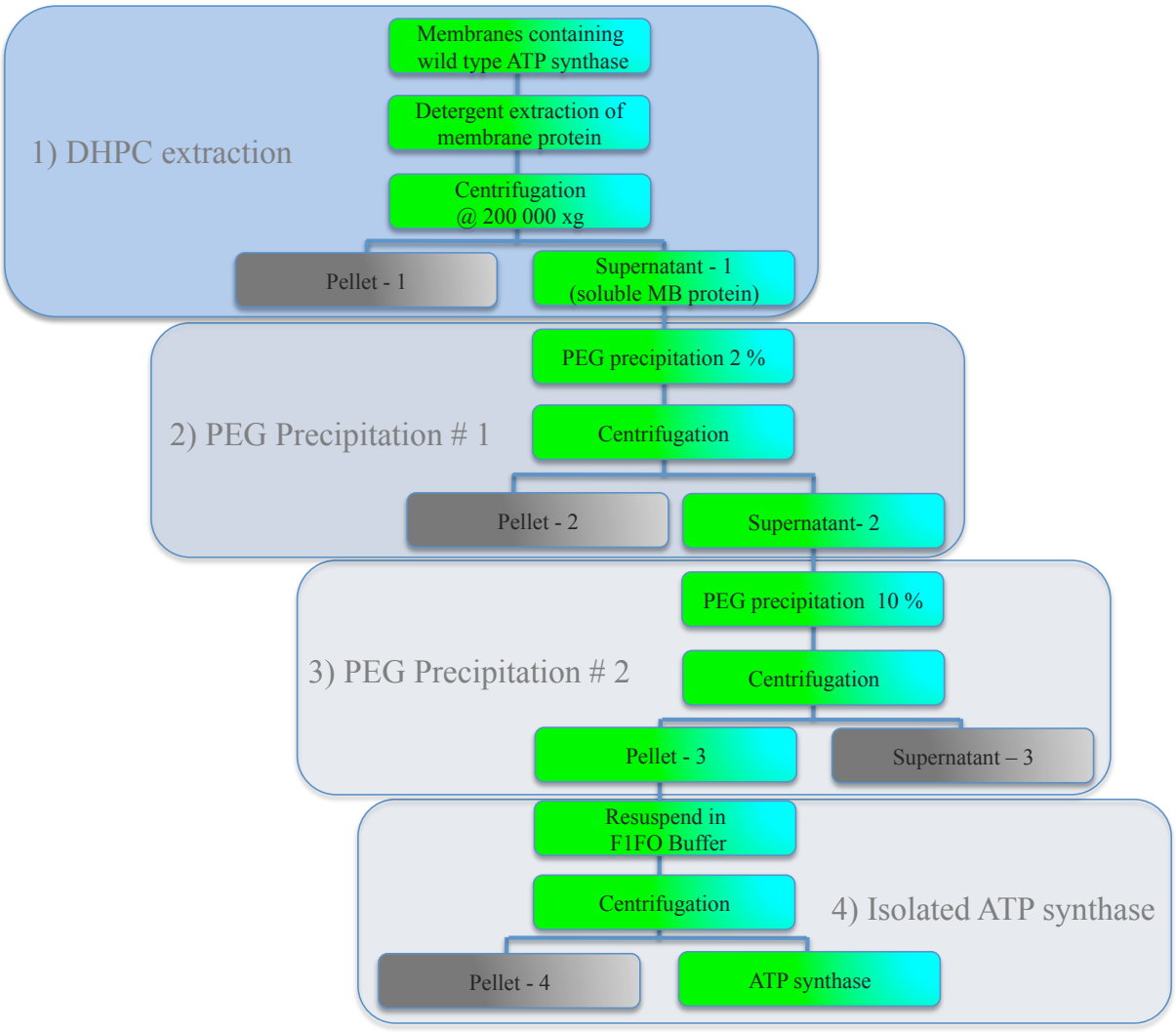

Figure 3.13: Flow diagram of the F_1F_0 ATP synthase isolation procedure. The major stages of purification are numbered 1 through 4. Green boxes indicate experimental steps where ATP synthase is present. Grey boxes indicate experimental steps where ATP synthase is not present.

Isolated F_1F_0 was diluted to a final concentration of 1 – 3 mg/ml in dissociation buffer (10 mM Tris-HCl, pH 8.0, 1 mM EDTA, 1 mM DTT, 3 M LiBr, 1 % (w/v) deoxycholate, and 5 % Zwittergent 3-14) and incubated at room temperature for twenty hours. The Ni-NTA purification was conducted essentially as described in section 3.4. Ni-NTA fractions containing subunit *a* were pooled and exchanged into LMPG-0 buffer using the BSA pre-treated concentration devices. The samples were concentrated to ~ 20 % of their original volume and

then diluted to their original volume in LMPG-0 buffer. The concentration / dilution procedure was carried out three times to reduce the imidazole concentration to trace amounts. After the final concentration step, the protein solution was mixed 1 : 10 in R2-Disociation buffer (10 mM Tris-HCl, pH 8.0, 1 mM DTT, 3 M LiBr and 0.01 % LMPG). After dissociation, the samples were subjected to a second round of Ni-NTA chromatography as described in the previous paragraph, except, 0.01 % LMPG was substituted for sodium cholate in all cases.

3.6 Size exclusion chromatography

Purified subunit *a* was subjected to size exclusion chromatography using the Superdex-200 GL 10/300 (GE Healthcare, Baie d'Urfe, QC) column. The column was pre-equilibrated with GF buffer (15 mM MES, pH 6.0, 150 mM NaCl, and 0.01% LMPG). Purified subunit *a* was loaded onto the column and eluted in one bed volume of GF buffer at a rate of 0.4 mL / minute.

3.7 Isolation of F_1 from cellular membranes.

Membranes were prepared as described in section 3.4. A 5.7 μg sample of membranes from each strain was incubated in F_1 Stripping buffer (1 mM Tris-HCl, pH 7.5, 0.5 mM EDTA, 10 % v/v glycerol) at a ratio of 210 μl per 1 μg total membrane protein for 2 hours at room temperature. The membranes were separated from soluble detached F_1 by centrifugation at 150,000 x *g* for one hour at room temperature. F_1 samples were kept at room temperature.

3.8 Detergent exchange.

Purified subunit *a* was exchanged into various detergents using Ni-NTA chromatography. Subunit *a* was bound to Ni-NTA agarose pre-equilibrated with NMR buffer as described in section 3.4 and the column was washed with 10 bed volumes of exchange buffer (10 mM KH_2PO_4 pH 8.0, 1 mM DTT), supplemented with a detergent of choice. Subunit *a* was then eluted from the Ni-NTA column with exchange buffer containing 250 mM imidazole. Eluted protein was pooled and buffer exchanged to remove imidazole and adjust the pH to 6.0, using pre-treated Vivispin-6 centrifugal concentration devices as described in section 3.4. The samples were concentrated to a volume of approximately 400 μl for NMR studies.

3.9 NMR experiments.

Unless otherwise stated, ^{1}H, ^{15}N-HSQC experiments were carried out at 600 or 750 MHz at 310 or 315K. There were 128 increments in t_1 with 16 scans per increment.

3.10 Dynamic light scattering.

Wild type subunit *a* was examined by dynamic light scattering (DLS) on the DynaPro-MS800 instrument at the Saskatchewan Structural Sciences Centre using the Dynamics™ version 5.26.60 software package. Protein samples for DLS were prepared in 50 mM KH_2PO_4 pH 6.0 with 0.01 % LMPG and concentrated to approximately 7 mg/ml. DLS experiments were carried out at 20 ^{o}C and 27 ^{o}C with instrument sensitivity set to maximum and scan number greater than 100.

3.11 Crystallization trials.

3.11.1 High throughput screening.

Preliminary crystal screening for subunit *a* and the *a-c/2-c* construct was carried out at the High Throughput Crystallization Screening Facility at the Hauptman-Woodward Medical Research Institute (HWI-HTS) in Buffalo, New York. Protein samples were concentrated to 5 - 12 mg/mL in crystallization buffer (15 mM MES, pH 6.0 and 0.01 % LMPG). Samples were subjected to the MSC4-1563 cocktail screen, also known as Membrane Protein Crystallization Screen Generation Four.

3.11.2 Hanging drop vapor diffusion screens.

Several refined screening conditions were tested in the presence of micelles or bicelles. The purification procedure described in section 3.4 produces subunit *a* suspended in micelles. Bicelles were prepared with water, 1,2-dimyristoyl-*sn*-glycero-3-phosphocholine (DMPC), and 3-([3-Cholamidopropyl]dimethylammonio)-2-hydroxy-1-propanesulfonate (CHAPSO) at a ratio of 6:3:1. The water : DMPC : CHAPSO mixture was subjected to eight cycles of freezing in liquid nitrogen, heating to 55 ^{o}C, incubation on ice for 10 minutes, and vortexing. To reconstitute subunit *a* into bicelles, purified subunit *a* was mixed with bicelle solution at a ratio

4:1 and incubated on ice for 30 minutes. Precipitant solution was added 1:1 to purified subunit *a*, suspended in either micelles or bicelles, and the droplets were suspended over 1 mL of well solution using 'EasyXtal CrystalSupport' trays (Qiagen, Valencia, California). Table 3.6 lists the supplier and lot number of the various PEG types used in screening. Most plates were set up in duplicate, one set was incubated at 21 ^{o}C and the other was incubated at 4 ^{o}C.

Table 3.6: PEG parameters* for refined vapor diffusion screening conducted at the University of Saskatchewan.

PEG type	Supplier / (location)	Lot number
PEG 400	Fisher – Carbowax (Ottawa, ON, Canada)	121576
PEG MME 550	Hampton Research (Aliso Viejo, CA, USA)	261180
PEG 1500	Alfa Aesar (Ward Hill, MA, USA)	10161203
PEG 2000	Alfa Aesar (Ward Hill, MA, USA)	10172606
PEG 3350	J.T. Baker (Miami, FL, USA)	Y19585
PEG 4000	Alfa Aesar (Ward Hill, MA, USA)	10167045
PEG 6000	Alfa Aesar (Ward Hill, MA, USA)	10156829
PEG 8000	Fisher (Ottawa, ON, Canada)	110368

*PEG quality varies greatly from brand to brand as well as between batches. For reproducibility the PEG brand and lot number of each PEG molecular weight should be kept constant throughout crystal screening (Bergfors, 1999).

3.11.3 Lipidic cubic phase screens.

1-monooleoyl-*rac*-glycerol (monoolein) was melted at 45 ^{o}C and mixed with protein solution at a 2:3 (protein : monoolein) ratio. The mixture was extruded through a 0.5 mm diameter syringe coupler and mixed until translucent. The protein – monoolein mixture was loaded into a microdispenser syringe (Hamilton, Reno, NV). Refined screens as well as standard screens were set up on LaminexTM Glass Base 200 micron plates (Molecular Dimensions, Suffolk, UK). A single 0.2 µl dollop of protein – monoolein mixture was placed in the center of each well and overlaid with 1 µl of precipitant solution. The plates were incubated at 20 ^{o}C.

3.12 Enzyme activity assays.

3.12.1 Test for oxidative phosphorylation by cell growth on succinate.

A single colony of a given *E. coli* strain was streaked onto M63 minimal media agar plates containing 0.6 % succinate as the sole source of carbon. Plates were incubated for approximately 24 hours at 37 ºC. Growth levels were examined and recorded.

3.12.2 ATP dependent proton transport assay.

ATP dependent proton transport was measured using 9-amino-6-chloro-2-methoxyacridine (ACMA) fluorescence. ACMA fluorescence was recorded at 490 nm with excitation at 410 nm. Whole membrane vesicles containing 100 µg total protein were added to 1 mL of ACMA quench buffer (20 mM Tricine-NaOH, pH 8.0, 10 mM $MgCl_2$, 300 mM KCl). ACMA was added to the reaction mixture to a final concentration of 2 µM after base line fluorescence was recorded. The reaction was initiated by addition of 0.2 mM ATP, pH 8.0. 2µM Carbonylcyanide-4-(trifluoromethoxy)-phenylhydrazone (FCCP) was added to the reaction after approximately 3 minutes.

When ACMA is added to the assay solution it freely diffuses across the membrane in its uncharged form. When ATP is added to the reaction mixture, F_1F_0 hydrolyzes the ATP and actively pumps protons into the lumen of the vesicles, creating an acidic microenvironment. ACMA becomes protonated in the acidified vesicles and accumulates because it's protonated form is positively charged and cannot cross the lipid bilayer. A concentration dependent ACMA fluorescence quench is observed. The proton gradient uncoupler FCCP shuttles protons out the lumen and dissipates the ΔpH; this is a control to show that the observed fluorescence quench is caused by the generation of a proton gradient (Figure 3.14).

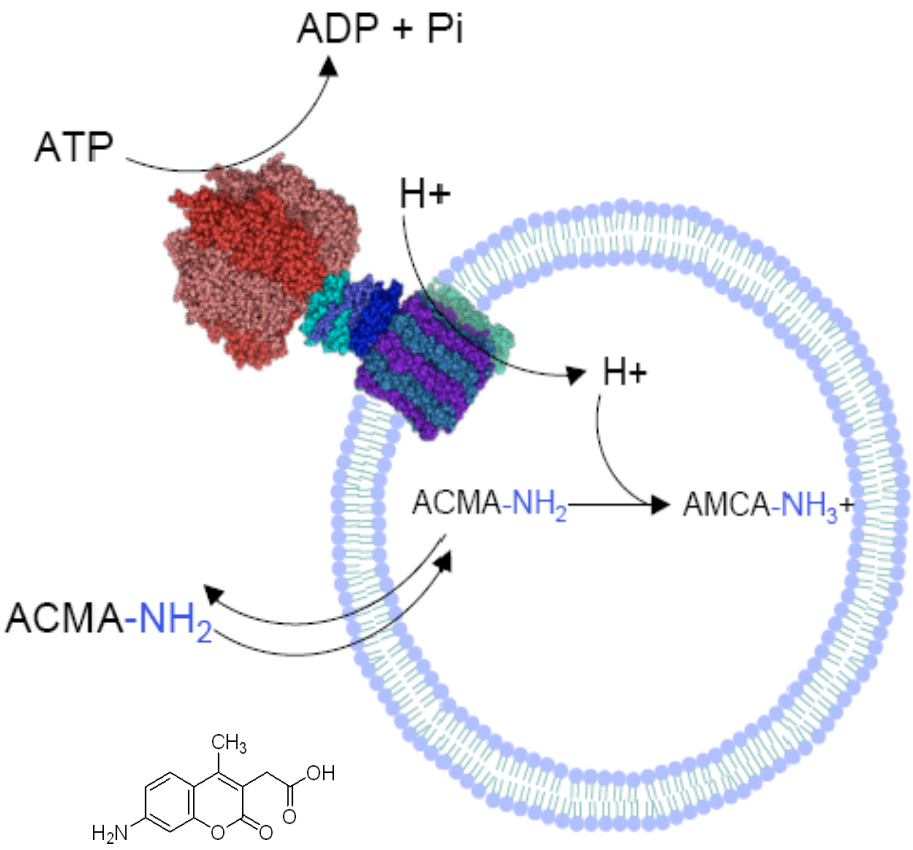

9-Amino-6-chloro-2-methoxyacridine

Figure 3.14: The principle of the ATP driven proton translocation assay. ATP synthase is shown in red and purple. The membrane vesicle is shown in blue. The NH_2 group of ACMA that becomes charged as a result of protonation is shown in blue. The structure of ACMA is illustrated on the bottom left.

3.12.3 Passive proton translocation assay.

Passive proton transport was measured similarly to the active transport assays described in section 3.12.2, except F_1-stripped membrane vesicles were used instead of whole membrane vesicles, and NADH hydrolysis via NADH dehydrogenase was used to generate the proton gradient instead of ATP (Figure 3.15). F_1 was stripped from the membranes essentially as described in section 3.7, except the incubation in F_1 stripping buffer was conducted for 16 hours at 4 ^{o}C. The stripped membranes were resuspended in TMDG buffer (50 mM Tris-HCl, pH 7.4, 5 mM $MgCl_2$, 1 mM DTT, 10 % glycerol v/v, 1 mM PMSF), flash frozen using liquid nitrogen, and stored at -80 ^{o}C.

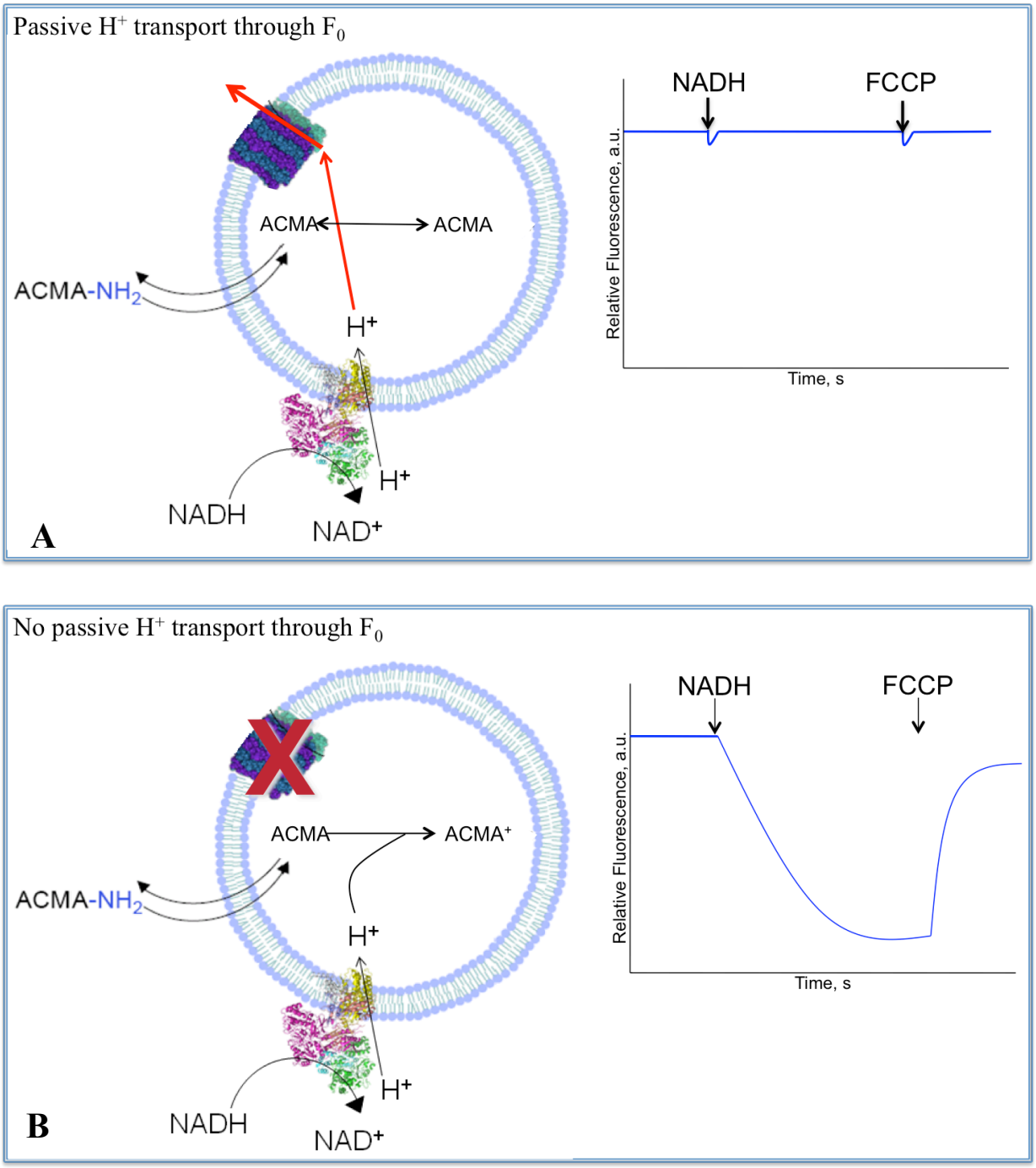

Figure 3.15: The principle of the passive proton translocation assay. The F_0 domain of ATP synthase is shown in green and purple. The membrane vesicle is shown in blue. NADH dehydrogenase is shown in pink, green, and yellow. A) The red arrows indicate the path of protons when F_0 is intact and functional (left); the theoretical fluoresence trace is shown (right). B) The large red 'X' represents a blockage in the F_0 pore which allows protons to accumulate inside the vesicle and facilitate ACMA quenching (left); the theoretical fluoresecnce trace is shown (right).

3.12.4 Assay for ATPase activity.

Whole membrane vesicles, isolated F_1, and F_1-stripped membranes were assayed for ATPase activity by quantification of liberated inorganic phosphate over time. Phosphate detection by malachite green was carried out essentially as described by (Ekman and Jager, 1993). Samples were suspended in TMDG buffer. ATP was added to a final concentration of 2 mM. All assays were conducted at 37 ^{o}C.

3.13 Other methods.

3.13.1 Molecular Biology Methods.

Plasmid preparation.

Single colonies were selected, used to inoculate 5 mL LB media containing antibiotic, and grown for 18 hours at 37 ^{o}C with shaking at 220 r.p.m. Plasmids were isolated using Mini-Prep kits (Qiagen, Burlington, ON) and suspended in sterile water. Plasmids were stored at – 20 ^{o}C.

Restriction digestion.

All restriction exonucleases were supplied by New England Biolabs (NEB) (NEB, Ipswich, MA). DNA restrictions were set up in 20 µl volumes with 0.5 – 2.0 µg of plasmid DNA, 5 U of each restriction enzyme, 2 µl of appropriate 10 x NEB reaction buffer, and 0. 1 µg BSA (if required). Restriciton digestions were incubated at 37 ^{o}C for 30 minutes.

Ligation reactions.

Ligation reactions were set up in 20 µl volumes. Each reaction contained 50 ng vector DNA, 80 ng insert DNA, 2 µl of 10 x T4 DNA ligase buffer, and 400 U of T4 DNA ligase (NEB, Ipswich, MA). Ligation mixtures were incubated for 18 hours at 16 ^{o}C.

E. coli transformations.

Chemically competent *E. coli* cells were prepared using $CaCl_2$, essentially as described by Dagert and Ehlrich (Dagert and Ehlrich, 1979). Fifty microliters of competent cells were incubated with 0.3 µg plasmid DNA on ice, for 30 minutes. The cells were then heat shocked for 45 seconds at 42 ^{o}C and re-equilibrated on ice for 10 minutes. Equilibrated cells were

transferred into 1 mL of LB broth and incubated at 37 ^{o}C for 1 hour with shaking at 220 r.p.m. After the 1 hour growth the cells were plated on LB agar containing antibiotic and incubated for 18 hours at 37 ^{o}C.

3.13.2 SDS-PAGE

SDS-PAGE was carried out essentially as described by Schagger & von Jagow (Schagger and von Jagow, 1987). The stacking gel layer contained 3 % acrylamide and the separating gel contained 10 % acrylamide unless otherwise stated.

3.13.3 Western blot analysis.

Western blot analysis was carried out as previously described (Towbin *et al.*, 1979). Protein was transferred to polyvinylidene fluoride (PVDF) membrane by electroblotting at either 0.4 or 0.9 Amp for 90 minutes. To detect hexahistidine (His_6) tagged proteins, Western blots were probed using the Qiagen monoclonal anti-pentahistidine horse radish peroxidase (HRP) conjugate antibody (1:10,000 dilution) (Qiagen, Mississauga, ON). Western blots specific for subunit *c* were probed with a primary polyclonal rabbit anti-*c* antibody (1:60,000 dilution in PBS with 0.1 % Tween-20 and 2 % BSA fraction-V) and with a secondary goat anti-rabbit HRP conjugate antibody (1:10,000 dilution in PBS with 0.1 % Tween-20).

3.13.4 Protein determination by the Lowry method.

Protein concentration determination was carried out as previously described (Lowry *et al.*, 1951). BSA standard curves ranging from 0.04 µg – 0.59 µg per sample were conducted with each assay.

4 Results.

4.1 The *a-c/2-c* fusion protein is integrated into the membrane in the absence of native *c*.

We have generated two fusion proteins consisting of subunits *a* and *c* of *E. coli* ATP synthase (Section 3.1 contains a full description of the fusion constructs). The transmembrane topology of subunit *a* has yet to be confirmed through high resolution structure determination; each fusion protein places subunit *c* in a different topology relative to subunit *a* to account for the two possible orientations of the carboxyl terminus of subunit *a* relative to the amino terminus of subunit *c*. We asked two questions: First, do the fusion proteins incorporate into the membrane? Second, does membrane incorporation of the *a/c* fusion proteins require native subunit *c*?

Initially, expression experiments with both wild type subunit *a* and the *a-c/2-c* fusion protein were carried out using the *E. coli* OM202 parental strain. RecA activity in the OM202 parental strain caused damage pHP808 plasmid, and the resultant expression product was a truncated version of the *a-c/2-c* construct. OM202*recA* was generated by P1 phage transduction to abolish RecA activity and allow expression of the full length *a-c/2-c* fusion protein (data not shown). The *a/c* fusion proteins were expressed in two different backgrounds. In both cases the fusion proteins were expressed from pBWU13 derivative plasmids, which encode the entire *atp* operon. However, in one case, the genes for both wild type subunits *a* and *c* were replaced with the fusion constructs. In the second case, only wild type subunit *a* was replaced, leaving the gene expressing native *c* intact (Figure 4.1).

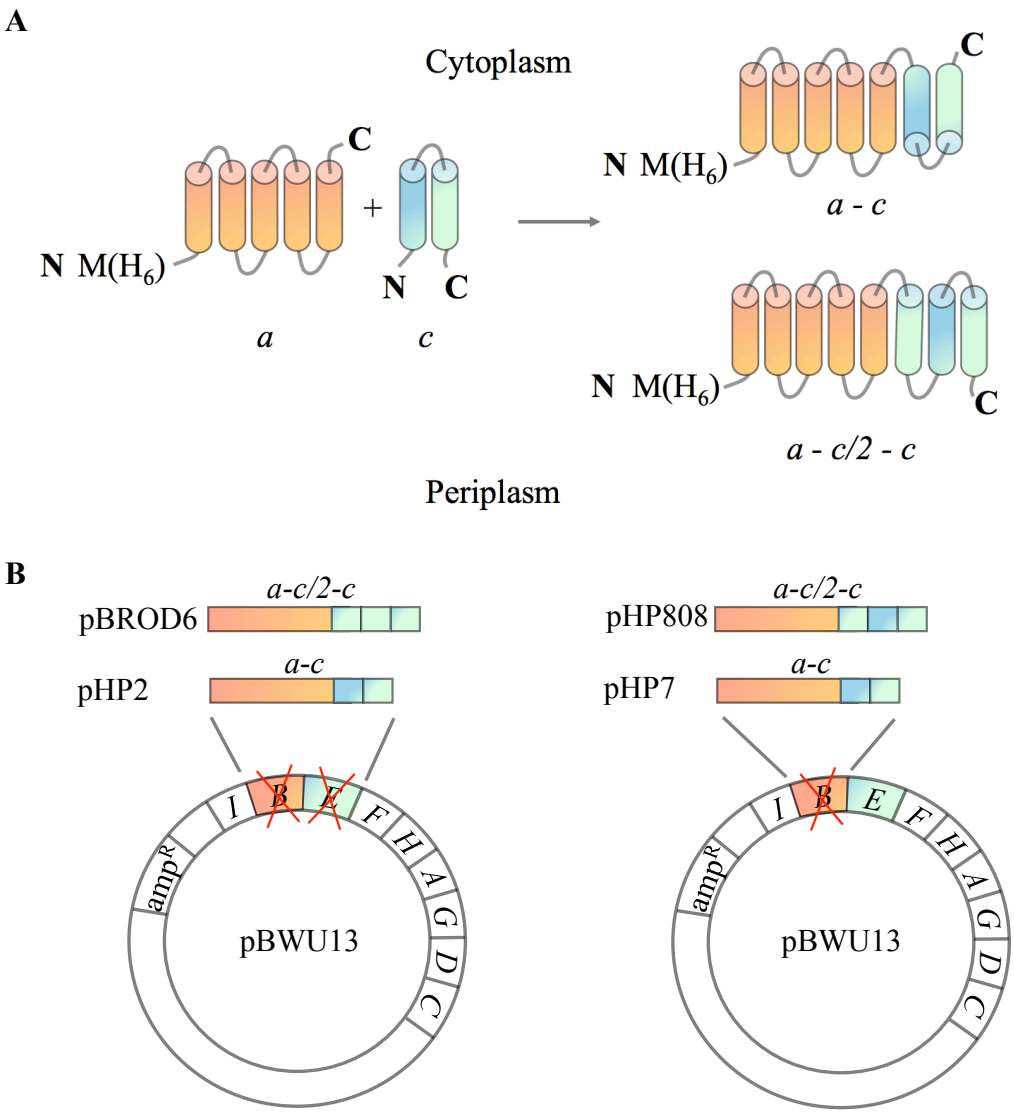

Figure 4.1: Design of the *a/c* fusion proteins and plasmid construction. A) Topology diagrams of the *a/c* fusion constructs. Subunits *a* and *c* are shown as well as both fusion construct expression products. The *a-c* protein is shown at the top right and the *a-c/2-c* protein is shown on the bottom right. The cytoplasmic side of the membrane is on top and the periplasmic side is on the bottom. B) The fusion construct genes and their positioning in the pBWU13 parental vector is shown. The *a/c* constructs replaced the genes encoding subunits *a* and *c* (*atp*B and *atp*E respectively) in the pBROD6 and pHP2 vectors. The *a/c* constructs replaced the gene encoding native subunit *a* (*atpB*) in pHP808 and pHP7.

When the *a-c/2-c* fusion protein was expressed in the presence of the c_{10} ring, from pHP808, it was produced and incorporated into the membrane at levels comparable to wild type (Figure 4.2). When the *a-c/2-c* fusion protein was expressed in the absence of the c_{10} ring expression and membrane incorporation were observed at a reduced level. The *a-c* fusion

protein also showed membrane incorporation at levels comparable to wild type when co-expressed with the c_{10} ring. However, in the absence of the c_{10} ring the *a-c* construct was not incorporated into the membrane at a detectable level.

Previous reports have shown that insertion of subunit *a* into the membrane is dependent on the presence of subunit *c* (Hermolin and Fillingame, 1995; Yi *et al.*, 2003). Membrane incorporation of the *a-c/2-c* fusion protein in the absence of native subunit *c* indicated that the fusion protein was properly folded because the fused *c* subunit allowed membrane integration of subunit *a*. Lack of membrane incorporation of the *a-c* construct in the absence of native subunit *c* was likely due to the incorrect transmembrane topology of the fused *c* subunit relative to *a*, which inhibited insertion of the *a-c* protein.

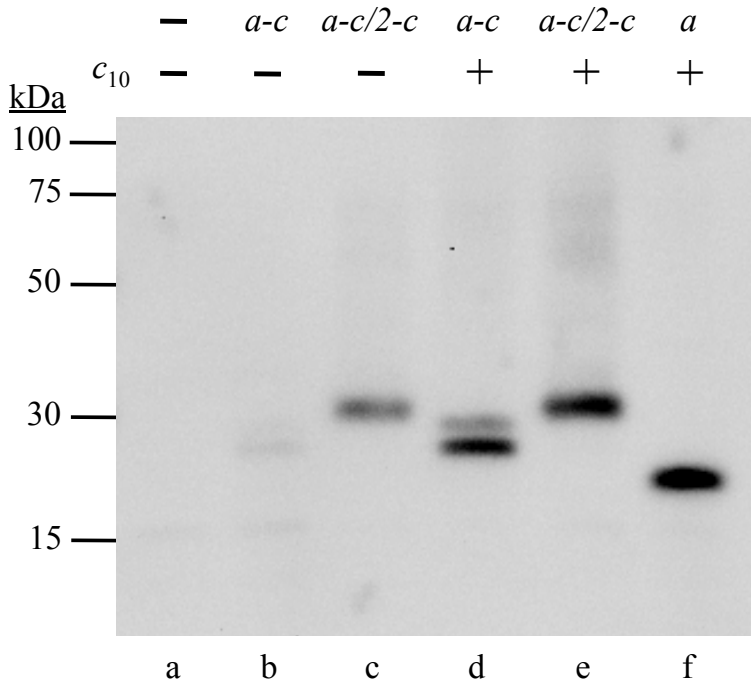

Figure 4.2: Membrane incorporation of the a/c fusion proteins. Western blot of cell membranes from the OM202*recA* strains containing no plasmid (a), expressing the *a-c* fusion protein from plasmid pHP2 (b) or pHP7 (d), the *a-c/2-c* fusion protein from plasmid pBROD6 (c) or pHP808 (e), or wild type subunit *a* from plasmid pBWU13 (f) with (d-f) or without (a-c) co-expression of the wild type subunit *c*. The Western blot was probed against the His_6 tag on the *a/c* constructs and wild type subunit *a*. Each lane contained 10 μg total membrane protein. Positions of the molecular weight markers and their masses in kDa are shown on the left. Subunit *a* and both fusion proteins display enhanced electrophoretic mobility which gives the appearance of lower than expected molecular weight, which is a common property of highly hydrophobic proteins.

4.2 An assembled c_{10} ring is not a prerequisite for membrane insertion of subunit *a*.

The results presented in section 4.1 showed that fused subunit *c* (of *a-c/2-c*) was sufficient to allow membrane incorporation of the fused *a*. This suggested that monomeric subunit *c*, rather than a pre-formed *c*-ring, facilitated subunit *a*'s entry into the membrane. To test this hypothesis further, we examined the effect of c_{10} ring assembly on the membrane incorporation of subunit *a*. Formation of the c_{10} ring is disrupted by two distinct mutations in subunit *c,* G23D and L31F (Jans *et al.*, 1983; Kol *et al.*, 2006). The *c*G23D or *c*L31F mutations do not disrupt membrane insertion of subunit *c*, but do disrupt the formation of *c*-rings in the membrane.

Wild type subunit *a* was expressed in the presence of the *c*G23D and *c*L31F mutations in the context of the full *atp* operon, from plasmids pHP9 and pHP10 respectively, in the OM202*recA* strain. ATP dependent proton translocation was tested in the cell membranes prepared from these strains and showed that ATP synthase with the *c*G23D mutation was inactive (Figure 4.3) when compared to wild type. In ATP synthase with the *c*L31F mutation only marginal activity was detected (Figure 4.3-B). These results were consistent with disrupted ring formation and indicated that the G23D and L31F mutations provided a suitable platform for our study on how *c*-ring assembly affects incorporation of subunit *a* into the membrane.

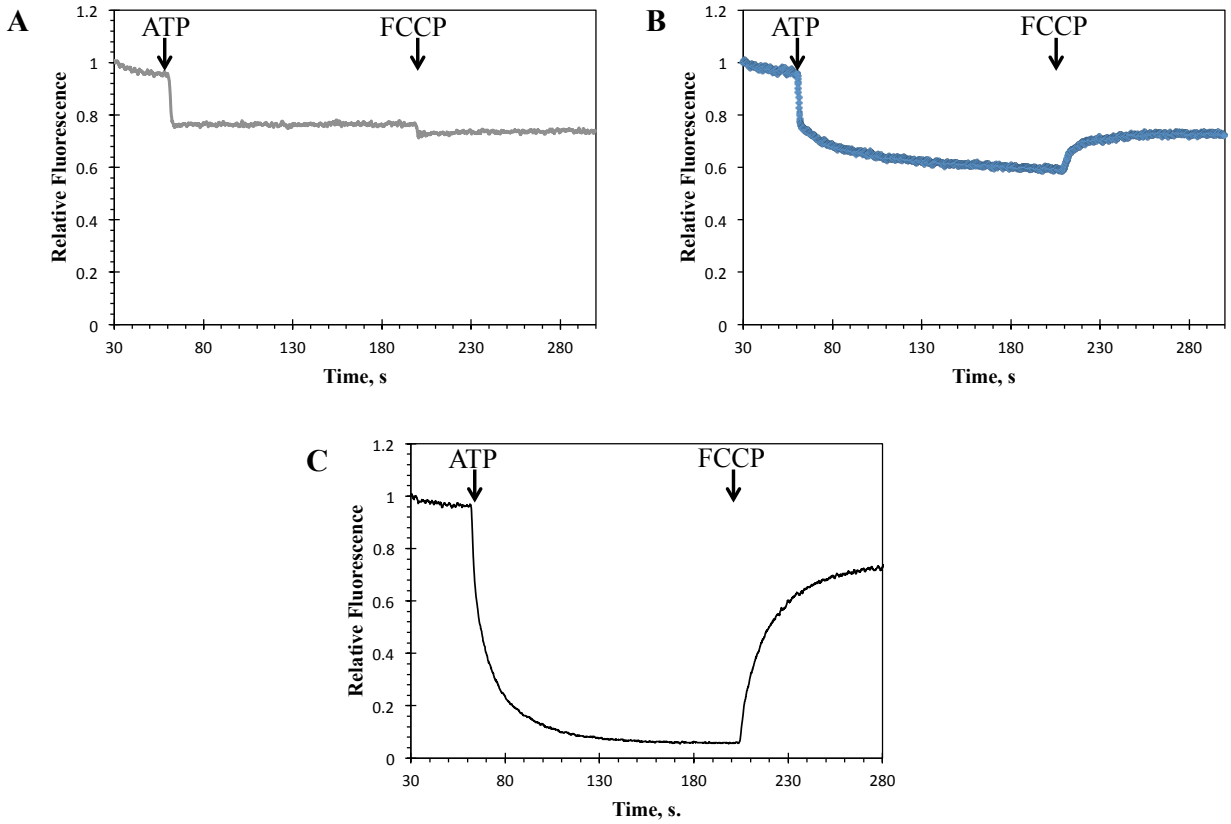

Figure 4.3: ATP dependent proton translocation in OM202*recA*/pHP9 (A), OM202*recA*/pHP10 (B), and OM202*recA*/pBWU13 (C) membranes. pBWU13 expresses wild type ATP synthase. pHP9 and pHP10 express native subunit *a* in the presence of the *c*G23D and *c*L31F mutations respectively. The trace shown in panel A is representative of the traces obtained from both *a/c* fusion proteins in the presence of either c_{10} assembly mutation.

We then expressed *a/c* fusion proteins in the presence of the *c*G23D and *c*L31F mutations. As expected, these ATP synthase variants were not active (data not shown). Western blot analysis on membrane vesicles prepared from the c_{10} mutant strains showed that wild type subunit *a* incorporated into the membrane in the presence of both the *c*L31F and *c*G23D mutations (Figure 4.4). This observation showed that formation of the c_{10} ring was not necessary for the incorporation of wild type subunit *a* into the membrane; supporting the results presented in section 4.1. In the presence of the *c*G23D and *c*L31F mutations the *a-c/2-c* fusion protein incorporated at a reduced level, which was comparable to expression in the absence of native *c*, while the *a-c* construct was not integrated into the membrane. The reduced membrane incorporation of the *a/c* fusion proteins when co-expressed with *c*G23D and *c*L31F was an unanticipated result and will be discussed further in section 5.4.

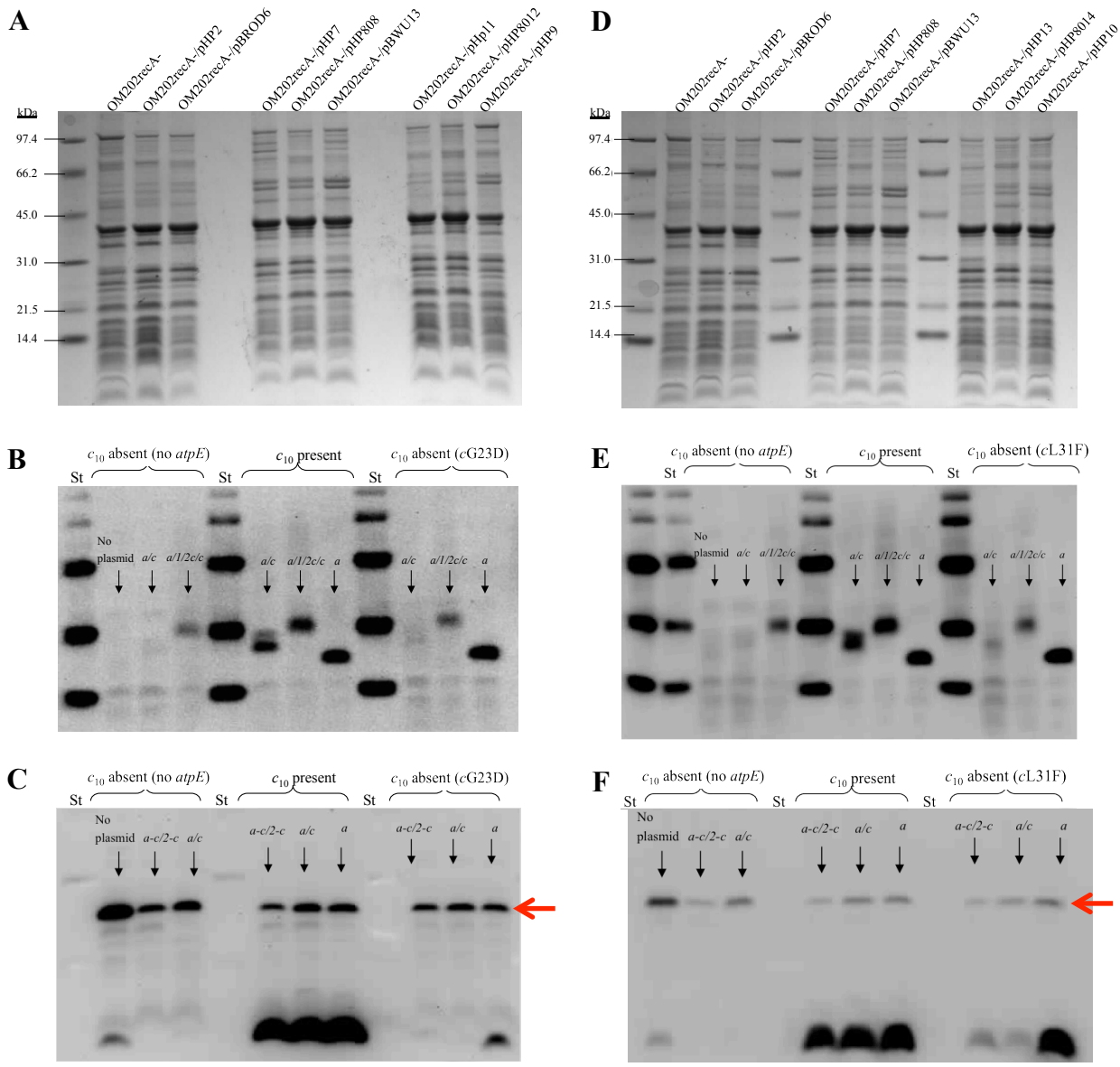

Figure 4.4: Expression of subunit *a* and the *a/c* constructs in the presence of c_{10} assembly mutations. Panels A, B and C correspond to expression experiments with the *c*G23D mutation. Panels D, E and F correspond to experiments with the *c*L31F mutation. A and D: Coomassie stained SDS-PAGE gels containing 10 µg total membrane protein from the various strains in each lane. B and E: Western blot equivalents of the gels in panels A and D, probed with anti-His_6 antibody. Panels C and F: Western blot equivalents of the gels in panels A and D, probed with anti-*c* antibody. The bands indicated by red arrows are caused by non-specific antibody binding.

The results shown in Figure 4.4 prompted us to examine the effects of the L31F mutation on the *a-c/2-c* fusion variant more closely. L31F was selected for further study

because subunit *c* is integrated into the membrane in stoichiometric amounts, but the *c*-ring does not form (Figure 4.4). We constructed three pHP808 derivative plasmids containing the *c*L31F mutation. In the pHP8014 plasmid the gene encoding subunit *c* contains the L31F point mutation. In the pHP8015 plasmid the gene encoding *a-c/2-c* contains the L31F mutation. In pHP8016 both the genes encoding native subunit *c* and *a-c/2-c* contain the L31F mutation.

Expression of the *a-c/2-c* fusion protein in the presence of the L31F mutations was examined in the OM202*recA* parental strain. Western blot analysis on membrane vesicles prepared from the *a-c/2-c* derivative strains showed that *a-c/2-c* incorporated into the membrane at levels comparable to wild type when L31F was present in the fused *c* subunit, as well as when L31F was present in both the fused and monomeric *c* (Figure 4.5). However, the *a-c/2-c* fusion protein was not efficiently integrated into the membrane when the L31F mutation was present only in monomeric *c*, which is consistent with the results shown in Figure 4.4. Interestingly, when monomeric *c* contained the L31F mutation it was not integrated into the membrane at stoichiometric amounts. However, native *c* was integrated into the membrane regardless of the presence of the L31F mutation in the *a-c/2-c* protein.

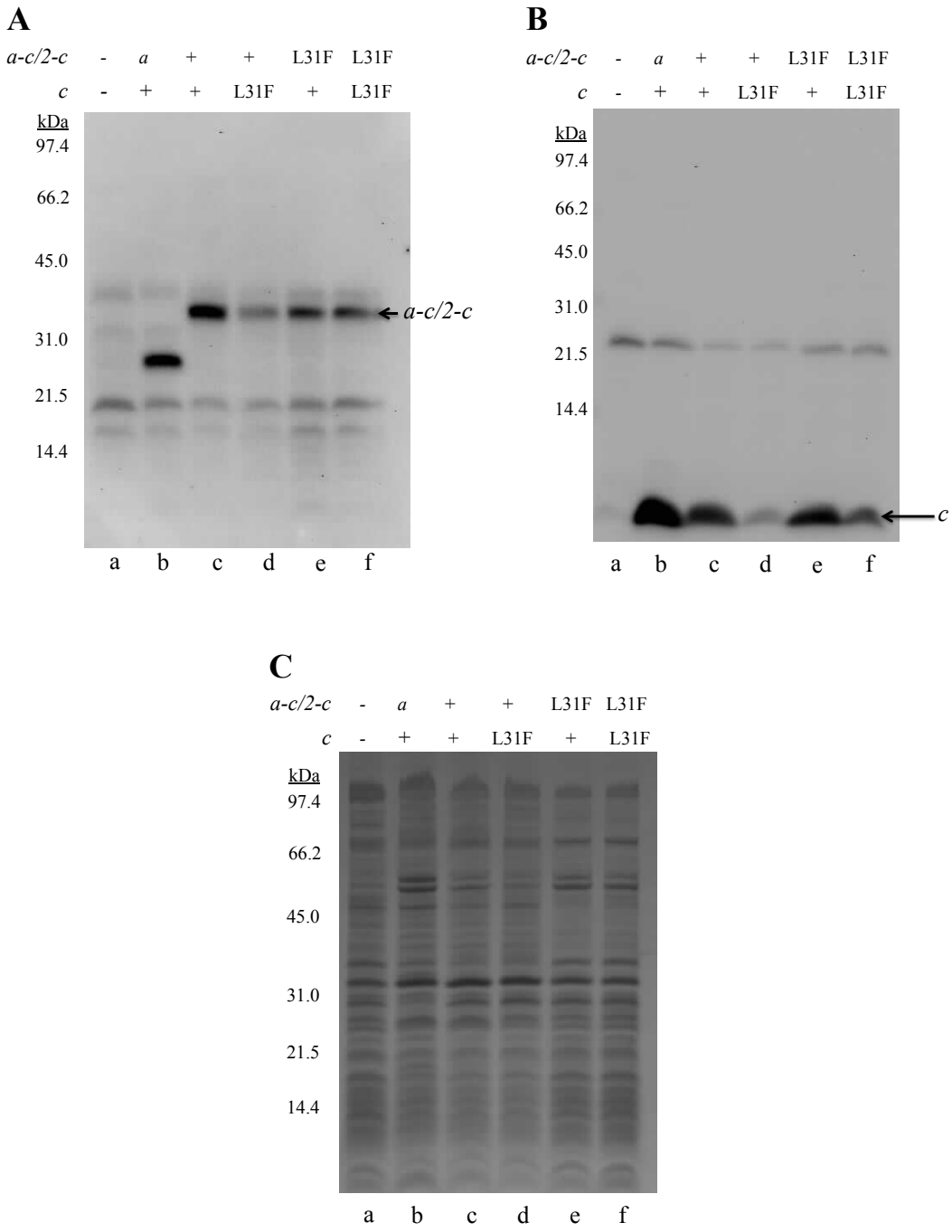

Figure 4.5: Western blot analysis of the membrane incorporation of *a-c/2-c* L31F derivatives. A) Western blot probed with anti pentaHis-HRP antibody (Qiagen, Mississauga, ON) which targets the His_6 tag on *a-c/2-c*. B) Western blot probed with anti-*c* antibodies. C) Coomassie stained 10 % SDS-PAGE gel equivalent of the blots shown in panels A and B. Each lane contains 10 µg total membrane protein. Cell membranes from the OM202*recA* strain containing no plasmid (a), wild type ATP synthase (b), the *a-c/2-c* fusion protein (c), the *a-c/2-c* protein coexpressed with monomeric *c* containing the L31F mutation (d), the *a-c/2-c* protein containing the L31F mutation (e-f) in the presence of native monomeric *c* (e) and in the presence of monomeric *c* containing the L31F mutation (f).

4.3 The *a/c* fusion proteins incorporate into the F_0 domain.

Once we had demonstrated that the *a/c* fusion proteins incorporated into the membrane we wanted to determine if they were integrated into the F_0 domain. The *a/c* constructs were expressed in *E. coli* cells in the context of the full *atp* operon (section 4.1), therefore, it was possible for them to assemble with b_2 and c_{10}. We tested if the fusion proteins were incorporated into the F_0 domain similar to wild type subunit *a*. The F_0 domain was purified from cells expressing the *a/c* constructs using a method established by Schneider and Altendorf (Schneider and Altendorf, 1984). F_0 isolated from wild type ATP synthase showed 3 major bands on SDS-PAGE, which correspond to subunits *a*, *b* and *c* (Figure 4.6). Both the *a-c* and *a-c/2-c* constructs co-purified with subunits *b* and *c* and were present in the F_0 preparations at ratios comparable to subunit *a* in the wild type F_0 (Figure 4.6). Co-purification of the *a/c* fusion proteins with subunits *b* and *c* indicated that the *a/c* fusion proteins were properly folded and incorporated into an assembled F_0 complex.

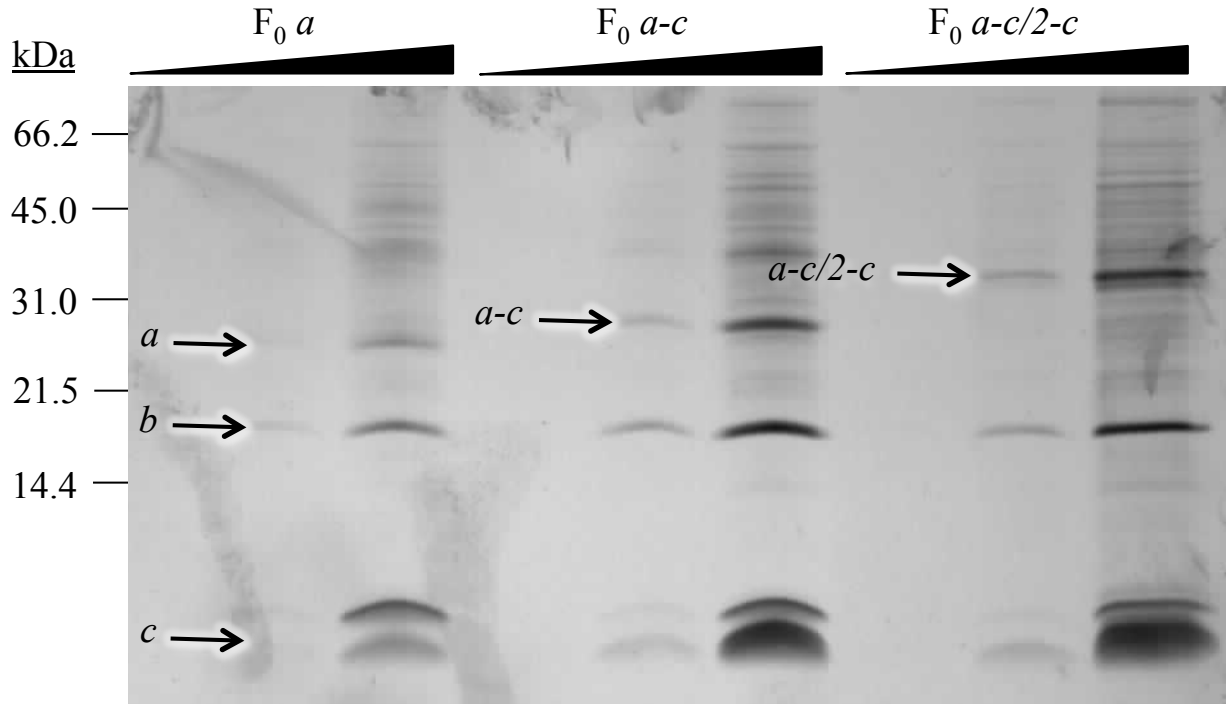

Figure 4.6: Silver stained 10 % SDS-PAGE gel of the isolated F_0 complexes from wild type ATP synthase and the *a/c* variants. 0.2 µg, 1.0 µg and 5 µg of each type of F_0 was loaded. The location of each fusion construct is indicated with arrows. The positions of subunits *a, b* and *c* are indicated in wild type F_0.

4.4 F_1F_0-ATPase containing the *a-c/2-c* construct is correctly assembled.

Once we had confirmed that the *a/c* fusion proteins were integrated into F_0 we wanted to determine if the entire F_1F_0 complex was assembled with the *a-c/2-c* fusion protein. Intact wild type F_1F_0 was isolated using a modified version (Haji and Dmitriev, unpublished data) of the protocol developed by Laubinger and Dimroth for isolation of the *P. modestum* F_1F_0-ATPase (Laubinger and Dimroth, 1988). Isolated F_1F_0 ATP synthase was highly purified. Wild type F_1F_0 ATP synthase isolated by this procedure remains functional and has normal subunit composition (Haji and Dmitriev, unpublished data). Therefore, this purification procedure provides a suitable test to determine the assembly status of the ATP synthase complex with the *a-c/2-c* fusion. The *a-c/2-c* fusion protein was found to co-purify with the full complement of F_1F_0 subunits (Figure 4.7), demonstrating that the *a-c/2-c* ATP synthase variant is assembled.

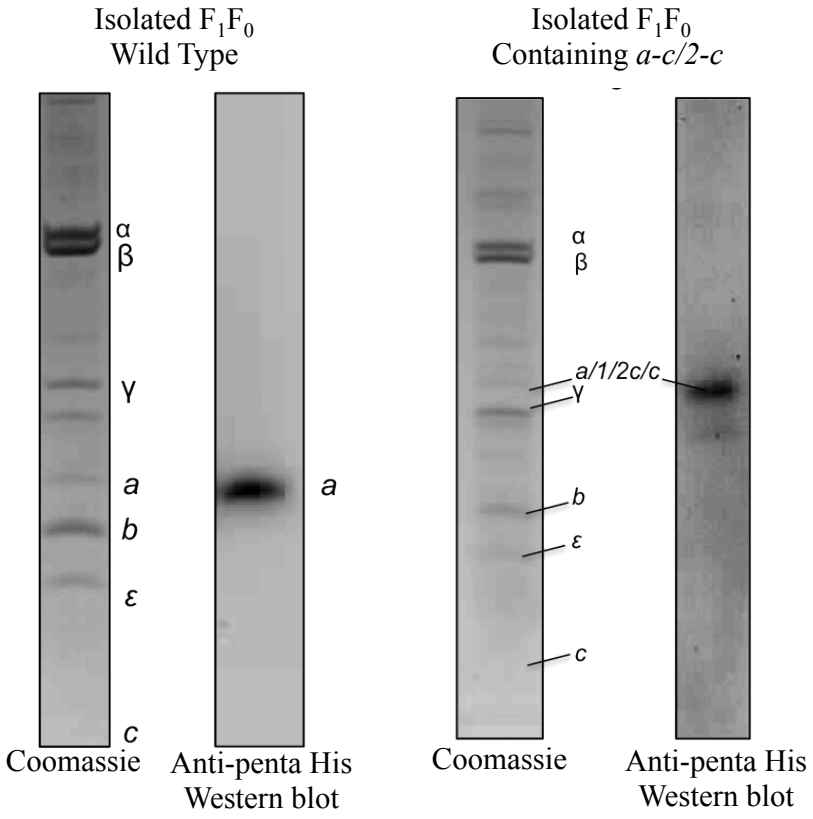

Figure 4.7: F_1F_0 isolated from OM202*recA*/pBWU13 (wild type ATP synthase) and OM202*recA*/pHP808 (ATP synthase with *a-c/2-c*). Coomassie stained gels as well as Western blots probed against the His_6 tag are shown for each preparation. The F_1F_0 subunits are labeled on the Coomassie stained gel panels. The positions of the *a* and *a-c/2-c* proteins are labeled on both the gels and blots.

4.5 Activity of the *a-c* and *a-c/2-c* ATP synthase variants.

4.5.1 The *a-c* fusion protein supports cell growth by oxidative phosphorylation but the *a-c/2-c* fusion does not.

The results presented in sections 4.3 and 4.4 showed that the *a/c* ATP synthase variants were assembled, which prompted us to examine their activity. Bacterial strains that do not contain functional ATP synthase cannot survive on media containing succinate as the sole source of carbon. Therefore, growth on these selective plates is indicative of the presence of functional ATP synthase. The strains OM202*recA*/pBWU13 (wild type), OM202*recA*/pHP7 (*a-c*), and OM202*recA*/pHP808 (*a-c/2-c*) were grown on succinate minimal plates to test the OxPhos capacity of the *a/c* ATP synthase variants (Figure 4.8). OM202*recA*/pHP2 (*a-c*, in the absence of c_{10}) and OM202*recA*/pBROD6 (*a-c/2-c*, in the absence of c_{10}) were also tested, although they were expected to be non-functional, and show no growth.

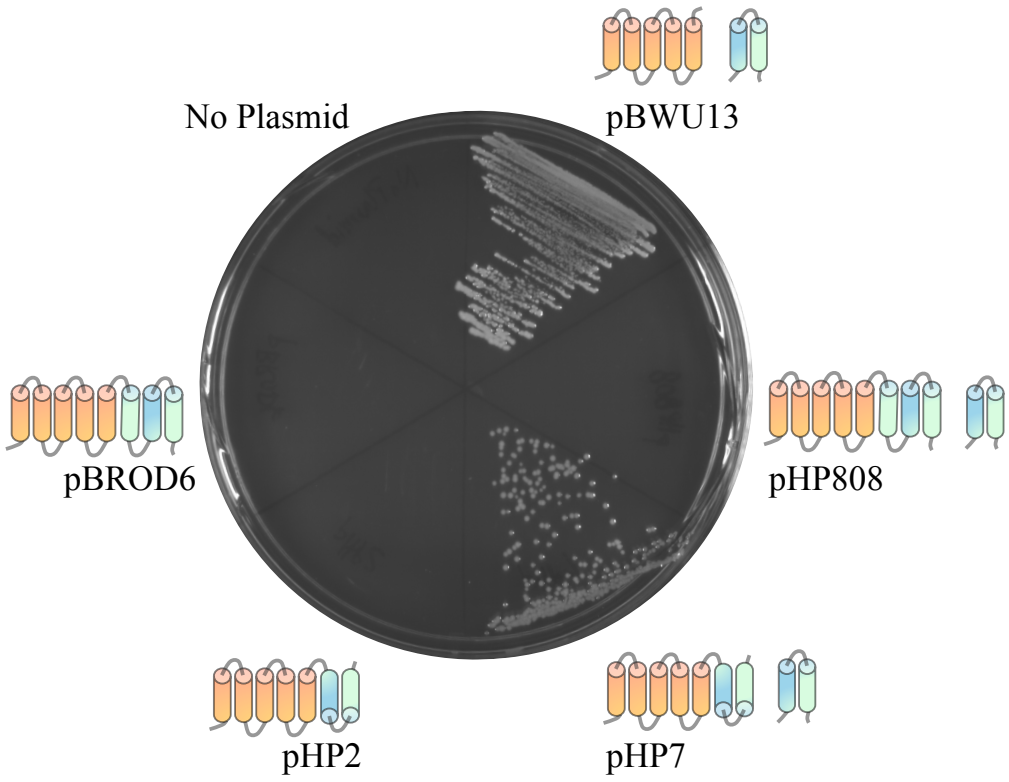

Figure 4.8: Growth of OM202*recA* cells transformed with plasmids encoding the ATP synthase variants on succinate. pBROD6 and pHP2 encode the *a-c/2-c* and *a-c* constructs respectively, in the absence of the native c_{10} oligomer. pHP808 and pHP7 encode the *a-c/2-c* and *a-c* constructs, in the context of the full ATP operon, respectively. pBWU13 encodes wild type ATP synthase.

The OM202*recA* parental strain contains a chromosomal deletion of the *atp* operon and was used as a negative control. OM202 showed no growth as expected. Cells expressing wild type ATP synthase and the *a-c* variant grew well on succinate, although the cells expressing wild type ATP synthase grew more robustly. Cells expressing the *a-c/2-c* variant showed no visible signs of growth, indicating that the *a-c/2-c* variant was unable to produce ATP. These results show that when the fused *c* subunit has incorrect transmembrane topology relative to subunit *a*, activity is retained. However, when the fused *c* has correct transmembrane topology relative to *a* activity is lost.

The capacity of the *a-c* construct to support OxPhos on succinate plates suggested that the *a* subunit of the *a-c* fusion protein was able to interact with the *c*-ring to facilitate proton transport. We hypothesized that because *a-c* had incorrect transmembrane topology, the fused *c* subunit may be displaced to the periphery of the ring allowing the *a*-c_{10} interaction to occur. Conversely, the *a-c/2-c* variant has correct transmembrane topology and it is therefore possible that the fused *c* subunit may integrate into the *c*-ring, obstructing movement of the rotor. We conducted a series of activity assays, examining both ATP driven proton transport and passive proton transport through the F_0 domain variants to test this hypothesis.

4.5.2 ATP driven proton transport activity of the *a/c* ATP synthase variants.

ATP dependent proton translocation, was measured for wild type ATP synthase as well as both *a/c* variants using ACMA fluorescence quenching assays (Figure 4.9). Wild type ATP synthase showed strong fluorescence quenching upon the addition of ATP. The *a-c* variant showed activity at approximately 50 % the level observed in wild type and the *a-c/2-c* variant showed negligible activity, which was consistent with oxidative phoshphorylation activity tests (section 4.5.1). Activity of each variant was also measured in the presence of dicyclohexylcarbodiimide (DCCD), a specific covalent inhibitor that binds to D61 of subunit *c* and blocks proton transit. Activity of the wild type enzyme and of the *a-c* variant was effectively blocked by DCCD, demonstrating that the fluorescence quench observed was truly related to F_1F_0 ATPase activity.

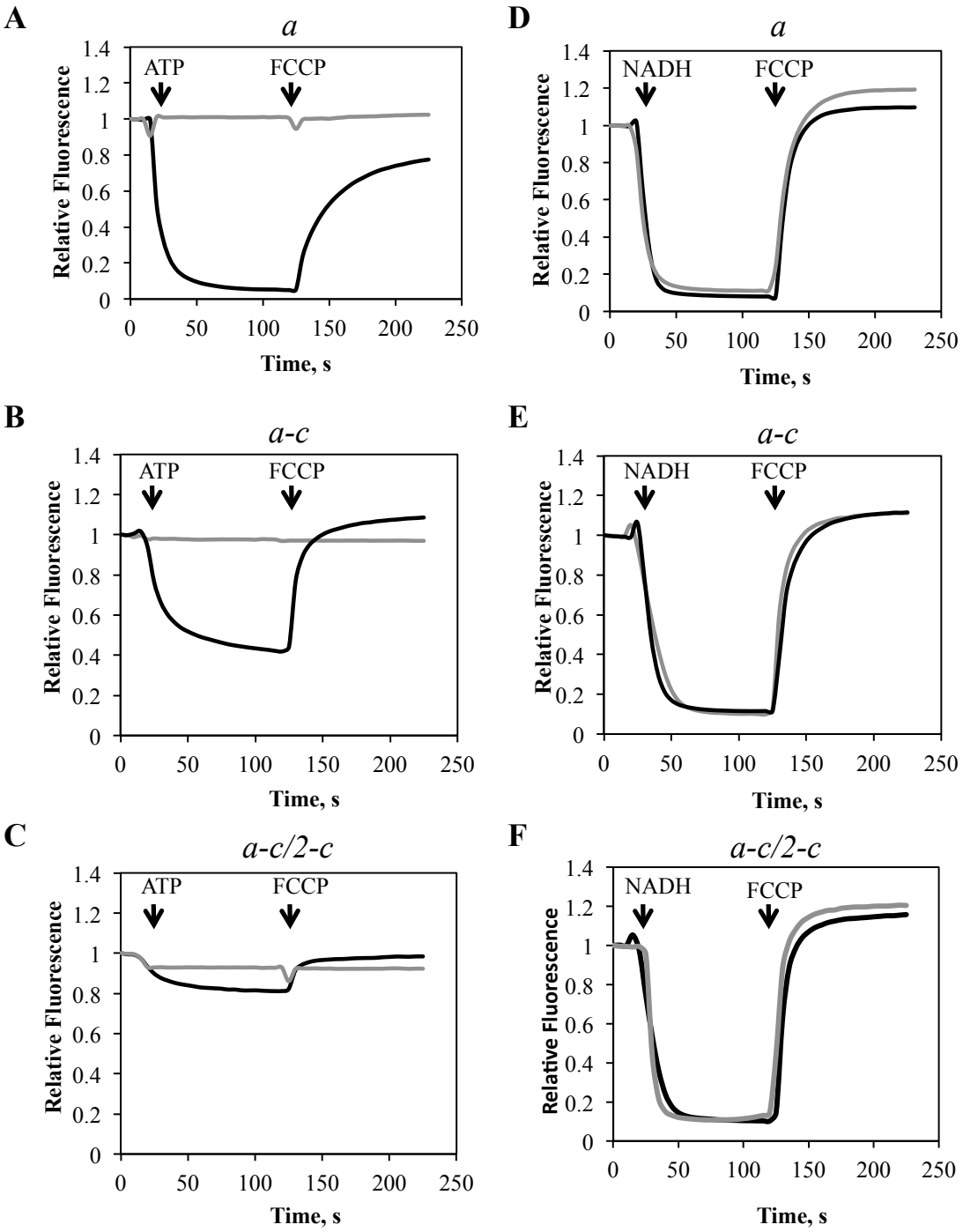

Figure 4.9: ATP driven (A-C) and NADH driven (D-F) proton translocation as measured by ACMA fluorescence quenching. Wild type subunit *a* was expressed from OM202*recA*/pBWU13 (A & D), *a-c* was expressed from OM202*recA*/pHP7 (B & E), and *a-c/2-c* was expressed from OM202*recA*/pHP808 (C & F). Time points where 2.0 mM ATP, 0.2 mM NADH, and 2.0 µM FCCP were injected are indicated with arrows. Black traces were recorded from untreated membranes, grey traces were recorded with membranes pretreated with 80 µM DCCD.

NADH driven proton transport was used as a control for integrity of the membrane preparations. NADH dehydrogenase is present in the membrane vesicles and upon the addition of NADH, protons are pumped into the lumen of the vesicles. Rapid ACMA fluorescence quenching was observed in all of the NADH driven assays and showed that the different quenching levels in the ATP driven assays were not caused by non-specific proton leaks through the membrane, but were truly a reflection of ATP driven proton transport activity of the F_1F_0 variants. As expected, DCCD had no effect on the NADH-driven proton transport, which confirmed that DCCD inhibition of ATP-dependent ACMA quenching resulted from specific inhibition of F_1F_0-ATPase, and not by causing protons to leak through the membrane.

4.5.3 Passive proton conductance through F_0 of the *a/c* variants.

We needed to demonstrate that the lack of proton transport activity in the *a-c/2-c* variant was truly caused by tethering of the rotor and stator. To test this, we examined proton transport through the F_0 domain directly. Removal of F_1 from F_0 by EDTA treatment converts the F_0 complex into a passive proton pore, which allows protons to flow across the membrane along their electrochemical gradient (Aris *et al.*, 1985). This process can be monitored by ACMA fluorescence quenching, using NADH dehydrogenase to create a proton gradient. When F_1 is attached to F_0, or the proton pore is blocked, a concentration dependent ACMA fluorescence quench is observed. However, if F_1 is removed from F_0, and the F_0 domain is functional, protons are passively shuttled out the lumen and the electrochemical proton gradient is dissipated resulting in a reduced level of ACMA fluorescence quench.

Passive proton translocation was measured for wild type ATP synthase as well as both *a/c* variants (Figure 4.10). As expected, the wild type F_0-domain showed a strong proton leak, which was blocked by treatment with the covalent proton transport inhibitor DCCD. The *a-c/2-c* variant showed very weak proton permeability. This observation was consistent with the lack of growth on succinate and negligible ATP driven proton transport, and supported our hypothesis that the rotor and stator are tethered. The *a-c* variant showed reduced capacity for passive proton transport compared to the wild type, which was also consistent with the reduced level of ATP-dependent proton transport and reduced growth on succinate. The OM202*recA*

parental strain showed no proton leak before or after EDTA treatment, indicating that the membrane vesicles maintained their integrity through the F_1 stripping procedure.

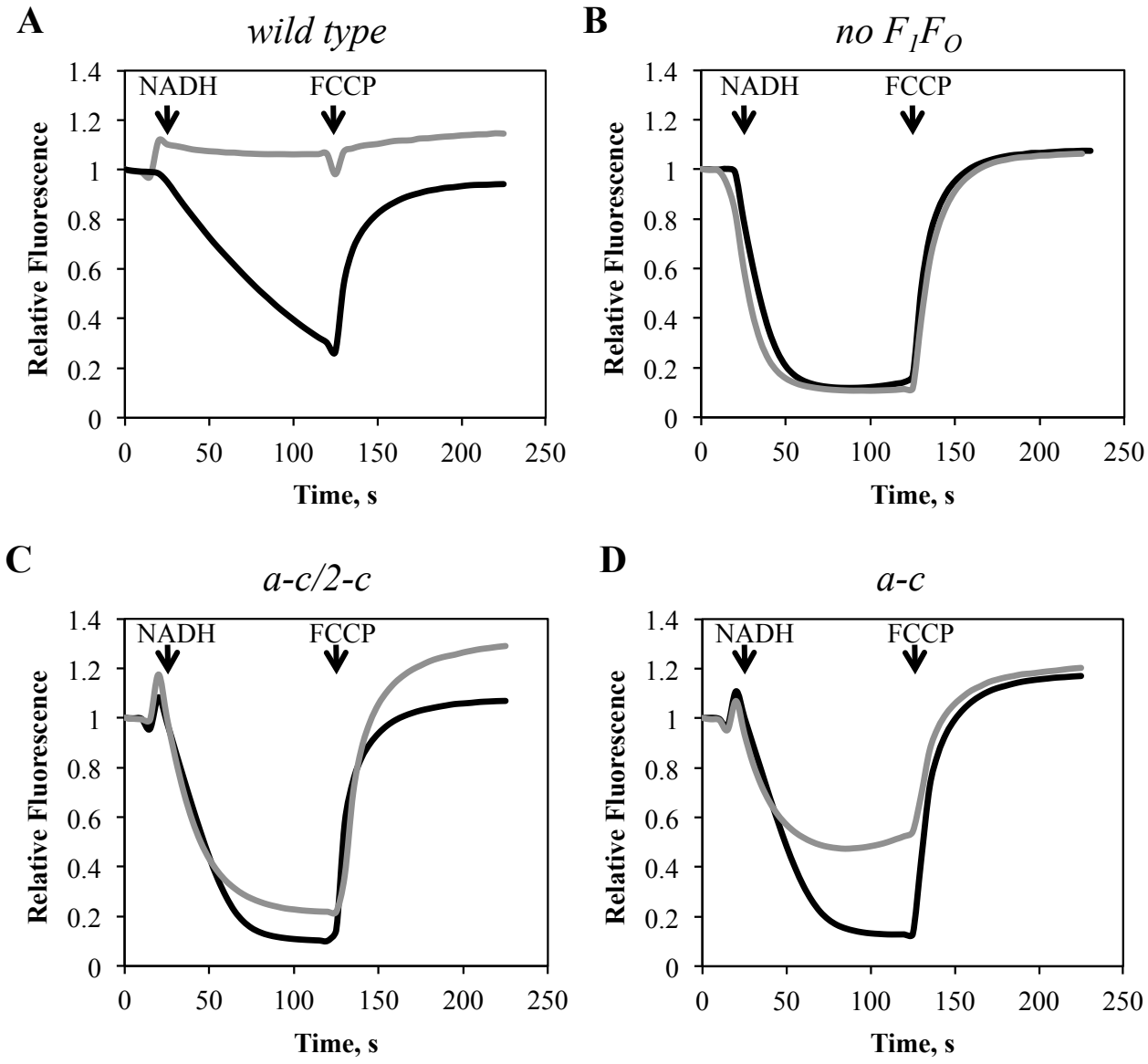

Figure 4.10: Proton permeability of the F_0 complexes with the *a-c* fusion proteins incorporated. NADH driven proton transport measured by ACMA fluorescence quenching with wild type subunit *a* from OM202*recA*/pBWU13 (A), control membranes from the parental OM202*recA* strain (B), the *a-c/2-c* fusion protein from OM202*recA*/pHP808 (C), and the *a-c* fusion protein from OM202*recA*/pHP7. Additions of NADH and FCCP are indicated with arrows. The grey and black traces indicate activity measured from whole membranes, and whole membranes in the presence of 80 μM DCCD respectively.

4.5.4 F_1-ATPase activity of the *a-c/2-c* ATP synthase variant.

We wanted to confirm that the lack of ATP dependent proton translocation in the *a-c/2-c* ATP synthase variant was truly related to an immobilized rotor, and not a side effect of an assembly defect or uncoupling between F_1 and F_0. The activities of the F_1 and F_0 domains of ATP synthase are tightly coupled; inhibition of activity in the F_1 sector will cause reduced capacity for proton transport through F_0, and vice versa. However, the F_1 domain of ATP synthase retains efficient ATPase activity when it is removed from the transmembranous F_0 domain. The tether between the rotor and stator would prohibit c_{10} ring rotation and cause the apparent lack of proton transport seen in sections 4.5.1 – 4.5.3. However, it was also possible that the presence of the *a-c/2-c* construct interferes with ATP synthase assembly, or coupling between F_1 and F_0, and the lack of activity may have been due to an improperly assembled or uncoupled F_1F_0 complex. We hypothesized that the fused *c* subunit of the *a-c/2-c* variant, which is expected to have correct transmembrane topology, integrates into the c_{10} ring preventing rotation. We also hypothesized that if the *a-c/2-c* variant were assembled and the coupling mechanism were intact, we should observe low or absent ATPase activity when F_1 is bound to F_0, and a subsequent restoration of ATPase activity when F_1 is released from the obstructed F_0 domain.

To test our hypotheses, we examined the amount of F_1 bound to F_0 in both wild type ATP synthase and in the *a-c/2-c* variant. The α and β subunits of the F_1 domain were present in the membranes of cells expressing the *a-c/2-c* variant at approximately 60 % of the level observed in wild type (Figure 4.11). However, the ATPase assays showed that the *a-c/2-c* variant had less than 20 % of the activity observed in wild type when F_1 was bound to F_0. A significant increase in ATPase activity was observed upon removal of F_1 from the *a-c/2-c* containing F_0-complex. Free F_1 activity of the *a-c/2-c* variant per milligram membrane protein was approximately 50 % of the wild type, demonstrating that the *a-c/2-c* fusion protein does not interfere with assembly or coupling of the F_1F_0 complex. Taken together, the results in sections 4.1 – 4.5 lead us to conclude that the the *a-c/2-c* fusion protein is properly folded and the fused *c* of *a-c/2-c* becomes integrated into the c_{10} ring.

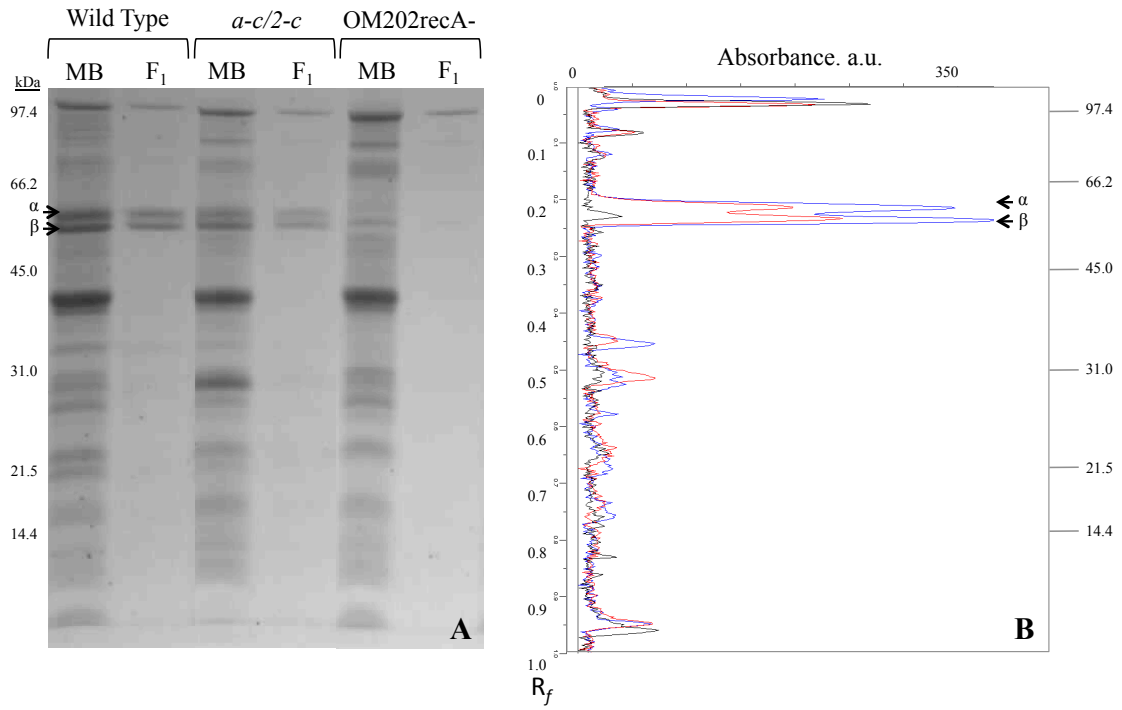

Figure 4.11: Coomassie stained SDS-PAGE gel of membranes and F_1 isolated from cells expressing wild type ATP synthase and the *a-c/2-c* variant. A) MB: indicates lanes containing whole membranes. F_1: indicates lanes containing isolated F_1. Each lane showing whole membranes was loaded with 10 µg total membrane protein. The amount of isolated F_1 loaded on the gel was equalized per µg of membranes. The positions of the F_1 α and β subunits are shown. B) Band density traces from the isolated F_1 lanes in the coomassie gel. The red trace corresponds to the F_1 lane from the *a-c/2-c* variant and the blue trace corresponds to the F_1 lane from wild type ATP synthase. The black trace corresponds to the background strain.

Table 4.1: F_1-ATPase activity of the *a-c/2-c* variant.
Units of activity are µmol of P_i released per minute per milligram of protein (µmolP_i/min*mg). Wild type and *a-c/2-c* variant ATP synthases were expressed in OM202*recA E. coli* cells. OM202*recA* cells that did not contain an ATP synthase expression vector were used as the negative control. ND – not determined.

F_1-ATPase activity of the ATP synthase with the *a-c/2-c* fusion protein				
	ATPase activity of whole membranes	DCCD inhibition	Released F_1 activity	
			Units/mg membrane protein	% wild type
	Units / mg	%		
Wild type (pBWU13)	2.09 ± 0.10	62	0.42 ± 0.02	100
a-c/2-c (pHP808)	0.40 ± 0.02	15	0.2 ± 0.01	50
OM202recA- (no plasmid)	0.02 ± 0.002	ND	< 0.01	< 0.5

4.6 Extending the tether between *a* and *c/2-c* of the *a-c/2-c* fusion does not enhance proton transport.

We demonstrated that the *a-c/2-c* fusion protein is incorporated into an assembled ATP synthase complex, and that the fused subunit *c* is integrated into the c_{10} ring (sections 4.1 – 4.5). The short linker connecting the fused *a* and *c* subunits restricts movement of the rotor and prevents efficient proton transport. Theoretically, it is plausible for limited back – and – forth movements of the *c*-ring, relative to subunit *a*, to facilitate proton transport through the uncoupled F_0-complex. In the *a-c/2-c* fusion variant, low levels of passive proton transport were observed (section 4.5.3) suggesting that although the tether between fused *a* and *c* occluded *c*-ring rotation, the length of the linker was sufficient to allow some back and forth oscillations of c_{10} relative to *a*.

We hypothesized that lengthening the tether between *a* and *c/2-c* of *a-c/2-c* may enhance passive proton transit via oscillation of the *c*-ring. Two linker extensions, four and twelve amino acids in length, were designed and incorporated between the *a* and *c/2-c* polypeptides in the *a-c/2-c* fusion (section 3.2.3). Linker 1 was designed to allow back and forth oscillation of the c_{10} ring relative to the stator; it was short enough to occlude full rotation of the c_{10} ring. Linker 2 was designed to be long enough to allow complete rotation of the c_{10} ring, in principle, although the activation energy barriers of the linker passing through energetically unfavorable parts of conformational space may preclude full rotation in practice. The first linker (*a-c/2-c-linker-1*) encoded 'GSAG' and the second linker *(a-c/2-c-linker-2)* encoded 'GSAGTASANSGA' (Figure 4.12).

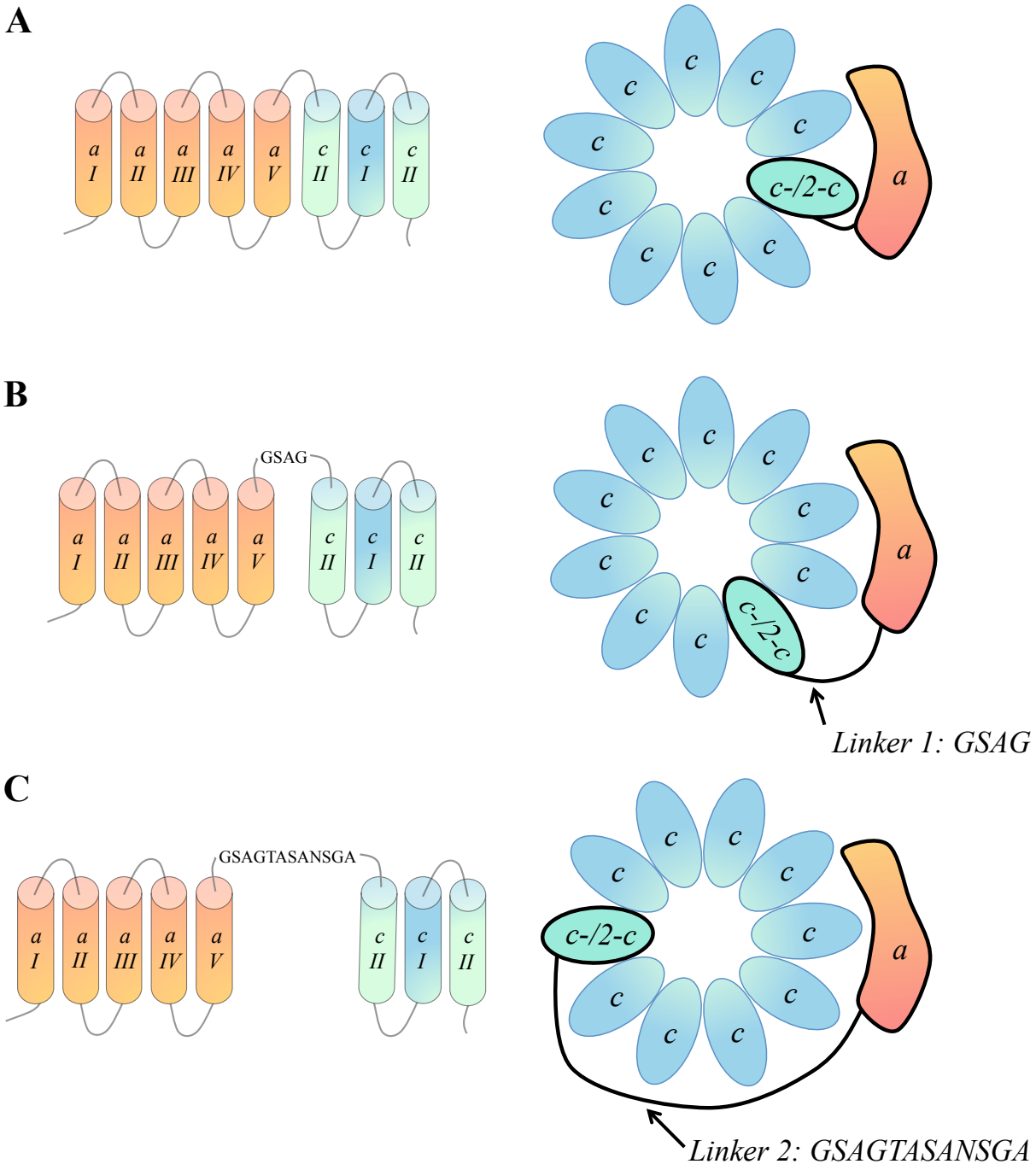

Figure 4.12: Location of the linker extensions and theoretical geometries of the F_0 domains containing the *a-c/2-c* fusion protein and its derivatives. Subunit *a* is shown in orange, fused subunit *c* is shown in green. Topology diagrams and the theoretical F_0 domain geometries of the *a-c/2-c* (A), *a-c/2-c-linker1* (B), and *a-c/2-c-linker2* (C) fusion constructs are shown, linkers are not to scale.

In OM202*recA* cells, both the *a-c/2-c-linker-1* and *a-c/2-c-linker-2* constructs incorporated into cellular membranes at levels comparable to the original fusion protein (Figure 4.13). The *a-c/2-c-linker-1* and *a-c/2-c-linker-2* proteins migrated at a higher molecular weights than the original *a-c/2-c* protein because of the additional 4 and 12 amino acids.

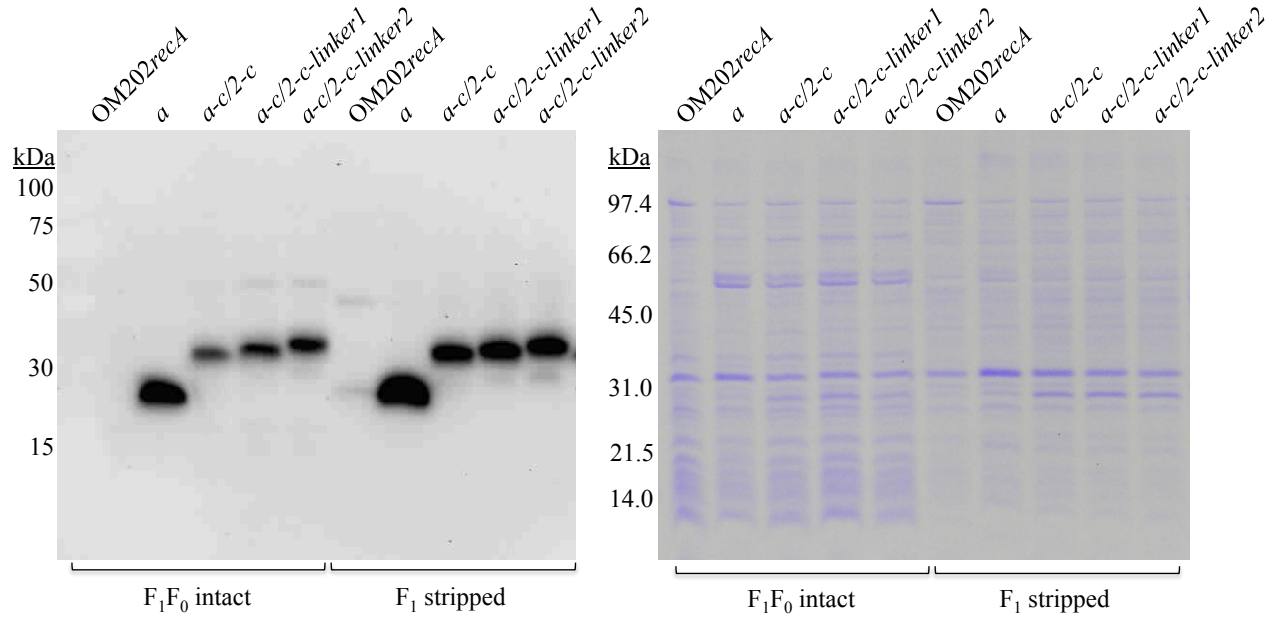

Figure 4.13: Western blot (left) and Coomassie stained gel (right) of whole membranes prepared from OM202*recA* cells expressing subunit *a,* the original *a-c/2-c* construct and the *a-c/2-c* construct with extended linkers between *a* and *c/2-c*. Expression of wild type subunit *a* is shown for comparison. Each lane was loaded with 10 µg total membrane protein. The Western blot was probed using anti-pentaHis HRP antibody (Qiagen, Mississauga, ON). Membranes from the parental OM202*recA* strain were loaded as a negative control. Samples from intact membranes (F_1F_0 intact) and stripped membranes after F_1 removal (F_1 stripped) were loaded. The bands corresponding to the α and β subunits of F_1 are within the black box.

Once we had established that the fusion protein derivatives were fully incorporated into cellular membranes we tested their ability to passively transport protons. As discussed in section 4.5.3, F_1 can be removed from F_0 to generate a passive proton pore that allows protons to leak across the membrane. Passive proton translocation was measured in F_1 stripped membrane vesicles containing wild type F_0, as well as the *a-c/2-c* fusion protein and its linker derivatives, using ACMA fluorescence quenching assays (Figure 4.14). Wild type F_0 facilitated rapid proton transport. Consistent with the previous results (Figure 4.10), F_0 with the original *a-c/2-c* fusion protein showed weak proton transport. Both proteins with extended linkers

showed similar levels of passive proton transport and were undistinguishable from the original *a-c/2-c* construct. There are two possible conclusions from this set of experiments: 1) the *a-c/2-c* fusion protein facilitates low level proton transport through small back and forth movements of the *c*-ring, which cannot be enhanced by increasing mobility of the *c*-ring via longer tethers, or 2) proton transport does not occur through oscillatory mechanisms.

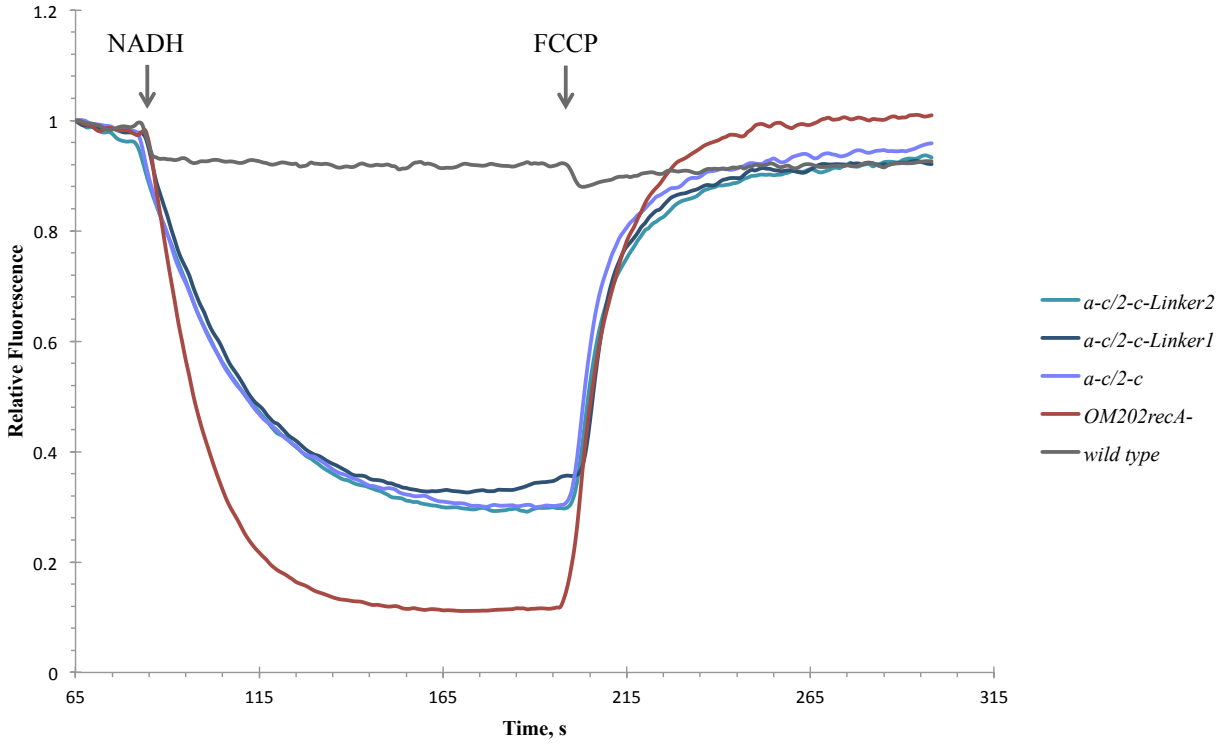

Figure 4.14: Proton permeability of the F_0 complexes with the *a-c/2-c* linker variant fusion proteins incorporated. NADH driven proton transport measured by ACMA fluorescence quenching with wild type subunit *a* from OM202*recA*/pBWU13 (grey), control membranes from the parental OM202*recA* strain (red), and each of the *a-c/2-c* and the linker variants (shades of blue). Additions of NADH and FCCP are indicated with arrows.

4.7 Expression and purification of subunit *a* and the *a-c/2-c* fusion.

4.7.1 Optimization of protein expression.

We needed to achieve a high level of overexpression for both wild type subunit *a* and the *a-c/2-c* fusion protein for structural studies. Initially, expression experiments with both wild type subunit *a* and the *a-c/2-c* protein were carried out using the OM202 parental strain. RecA activity in the OM202 parental strain caused a deletion mutation in the pHP808 plasmid, resulting in a truncated *a-c/2-c* expression product. To abolish RecA activity and allow expression of the full length *a-c/2-c* protein, we generated a RecA deficient strain, OM202*recA*, by P1 transduction. However, expression level in OM202*recA* was not high enough to produce sufficient quantities of protein for structural studies.

Expression of subunit *a* and the *a-c/2-c* protein was tested in C43(DE3) *E. coli* cells, which contain an uncharacterized mutation that allows them to highly overexpress toxic membrane proteins. C43(DE3) *E. coli* cells expressed wild type subunit *a* approximately ten times better than OM202 or OM202*recA* (Figure 4.15). Expression of the *a/c* constructs did not appear to be significantly improved relative to OM202*recA* expression. When expressed in C43(DE3) cells the *a-c/2-c* construct migrated identically to wild type subunit *a* on SDS-PAGE, indicating that the *a-c/2-c* construct was truncated when expressed in C43(DE3). Like OM202, C43(DE3) expresses active RecA, which recognizes and recombines repetitive sequences of DNA, which can lead to deletions of repetitive DNA sequences. RecA activity was also the likely cause of the low level of *a-c/2-c* expression in C43(DE3). We generated a C43*recA* strain for testing expression of the *a-c/2-c* protein. An approximate three-fold increase in expression levels was observed between OM202*recA*/pHP808 and C43*recA*/pHP808 (Figure 4.16).

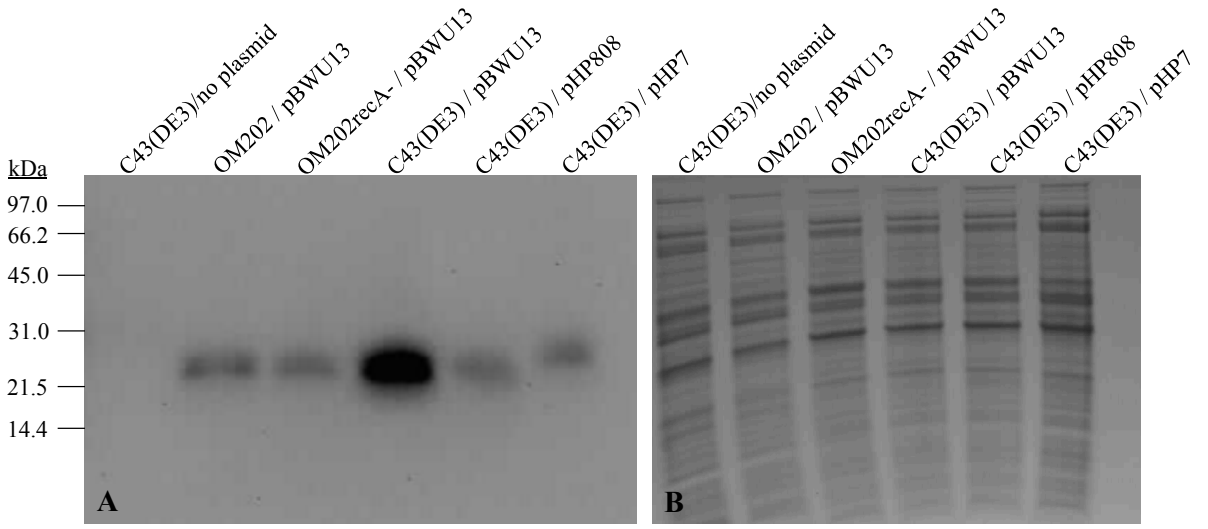

Figure 4.15: Western blot analysis of C43(DE3) expression of wild type subunit *a* and the *a/c* constructs relative to OM202 and OM202*recA*. A) Western blot probed against the His_6 tag on subunit *a* and each construct using anti-pentaHis HRP antibody (Qiagen, Mississauga ON). B) Coomassie stained SDS-PAGE equivalent of the Western blot in panel A shown as load control. Each lane contains 10 µl of raw cells equalized to an optical density (OD_{600}) of 0.9. The positions of the molecular weight markers in kDa is indicated on the left. C43(DE3) without plasmid was loaded as a negative control. OM202, OM202*recA*, and C43(DE3) transformed with pBWU13 express wild type subunit *a*. C43(DE3) /pHP808 expresses the *a-c/2-c* construct and C43(DE3) /pHP7 expresses the *a-c* construct.

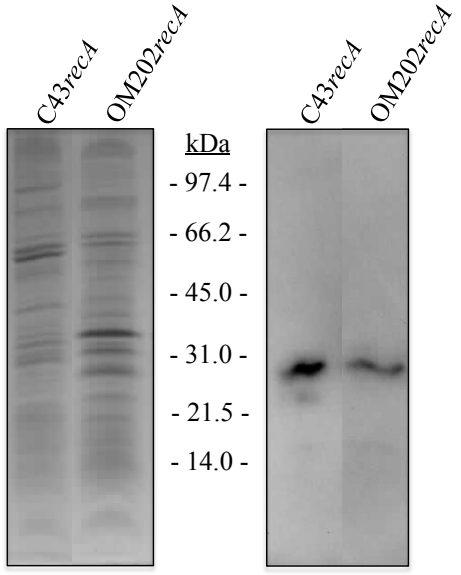

Figure 4.16: Western blot analysis of *a-c/2-c* expression in the C43*recA* and OM202*recA* background strains. Coomassie stained gel (left) and western blot (right) probed using the anti-pentaHis HRP conjugate antibody (Qiagen, Mississauga, ON). Each lane contains 10 µg total membrane protein, lanes containing membranes from either C43*recA*/pHP808 or OM202*recA*/pHP808. The positions of the molecular weight markers in kDa are indicated in the center.

4.7.2 Optimization of purification of subunit *a* and the *a-c/2-c* fusion protein from isolated F_0.

Optimization of purification followed optimization of protein expression. Wild type F_0 was isolated using the method of Schneider and Altendorf (section 4.3) and used as the starting material for protein purification (Schneider and Altendorf, 1985). Schneider and Altendorf developed a method for dissociating the F_0 subunits from one another using trichloroacetate. We modified this protocol to use LiBr as a dissociation agent because it is safer and easier to handle. Initially, we used size exclusion chromatography to separate the dissociated F_0 subunits. However, we could not obtain samples of subunit *a* of sufficient purity using this method (data not shown). We decided to use Ni-NTA chromatography to separate the His_6 tagged subunit *a* from the other F_0 subunits. Dissociated F_0 samples were subjected to Ni-NTA affinity chromatography and subunit *a* was optimally eluted subunit *a* from the Ni-NTA resin between 20 mM and 250 mM imidazole.

Initially, with the purification method described above, we achieved a maximum experimental yield of 22 % of the theoretical yield with wild type subunit *a*. We found that as much as 60 % of the loss occurred during concentration of purified protein samples. We developed a method for pre-treating Vivaspin-6 concentration devices to minimize protein loss (section 3.4). Recovery of the purified protein was increased to approximately 80 % with the use of pre-treated Vivaspin-6 concentrators. The final purification procedure, as described in section 3.4, yields highly purified subunit *a* (> 95 % pure) (Figure 4.17).

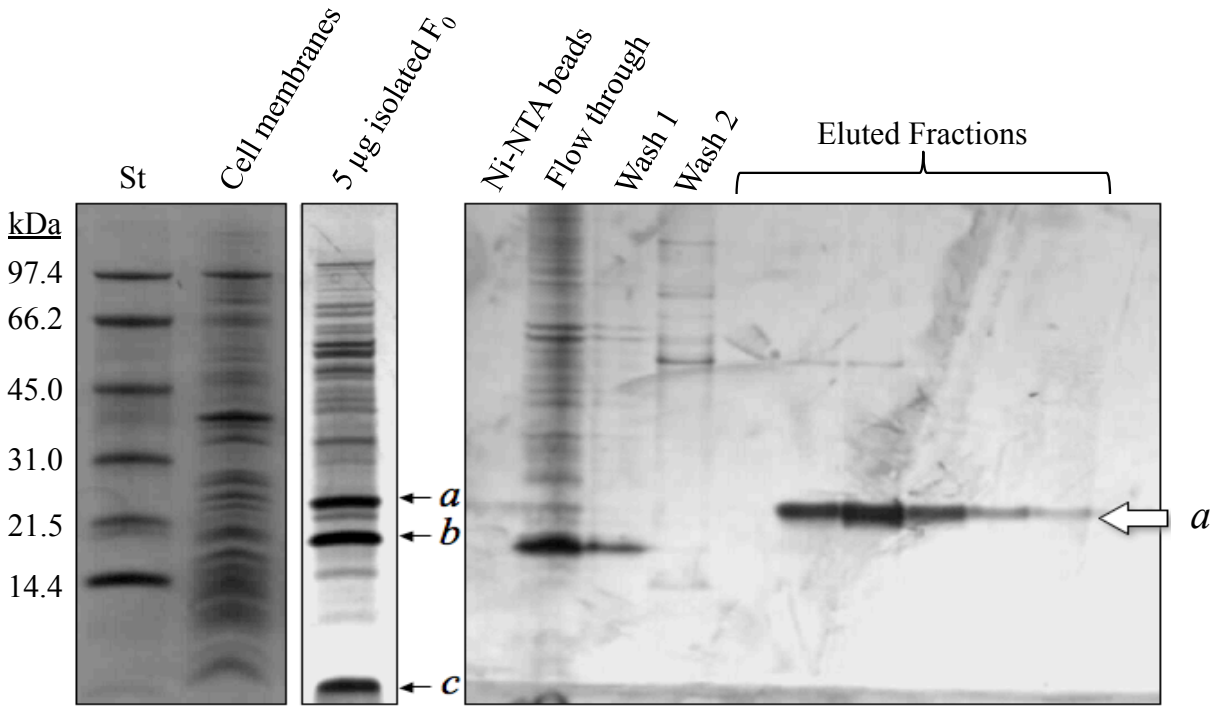

Figure 4.17: Stages of purification for wild type subunit *a*. Molecular weights of the marker proteins in kDa (St) are shown on the left. Samples of whole cell membranes, isolated F_0 domain (5 µg), column washes (10 µl), and elution steps (10 µl) are shown.

The same procedure was applied to the *a-c/2-c* fusion protein. Although the *a-c/2-c* fusion protein was highly purified using this method, the final purity was lower than observed with native subunit *a* (Figure 4.18). Size exclusion chromatography and anion exchange chromatography did not significantly improve the purity of the *a-c/2-c* fusion protein (data not shown). The final yields of purified subunit *a* and *a-c/2-c* fusion protein were 0.3 and 0.17 mg/L of cell culture respectively, corresponding to the theoretical yield of approximately 80 %, which was calculated from the amount of F_0 starting material.

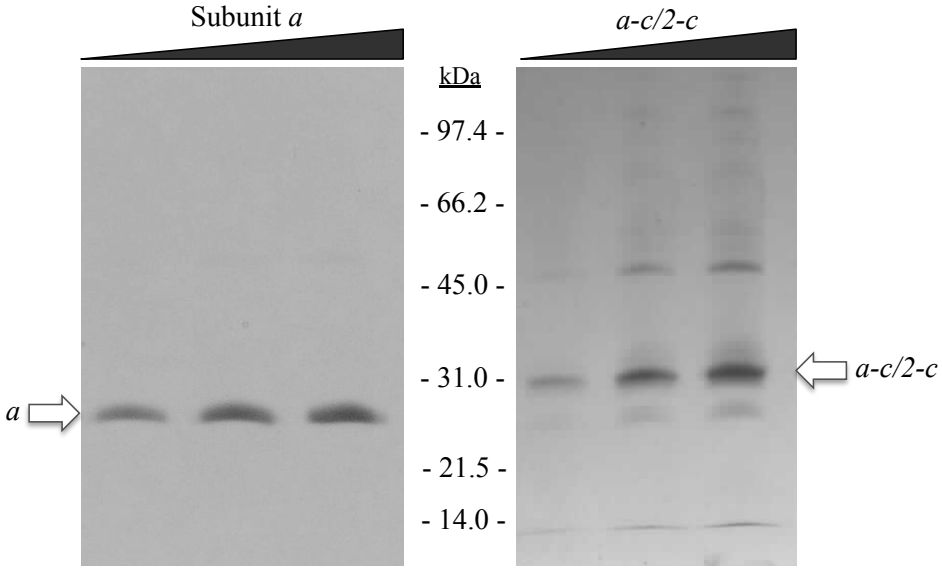

Figure 4.18: Purified subunit *a* and *a-c/2-c* fusion protein. The Coomassie stained SDS-PAGE gels contain samples of 1 µg, 3µg, and 5 µg of either purified protein. The positions of molecular weight markers are indicated in kDa.

4.7.3 Purification of the wild type subunit *a* from intact F_1F_0-ATP synthase.

We developed a second novel strategy for purification of subunit *a* from intact F_1F_0 (section 3.5). The aim of this procedure was to isolate subunit *a* using milder detergents than the sodium cholate and octylglucopyranoside used during purification of subunit *a* from isolated F_0 (sections 3.4 and 4.7.1). To do this, the intact F_1F_0 complex was isolated using a modified version of the protocol developed by Laubinger and Dimroth for isolation of the *P. modestum* F_1F_0-ATPase (Laubinger and Dimroth, 1988) (Haji and Dmitriev, unpublished data). This method involves solubilization of the F_1F_0 complex from the membrane using DHPC (a relatively mild detergent) and PEG fractionation to enhance purity of the intact ATP synthase. ATP synthase isolated by this method is approximately 76 % pure (Figure 4.19).

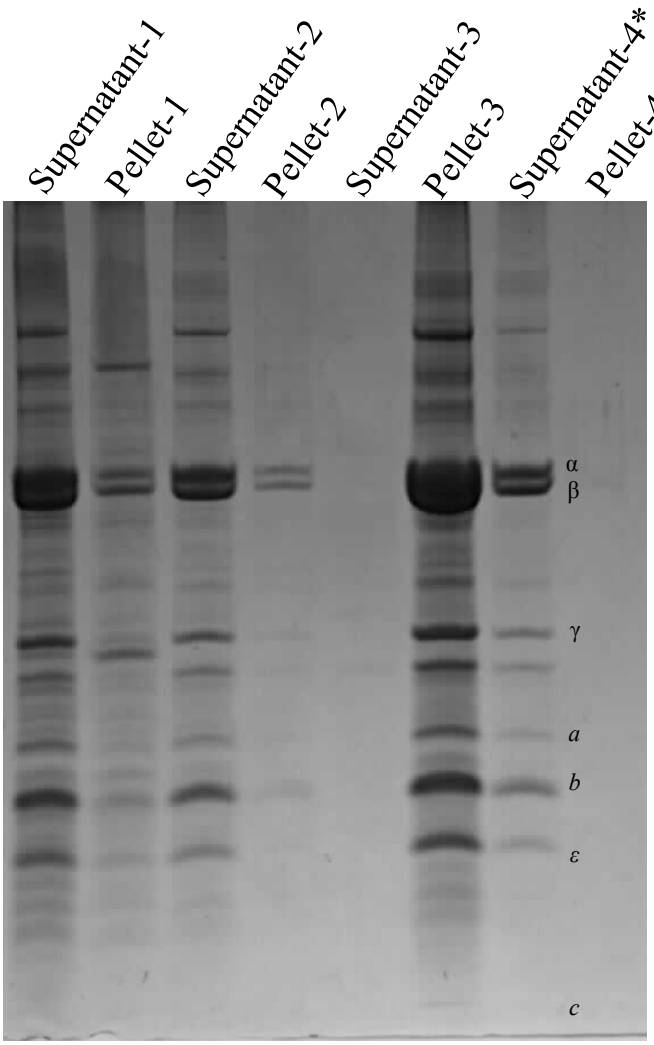

Figure 4.19: Coomassie stained 10 % SDS-PAGE gel containing samples taken at each stage of ATP synthase isolation. The numbers of the supernatants and pellets coorespond those in the purification scheme shown in Figure 3.13. The subunits of ATP synthase are labeled on the gel. * Supernatant-4 is the final purified F_1F_0 sample.

Subunit *a* was dissociated from the other F_1F_0 subunits and isolated using Ni-NTA chromatography (section 3.5). After one round of Ni-NTA chromatography, subunit *a* was not sufficiently purified using this method. Therefore, the elutant from the Ni-NTA column was buffer exchanged to remove imidazole and then loaded onto a second Ni-NTA column for another round of purification (Figure 4.20). After two subsequent rounds of Ni-NTA chromatography the purified subunit *a* samples were of sufficient purity for structure studies.

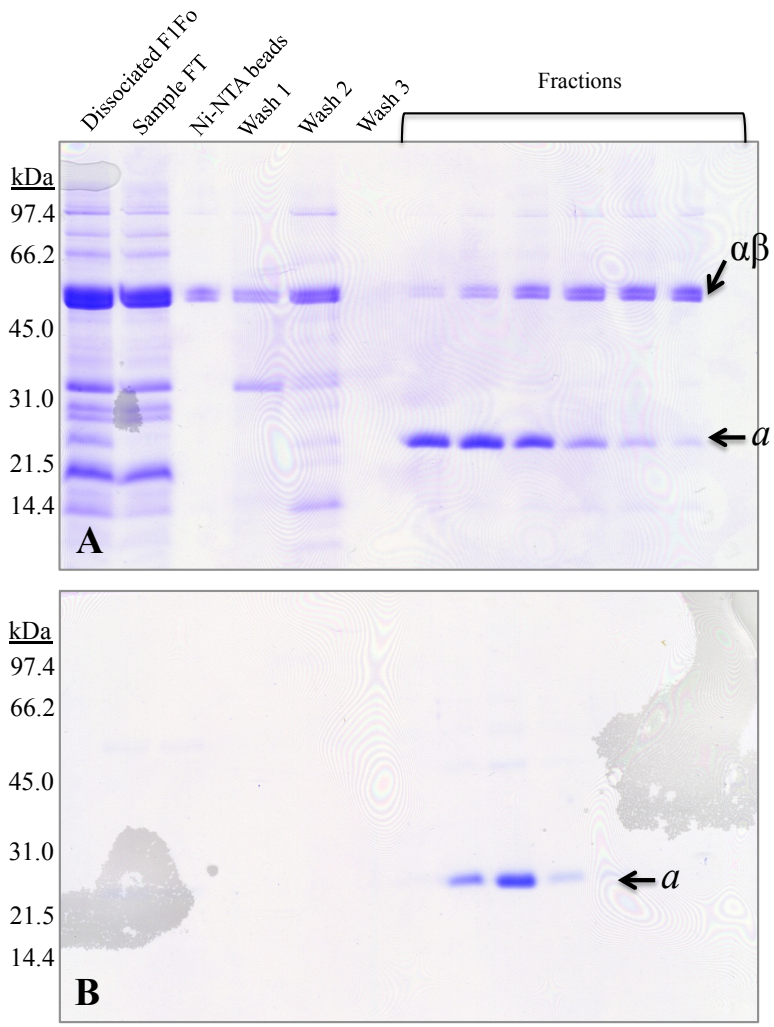

Figure 4.20: Stages of purification of subunit *a* from F_1F_0. 10 % coomassie stained SDS-PAGE gels containing samples taken from the first round of Ni-NTA chromatography (A) and the second round (B). The position of subunit *a* is indicated on each gel and the positions of the molecular weight markers (kDa) are indicated to the left of each gel.

4.8 Characterization of subunit *a* preparations by NMR.

4.8.1 Efforts to optimize spectral resolution of subunit *a*.

NMR experiments were conducted with ^{15}N labeled subunit *a* purified in LMPG micelles to assess spectral quality for structure studies. LMPG was chosen because it is structurally similar to the naturally occurring phospholipids in cellular membranes and it has been shown to produce high quality NMR spectra with several other membrane proteins (Kruger-Koplin *et al.*, 2004). The HSQC spectrum of subunit *a* purified in LMPG micelles did not have high spectral resolution (Figure 4.21). Several peaks corresponding to backbone and

side chain amide groups were well resolved, but spectral quality was not sufficient to make backbone amide chemical shift assignments.

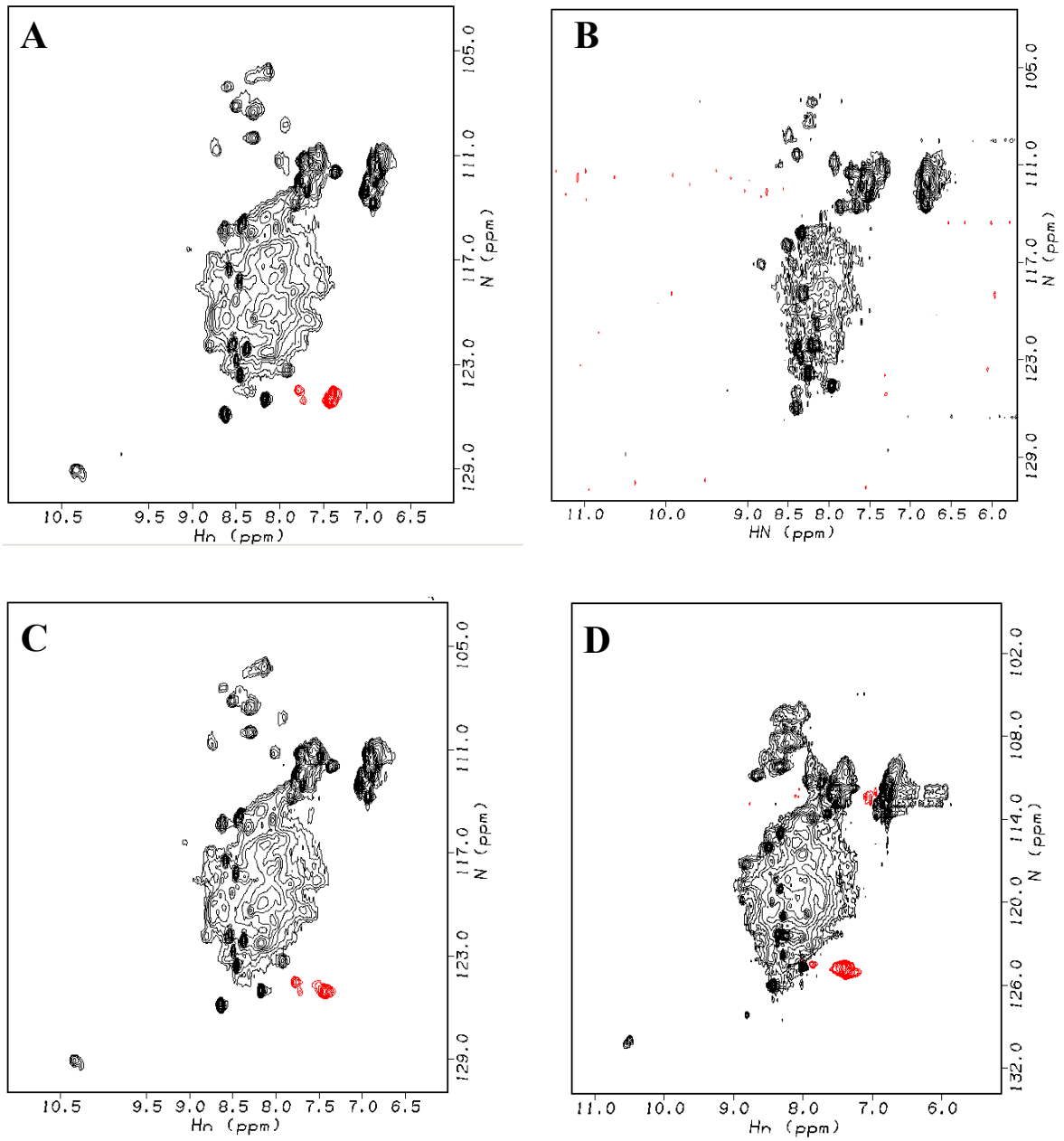

Figure 4.21: ^{1}H, ^{15}N HSQC spectra obtained from subunit *a* purified in LMPG micelles (A), LDAO micelles (B), LPPG micelles (C), and ^{2}H-DPC micelles (D). Backbone amide chemical shifts, as well as the side chain chemical shifts of glutamine and asparagine are shown in black. Peaks corresponding to arginine side chains are shown in red. Spectra were recorded at 600 MHz, 310 K, 128 increments in t_1 with 16 scans per increment.

Detergent type and concentration are critical factors for NMR spectral quality of membrane proteins. We developed a procedure for exchanging purified subunit *a* into different detergents and systematically screened several detergents in an effort to improve spectral resolution. The detergents screened were: *N,N-dimethyldodecylamine-N-oxide* (LDAO), 1-myristoyl-2-hydroxy-*sn*-glycero-3-[phospho-*rac*-(1-glycerol)] (LMPG), palmitoyl-2-hydroxy-sn-glycero-3-[phospho-*rac*-(1-glycerol)] (LPPG), and deuterated n-dodecylphosphocholine (DPC). The spectra obtained from subunit *a* purified in LDAO, LPPG and ^{2}H-DPC micelles are shown in Figure 4.21 (C-D). None of the detergents tested improved spectral resolution. Protein purified in LPPG had very similar spectral quality to the LMPG spectra shown in Figure 4.21-A. Spectra obtained from subunit *a* purified in LDAO and ^{2}H-DPC had lower resolution that the LMPG spectra.

Our standard purification procedure for subunit *a* involves isolation of the F_0 domain, dissociation of the ab_2c_{10} complex, and Ni-NTA chromatography to isolate the His_6 tagged subunit *a* (section 3.4). The sodium cholate used to solubilize F_0 in the standard purification procedure is a relatively harsh detergent, which may cause misfolding of subunit *a*, leading to poor spectral quality. We decided to purify subunit *a* using milder solubilization and purification conditions in an attempt to improve spectral resolution. Isolation of the intact F_1F_0 ATP synthase, where DHPC is used for solubilization, is a relatively mild procedure that preserves functionality of the enzyme (Haji and Dmitriev, unpublished data). We purified subunit *a* from the intact F_1F_0 ATP synthase in DHPC micelles. However, the NMR spectra obtained had lower resolution than subunit *a* isolated from F_0 (Figure 4.22-A). Subunit *a* isolated by this method was exchanged from DHPC to LMPG and spectra were recorded (Figure 4.22-B). Despite the mild purification conditions no improvement to spectral resolution was observed when compared to samples isolated using the standard protocol.

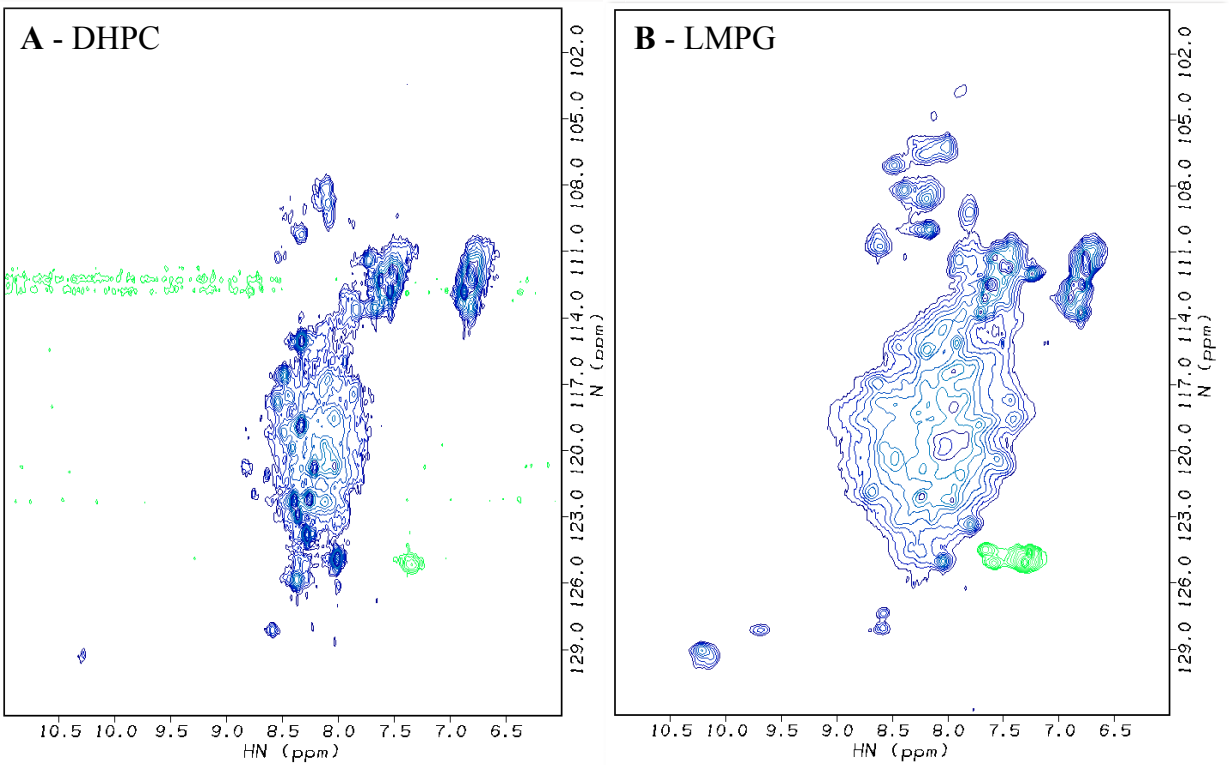

Figure 4.22: HSQC spectra of ^{15}N labeled *a* purified from intact F_1F_0. A) HSQC spectrum from subunit *a* in DHPC micelles. B) HSQC spectrum from subunit *a* in LMPG micelles. In both panels backbone amide chemical shifts are shown in blue. The arginine side chain peaks are shown in green.

4.8.2 Assignment of the R210 side chain peak for future functional studies.

The chemical properties and surrounding environment of each residue in subunit *a* contribute to the position of the chemical shift of each backbone amide group in the HSQC spectra. Arginine side chain amide groups have a characteristic chemical shifts and are expected to occur in a predictable zone on the HSQC spectra. Subunit *a* contains four arginine residues and four well resolved peaks were visible in the arginine side chain region of the HSQC spectrum. We used selective mutagenesis to determine which of the arginine side chain peaks corresponded to R210 (Figure 4.23). Subunit *a* with arginine 210 mutated to glutamine was expressed from the C43(DE3)/pHP20Q strain, ^{15}N labeled during expression, purified, and analyzed by NMR. The R210Q mutant of subunit *a* produced a similar spectrum to that of wild type subunit *a*, except for the absence of the peak corresponding to the side chain amide of arginine 210. We assigned the side chain amide peak of arginine 210 by overlaying the wild

type subunit *a* spectrum with the *a*R210Q spectrum and identifying the peak in the wild type spectrum that was absent in the *a*R210Q spectrum (Figure 4.23). Ultimately, chemical shift assignment of R210 is meaningful because it provides an excellent reporter group for functional studies. For example, we may conduct functional NMR studies to determine the pKa of R210. Furthermore, we may be able to use the R210 reporter group to investigate the binding of novel proton transport inhibitors to the proton channel.

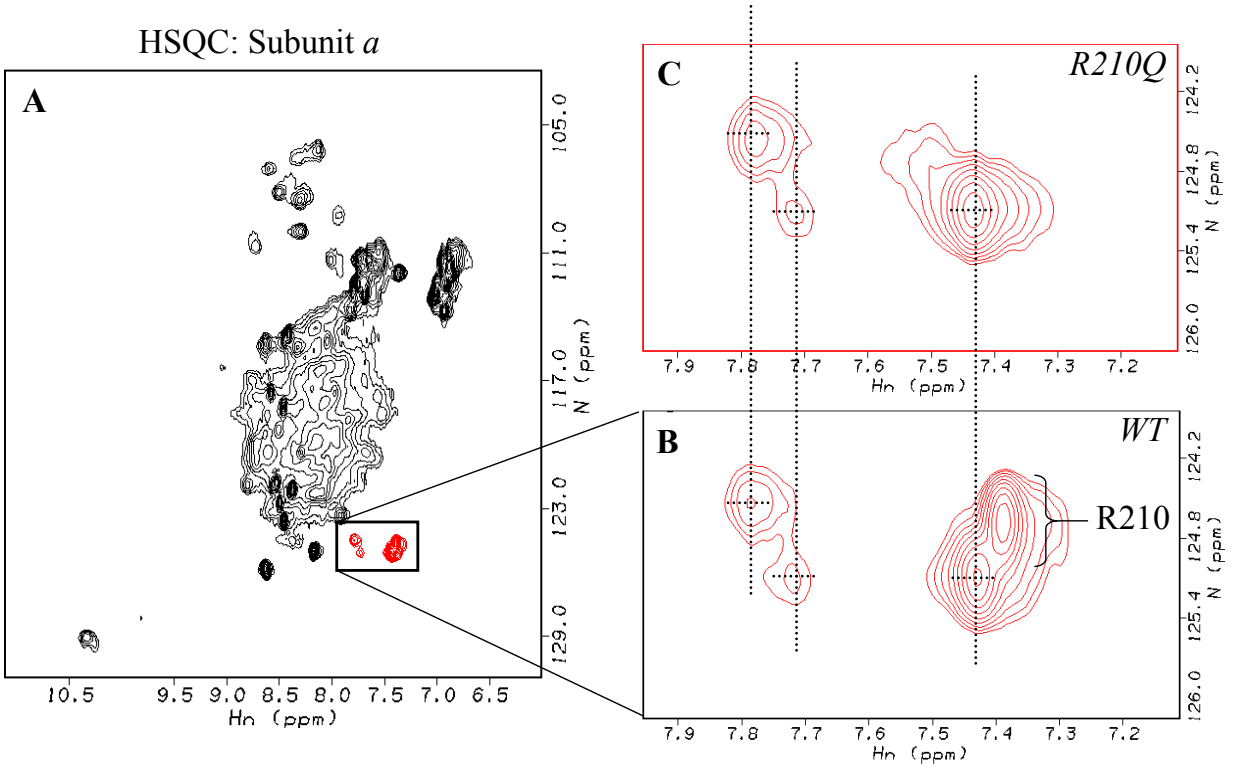

Figure 4.23: Chemical shift assignment of the R210 side chain amide. A) HSQC spectrum of wild type subunit *a*. B) Expanded view of the wild type arginine side chain region. C) Expanded view of the R210Q mutant arginine side chain region. Identical arginine peaks from each spectrum are aligned. The position of arginine 210 is indicated.

4.8.3 R210 is not resolved in HSQC spectra recorded from *a-c/2-c*.

The *a-c/2-c* construct was originally designed for X-ray crystallographic studies. However, the fusion protein also had the potential to allow NMR functional investigations into the chemical shift perturbations of the critical R210 residue in an environment that mimics the proton channel. We recorded NMR spectra from the *a-c/2-c* fusion protein to see if the arginine side chain region would be well resolved for functional studies (Figure 4.24). Spectral

resolution of the *a-c/2-c* construct was poor and the arginine side chain region was heavily overlapped making the R210 peak indiscernible. There are two key factors contributing to the poor spectral resolution in the arginine side chain region of the *a-c/2-c* fusion protein spectra relative to wild type subunit *a*. First, the *a-c/2-c* fusion protein contains eight arginine residues, while subunit *a* contains only four, which complicates the spectra. Second, the *a-c/2-c* construct is considerably larger than subunit *a*, which potentially reduces resolution.

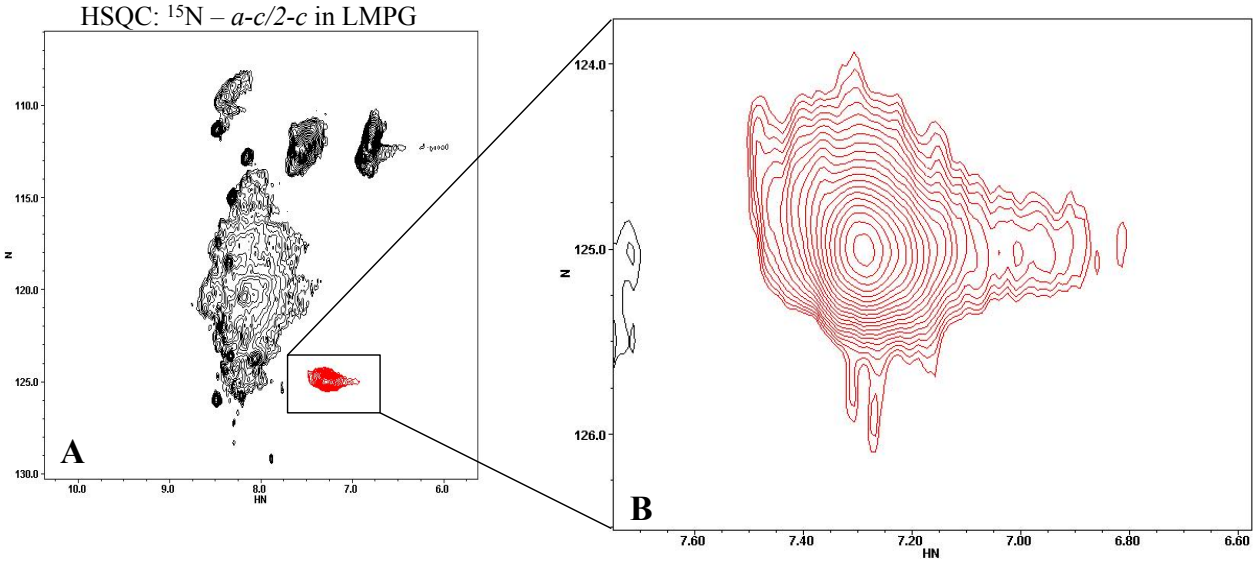

Figure 4.24: ^{1}H, ^{15}N HSQC spectrum from the *a-c/2-c* fusion protein purified in LMPG micelles. A) Full HSQC spectrum, backbone amide signals are shown in black and arginine side chain signals are shown in red. B) Expanded view of the arginine side chain region. Spectra were recorded at 600 MHz, 310 K, with 80 increments in t_1 and 256 scans per increment.

Arginine 210 is thought to form a salt bridge with aspartic acid 61 of subunit *c*; the pKa of R210 is suspected to be uncharacteristically low due to close interaction with *c*D61. We hypothesized that it may have been possible to resolve the R210 peak from the other arginine peaks based on its low pKa. HSQC spectra were recorded at various pH values in an effort to separate the R210 signal from the other arginine side chain peaks. We titrated a sample of purified *a-c/2-c* from pH 4.0 to 8.5, and recorded HSQC spectra at each pH. Spectra recorded with the *a-c/2-c* construct below pH 5.5 showed some relative changes compared to spectra recorded at the standard pH 6.0. The spectra recorded at pH 5.0 showed the appearance of one

peak outside the unresolved region (Figure 4.25). Spectra recorded with the *a-c/2-c* sample at pH levels higher than 7.0 had no detectable signal in the arginine side chain region; this was not unforeseen because NMR spectral quality is dependent on the pH of the sample. Samples at high pH values experience rapid proton exchange with water, which causes line broadening and loss of signal intensity. The optimal pH range for protein NMR is 4.0 to 6.0. Although we did observe minimal chemical shift perturbations in response to pH, we were unable to determine if the spectral differences were genuine or an experimental artifact. Therefore, we were unable to assign the *a-c/2-c* R210 side chain peak.

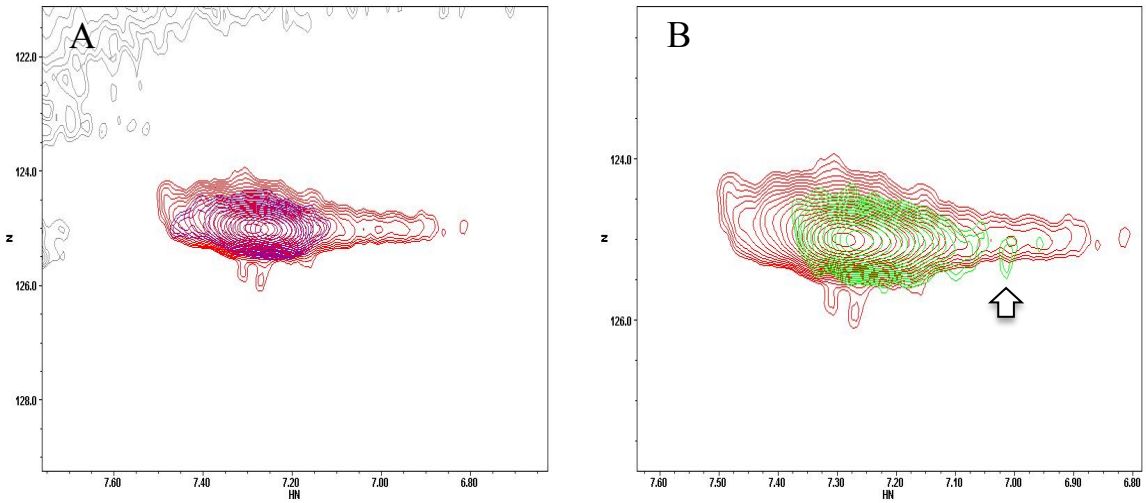

Figure 4.25: Arginine region of the *a-c/2-c* HSQC spectra. Arginine side chain peaks from spectra recorded at pH 6.0 are shown in red. A) arginine side chain peaks from spectra recorded at pH 4.5 are shown in purple. B) Arginine side chain peaks from spectra recorded at pH 5.0 are shown in green. The peak appearing outside of the unresolved region is denoted with an arrow.

4.9 Crystallization of subunit *a*.

The ultimate goal of our work is to determine the high resolution structure of subunit *a* and gain a detailed understanding of the mechanism of proton transport. Although the NMR work discussed in section 4.8 provides opportunities for functional studies, the poor spectral resolution makes structure determination by NMR impossible. We worked to crystallize both wild type subunit *a* and the *a-c/2-c* fusion protein for structure determination.

4.9.1 Crystal screening: aggregation state of subunit *a*.

Monodisperse protein samples have a higher propensity toward crystallization. DLS analysis as well as gel filtration chromatography allowed us to assess the aggregation state of subunit *a* purified in LMPG micelles. DLS experiments showed that subunit *a* was monodisperse in solution both at 20 ^{o}C and 25 ^{o}C (Figure 4.26). Purified subunit *a* samples produced one broad DLS peak where the peak maximum corresponded to a calculated hydrodynamic radius of approximately 2.6 nm (Figure 4.26). The theoretical Rh value for subunit *a* in detergent micelles is approximately 3.0 nm, which is close to the experimental value of 2.6 nm, leading us to conclude that purified subunit *a* was monomeric and monodisperse.

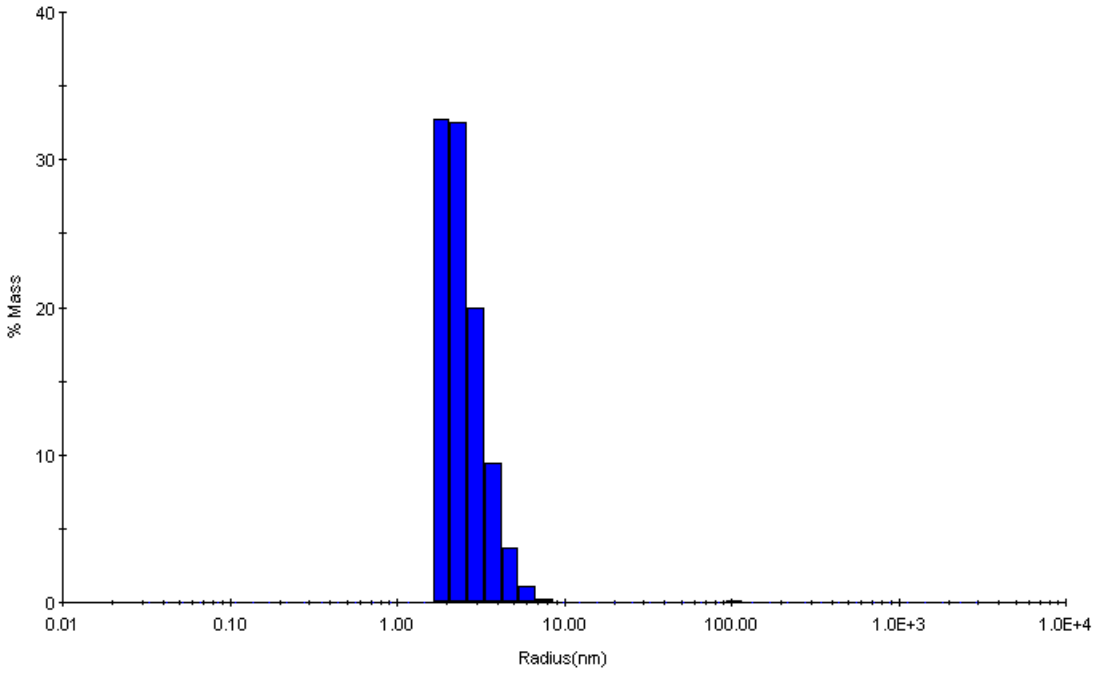

Figure 4.26: DLS of pure subunit *a* in LMPG micelles. Purified subunit *a* was concentrated to 7.0 mg/mL for DLS experiments. This trace was recorded at 27 ^{o}C.

Analytical gel filtration chromatography is another a commonly used method for determining protein aggregation state. Purified subunit *a* was subjected to gel filtration chromatography using a Superdex-200 GL 10/300 column. One sharp peak was observed in the elution profile at a retention volume of 14.6 mL (Figure 4.27). To determine the molecular

weight of subunit *a* the retention volume of 14.6 mL was compared to retention volumes of protein standards. The molecular weight of subunit *a* was calculated to be 48 kDa, which was in the expected range for monomeric subunit *a* in LMPG micelles. The peak had a shoulder extending from 16.5 mL to 22.5 mL. We assumed that the shoulder was caused by protein-detergent complexes with various numbers of LMPG molecules.

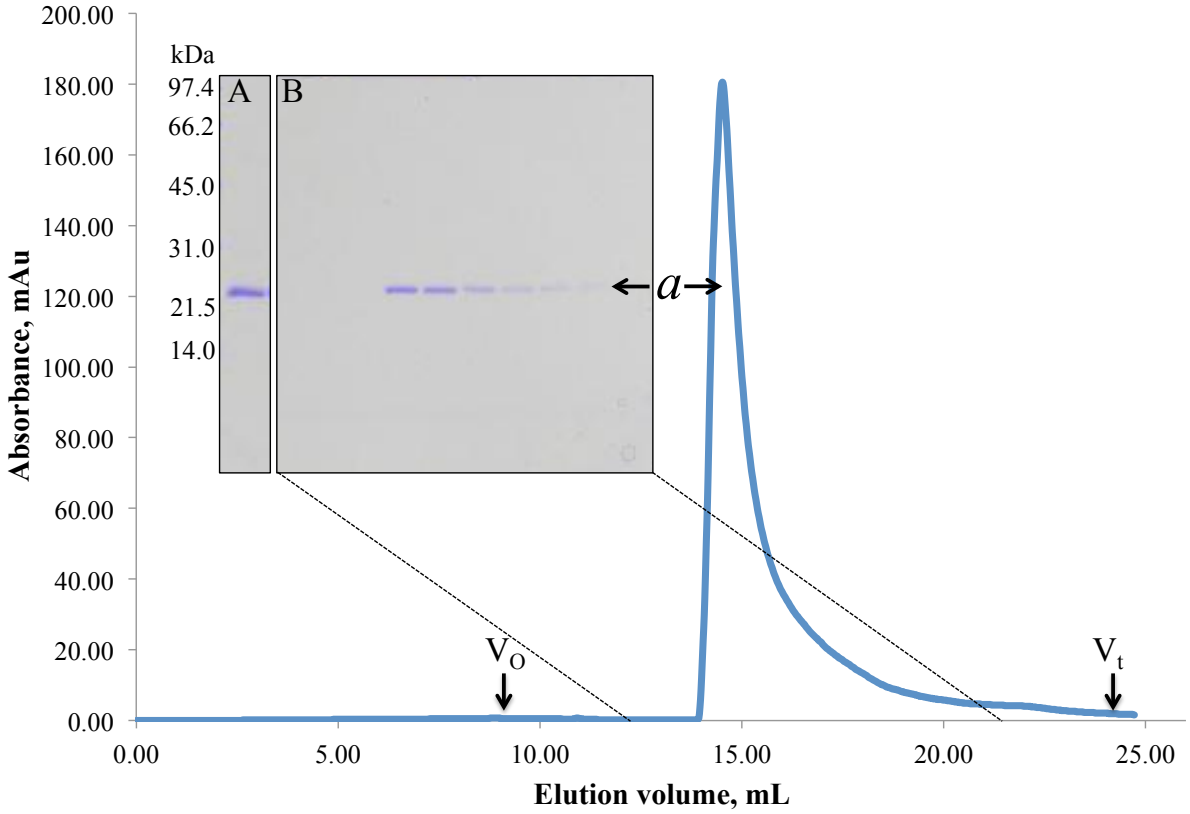

Figure 4.27: Elution profile of subunit *a* on the Superdex 200 GL 10/300 gel filtration column. The elution trace is shown in blue. 10 % coomassie stained SDS-PAGE gel containing a sample of purified subunit *a* before gel filtration (A) as well as samples from the peak gel filtration fractions (B). The void volume (V_O) was 7.6 mL and the total volume (V_t) was 24 mL. The k_{av} for subunit *a* was calculated to be 0.427. The estimated molecular weight of subunit *a* in LMPG micelles was 48 kDa.

4.9.2 Subunit *a* has been successfully crystallized.

Subunit *a* was purified in LMPG micelles for preliminary crystal screening (section 3.4). The high throughput screens were conducted at the high throughput crystal screening facility at the Hauptman Woodward Institute, in Buffalo New York, using the microbatch under

oil crystallization method. Promising conditions from the initial 1,536 conditions were identified (Figure 4.28).

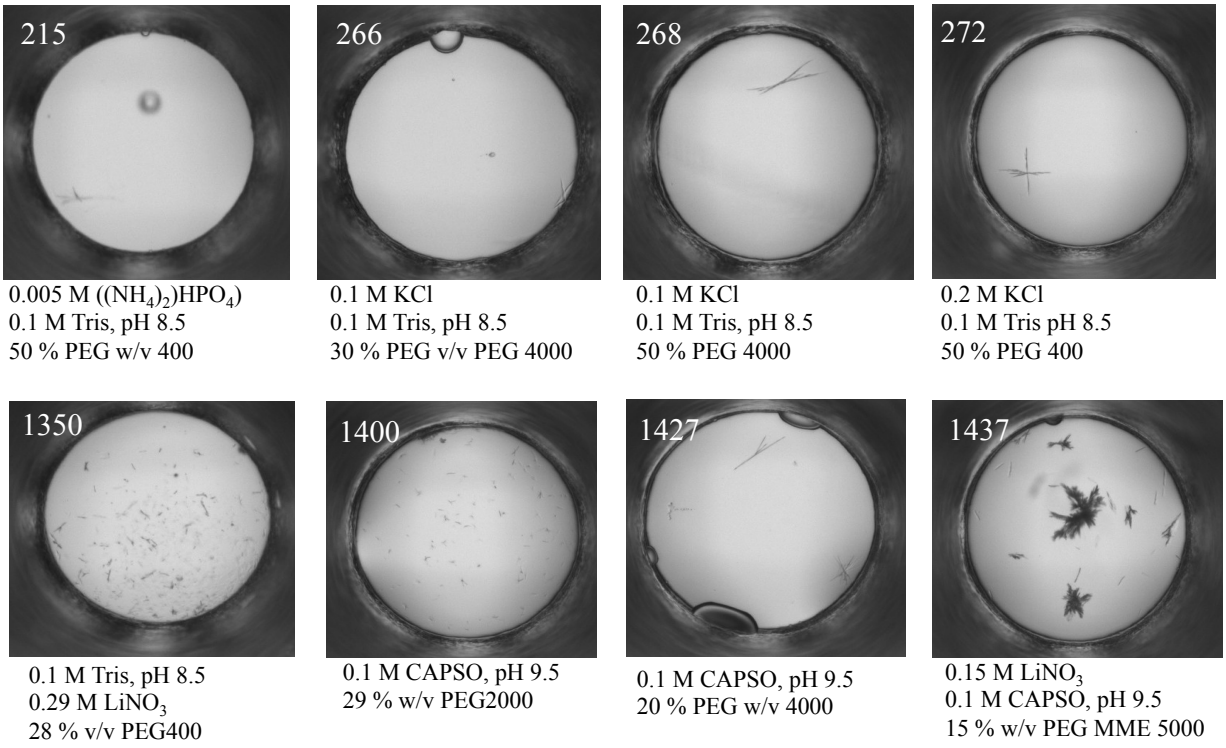

Figure 4.28: Preliminary hits from the 'Membrane Protein Crystallization Screen' – MSC4-1563 cocktail screen. Purified subunit *a* was concentrated to 7.0 mg/mL for preliminary crystal screening. The well number of the MC4 cocktail screen is indicated in at the top left of each image. The crystallization conditions are written below each image.

We also conducted primary LCP screening in collaboration with professor Hartmut Luecke (University of California – Irvine). Preliminary LCP screening of subunit *a* was carried out using the following standard membrane protein crystallization screening kits from Molecular Dimensions: MemGold 1-36, MemFac 1-48, MD 1-25, and MD 1-44. The most promising conditions from the preliminary LCP screens are shown in Figure 4.29. The crystals shown in panels A and B of Figure 4.29 showed weak birefringence and were confirmed to be proteinaceous by X-Ray diffraction. Diffraction experiments were carried out at the Stanford Synchrotron Radiation Lightsource (SSRL) in collaboration with Dr. Luecke.

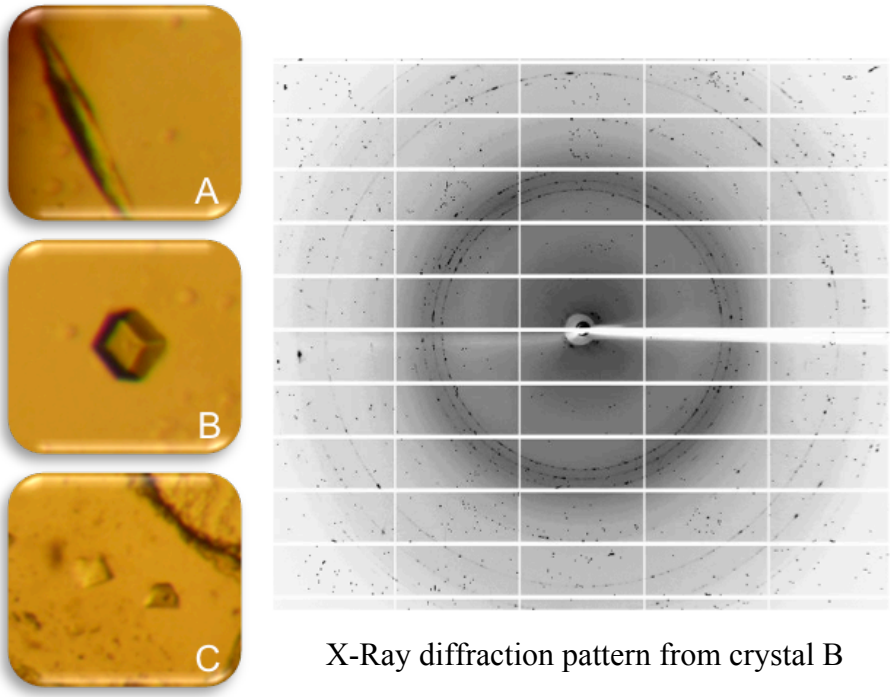

Figure 4.29: Crystals of subunit *a* obtained from preliminary LCP screening. A) Proteinaceous object grown in 44 % PEG 400, 0.1 M Tris-HCl pH 8.0, and 0.2 M $CaCl_2$. B) Different crystalline form of subunit *a* grown in the same condition as the object shown in panel A. C) Crystals grown in 7.7 % w/v PEG-1500, 0.02 M MES, pH 6.5, 0.02 M NaCl, 0.01 M $MgSO_4$, 0.02 M $CaCl_2$. The diffraction pattern obtained from the crystal in panel B is shown on the right.

The crystals shown in Figure 4.29 – A and B, had poor diffraction quality. The resolution of the diffraction pattern was in the range of 30 Å. High resolution structure determination is dependent on diffraction resolution below 4 Å. No diffraction data was obtained with sample C. Therefore, further screening was required. We have continued in-house refined crystal screening at the University of Saskatchewan using the hanging drop vapor diffusion method. Promising conditions from both the Hauptman Woodward screen and the preliminary LCP screens were selected for refinement. The components of the crystallization conditions were systematically altered: the buffer concentration, buffer type, pH, salt concentration, salt type, PEG concentration and PEG type were adjusted. Approximately 900 refined vapor diffusion conditions were screened. Several promising conditions were identified and subjected to diffraction on the small gap undulator beamline (08-ID-1) at the Canadian Light Source (CLS) at the University of Saskatchewan. One set of conditions produced

proteinaceous crystals. The crystals formed platelike clumps made up of several smaller crystals, showed minimal birefringence under polarizer analysis, and had a slightly yellowish appearance under white light. The crystals showed Bragg reflections from 30 Å – 14 Å resolution (Figure 4.30).

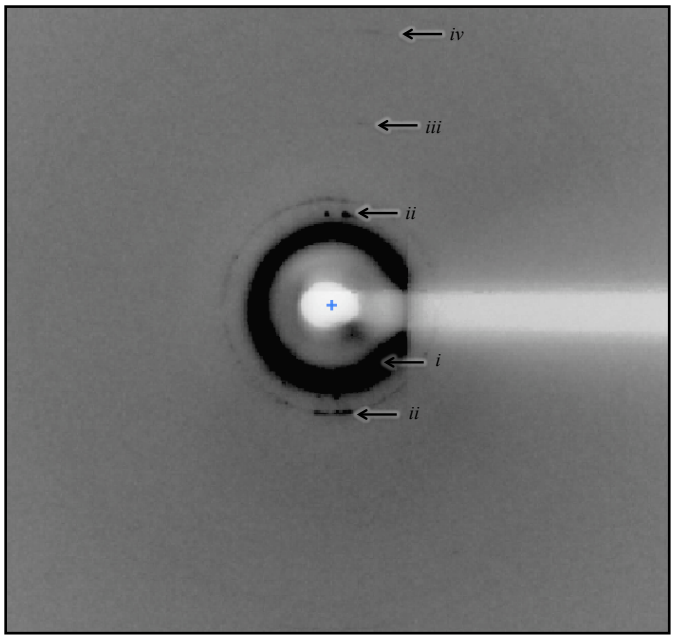

Figure 4.30: Diffraction pattern collected from subunit *a* crystals at the small gap undulator beamline at the CLS. Crystallization conditions: 18 % PEG 400, 0.2 M CAPSO, pH 9.5, 0.2 M LiBr. The white spot marked with a blue '+' is a void in the diffraction pattern caused by the beam stop. *i*) potentially, averaged diffraction from alpha helical segments. *ii*) Individual Bragg reflections at ~ 25 – 20 Å resolution. *iii*) Bragg reflections at ~18 Å resolution. *iv*) Bragg reflections at ~ 14 Å resolution.

4.10 Optimization of purified *a-c/2-c* protein yield and stability for future crystallization trials.

The *a-c/2-c* fusion protein could be obtained at an approximate 82 % purity (as estimated by band densitometry, data not shown). As a general rule for protein crystallography, samples should be greater than 90 % pure, but high resolution structure determination is still possible with protein samples of less than 90 % purity. Therefore, we accepted that the optimized 82 % purity of our *a-c/2-c* samples was sufficient for preliminary crystal screening. In addition to relatively low purity, the *a-c/2-c* fusion protein presented us with three

challenges: 1) the purified samples formed aggregates in solution, 2) truncation of the *a-c/2-c* protein occurs during optimal overexpression in C43*recA* cells, and 3) the yield of purified protein was very low (0.17 mg per liter of cell culture).

Purified *a-c/2-c* was subjected to SDS-PAGE analysis. We found that purified *a-c/2-c* formed high molecular weight aggregates, which react with anti pentaHis antibody (Figure 4.31). Since the purity of the *a-c/2-c* samples exceeded 80 % it was unlikely that the aggregates were occurring between *a-c/2-c* and other protein types. Enhanced electrophoretic mobility is a common property among membrane proteins. Therefore, the bands between 45 and 97 kDa in Figure 4.31 may correspond to dimers, trimers, and tetramers of *a-c/2-c*, although it does not appear that the molecular weights of the aggregates correlate to multimers. However, the C43*recA* strain, which optimally overexpressed the *a-c/2-c* fusion protein (section 4.7.1) also expressed a truncated *a-c/2-c* product at approximately 5 – 10 % the level of full length *a-c/2-c* (Figure 4.31). Therefore, we cannot exclude the possibility that the aggregates correspond to multimers of the truncated *a-c/2-c* protein. A third possibility is that the aggregates are formed by complexes of *a-c/2-c* with native subunit *c*. We conducted several experiments in an effort to isolate the monomeric *a-c/2-c*. Size exclusion chromatography, ion exchange chromatography, and re-purification under stringent dissociation conditions were all insufficient to remove the aggregates (data not shown).

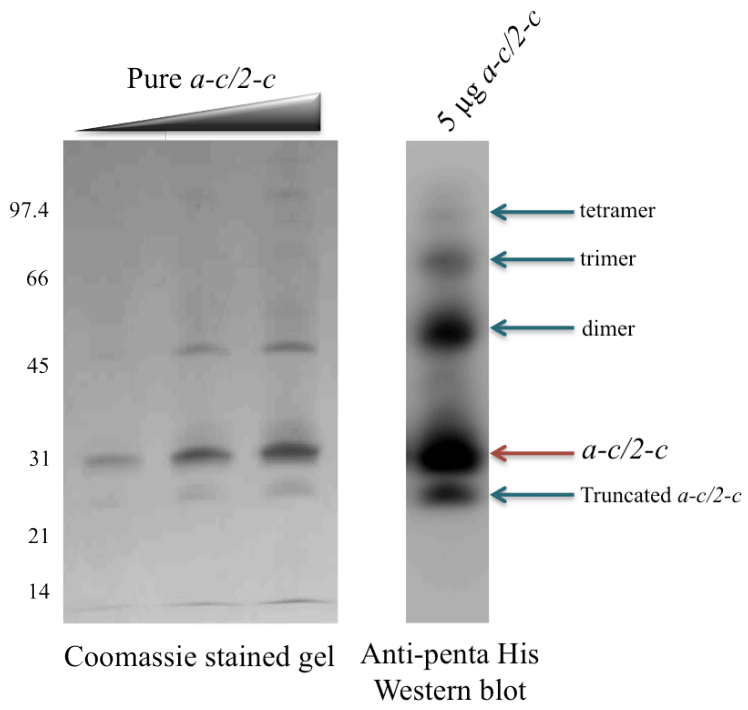

Figure 4.31: Coomassie stained 10 % SDS-PAGE gel and Western blot of purified *a-c/2-c* fusion protein. Molecular weight standards (kDa) are indicated. Left panel: Coomassie stained gel showing samples of 1µg, 3 µg, and 5 µg purified *a-c/2-c*. Right panel: Western blot probed against the His_6 tag on *a-c/2-c*. The position of the monomeric full length *a-c/2-c* protein is indicated with a red arrow. Positions of the potential dimeric, trimeric and tetrameric *a-c/2-c* aggregates are indicated with blue arrows. The position of truncated *a-c/2-c* fusion protein is also indicated.

The truncated expression product was not observed when *a-c/2-c* was expressed in the OM202*recA* strain. We believed the truncation occurred because of residual RecA activity in the C43*recA* parental strain. RecA recognizes and recombines repetitive sequences of DNA, like the repeating gene segments encoding *c*TMH-II of the *a-c/2-c* fusion protein. We used two strategies to eliminate the truncated protein. First, we screened several C43*recA* P1 transductants for RecA activity and chose the transductant with the highest UV sensitivity, and presumably the lowest RecA activity, for additional expression testing (data not shown). There was only marginal reduction in the level of truncated expression product using this approach. Second, we moved the N-terminal His_6 tag of *a-c/2-c* to the C-terminus in an attempt to prevent binding of the truncated product to Ni-NTA agarose during purification. Consistent with previous observations in our lab (Uhlemann and Dmitriev, unpublished data) the C-terminal

His_6 tag on subunit *c* was not detectable by Western blot, and was not useful for protein purification (data not shown). Therefore, we were unable to prevent formation of the truncated expression product. Because the truncated expression product is present at less than 10 % the level of the full length *a-c/2-c* fusion protein, we are hopeful that it will not interfere with future crystallization trials.

Subunit *c* is a naturally oligomeric protein and interactions between the fused *c* subunits may contribute to oligomerization of the purified *a-c/2-c* fusion protein samples. We hypothesized that if the *c*L31F assembly mutation was introduced into the fused *c* subunit of *a-c/2-c*, oligomerization may not occur in the purified protein samples. As discussed in section 4.2, we generated a series of pHP808 derivative plasmids that contain the L31F mutation to investigate the membrane insertion requirements of *a-c/2-c*. These same plasmids were also used to express the *a-c/2-c* fusion protein in the presence of the L31F assembly mutant, in an attempt to prevent aggregation in the purified *a-c/2-c* samples, as well as to prevent potential aggregation with native subunit *c*. In the pHP8014 plasmid the gene encoding subunit *c* contains the L31F point mutation. In the pHP8015 plasmid the gene encoding *a-c/2-c* contains the L31F mutation. In pHP8016 both the genes encoding native subunit *c* and *a-c/2-c* contain the L31F mutation. C43(DE3) *E.coli* cells transformed with the pHP808, pHP8014, pHP8015 and pHP8016 plasmids expressed the *a-c/2-c* fusion protein at similar levels (Figure 4.32). The *a-c/2-c* fusion protein was purified from each strain by Ni-NTA affinity chromatography (section 3.6). Unfortunately, the L31F mutations, regardless of their location, had only marginal effects on the aggregation state of *a-c/2-c* and did not improve purity of the *a-c/2-c* preparations compared to the original construct (Figure 4.33).

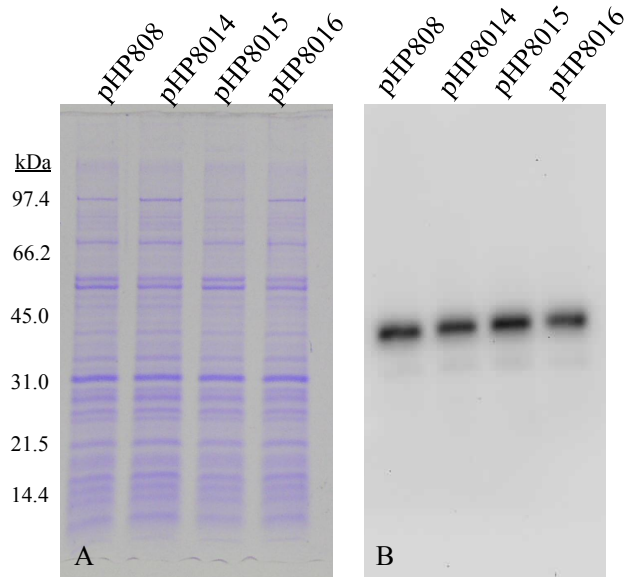

Figure 4.32: Expression of the *a-c/2-c* construct in the presence of the L31F mutations. Expression was tested in the C43*recA* background strain. Each lane was loaded with 10 µg total membrane protein. A) Coomassie stained 10 % SDS-PAGE gel. B) Western blot probed against the His_6 tag on the *a-c/2-c* fusion protein using anti-pentaHis HRP conjugate antibody (Qiagen, Mississauga, ON).

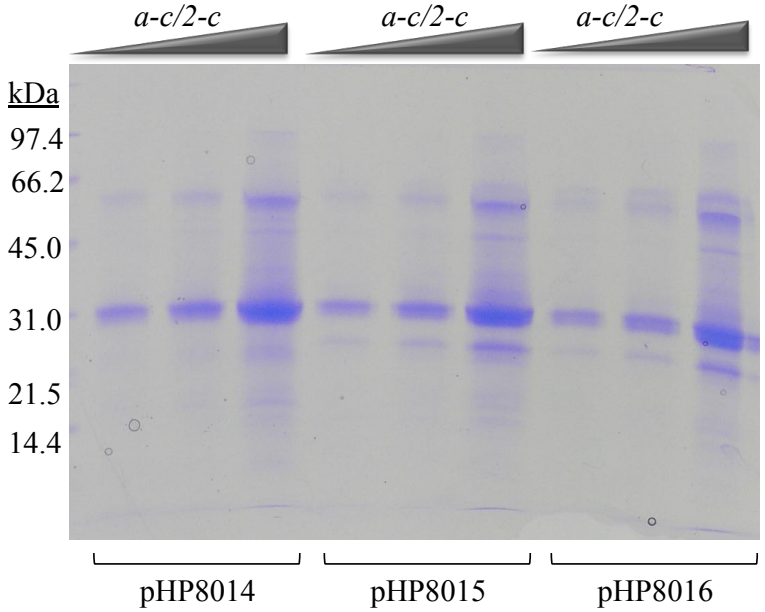

Figure 4.33: Coomassie stained 10 % SDS-PAGE gel of purified *a-c/2-c* with L31F mutations present in monomeric *c*, fused *c*, and both fused and monomeric *c*. 1.0 µg, 5.0 µg and 20.0 µg of each purified protein were loaded. pHP8014 expresses *a-c/2-c* with the L31F mutant in monomeric *c*. pHP8015 expresses *a-c/2-c* with the L31F mutation in fused *c*. pHP8016 expresses the *a-c/2-c* with the L31F mutation present in both fused and monomeric *c*.

We also attempted to express the *a-c/2-c* fusion protein under the control of an inducible promoter to improve the yield of purified protein. We observed that the *a-c/2-c* fusion protein was incorporated into cellular membranes in the absence of native subunit *c* (Figure 4.2) and hypothesized that the *a-c/2-c* fusion construct could be expressed independently of the other ATP synthase subunits. pBAD-102 is an expression vector which tightly regulates gene expression through an arabinose inducible promoter. The gene encoding the *a-c/2-c* fusion protein was inserted into pBAD-102 (plasmid pHP805) and expression was tested in both TOP10 and OM202*recA E. coli* cells (Figure 4.34). Expression of MdfA, an alpha-helical transmembrane multidrug transport protein, from pBAD-102 was used as a control. Unfortunately, the *a-c/2-c* fusion protein was not expressed from pBAD-102 under any of the conditions that worked well for MdfA. The weak bands in Figure 4.34 – B, at approximately 27 kDa, 21 kDa and 8 kDa were attributed to non-specific antibody binding.

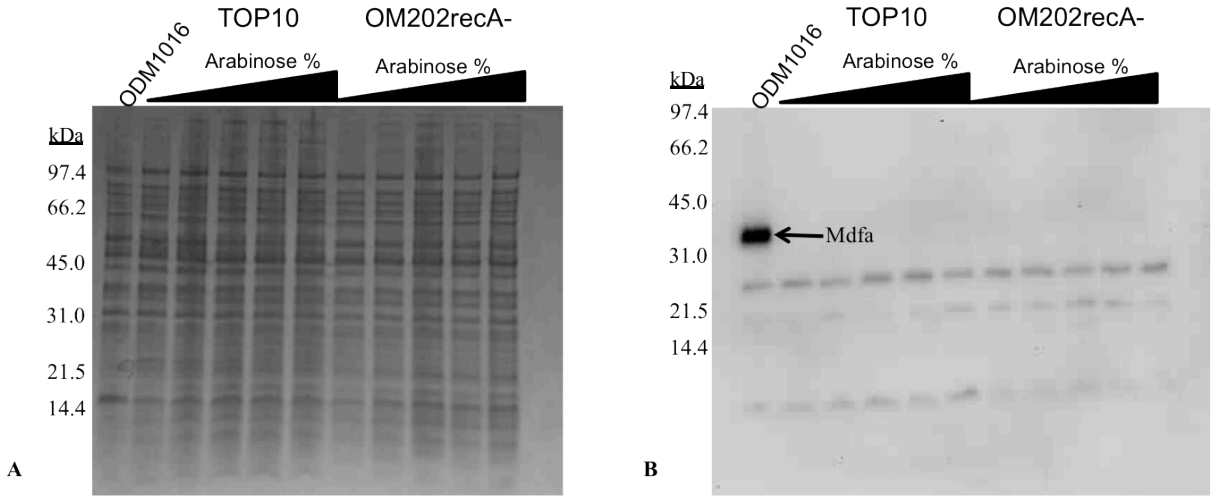

Figure 4.34: Expression of the *a-c/2-c* fusion protein from pBAD102. Panel A: Coomassie stained SDS-PAGE. Panel B: Western blot probed with Anti-pentaHis HRP conjugate antibody (Qiagen, Mississauga, ON). All lanes contain samples of whole cells taken from TOP10/pHP805 or OM202*recA*/pHP805. Increasing arabinose concentration from 0.00002 % to 0.2 % (TOP10) and 0.002 to 0.8 % (OM202recA) is indicated at the top of each panel. ODM1016 cells express the multi-drug transport protein, MdfA, were loaded as a positive control for expression.

Membrane incorporation of subunit *a* is thought to be dependent on the presence of subunits *b* and *c* (Hermolin and Fillingame, 1995). Subunit *a* is rapidly degraded when it is not

incorporated into the membrane (Akiyama *et al.*, 1996). We hypothesized that the apparent lack of expression observed from pHP805 was due to rapid breakdown of the *a-c/2-c* protein, because of the absence of subunit *b*. Therefore, we generated two additional pBAD102 derivative plasmids, where the *a-c/2-c* fusion protein was co-expressed either with the gene encoding subunit *b* only (pHP80-102), or with the genes encoding atpI, subunit *b*, and subunit *c* (pHP8024). Unfortunately, the *a-c/2-c* fusion protein was not expressed at detectable levels in either case (data not shown).

Despite the difficulties we experienced with protein purity, stability, and yield, we conducted crystallization trials of the *a-c/2-c* fusion protein using the same approach as described for subunit *a* (section 4.9). The *a-c/2-c* fusion protein was expressed in C43*recA* cells, purified using the method described in section 3.4, concentrated to approximately 5 mg/mL, and sent for preliminary screening at the Hauptman Woodward Institute (Buffalo, NY). Some promising conditions were identified (Figure 4.35).

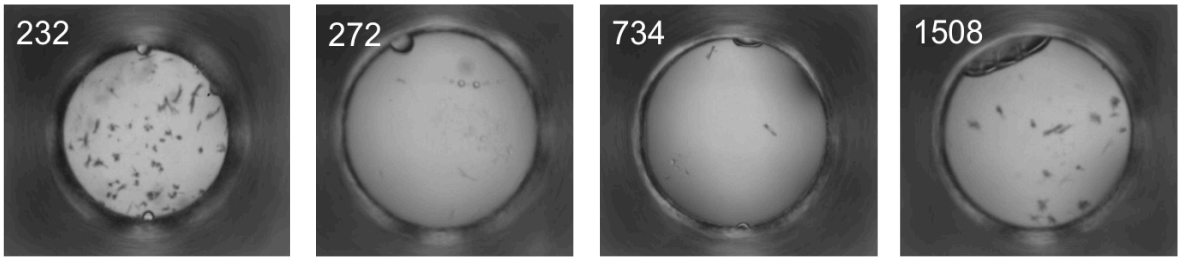

Figure 4.35: Promising conditions from the preliminary crystal screening of the *a-c/2-c* fusion protein. The well number of the MSC4 screen is indicated in at the top left of each image. The crystallization conditions are written below each image.

5 Discussion.

5.1 Assembly of the F_0 domain: Interaction with monomeric subunit *c* drives insertion of subunit *a* into the membrane and primes formation of the *a*-c_{10} complex.

The membrane insertion requirements for the F_0 components have been studied extensively. Previous reports have shown that insertion of subunit *a* into the membrane is dependent on the presence of subunits *b* and *c* (Hermolin and Fillingame, 1995). However, little is known about the stepwise assembly process of the F_0 domain. We posed the following question: is interaction with an assembled *c*-ring required for membrane insertion of subunit *a*, or is interaction with the monomeric *c* subunit sufficient? We hypothesized that if interaction with monomeric subunit *c* were sufficient, the *a-c/2-c* fusion protein would insert into the membrane in the absence of wild type *c*, which was indeed observed (Figure 4.2). Incorporation of the *a-c/2-c* fusion protein in the absence of native *c* shows that monomeric subunit *c* is able to chaperone the insertion of subunit *a* into the membrane and a pre-assembled c_{10} ring is not obligatorily required.

Formation of the c_{10} ring is known to be disrupted by two distinct mutations in subunit *c*, *c*G23D and *c*L31F (Kol *et al.*, 2006). Subunit *c* is incorporated into the membrane in the presence of the *c*G23D and *c*L31F mutations but the *c*-ring does not form. Both *c*-ring assembly mutants were able to facilitate membrane insertion of subunit *a* at levels comparable to the wild type (Figure 4.4) which further supports our hypothesis. Also, the *c*G23D mutant was incorporated into the membrane at sub-stoichiometric levels which indicates that 10:1 *c*:*a* stoichiometry is not required to bring subunit *a* into the membrane. Membrane insertion of the *a-c/2-c* construct in the absence of native *c*, incorporation of subunit *a* in the presence of the *c*-ring assembly mutants, and the normal level of subunit *a* incorporation at sub-stoichiometric levels of the G23D subunit *c* mutant demonstrate that monomeric subunit *c* chaperones insertion of subunit *a* and primes formation of the *a*-c_{10} complex. However, because the *a-c/2-c* construct contains two copies of *c*TMH-II we cannot rule out the possibility that two *c* monomers are needed to chaperone subunit *a* into the membrane. In the mature enzyme, subunit *a* is in direct contact with two *c* monomers (Lau and Rubinstein, 2012; Hakulinen *et al*., 2012; Moore and Fillingame, 2008); it is reasonable to assume that chaperoning of subunit *a* in the membrane is likely dependent on the presence of two *c* monomers rather than one.

In *E. coli* cells all of the ATP synthase subunits are encoded on the chromosomal DNA. However, in eukaryotic cells subunits *a* and *c* are encoded in the mitochondrial DNA while the remaining subunits are encoded in the nucleus. Subcellular localization of these genes in eukaryotic cells suggests that expression and insertion of subunits *a* and *c* into the membrane are tightly linked, which supports our findings. Interactions between subunit *b* and F_1 contribute the bulk of free energy required in binding F_1 to F_0 (Krebstakies *et al.*, 2005) and subunit *b* is undoubtedly crucial to the assembly of the mature complex (Perlin *et al.*, 1983). However, the stage at which subunit *b* is integrated into the F_0 domain is under debate. The findings of Aris and co-authors, and Pati and co-authors suggest that subunit *b* assembles with the *a*-c_{10} complex prior to the attachment of F_1 (Aris *et al.*, 1985; Pati *et al.*, 1991). Pre-assembly of the proton transport machinery in the membrane presents a potential problem: if the pre-fabricated ab_2c_{10} complex is embedded in the membrane it may facilitate passive proton transport and disrupt the PMF (Schneider and Altendorf, 1985), which could be fatal to cells. However, Pati and co-authors have suggested that all three components of the F_0 domain assemble as an 'immature proton impermeable form' that cannot facilitate efficient proton transport (Pati *et al.*, 1991), which supports the plausibility of the ab_2c_{10} complex as an intermediate of ATP synthase assembly in living cells. Reports have also shown that proton transport capability is induced after the attachment of the F_1 domain, to a pre-fabricated F_0 domain, (Brusilow, 1987) and remains even after F_1 is removed, suggesting that the binding of F_1 to F_0 displaces the unknown factors involved in modulating immature F_0 activity. There is also contradictory evidence showing that subunit *b* cannot insert into the membrane unless it is associated with the F_1 complex (Cox *et al.*, 1981) which leads to a model where the *a*-c_{10} complex is built and then the b_2-F_1 intermediate complex binds.

In yeast, formation of the F_1 $\alpha_3\beta_3$ hexamer is facilitated by chaperones (Ackerman *et al.*, 1992; Bowman *et al.*, 1991) and it is reasonable to assume that a similar process occurs in *E. coli*. Assembled F_1 can be readily associated with and dissociated from the F_0 domain in both bacterial and eukaryotic systems. The activity of F_1 ATPase is inhibited by the ε subunit when F_1 is detached from F_0, which implies that cells may indeed produce assembled F_1 that can be bound to the pre-assembled F_0 domain in one concerted step.

This information taken together leads us to posit the following model for F_1F_0 assembly. Monomeric or dimeric subunit *c* chaperones the insertion of subunit *a* and primes the formation of the *a*-c_{10} complex. Once the *a*-c_{10} complex is formed the assembly can take one of two routes: 1) the b_2 dimer can bind to *a*-c_{10} and serve as a docking point for F_1 binding, or 2) b_2 forms an intermediate complex with the F_1 subunits and binding of b_2-F_1 to the *a*-c_{10} complex occurs concertedly. Our model of F_1F_0 assembly is summarized in Figure 5.1.

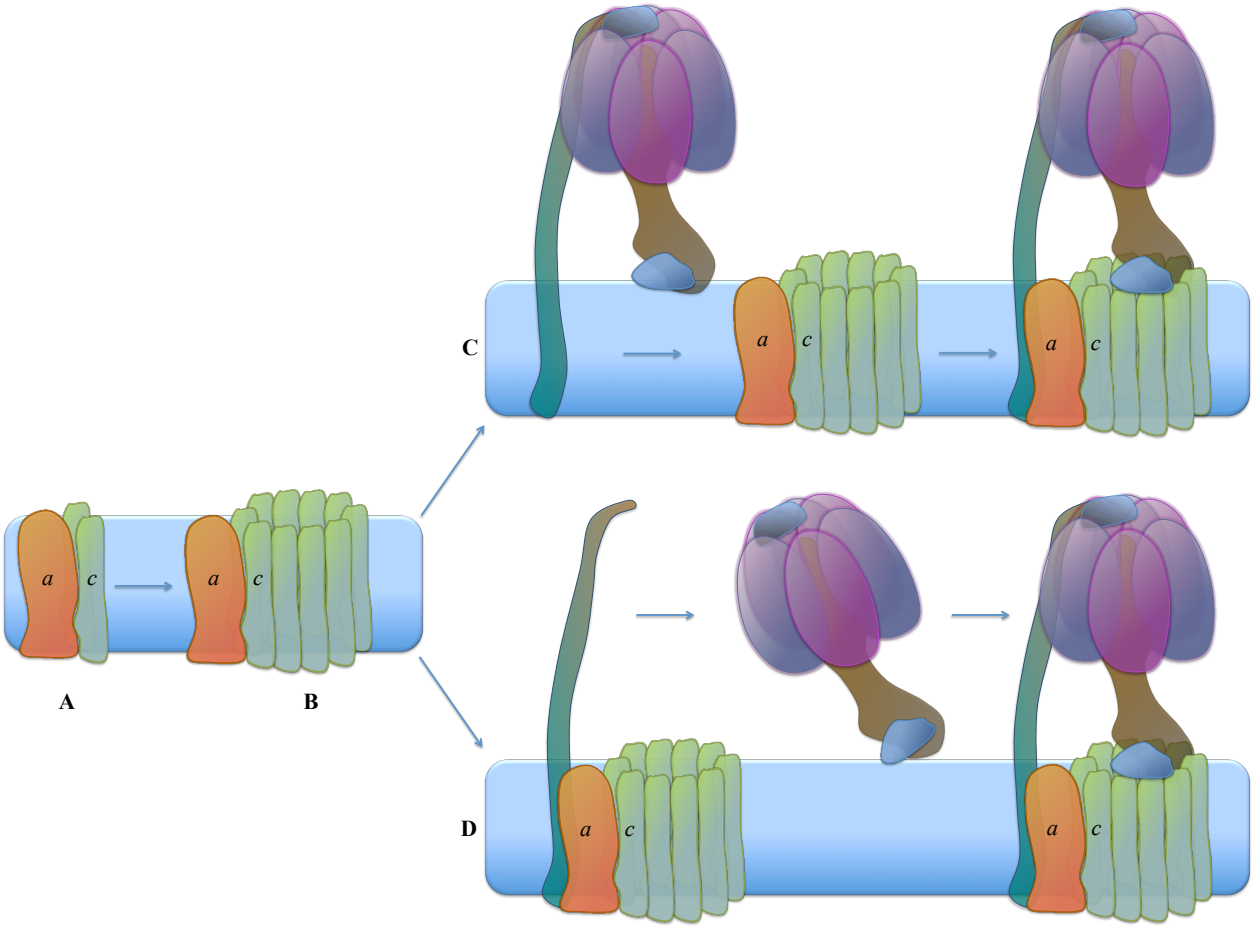

Figure 5.1: Theoretical model of the F_1F_0 assembly mechanism. A) Membrane integration of subunit *a* and its *c* chaperone (one or two copies may be present). B) Formation of the *a*-c_{10} complex. C) Attachment of the b_2F_1 intermediate complex in one concerted step. D) Interaction of subunit *b* with the *a*-c_{10} complex which serves as a docking point for the pre-assembled F_1 domain.

5.2 Membrane insertion of subunits *a* and *c* is a tightly linked process.

The data presented in section 4.1 showed that wild type subunit *a* was efficiently incorporated into the membrane when co-expressed either with wild type subunit *c*, or subunit *c* mutants containing *c*G23D or *c*L31F, which prevent the formation of *c*-rings in the membrane. In contrast, the *a-c/2-c* fusion protein incorporated into the membrane at the same high level as subunit *a* in the presence of the wild type subunit *c,* but not with the *c*L31F or *c*G23D variants. Interestingly, the amount of G23D or L31F mutant *c* subunit was also dramatically reduced in the presence of both *a/c* fusion constructs compared to the wild type subunit *a.* To better understand the cause of these unexpected differences, we investigated effect of the L31F mutation location on membrane incorporation of the *a-c/2-c* fusion protein. In the first *atp* operon construct, the L31F mutation was placed in the fused *c* subunit of the *a-c/2-c* protein, but not in native subunit *c*. In the second construct, L31F was present both in the *a-c/2-c* protein and in native *c*. The third construct, as described above, contained the L31F mutation only in native *c*, but not in the *a-c/2-c* protein. Intriguingly, the combination of wild type sequence in the fused copy of *c* with the L31F mutation in the monomeric *c*, resulted in the lowest level of *a-c/2-c* membrane incorporation and almost no detectable *c* in the membrane. The amounts of both *a-c/2-c* and monomeric *c* in the membrane for the other two constructs were significantly higher, although, still lower than with all wild type *c*-sequences. These complex results brought us to the conclusion that insertion of subunits *a* and *c* into the membrane may be best understood in terms of individual protein – protein interactions in a ternary complex consisting of subunit *a* and two copies of subunit *c* (*a*-c_2 priming complex). As discussed in section 5.1, formation of the *a*-c_2 complex is a crucial step in the insertion of subunits *a* and *c* in the membrane, and this priming event in F_0 assembly is also consistent with the fact that subunit *a* interacts with two *c*-subunits in the native ATP synthase enzyme. In the particular case of the *a-c/2-c* fusion protein, one of the *c*-subunit copies of the priming complex is covalently linked to *a,* whereas the other is a monomeric native *c* subunit.

Stability of the *a*-c_2 priming complex can be viewed as a sum of two types of protein – protein interactions, those between *a* and *c*, and those between *c* and *c*. Mutations which interfere with either the *a* – *c* or *c* – *c* interactions will decrease stability of the *a*-c_2 complex, and will cause poor membrane incorporation of both subunits *a* and *c* once their cumulative

effect exceeds a certain threshold. Although the *c*G23D and *c*L31F mutations destabilize the *c* – *c* interactions they have no significant effect on the *a* – *c* interactions, and the *a*-c_2 complex retains sufficient stability. Therefore, no difference in the levels of subunit *a* or subunit *c* in the membrane was observed when subunit *a* was co-expressed either with wild type subunit *c,* or the *c*G23D or *c*L31F mutations. By comparison, additional destabilizing factors come into play in the *a-c/2-c* protein. The unpaired *c*TMH-II in the *a-c/2-c* protein may interfere with optimal docking of the monomeric subunit *c*, and therefore result in less favorable *a* – *c* interactions. By itself, this effect is insufficient to significantly destabilize the *a*-c_2 complex, and therefore when co-expressed with wild type subunit *c*, the *a-c/2-c* protein is incorporated into the membrane as efficiently as wild type subunit *a.* However, combined with weakened *c* – *c* interactions caused by the L31F mutation, the destabilizing effect of the extra helix in *a-c/2-c* is sufficient to cause the breakdown of the priming complex and poor insertion of the *a-c/2-c* protein. The extent of destabilization caused by the L31F mutation will depend on its location, as indeed was observed in our experiments. The amount of L31F *c* in the membrane correlates with the amount of the *a-c/2-c* fusion protein, or subunit *a.* We believe that formation of a stable priming complex promotes partial oligomerization of *c*L31F in the form of *a*-c_x, or, in the case of the fusion protein, *a-c/2-c*-c_{x-1}, where x = 2 - 10, which protects subunit *c* from proteolytic degradation. In the absence of the priming complex, L31F *c* remains mostly monomeric and undergoes proteolytic degradation, which explains its low amounts in the membrane. This explanation appears to contradict the earlier statement that L31F mutation impairs assembly of the c_{10} ring, however, there is no evidence that the subunit *c* containing the L31F mutation exists in the membrane strictly in monomeric state. In fact, the *c*L31F mutation did not completely abolish ATP driven proton transport (Figure 4.3; Kol *et al.*, 2006), suggesting that the mutant protein retains some oligomerization propensity. Therefore, there are likely multiple oligomeric species of L31F *c*-subunits present in the membrane. The G23D mutant appears to have an even lower oligomerization propensity than L31F. Therefore, *c*G23D would be mostly present in the monomeric form, which is rapidly degraded in the membrane, or it would be integrated into the *a*-c_2 complex and protected from degradation. Indeed, even in the presence of wild type *a,* G23D subunit *c*, was present in the membrane in much lower amounts than either wild type, or L31F mutant (Figure 4.4).

5.3 Validation of the *a-c/2-c* fusion construct as a model protein for studying the dynamic *a/c* interface.

The *a-c/2-c* fusion protein consists of genetically linked subunits *a* and *c*, in theoretically correct transmembrane topology. The *a-c/2-c* fusion protein was generated in an effort to produce a stable, single protein model of the dynamic *a/c* interface for structural studies on the *E. coli* ATP synthase proton channel. We wanted to confirm that the *a-c/2-c* fusion protein adopted a conformation that was representative of the native *a/c* interface to validate it as a model polypeptide for structural analysis of the proton channel. The first piece of evidence suggesting that the *a* and *c* proteins maintained their native folds and contact interface, when fused together, was observed in the membrane incorporation tests. The *a-c/2-c* fusion protein incorporated into the membrane in the absence of native subunit *c*. Membrane insertion of subunit *a* is known to be dependent on the presence of subunit *c.* The cellular machinery that inserts subunit *a* into the membrane was able to recognize the *a* and *c* components of the fusion protein and facilitate membrane incorporation of *a-c/2-c* in the absence of native subunit *c*, demonstrating that the fusion protein was properly folded. This evidence was further supported when we observed that the *a-c/2-c* protein co-purified with the other F_0 subunits in stoichiometric amounts, which showed that it was integrated into an assembled F_0 domain. We also examined the assembly status of the complete F_1F_0 complexes containing either wild type subunit *a* or the *a-c/2-c* fusion and found that *a-c/2-c* fusion does not interfere with F_1F_0 assembly, which further supports the conclusion that *a-c/2-c* adopts the native folds of both the *a* and *c* components.

Assuming the five-helix model of subunit *a,* the *a-c* fusion protein has inverted orientation of the fused subunit *c* TMHs relative to subunit *a.* Consequently, the *a-c* fusion did not insert into the membrane in the absence of the native subunit *c*. However, in the presence of native *c*, the *a* component of the *a-c* construct inserted into the membrane and assembled correctly with the other F_0 subunits, suggesting that the *a* subunit determines the transmembrane orientation of the *a/c* fusion proteins. This, taken together with the membrane incorporation of the *a-c/2-c* construct in the absence of native *c* provides additional supporting evidence for the five-helix model of subunit *a* with the carboxyl terminal end located in the cytoplasm.

The *a-c* construct was able to sustain growth on succinate and showed both ATP driven and passive proton transport activity at levels approximately 50 % the level of wild type ATP synthase. The most likely explanation for this observation is that the *a* subunit of *a-c* interacts with the c_{10} ring normally to allow coupled proton transport. In order for this to occur, the fused *c* subunit would have to be displaced to the periphery of the ring. The fact that the rate of proton transport was half the rate observed in wild type can be attributed to a reduced turnover rate of the *a-c* ATP synthase variant, fewer functional ATPase molecules present in the membrane, or non-specific leaks in the membrane. However, the specific proton transport inhibitor, DCCD, effectively suppressed both ATP driven and passive proton transport in the *a-c* variant, demonstrating that subunit *a* of *a-c* does in fact contribute to a functional proton channel in connection with c_{10}.

Conversely we observed no growth on succinate with the *a-c/2-c* fusion protein and very low passive proton transport when compared to wild type. The question raised at this point was, is the lack of activity due to misfolding of *a-c/2-c*, or is it caused by tethering of the rotor and stator? The *a-c* fusion protein retained the native fold of subunit *a* and was able to facilitate proton transport, indicating that the *a-c/2-c* fusion protein should be able to tolerate one additional helix (*c/2*) without misfolding. Additionally, we had established that *a-c/2-c* did not interfere with assembly of the F_1F_0 complex, suggesting that the fold was native. We hypothesized that because the *a-c/2-c* fusion protein had correct transmembrane topology, the fused *c* subunit could be readily incorporated into the *c*-ring. In this case, the assembled ATP synthase was expected to be inactive, because the rotor would be tethered to the stator by the linker peptide. Both passive and active proton transport were dramatically reduced in the *a-c/2-c* ATP synthase variant, supporting this hypothesis.

In addition to the proton transport assays, we examined the coupling status of the F_1 and F_0 sectors of the *a-c/2-c* ATP synthase variant. The activities of the F_1 and F_0 domains are tightly coupled; a blockage in proton transit through F_0 will cause reduced catalytic activity in the F_1 sector, and vise versa. When the F_1 domain is released from F_0, for example by EDTA treatment, it retains ATPase activity. If the lack of ATP dependent proton translocation observed in the *a-c/2-c* variant was truly caused by an immobilized rotor, we expected to

observe a restoration of ATPase activity when F_1 was released from F_0. If, on the other hand, the rotor was not properly assembled or subunit *a* was misfolded, and the fine coupling between F_0 and F_1 was disrupted, we expected to see comparable F_1 ATPase activity in both bound and free F_1. In the intact membranes containing *a-c/2-c*, the α and β subunits were present at approximately 60 % the level observed in the wild type. However, the specific ATPase activity of the *a-c/2-c* membranes was less than 20 % of the wild type. When F_1 was released from the membranes by EDTA treatment, we observed a restoration of ATPase activity to approximately 50 % of the wild type level. The reduced level of F_1 present in the *a-c/2-c* membranes can be explained in three ways: 1) the introduction of *a-c/2-c* fusion construct in the *atp* operon may cause lower expression of the other F_0 and/or F_1 subunits, 2) the expression level of the *a-c/2-c* fusion protein may be lower than that of wild type subunit *a*, and 3) the F_1F_0 complex containing *a-c/2-c* may not be assembled efficiently in the cell. These data demonstrated that although the amount of *a-c/2-c* containing ATP synthase was approximately 40 % lower than wild type, the majority of F_1F_0 present in the membrane was assembled and coupled. The ATP driven proton transport data, taken together with the F_1-ATPase data described above, demonstrate that the the fused *c* of *a-c/2-c* integrates into the *c*-ring and tethers the rotor to the stator. We then considered the possible geometries of F_0 containing the *a/c* fusion variants (Figure 5.2).

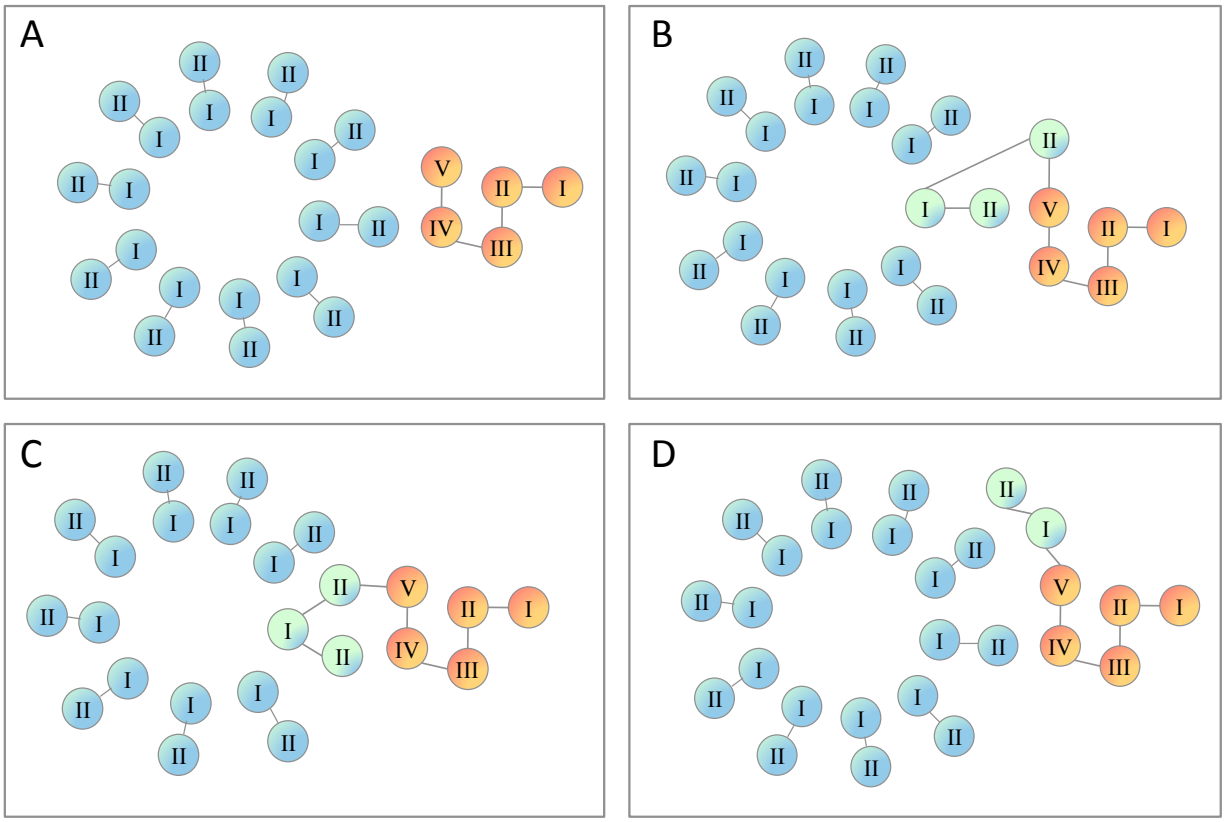

Figure 5.2: Models of *a/c* fusion protein incorporation into F_0. The TMH segments of native subunit *c*, subunit *a*, and the fused subunit *c* are shown in blue, orange and green respectively. A) Wild type F_0, B – C) F_0 containing the *a-c/2-c* fusion protein shown in two possible configurations, and D) F_0 containing the *a-c* fusion protein with fused *c* displaced to the periphery of the ring.

The location of the unpaired *c*TMH-II in the assembled F_0 domain is not clear. Structural modeling experiments published by Fillingame's group indicate that the *c*-ring is inherently flexible and can readily accommodate up to two additional *c* subunits without significantly altering helical contact points (Fillingame and Dmitriev, 2002). Intuitively, the model shown in panel C of Figure 5.2 is the most favorable. The inner ring, which is composed of multiple copies of *c*TMH-I, is tightly packed, while the outer ring (consisting of the *c*TMH-II) is less compressed and can feasibly accommodate the unpaired *c*TMH-II of *a-c/2-c*. This scenario is also favorable because it would maintain the *a* to *c* helical interactions that occur in the native enzyme. However, it is possible that the unpaired *c*TMH-II is displaced to the periphery of the rotor, similarly to the helix arrangement proposed for *a-c*.

The data discussed above demonstrate that the *a-c/2-c* fusion protein adopts a fold which is representative of the interaction between native subunits *a* and *c* in the assembled ATP synthase enzyme. This work validates that the *a-c/2-c* as a suitable model system for structural studies on the dynamic *a/c* interface.

5.4 Letting out the leash: lengthening the tether between *a* and *c/2-c* of *a-c/2-c* did not enhance passive proton transport.

We demonstrated that the *a-c/2-c* fusion protein is incorporated into an assembled ATP synthase complex, and that the fused *c* subunit is integrated into the c_{10} ring. The short linker connecting the fused *a* and *c* subunits restricts movement of the rotor and prevents efficient proton transport. The F_0 domain with the *a-c/2-c* fusion protein incorporated retained a very low level of proton transport activity (section 4.5) relative to the wild type. This low level of activity was DCCD sensitive both in passive and active transport assays. It is possible that the very short linker connecting *a* and *c* of the *a-c/2-c* fusion protein is sufficient to allow limited back and forth oscillation of the *c*-ring relative to the fused ab_2 stator in the passive transport assays. If passive proton transport truly occurs through an oscillatory mechanism it would imply that the 'ratchet' which prevents the rotor from slipping backwards, or moving in the wrong direction, must be located within F_1 rather than F_0. We hypothesized that increasing the length of the linker between subunits *a* and *c* may enhance proton transport though F_0 containing the *a-c/2-c* construct by allowing more back and forth oscillation of the c_{10} ring relative to the fused stator. The results presented in section 4.6 showed that increasing the length of the tether in the *a-c/2-c* fusion protein did not enhance proton translocation relative to the original *a-c/2-c* F_0 domain variant. Although low levels of proton transport were observed in the *a-c/2-c* F_0 variant, activity appears to be independent of the length of the tether. Perhaps the low level of passive proton transport observed in the *a-c/2-c* construct is the maximum capacity attainable through oscillatory mechanisms; or proton transport does not occur through oscillatory mechanisms. Unfortunately, the results we obtained were inconclusive.

5.5 Towards the structure of the proton channel.

We have made some progress toward solving the structure of subunit *a* and the proton channel. We have designed and validated a stable model protein for structural investigations on the dynamic *a/c* interface. Wild type subunit *a* was found to be optimally overexpressed in the C43(DE3) parental strain, while the *a-c/2-c* fusion protein was optimally expressed in C43*recA* cells. We have also developed a novel and efficient method for the purification of both wild type subunit *a* and the *a-c/2-c* fusion protein. We have achieved greater than 95 % purity with wild type subunit *a* and greater than 80 % purity with the *a-c/2-c* fusion protein. We have conducted primary NMR experiments using subunit *a* and the fusion protein. Primary crystallization screens have been conducted with the *a-c/2-c* fusion protein and have yielded promising results. Finally, we have successfully crystallized wild type subunit *a* in multiple crystal forms for X-ray crystallographic studies.

NMR analysis of wild type subunit a and the a-c/2-c fusion protein

NMR can be used to determine protein structures as well as study the functional dynamics of proteins. Extensive NMR studies have been conducted on subunit *a* purified in a mixed polarity solvent (4:4:1, chloroform : methanol : water) (Dmitriev *et al.*, 2004). Dmitriev and co-authors were able to obtain high quality NMR spectral data and make nearly complete backbone amide chemical shift assignments for subunit *a* (Figure 5.3). The effects of mixed polarity solvents on membrane proteins are unknown and spectral data obtained from subunit *a* purified in mixed organic solvents may not be biologically relevant. Therefore, NMR investigation of subunit *a* purified in detergent micelles that closely mimic the environment of the lipid membrane was necessary. The NMR spectrum shown in Figure 5.3 serves as a benchmark for comparing the quality of spectral data collected from subunit *a* purified in detergent.

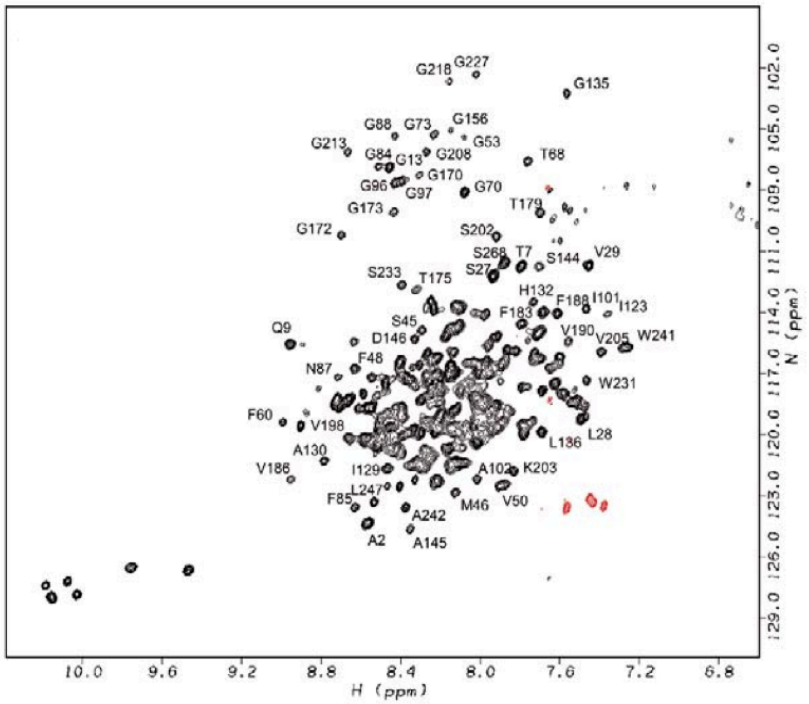

Figure 5.3: TROSY spectrum of subunit *a* purified in chloroform, methanol and water (4:4:1). Each peak in this spectrum corresponds to a single backbone amide group or side chain amide group from arginine and tryptophan. The chemical shift assignments are indicated. [Image taken from (Dmitriev, 2004a)]. Reprinted with permission from J. Biol. NMR.

The HSQC spectra obtained from subunit *a* purified in LMPG micelles did not have sufficient spectral resolution for structure determination (Figure 4.21). Detergent screening and optimization of NMR experiments did not improve the resolution. We hypothesized that the use of harsh detergents during isolation of the F_0 complex may have caused partial misfolding of the protein which contributed to the poor spectral resolution. However, previous experiments have shown that preparations of purified subunits *a*, *b*, and *c* using these same detergents could be reconstituted into proteoliposomes to generate a functional proton channel (Altendorf *et al.*, 2000; Schneider and Altendorf, 1987), suggesting that any denaturing effects are reversible. We developed a second novel purification procedure to isolate subunit *a* using milder detergents. The method developed by Laubinger and Dimroth for isolation of ATP synthase from *P. modestum* (Laubinger and Dimroth, 1988), under relatively mild conditions, was adapted for *E. coli* ATP synthase (Haji and Dmitriev, unpublished data). This alternate purification procedure did not contribute any significant improvement to spectral resolution (Fig 4.22). Molecular weight plays a role in spectral resolution. The gel filtration experiment

showed that subunit *a* in detergent micelles is approximately 48 kDa in size, which is significantly larger than the calculated molecular weight of subunit *a* alone (approximately 31 kDa). Although it is possible that the poor spectral resolution is caused by misfolding of subunit *a* it is also possible that the large size of the protein – detergent complex results in poor resolution. It is also possible that the optimal sample conditions and NMR experimental conditions were not found in this study and that resolution may still be improved under different conditions.

The resolution in the arginine side chain region of the HSQC spectrum was sufficient to allow assignment of the arginine 210 side chain chemical shift. Assignment of the R210 side chain is important because the chemical shift is very sensitive to the chemical environment. Therefore, assignment of R210 provides an excellent reporter group for functional studies, including determination of the pKa of R210 and characterization of the binding of novel antibiotic compounds to the proton channel.

The *a-c/2-c* fusion protein exceeds the current size restrictions for NMR and was designed for X-Ray crystallographic structure determination. However, we hypothesized that the arginine side chain region of the *a-c/2-c* spectra may have had sufficiently high resolution to conduct functional studies on R210 in an environment that mimics the proton channel. HSQC spectra were recorded with purified *a-c/2-c*, but the arginine side chain regions of the spectra were poorly resolved. There were two main factors contributing to poor resolution in the arginine side chain region. The size of the *a-c/2-c* construct is considerably larger than wild type subunit *a*, which potentially reduces resolution. Also, wild type subunit *a* contains four arginine side chain residues while the *a-c/2-c* fusion protein contains eight, which contributes to signal overlap in the *a-c/2-c* spectra.

Subunit *a*'s arginine 210 and subunit *c*'s aspartic acid 61 are thought to form a salt bridge, which is expected to cause the pKa of arginine 210 to be uncharacteristically low. We hypothesized that it may have been possible to resolve the R210 peak from the other arginine side chain peaks in the *a-c/2-c* spectra based on it's low pKa. HSQC spectra were recorded at various pH values in an effort to perturb the R210 side chain amide peak. Unfortunately, pH

titration did not have a significant impact on the chemical shift of the R210 side chain, which eliminated the option of using the *a-c/2-c* fusion protein to study the functional dynamics of R210 in the environment of the proton channel. For future studies it may be possible to examine this interaction by recording HSQC spectra with ^{15}N labeled wild type subunit *a*, titrated with unlabeled (NMR invisible) wild type subunit *c*. If the two subunits interact in a way that is representative of their interaction in the native enzyme this type of study could provide valuable information on role of R210 in proton transport.

Crystallography

Monodisperse protein samples have a higher propensity towards crystallization than polydisperse samples. DLS and size exclusion chromatography are commonly used methods for determination of protein aggregation state. Membrane proteins solubilized in detergent micelles are not ideal for DLS analysis because micellar dynamics can cause changes in particle size and lead to broad DLS peaks. Subunit *a* samples showed one broad peak with an approximate hydrodynamic radius of 2.6 nm corresponding to 99 % mass in the DLS analysis. Although the peak was broad compared to a monodisperse soluble protein, the absence of higher order peaks indicated that purified subunit *a* was monomeric. The gel filtration experiment supported this conclusion: subunit *a* eluted in one sharp peak, which corresponded to the estimated molecular weight of 48 kDa, the expected size for monomeric subunit *a* in LMPG micelles. Both the DLS and gel filtration data demonstrate that purified subunit *a* samples are monomeric, although micellar dynamics create a range of micelle sizes.

We have conducted extensive crystallization screening with wild type subunit *a* and obtained three distinct subunit *a* crystal forms. The diffraction quality of the crystals obtained from LCP screening was poor, with diffraction in the range of 30 Å. A second crystal form was obtained during the refined vapor diffusion screening and the resultant diffraction resolution was improved to a maximum resolution of 14 Å. However, the improved diffraction resolution was still not sufficient for high resolution structure determination. The successful crystallization of subunit *a* constitutes a significant step toward determining the structure of the proton channel, and efforts toward improving diffraction resolution will be continued in the

future. Many hurdles remain, including optimization of crystal quality to achieve diffraction resolution better than 4 Å, phase determination, and structural modeling.

The *a-c/2-c* construct has presented more challenges than subunit *a*. The yield of purified *a-c/2-c* was very low in comparison to subunit *a*. Samples of purified *a-c/2-c* had poor stability and formed aggregates in solution. Subunit *c* is a naturally oligomeric protein and interactions between the fused *c* subunits may have contributed to the oligomerization of the purified *a-c/2-c* protein samples. We hypothesized that if the *c*L31F point mutation, was introduced into the fused *c* subunit of *a-c/2-c*, oligomerization may not occur in the purified samples. However, the introduction of the *c*L31F mutation did not alleviate the aggregation problem. The L31F mutant did not fully abolish proton transport activity when co-expressed with wild type subunit *a* (Figure 4.3). Therefore, it was possible that the L31F mutant did not completely inhibit oligomerization of subunit *c*. The *c*G23D mutation may provide more effective suppression of oligomerization of the purified *a-c/2-c* samples, in future studies. The *a-c/2-c* fusion protein could only be isolated at 0.17 mg / L of cell culture, which was prohibitive to in house crystal screening trials. We also worked to improve the yield of the *a-c/2-c* fusion protein to provide more material for crystal screens. Several plasmids containing different combinations of F_0 subunits, under the control of the PBAD promoter, were generated in an effort to overcome poor expression (section 4.10). Unfortunately, each inducible expression system failed to express *a-c/2-c* at detectable levels. In future studies a more suitable inducible vector that can accommodate the entire *atp* operon may provide better yields.

6 Conclusions and Future Work.

6.1 Conclusions.

We have successfully generated and validated a stable, single polypeptide model of the dynamic *a/c* interface for structural studies on the proton channel. We have demonstrated that monomeric subunit *c* chaperones membrane insertion of subunit *a* and primes formation of the *a*-c_{10} complex. In 2011, we published our work demonstrating that the *a-c/2-c* fusion protein provides a suitable platform for structure studies on the proton channel, as well as the work showing that monomeric *c* facilitates membrane incorporation of subunit *a*, in the Journal of Biological Chemistry (Pierson *et al.*, 2011). Our studies with the *c*-ring assembly mutants and the *a/c* fusion proteins have shown that the mechanisms that govern membrane insertion of subunits *a* and *c* are linked in a complex manner. A novel purification method for wild type subunit *a* was developed; purity exceeded 95 % which is excellent for structural studies. The purification procedure developed for subunit *a* can also be used to isolate the *a-c/2-c* fusion protein, although at lower purity. Wild type subunit *a* was successfully crystallized during our studies, which constitutes a major step toward determining the structure of the proton channel. In 2012, the procedure for purification of wild type subunit *a*, and the preliminary NMR data were published in Protein Science (Uhlemann *et al.*, 2012).

6.2 Future Work.

The ultimate goal for future studies is to determine the high resolution structure of the proton channel of *E. coli* ATP synthase. The *a-c/2-c* fusion protein is a very attractive target for structure studies, because it provides a stable snapshot of the *a*-c_{10} interaction. Currently, the relatively low purity and poor yield constitute major hurdles toward structure studies with the *a-c/2-c* protein. Overexpression of *a-c/2-c* should be optimized to improve the yield of pure protein. Also, the purification procedure should be optimized to enhance the purity of *a-c/2-c* samples for crystallization trials. The G23D mutation should be introduced into the fused *c* subunit of *a-c/2-c* to prevent protein oligomerization in the purified samples; G23D has a stronger effect than L31F and may be more effective. When the sufficient the purity and yield are achieved , preliminary and refined crystallization screening should be conducted.

Optimal overexpression and purification of the wild type subunit *a* was achieved during this study, however, more work needs to be done to optimize crystallization conditions to enhance diffraction resolution. This should be done concurrently with NMR experiments aimed at determining the global fold of subunit *a* through selective isotopic labeling. Both the crystal structure and the global fold of subunit *a* will be significant contributions to the field. Functional NMR experiments to determine the pKa of subunit *a*'s R210 residue should be conducted to confirm the *a*R210 – *c*D61 salt bridge. Additionally, this should be complemented with pKa measurements in an environment which mimics proton channel. The *a-c/2-c* fusion protein mimics the proton channel, but was not suitable for such measurements. However, NMR investigation of the interaction between isolated subunits *a* and *c* may help to reconstruct the chemical environment of R210 in the proton channel for analysis of the *a*R210 – *c*D61 interaction.

7 Appendix-I

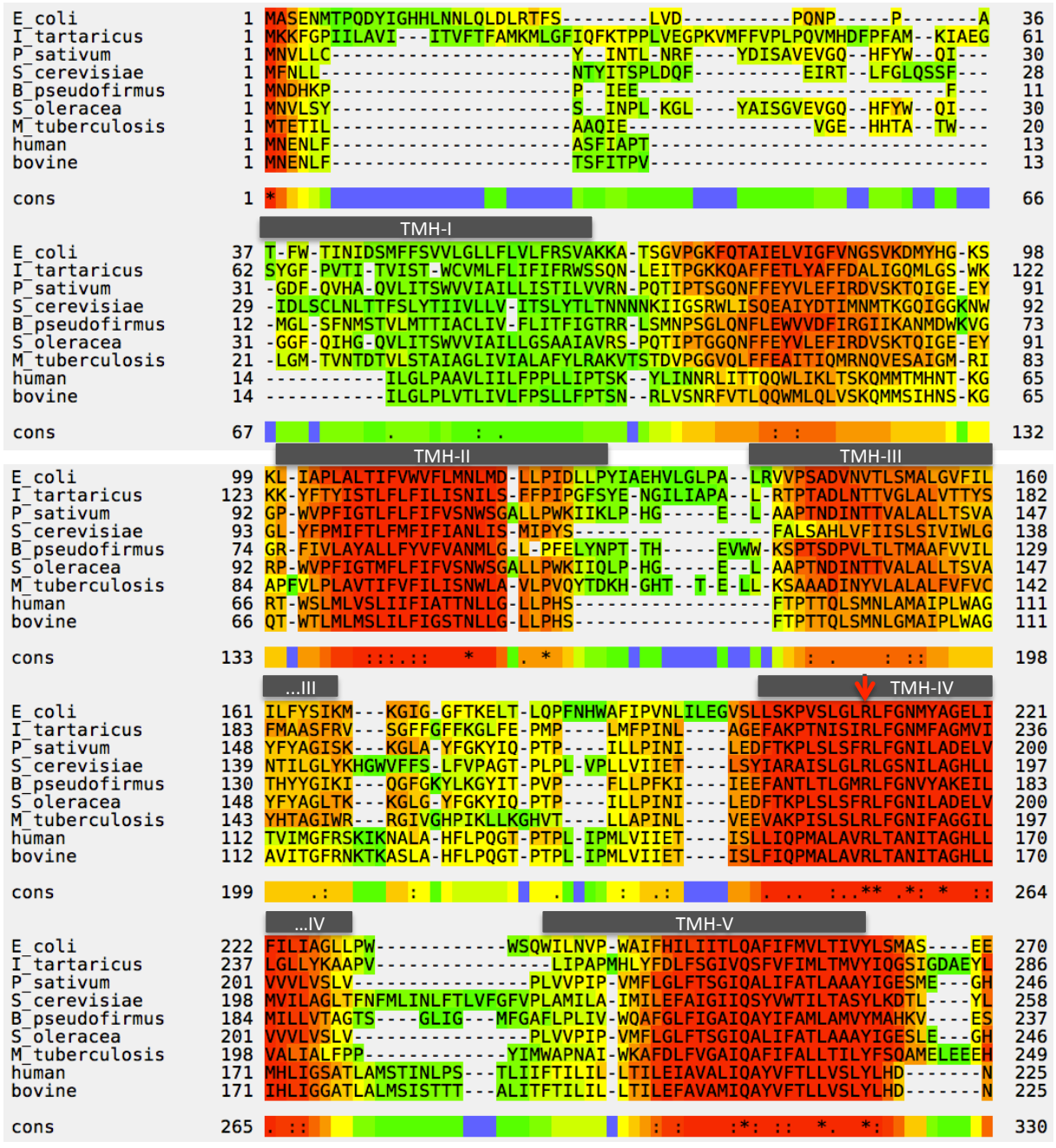

Figure 7.1: Multiple sequence alignment of ATP synthase subunit *a* from various species. Residues colored with blue and green align poorly. Residues colored in orange and yellow align well. Residues colored in red are highly conserved. TMH segments are indicated above each segment of the sequence alignment. The universally conserved arginine residue is indicated with the red arrow. Sequence alignment was conducted using the T-Coffee server (Notredame *et al*., 2000).

8 References.

Abrahams, J.P., Leslie, A.G., Lutter, R., and Walker, J.E. (1994). Structure at 2.8 Å resolution of F_1-ATPase from bovine heart mitochondria. Nature *370*, 621-628.

Ackerman, S.H., Martin, J., and Tzagoloff, A. (1992). Characterization of ATP11 and detection of the encoded protein in mitochondria of *Saccharomyces cerevisiae*. J. Biol. Chem *267*, 7386-7394.

Adolfsen, R., and Moudrianakis, E.N. (1976). Binding of adenine nucleotides to the purified 13S coupling factor of bacterial oxidative phosphorylation. Arch. Biochem. Biophys. *172*, 425-433.

Akiyama, Y. (2002). Proton-motive force stimulates the proteolytic activity of FtsH, a membrane-bound ATP-dependent protease in *Escherichia coli*. Proc. Natl. Acad. Sci. U. S. A. *99*, 8066-8071.

Akiyama, Y., Kihara, A., and Ito, K. (1996). Subunit *a* of proton ATPase F_0 sector is a substrate of the FtsH protease in *Escherichia coli*. FEBS Lett. *399*, 26-28.

Aksimentiev, A., Balabin, I.A., Fillingame, R.H., and Schulten, K. (2004). Insights into the molecular mechanism of rotation in the F_0 sector of ATP synthase. Biophys. J. *86*, 1332-1344.

Allchin, D. (1997). A Twentieth-Century Phlogiston: Constructing error and differentiating domains. Perspectives on Science, 81 - 127.

Altendorf, K., Stalz, W., Greie, J., and Deckers-Hebestreit, G. (2000). Structure and function of the F_0 complex of the ATP synthase from *Escherichia coli*. J. Exp. Biol. *203*, 19-28.

Andries, K., Verhasselt, P., Guillemont, J., Gohlmann, H.W., Neefs, J.M., Winkler, H., Van Gestel, J., Timmerman, P., Zhu, M., Lee, E., Williams, P., de Chaffoy, D., Huitric, E., Hoffner, S., Cambau, E., Truffot-Pernot, C., Lounis, N., and Jarlier, V. (2005). A diarylquinoline drug active on the ATP synthase of *Mycobacterium tuberculosis.* Science *307*, 223-227.

Angevine, C.M., and Fillingame, R.H. (2003). Aqueous access channels in subunit *a* of rotary ATP synthase. J. Biol. Chem. *278*, 6066-6074.

Angevine, C.M., Herold, K.A., and Fillingame, R.H. (2003). Aqueous access pathways in subunit *a* of rotary ATP synthase extend to both sides of the membrane. Proc. Natl. Acad. Sci. U. S. A. *100*, 13179-13183.

Angevine, C.M., Herold, K.A., Vincent, O.D., and Fillingame, R.H. (2007). Aqueous access pathways in ATP synthase subunit *a*. Reactivity of cysteine substituted into transmembrane helices 1, 3, and 5. J. Biol. Chem *282*, 9001-9007.

Arechaga, I., Butler, P.J., and Walker, J.E. (2002). Self-assembly of ATP synthase subunit *c* rings. FEBS Lett. *515*, 189-193.

Aris, J.P., Klionsky, D.J., and Simoni, R.D. (1985). The F_0 subunits of the *Escherichia coli*

F_1F_0-ATP synthase are sufficient to form a functional proton pore. J. Biol. Chem *260*, 11207-11215.

Aris, J.P., and Simoni, R.D. (1983). Cross-linking and labeling of the *Escherichia coli* F_1F_0-ATP synthase reveal a compact hydrophilic portion of F_0 close to an F_1 catalytic subunit. J. Biol. Chem. *258*, 14599-14609.

Arora, A., and Tamm, L.K. (2001). Biophysical approaches to membrane protein structure determination. Curr. Opin. Struct. Biol. *11*, 540-547.

Baracca, A., Barogi, S., Carelli, V., Lenaz, G., and Solaini, G. (2000). Catalytic activities of mitochondrial ATP synthase in patients with mitochondrial DNA T8993G mutation in the ATPase 6 gene encoding subunit *a*. J. Biol. Chem. *275*, 4177-4182.

Bergfors, T.M. (1999). Protein crystallization : techniques, strategies, and tips : a laboratory manual (La Jolla, Calif., International University Line).

Birkenhager, R., Hoppert, M., Deckers-Hebestreit, G., Mayer, F., and Altendorf, K. (1995). The F_0 complex of the *Escherichia coli* ATP synthase. Investigation by electron spectroscopic imaging and immunoelectron microscopy. Eur. J. Biochem. *230*, 58-67.

Bowie, J.U. (2001). Stabilizing membrane proteins. Curr. Opin. Struct. Biol. *11*, 397-402.

Bowman, S., Ackerman, S.H., Griffiths, D.E., and Tzagoloff, A. (1991). Characterization of ATP12, a yeast nuclear gene required for the assembly of the mitochondrial F_1-ATPase. J. Biol. Chem. *266*, 7517-7523.

Boyer, P.D. (1963). Phosphohistidine. Science. *141*, 1147-1153.

Boyer, P.D. (1988). Bioenergetic coupling to protonmotive force: should we be considering hydronium ion coordination and not group protonation? Trends Biochem. Sci. *13*, 5-7.

Boyer, P.D. (1993). The binding change mechanism for ATP synthase--some probabilities and possibilities. Biochim. Biophys. Acta. *1140*, 215-250.

Boyer, P.D., Cross, R.L., and Momsen, W. (1973). A new concept for energy coupling in oxidative phosphorylation based on a molecular explanation of the oxygen exchange reactions. Proc. Natl. Acad. Sci. U. S. A. *70*, 2837-2839.

Boyer, P.D., Falcone, A.B., and Harrison, W.H. (1954). Reversal and mechanism of oxidative phosphorylation. Nature. *174*, 401-402.

Boyer, P.D.L., C. P., Schatz, G., and Ernster, L, eds) (1979). The binding-change mechanism of ATP synthesis. Membrane Bioenergetics *Addison-Wesley, Reading, Massachusetts*, 461-479.

Brusilow, W.S. (1987). Proton leakiness caused by cloned genes for the F_0 sector of the proton-translocating ATPase of *Escherichia coli*: requirement for F_1 genes. J. Bacteriol. *169*, 4984-4990.

Caffrey, M., and Cherezov, V. (2009). Crystallizing membrane proteins using lipidic mesophases. Nat Protoc. *4*, 706-731.

Cain, B.D. (2000). Mutagenic analysis of the F_0 stator subunits. J. Bioenerg. Biomembr. *32*, 365-371.

Cain, B.D., and Simoni, R.D. (1988). Interaction between Glu-219 and His-245 within the a subunit of F_1F_0-ATPase in *Escherichia coli*. J. Biol. Chem. *263*, 6606-6612.

Chen, K., Kurgan, L., and Rahbari, M. (2007). Prediction of protein crystallization using collocation of amino acid pairs. Biochem. Biophys. Res. Commun. *355*, 764-769.

Chintakrindi, A., D'Souza, C., and Kanyalkar, M. (2012). Rational development of neuraminidase inhibitor as novel anti-flu drug. Mini Rev Med Chem. *12*, 1273-1281

Clunes, M.T., and Boucher, R.C. (2007). Cystic Fibrosis: The mechanisms of pathogenesis of an inherited lung disorder. Drug Discov. Today. Dis. Mech. *4*, 63-72.

Cox, G.B., Downie, J.A., Langman, L., Senior, A.E., Ash, G., Fayle, D.R., and Gibson, F. (1981). Assembly of the adenosine triphosphatase complex in *Escherichia coli*: assembly of F_0 is dependent on the formation of specific F_1 subunits. J. Bacteriol. *148*, 30-42.

Dagert, M., and Ehlrich, S. (1979). Prolonged incubation in calcium chloride improves the competence of *Escherichia coli* cells. Gene. *6*, 23-28.

De Meirleir, L., Seneca, S., Lissens, W., Schoentjes, E., and Desprechins, B. (1995). Bilateral striatal necrosis with a novel point mutation in the mitochondrial ATPase 6 gene. Pediatr. Neurol. *13*, 242-246.

de Vries, D.D., van Engelen, B.G., Gabreels, F.J., Ruitenbeek, W., and van Oost, B.A. (1993). A second missense mutation in the mitochondrial ATPase 6 gene in Leigh's syndrome. Ann. Neurol. *34*, 410-412.

Derewenda, Z.S. (2004). Rational protein crystallization by mutational surface engineering. Structure. *12*, 529-535.

De Rizzo, P., Bi, Y., Dunn, S., and Shilton, B. (2002). The "second stalk" of *Escherichia coli* ATP synthase: structure of the isolated dimerization domain. Biochem. *41*, 6875-6884.

DiMauro, S. (2004). Mitochondrial diseases. Biochim. Biophys. Acta *1658*, 80-88.

DiMauro, S. (2007). Mitochondrial DNA medicine. Biosci. Rep. *27*, 5-9.

Dimroth, P., Matthey, U., and Kaim, G. (2000). Critical evaluation of the one-versus the two-channel model for the operation of the ATP synthase's F_0 motor. Biochim. Biophys. Acta. *1459*, 506-513.

Dmitriev, O., Abildgaard, F., Markley, J., Fillingame, R. (2004a). Letter to the Editor: Backbone ^{1}H, ^{15}N and ^{13}C assignments for the subunit *a* of the *E. coli* ATP synthase J. Biomol.

NMR. *29*, 439-440.

Dmitriev, O., Altendorf, K., Fillingame, R. (2004b). Subunit *a* of the *E. coli* ATP synthase: reconstitution and high resolution NMR with protein purified in a mixed polarity solvent FEBS Lett. *556*, 35-38.

Dmitriev, O., Jones, P.C., Jiang, W., and Fillingame, R.H. (1999a). Structure of the membrane domain of subunit *b* of the *Escherichia coli* F_0F_1 ATP synthase. J. Biol. Chem. *274*, 15598-15604.

Dmitriev, O.Y., Jones, P.C., and Fillingame, R.H. (1999b). Structure of the subunit *c* oligomer in the F_1F_0 ATP synthase: model derived from solution structure of the monomer and cross-linking in the native enzyme. Proc. Natl. Acad. Sci. *96*, 7785-7790.

Dmitriev, O.Y., Abildgaard, F., Markley, J.L., and Fillingame, R.H. (2004). Backbone ^{1}H, ^{15}N and ^{13}C assignments for the subunit *a* of the *E. coli* ATP synthase. J. Biomol. NMR. *29*, 439-440.

Dmitriev, O.Y., Freedman, K.H., Hermolin, J., and Fillingame, R.H. (2008). Interaction of transmembrane helices in ATP synthase subunit *a* in solution as revealed by spin label difference NMR. Biochim. Biophys. Acta. *1777*, 227-237.

Duncan, T.M., Bulygin, V.V., Zhou, Y., Hutcheon, M.L., and Cross, R.L. (1995). Rotation of subunits during catalysis by *Escherichia coli* F_1-ATPase. Proc. Natl. Acad. Sci. U. S. A. *92*, 10964-10968.

Dunn, S.D., and Chandler, J. (1998). Characterization of a $b_2\delta$ complex from *Escherichia coli* ATP synthase. J. Biol. Chem. *273*, 8646-8651.

Duser, M.G., Bi, Y., Zarrabi, N., Dunn, S.D., and Borsch, M. (2008). The proton-translocating a subunit of F_0F_1-ATP synthase is allocated asymmetrically to the peripheral stalk. J. Biol. Chem. *283*, 33602-33610.

Ekman, P., and Jager, O. (1993). Quantification of subnanomolar amounts of phosphate bound to seryl and threonyl residues in phosphoproteins using alkaline hydrolysis and malachite green. Anal. Biochem. *214*, 138-141.

Elston, T., Wang, H., and Oster, G. (1998). Energy transduction in ATP synthase. Nature *391*, 510-513.

Engelhardt, W. (1932). Correlation between respiration and conversion of prophosphate in avian erythrocytes. Biochem. Z. *251*, 343-368.

Evans, J.N.S. (1995). Biomolecular NMR spectroscopy (Oxford ; New York, Oxford University Press).

Fagerberg, L., Jonasson, K., von Heijne, G., Uhlen, M., and Berglund, L. (2010). Prediction of the human membrane proteome. Proteomics. *10*, 1141-1149.

Faham, S., and Bowie, J.U. (2002). Bicelle crystallization: a new method for crystallizing membrane proteins yields a monomeric bacteriorhodopsin structure. J. Mol. Biol. *316*, 1-6.

Fillingame, R.H., Angevine, C.M., and Dmitriev, O.Y. (2002). Coupling proton movements to *c*-ring rotation in F_1F_0 ATP synthase: aqueous access channels and helix rotations at the *a*-*c* interface. Biochim. Biophys. Acta. *1555*, 29-36.

Fillingame, R.H., Angevine, C.M., and Dmitriev, O.Y. (2003). Mechanics of coupling proton movements to *c*-ring rotation in ATP synthase. FEBS Lett. *555*, 29-34.

Fillingame, R.H., and Dmitriev, O.Y. (2002). Structural model of the transmembrane F_0 rotary sector of H^+-transporting ATP synthase derived by solution NMR and intersubunit cross-linking in situ. Biochim. Biophys. Acta. *1565*, 232-245.

Fillingame, R.H., Jiang, W., Dmitriev, O.Y., and Jones, P.C. (2000). Structural interpretations of F_0 rotary function in the *Escherichia coli* F_1F_0 ATP synthase. Biochim. Biophys. Acta. *1458*, 387-403.

Flynn, D.C. (2001). Adaptor proteins. Oncogene. *20*, 6270-6272.

Foster, J.W. (2004). *Escherichia coli* acid resistance: tales of an amateur acidophile. Nat Rev Microbiol *2*, 898-907.

Fraga, D., Hermolin, J., and Fillingame, R.H. (1994). Transmembrane helix-helix interactions in F_0 suggested by suppressor mutations to Ala24-->Asp/Asp61-->Gly mutant of ATP synthase subunit. J. Biol. Chem. *269*, 2562-2567.

Garbuzynskiy, S.O., Melnik, B.S., Lobanov, M.Y., Finkelstein, A.V., and Galzitskaya, O.V. (2005). Comparison of X-ray and NMR structures: is there a systematic difference in residue contacts between X-ray- and NMR-resolved protein structures? Proteins. *60*, 139-147.

Gautier, A., Mott, H.R., Bostock, M.J., Kirkpatrick, J.P., and Nietlispach, D. (2010). Structure determination of the seven-helix transmembrane receptor sensory rhodopsin II by solution NMR spectroscopy. Nat. Struct. Mol. Biol. *17*, 768-774.

Gibbons, C., Montgomery, M., Leslie, A., and Walker, J. (2000). The structure of the central stalk in bovine F_1-ATPase at 2.4 Å resolution. Nat. Struct. Biol. *7*, 1055-1061.

Girvin, M.E., Rastogi, V.K., Abildgaard, F., Markley, J.L., and Fillingame, R.H. (1998). Solution structure of the transmembrane H^+-transporting subunit *c* of the F_1F_0 ATP synthase. Biochemistry (Mosc). *37*, 8817-8824.

Goldschmidt, L., Cooper, D.R., Derewenda, Z.S., and Eisenberg, D. (2007). Toward rational protein crystallization: A Web server for the design of crystallizable protein variants. Prot. Sci. *16*, 1569-1576.

Greie, J.C., Deckers-Hebestreit, G., and Altendorf, K. (2000). Subunit organization of the stator part of the F_0 complex from *Escherichia coli* ATP synthase. J. Bioenerg. Biomembr. *32*, 357-

364.

Hakulinen, J.K., Klyszejko, A.L., Hoffmann, J., Eckhardt-Strelau, L., Brutschy, B., Vonck, J., and Meier, T. (2012). Structural study on the architecture of the bacterial ATP synthase F_0 motor. Proc. Natl. Acad. Sci. U. S. A. *109*, E2050-2056.

Harris, D.A., Rosing, J., van de Stadt, R.J., and Slater, E.C. (1973). Tight binding of adenine nucleotides to beef-heart mitochondrial ATPase. Biochim. Biophys. Acta. *314*, 149-153.

Hartzog, P.E., and Cain, B.D. (1994). Second-site suppressor mutations at glycine 218 and histidine 245 in the alpha subunit of F_1F_0 ATP synthase in *Escherichia coli.* J. Biol. Chem. *269*, 32313-32317.

Hasurath, A., Capaldi, R., and Matthews, B. (2001). The conformation of the ε - and γ - subunits within the *Escherichia coli* F_1 ATPase. J. Biol. Chem. *276*, 47227-47232.

Hatch, L.P., Cox, G.B., and Howitt, S.M. (1995). The essential arginine residue at position 210 in the α subunit of the *Escherichia coli* ATP synthase can be transferred to position 252 with partial retention of activity. J. Biol. Chem. *270*, 29407-29412.

Hermolin, J., and Fillingame, R.H. (1995). Assembly of F_0 sector of *Escherichia coli* H^+ ATP synthase. Interdependence of subunit insertion into the membrane. J. Biol. Chem. *270*, 2815-2817.

Hermolin, J., Gallant, J., and Fillingame, R.H. (1983). Topology, organization, and function of the ψ subunit in the F_0 sector of the H^+-ATPase of *Escherichia coli*. J. Biol. Chem *258*, 14550-14555.

Hiroaki, H., Umetsu, Y., Nabeshima, Y., Hoshi, M., and Kohda, D. (2011). A simplified recipe for assigning amide NMR signals using combinatorial ^{14}N amino acid inverse-labeling. J. Struct. Funct. Genomics. *12*, 167-174.

Howitt, S.M., Lightowlers, R.N., Gibson, F., and Cox, G.B. (1990). Mutational analysis of the function of the *a*-subunit of the F_0F_1-ATPase of *Escherichia coli.* Biochim. Biophys. Acta. *1015*, 264-268.

Hubbell, W.L., Gross, A., Langen, R., and Lietzow, M.A. (1998). Recent advances in site-directed spin labeling of proteins. Curr. Opin. Struct. Biol. *8*, 649-656.

Huitric, E., Verhasselt, P., Koul, A., Andries, K., Hoffner, S., and Andersson, D.I. (2010). Rates and mechanisms of resistance development in Mycobacterium tuberculosis to a novel diarylquinoline ATP synthase inhibitor. Antimicrob. Agents Chemother. *54*, 1022-1028.

Ishmukhametov, R.R., Pond, J.B., Al-Huqail, A., Galkin, M.A., and Vik, S.B. (2008). ATP synthesis without R210 of subunit *a* in the *Escherichia coli* ATP synthase. Biochim. Biophys. Acta. *1777*, 32-38.

Jans, D.A., Fimmel, A.L., Langman, L., James, L.B., Downie, J.A., Senior, A.E., Ash, G.R.,

Gibson, F., and Cox, G.B. (1983). Mutations in the uncE gene affecting assembly of the *c*-subunit of the adenosine triphosphatase of *Escherichia coli.* Biochem. J. *211*, 717-726.

Jia, Y., and Liu, X.Y. (2006). From surface self-assembly to crystallization: prediction of protein crystallization conditions. J. Phys. Chem. B. *110*, 6949-6955.

Jiang, W., and Fillingame, R.H. (1998). Interacting helical faces of subunits *a* and *c* in the F_1F_0ATP synthase of *Escherichia coli* defined by disulfide cross-linking. Proc. Natl. Acad. Sci. U. S. A. *95*, 6607-6612.

Jiang, W., Hermolin, J., and Fillingame, R.H. (2001). The preferred stoichiometry of *c* subunits in the rotary motor sector of *Escherichia coli* ATP synthase is 10. Proc. Natl. Acad. Sci. *98*, 4966-4971.

Jones, P.C., and Fillingame, R.H. (1998). Genetic fusions of subunit *c* in the F_0 sector of H^+-transporting ATP synthase. Functional dimers and trimers and determination of stoichiometry by cross-linking analysis. J. Biol. Chem. *273*, 29701-29705.

Jones, P.C., Hermolin, J., Jiang, W., and Fillingame, R.H. (2000). Insights into the rotary catalytic mechanism of F_0F_1 ATP synthase from the cross-linking of subunits *b* and *c* in the *Escherichia coli* enzyme. J. Biol. Chem. *275*, 31340-31346.

Jones, P.C., Jiang, W., and Fillingame, R.H. (1998). Arrangement of the multicopy H^+-translocating subunit *c* in the membrane sector of the *Escherichia coli* F_1F_0 ATP synthase. J. Biol. Chem. *273*, 17178-17185.

Judge, P.J., and Watts, A. (2011). Recent contributions from solid-state NMR to the understanding of membrane protein structure and function. Curr. Opin. Chem. Biol. *15*, 690-695.

Junge, W., Lill, H., and Engelbrecht, S. (1997). ATP synthase: an electrochemical transducer with rotatory mechanics. Trends Biochem. Sci. *22*, 420-423.

Kagawa, Y., and Racker, E. (1966). Partial resolution of the enzymes catalyzing oxidative phosphorylation. 8. Properties of a factor conferring oligomycin sensitivity on mitochondrial adenosine triphosphatase. J. Biol. Chem. *241*, 2461-2466.

Katona, G., Andreasson, U., Landau, E.M., Andreasson, L.E., and Neutze, R. (2003). Lipidic cubic phase crystal structure of the photosynthetic reaction centre from *Rhodobacter sphaeroides* at 2.35Å resolution. J. Mol. Biol. *331*, 681-692.

Kayalar, C., Rosing, J., and Boyer, P.D. (1977). An alternating site sequence for oxidative phosphorylation suggested by measurement of substrate binding patterns and exchange reaction inhibitions. J. Biol. Chem. *252*, 2486-2491.

Ke, S.H., and Madison, E.L. (1997). Rapid and efficient site-directed mutagenesis by single-tube 'megaprimer' PCR method. Nucleic Acids Res. *25*, 3371-3372.

Kim, D.E., Chivian, D., and Baker, D. (2004). Protein structure prediction and analysis using the Robetta server. Nucleic Acids Res. *32*, W526-531.

Kol, S., Nouwen, N., and Driessen, A.J. (2008). The charge distribution in the cytoplasmic loop of subunit *c* of the F_1F_0 ATPase is a determinant for YidC targeting. J. Biol. Chem. *283*, 9871-9877.

Kol, S., Turrell, B.R., de Keyzer, J., van der Laan, M., Nouwen, N., and Driessen, A.J. (2006). YidC-mediated membrane insertion of assembly mutants of subunit *c* of the F_1F_0 ATPase. J. Biol. Chem. *281*, 29762-29768.

Krebstakies, T., Zimmermann, B., Graber, P., Altendorf, K., Borsch, M., and Greie, J.C. (2005). Both rotor and stator subunits are necessary for efficient binding of F_1 to F_0 in functionally assembled *Escherichia coli* ATP synthase. J. Biol. Chem. *280*, 33338-33345.

Kreil, G., and Boyer, P.D. (1964). Detection of bound phosphohistidine in *E. coli* succinate thiokinase. Biochem. Biophys. Res. Commun. *16*, 551-555.

Kruger-Koplin, R., Sorgen, P., Kruger-Koplin, S., Rivera-Torres, I., Cahill, S., Hicks, D., Grinius, L., Kulwich, T., and Girvin, M. (2004). An evaluation of detergents for NMR structural studies of membrane proteins. J. Biol. NMR. *28*, 43-57.

Kucharczyk, R., Giraud, M.F., Brethes, D., Wysocka-Kapcinska, M., Ezkurdia, N., Salin, B., Velours, J., Camougrand, N., Haraux, F., and di Rago, J.P. (2012). Defining the pathogenesis of human mtDNA mutations using a yeast model: The case of T8851C. Int. J. Biochem. cell biol. *45*, 130-140.

Kucharczyk, R., Zick, M., Bietenhader, M., Rak, M., Couplan, E., Blondel, M., Caubet, S.D., and di Rago, J.P. (2009). Mitochondrial ATP synthase disorders: molecular mechanisms and the quest for curative therapeutic approaches. Biochim. Biophys. Acta *1793*, 186-199.

Kumamoto, C.A., and Simoni, R.D. (1986). Genetic evidence for interaction between the *a* and *b* subunits of the F_0 portion of the *Escherichia coli* proton translocating ATPase. J. Biol. Chem *261*, 10037-10042.

Kuo, P.H., and Nakamoto, R.K. (2000). Intragenic and intergenic suppression of the *Escherichia coli* ATP synthase subunit *a* mutation of Gly-213 to Asn: functional interactions between residues in the proton transport site. Biochem. J. *347 Pt 3*, 797-805.

Lamminen, T., Majander, A., Juvonen, V., Wikstrom, M., Aula, P., Nikoskelainen, E., and Savontous, M.L. (1995). A mitochondrial mutation at nt 9101 in the ATP synthase 6 gene associated with deficient oxidative phosphorylation in a family with Leber hereditary optic neuroretinopathy. Am. J. Hum. Genet. *56*, 1238-1240.

Landau, E.M., and Rosenbusch, J.P. (1996). Lipidic cubic phases: a novel concept for the crystallization of membrane proteins. Proc. Natl. Acad. Sci. U. S. A. *93*, 14532-14535.

Lardy, H.A., and Elvehjem, C.A. (1945). Biological oxidations and reductions. Annu. Rev.

Biochem. *14*, 1-30.

Lau, W.C., and Rubinstein, J.L. (2012). Subnanometre-resolution structure of the intact

Thermus thermophilus H^+-driven ATP synthase. Nature. *481*, 214-218.

Laubinger, W., and Dimroth, P. (1988). Characterization of the ATP synthase of *Propionigenium modestum* as a primary sodium pump. Biochemistry (Mosc). *27*, 7531-7537.

Lawson, D.M., Artymiuk, P.J., Yewdall, S.J., Smith, J.M., Livingstone, J.C., Treffry, A., Luzzago, A., Levi, S., Arosio, P., Cesareni, G., and et al. (1991). Solving the structure of human H ferritin by genetically engineering intermolecular crystal contacts. Nature. *349*, 541-544.

Lehninger, A.L., Nelson, D.L., and Cox, M.M. (2008). Lehninger principles of biochemistry, 5th edn (New York, W.H. Freeman).

Leone, V., Krah, A., and Faraldo-Gomez, J.D. (2010). On the question of hydronium binding to ATP-synthase membrane rotors. Biophys. J. *99*, L53-55.

Long, J., Wang, S., Vik, B. (1998). Membrane topology of subunit *a* of the F_1F_0 ATP synthase as determined by labeling of unique cysteine residues. J. Biol. Chem. *273*, 16235-16240.

Long, J.C., DeLeon-Rangel, J., and Vik, S.B. (2002). Characterization of the first cytoplasmic loop of subunit *a* of the *Escherichia coli* ATP synthase by surface labeling, cross-linking, and mutagenesis. J. Biol. Chem. *277*, 27288-27293.

Long, J.C., Wang, S., and Vik, S.B. (1998). Membrane topology of subunit *a* of the F_1F_0 ATP synthase as determined by labeling of unique cysteine residues. J. Biol. Chem. *273*, 16235-16240.

Lowry, O.H., Rosebrough, N.J., Farr, A.L., and Randall, R.J. (1951). Protein measurement with the Folin phenol reagent. J. Biol. Chem. *193*, 265-275.

Lu, Q., and Miller, C. (1995). Silver as a probe of pore-forming residues in a potassium channel. Science. *268*, 304-307.

Luecke, H., Schobert, B., Lanyi, J.K., Spudich, E.N., and Spudich, J.L. (2001). Crystal structure of sensory rhodopsin II at 2.4 Å: insights into color tuning and transducer interaction. Science. *293*, 1499-1503.

Man, P.Y., Griffiths, P.G., Brown, D.T., Howell, N., Turnbull, D.M., and Chinnery, P.F. (2003). The epidemiology of Leber hereditary optic neuropathy in the North East of England. Am. J. Hum. Genet. *72*, 333-339.

Martucci, W.E., Udier-Blagovic, M., Atreya, C., Babatunde, O., Vargo, M.A., Jorgensen, W.L., and Anderson, K.S. (2009). Novel non-active site inhibitor of *Cryptosporidium hominis* TS-DHFR identified by a virtual screen. Bioorg. Med. Chem. Lett. *19*, 418-423.

McLachlin, D.T., Coveny, A.M., Clark, S.M., and Dunn, S.D. (2000). Site-directed cross-linking of *b* to the α, β and *a* subunits of the *Escherichia coli* ATP synthase. J. Biol. Chem. *275*, 17571-17577.

McLachlin, D.T., and Dunn, S.D. (2000). Disulfide linkage of the *b* and δ subunits does not affect the function of the *Escherichia coli* ATP synthase. Biochemistry (Mosc). *39*, 3486-3490.

Meier, T., Polzer, P., Diederichs, K., Welte, W., and Dimroth, P. (2005). Structure of the rotor ring of F-Type Na^+-ATPase from *Ilyobacter tartaricus.* Science. *308*, 659-662.

Miller, J.H. (1972). Experiments in molecular genetics (Cold Spring Harbor, N.Y., Cold Spring Harbor Laboratory).

Miroux, B., and Walker, J.E. (1996). Over-production of proteins in *Escherichia coli*: mutant hosts that allow synthesis of some membrane proteins and globular proteins at high levels. J. Mol. Biol. *260*, 289-298.

Mitchell, P. (1961). Coupling of phosphorylation to electron and hydrogen transfer by a chemi-osmotic type of mechanism. Nature. *191*, 144-148.

Mitchell, R.A., Butler, L.G., and Boyer, P.D. (1964). The association of readily-soluble bound phosphohistidine from mitochondria with succinate thiokinase. Biochem. Biophys. Res. Commun. *16*, 545-550.

Moore, K. (2008). Structural interactions between transmembrane helices 4 and 5 of subunit *a* and the subunit *c* ring of *Escherichia coli* ATP synthase. J. Biol. Chem. *283*, 31726-31735.

Moore, K.J., Angevine, C.M., Vincent, O.D., Schwem, B.E., and Fillingame, R.H. (2008). The cytoplasmic loops of subunit *a* of *Escherichia coli* ATP synthase may participate in the proton translocating mechanism. J. Biol. Chem. *283*, 13044-13052.

Moore, K.J., and Fillingame, R.H. (2008a). Structural interactions between transmembrane helices 4 and 5 of subunit *a* and the subunit *c* ring of *Escherichia coli* ATP synthase. J. Biol. Chem. *283*, 31726-31735.

Moore, K.J., and Fillingame, R.H. (2008b). Structural interactions between transmembrane helices 4 and 5 of subunit *a* and the subunit *c* ring of *Escherichia coli* ATP synthase. J Biol Chem. *283*, 31726-31735.

Mosher, M.E., White, L.K., Hermolin, J., and Fillingame, R.H. (1985). H^+-ATPase of *Escherichia coli.* An uncE mutation impairing coupling between F_1 and F_0 but not F_0-mediated H^+ translocation. J. Biol. Chem. *260*, 4807-4814.

Murata, T., Yamato, I., Kakinuma, Y., Leslie, A.G., and Walker, J.E. (2005). Structure of the rotor of the V-Type Na^+-ATPase from *Enterococcus hirae*. Science. *308*, 654-659.

Nagle, J.F., and Morowitz, H.J. (1978). Molecular mechanisms for proton transport in membranes. Proc. Natl. Acad. Sci. U. S. A. *75*, 298-302.

Nakano, T., Ikegami, T., Suzuki, T., Yoshida, M., and Akutsu, H. (2006). A new solution structure of ATP synthase subunit *c* from thermophilic bacillus PS3, suggesting a local conformational change for H+-translocation. J. Mol. Biol. *358*, 132-144.

Noji, H., and Yoshida, M. (2001). The rotary machine in the cell, ATP synthase. J. Biol. Chem. *276*, 1665-1668.

Notredame, Higgins, D., and Heringa, J. (2000). T-Coffee: A novel method for fast and accurate multiple sequence alignment. J. Mol. Biol. *302*, 205-217.

O'Grady, C., Rempel, B.L., Sokaribo, A., Nokhrin, S., and Dmitriev, O.Y. (2012). One-stepamino acid selective isotope labeling of proteins in prototrophic *Escherichia coli* strains. Anal. Biochem. *426*, 126-128.

Overton, I.M., and Barton, G.J. (2006). A normalised scale for structural genomics target ranking: the OB-Score. FEBS Lett. *580*, 4005-4009.

Ozaki, Y., Suzuki, T., Kuruma, Y., Ueda, T., and Yoshida, M. (2008). UncI protein can mediate ring-assembly of *c*-subunits of F_0F_1-ATP synthase in vitro. Biochem. Biophys. Res. Commun. *367*, 663-666.

Pati, S., Brusilow, W.S., Deckers-Hebestreit, G., and Altendorf, K. (1991). Assembly of the F_0 proton channel of the *Escherichia coli* F_1F_0 ATPase: low proton conductance of reconstituted F_0 sectors synthesized and assembled in the absence of F_1. Biochemistry (Mosc). *30*, 4710-4714.

Penefsky, H.S., Pullman, M.E., Datta, A., and Racker, E. (1960). Partial resolution of the enzymes catalyzing oxidative phosphorylation. II. Participation of a soluble adenosine tolphosphatase in oxidative phosphorylation. J. Biol. Chem. *235*, 3330-3336.

Perlin, D.S., Cox, D.N., and Senior, A.E. (1983). Integration of F_1 and the membrane sector of the proton-ATPase of *Escherichia coli*. Role of subunit "*b*" (uncF protein). J. Biol. Chem. *258*, 9793-9800.

Petrella, S., Cambau, E., Chauffour, A., Andries, K., Jarlier, V., and Sougakoff, W. (2006). Genetic basis for natural and acquired resistance to the diarylquinoline R207910 in mycobacteria. Antimicrob. Agents Chemother. *50*, 2853-2856.

Pierson, H.E., Uhlemann, E.M., and Dmitriev, O.Y. (2011). Interaction with monomeric subunit *c* drives insertion of ATP synthase subunit *a* into the membrane and primes *a-c* complex formation. J. Biol. Chem. *286*, 38583-38591.

Pogoryelov, D., Yildiz, O., Faraldo-Gomez, J.D., and Meier, T. (2009). High-resolution structure of the rotor ring of a proton-dependent ATP synthase. Nat. Struct. Mol. Biol. *16*, 1068-1073.

Preiss, L., Yildiz, O., Hicks, D.B., Krulwich, T.A., and Meier, T. (2010). A new type of proton coordination in an F_1F_0-ATP synthase rotor ring. PLoS Biol. *8*, e1000443.

Pullman, M.E., Penefsky, H., and Racker, E. (1958). A soluble protein fraction required for coupling phosphorylation to oxidation in submitochondrial fragments of beef heart mitochondria. Arch. Biochem. Biophys. *76*, 227-230.

Racker, E., and Kandrach, A. (1973). Partial resolution of the enzymes catalyzing oxidative phosphorylation. XXXIX. Reconstitution of the third segment of oxidative phosphorylation. J. Biol. Chem. *248*, 5841-5847.

Ragan, C.I., and Racker, E. (1973). Partial resolution of the enzymes catalyzing oxidative phosphorylation. 28. The reconstitution of the first site of energy conservation. J. Biol. Chem. *248*, 2563-2569.

Rak, M., Tetaud, E., Duvezin-Caubet, S., Ezkurdia, N., Bietenhader, M., Rytka, J., and di Rago, J.P. (2007). A yeast model of the neurogenic ataxia retinitis pigmentosa (NARP) T8993G mutation in the mitochondrial ATP synthase-6 gene. J. Biol. Chem. *282*, 34039-34047.

Rasmussen, S.G., Choi, H.J., Rosenbaum, D.M., Kobilka, T.S., Thian, F.S., Edwards, P.C., Burghammer, M., Ratnala, V.R., Sanishvili, R., Fischetti, R.F., Schertler, G.F., Weis, W.I., and Kobilka, B.K. (2007). Crystal structure of the human β_2 adrenergic G-protein-coupled receptor. Nature. *450*, 383-387.

Rastogi, V.K., and Girvin, M.E. (1999). Structural changes linked to proton translocation by subunit *c* of the ATP synthase. Nature. *402*, 263-268.

Rees, D., Leslie, A., and Walker, J. (2009). The structure of the membrane extrinsic region of bovine ATP synthase. PNAS. *106*, 21597-21601.

Roberts, N.A., Martin, J.A., Kinchington, D., Broadhurst, A.V., Craig, J.C., Duncan, I.B., Galpin, S.A., Handa, B.K., Kay, J., Krohn, A., and et al. (1990). Rational design of peptide-based HIV proteinase inhibitors. Science. *248*, 358-361.

Rodgers, A.J., and Capaldi, R.A. (1998). The second stalk composed of the *b*- and δ-subunits connects F_0 to F_1 via an α-subunit in the *Escherichia coli* ATP synthase. J. Biol. Chem. *273*, 29406-29410.

Rodgers, A., Wilkens, S., Aggeler, R., Morris, M., Howitt, S., and Capaldi, R. (1997). The subunit δ - subunit *b* domain of the *Escherichia coli* F_1F_0 ATPase. The *b* subunits interact with F_1 as a dimer and through the δ subunit. J. Biol. Chem. *272*, 31058-31064.

Rodgers, A., and Wilce, M. (2000). Structure of the γ-ε complex of ATP synthase. Nat. Struct. Biol. *7*, 1051-1054.

Rosenbaum, D.M., Zhang, C., Lyons, J.A., Holl, R., Aragao, D., Arlow, D.H., Rasmussen, S.G., Choi, H.J., Devree, B.T., Sunahara, R.K., Chae, P.S., Gellman, S.H., Dror, R.O., Shaw, D.E., Weis, W.I., Caffrey, M., Gmeiner, P., and Kobilka, B.K. (2011). Structure and function of an irreversible agonist-β_2 adrenoceptor complex. Nature. *469*, 236-240.

Royant, A., Nollert, P., Edman, K., Neutze, R., Landau, E.M., Pebay-Peyroula, E., and Navarro,

J. (2001). X-ray structure of sensory rhodopsin II at 2.1-Å resolution. Proc. Natl. Acad. Sci. U. S. A. *98*, 10131-10136.

Rule, G.S., and Hitchens, T.K. (2006). Fundamentals of protein NMR spectrosopy (Dordrecht, Springer).

Saint-Georges, Y., Hamel, P., Lemaire, C., and Dujardin, G. (2001). Role of positively charged transmembrane segments in the insertion and assembly of mitochondrial inner-membrane proteins. Proc. Natl. Acad. Sci. U. S. A. *98*, 13814-13819.

Santorelli, F., and Tessa, A. (2004). Neuropathy, ataxia and retinitis pigmentosa (NARP) syndrome. orphanet.

Santorelli, F.M., Mak, S.C., Vazquez-Memije, M.E., Shanske, S., Kranz-Eble, P., Jain, K.D., Bluestone, D.L., De Vivo, D.C., and DiMauro, S. (1996). Clinical heterogeneity associated with the mitochondrial DNA T8993C point mutation. Pediatr. Res. *39*, 914-917.

Santorelli, F.M., Shanske, S., Jain, K.D., Tick, D., Schon, E.A., and DiMauro, S. (1994). A T-->C mutation at nt 8993 of mitochondrial DNA in a child with Leigh syndrome. Neurology. *44*, 972-974.

Saroussi, S., Schushan, M., Ben-Tal, N., Junge, W., and Nelson, N. (2012). Structure and flexibility of the *c*-ring in the electromotor of rotary F_1F_0 -ATPase of pea chloroplasts. PLoS One. *7*, e43045.

Schagger, H., and von Jagow, G. (1987). Tricine-sodium dodecyl sulfate-polyacrylamide gel electrophoresis for the separation of proteins in the range from 1 to 100 kDa. Anal. Biochem. *166*, 368-379.

Schneider, E., and Altendorf, K. (1984). Subunit *b* of the membrane moiety (F_0) of ATP synthase (F_1F_0) from *Escherichia coli* is indispensable for H^+ translocation and binding of the water-soluble F_1 moiety. Proc. Natl. Acad. Sci. U. S. A. *81*, 7279-7283.

Schneider, E., and Altendorf, K. (1985). All three subunits are required for the reconstitution of an active proton channel (F_0) of *Escherichia coli* ATP synthase (F_1F_0). EMBO J. *4*, 515-518.

Schneider, E., and Altendorf, K. (1987). Bacterial adenosine 5'-triphosphate synthase (F_1F_0): purification and reconstitution of F_0 complexes and biochemical and functional characterization of their subunits. Microbiol. Rev. *51*, 477-497.

Schwem, B.E., and Fillingame, R.H. (2006). Cross-linking between helices within subunit *a* of *Escherichia coli* ATP synthase defines the transmembrane packing of a four-helix bundle. J. Biol. Chem. *281*, 37861-37867.

Segala, E., Sougakoff, W., Nevejans-Chauffour, A., Jarlier, V., and Petrella, S. (2012). New mutations in the mycobacterial ATP synthase: new insights into the binding of the diarylquinoline TMC207 to the ATP synthase *c*-ring structure. Antimicrob. Agents Chemother. *56*, 2326-2334.

Sgarbi, G., Baracca, A., Lenaz, G., Valentino, L.M., Carelli, V., and Solaini, G. (2006). Inefficient coupling between proton transport and ATP synthesis may be the pathogenicmechanism for NARP and Leigh syndrome resulting from the T8993G mutation in mtDNA. Biochem. J. *395*, 493-500.

Singh, S., Turina, P., Bustamante, C.J., Keller, D.J., and Capaldi, R. (1996). Topographical structure of membrane-bound *Escherichia coli* F_1F_0 ATP synthase in aqueous buffer. FEBS Lett. *397*, 30-34.

Slater, E.C. (1953). Mechanism of phosphorylation in the respiratory chain. Nature. *172*, 975-978.

Stalz, W.D., Greie, J.C., Deckers-Hebestreit, G., and Altendorf, K. (2003). Direct interaction of subunits *a* and *b* of the F_0 complex of *Escherichia coli* ATP synthase by forming an ab_2 subcomplex. J. Biol. Chem. *278*, 27068-27071.

Suzuki, T., Ozaki, Y., Sone, N., Feniouk, B.A., and Yoshida, M. (2007). The product of uncI gene in F_1F_0-ATP synthase operon plays a chaperone-like role to assist *c*-ring assembly. Proc. Natl. Acad. Sci. U. S. A. *104*, 20776-20781.

Symersky, J., Pagadala, V., Osowski, D., Krah, A., Meier, T., Faraldo-Gomez, J.D., and Mueller, D.M. (2012). Structure of the c_{10} ring of the yeast mitochondrial ATP synthase in the open conformation. Nat. Struct. Mol. Biol. *19*, 485-491, S481.

Takeyasu, K., Omote, H., Nettikadan, S., Tokumasu, F., Iwamoto-Kihara, A., and Futai, M. (1996). Molecular imaging of *Escherichia coli* F_0F_1-ATPase in reconstituted membranes using atomic force microscopy. FEBS Lett. *392*, 110-113.

Tamura, N., Konishi, S., Iwaki, S., Kimura-Someya, T., Nada, S., and Yamaguchi, A. (2001). Complete cysteine-scanning mutagenesis and site-directed chemical modification of the Tn10-encoded metal-tetracycline/H^+ antiporter. J. Biol. Chem. *276*, 20330-20339.

Tatuch, Y., and Robinson, B.H. (1993). The mitochondrial DNA mutation at 8993 associated with NARP slows the rate of ATP synthesis in isolated lymphoblast mitochondria. Biochem. Biophys. Res. Commun. *192*, 124-128.

Todokoro, Y., Kobayashi, M., Sato, T., Kawakami, T., Yumen, I., Aimoto, S., Fujiwara, T., and Akutsu, H. (2010). Structure analysis of membrane-reconstituted subunit *c*-ring of *E. coli* H^+-ATP synthase by solid-state NMR. J. Biomol. NMR. *48*, 1-11.

Torizawa, T., Shimizu, M., Taoka, M.,Miyano, H., Kainosho, M. (2004). Efficient production of isotopically labeled proteins by cell-free synthesis: a practical protocol Journal of Biological NMR. *3*, 311-325.

Towbin, H., Staehelin, T., and Gordon, J. (1979). Electrophoretic transfer of proteins from polyacrylamide gels to nitrocellulose sheets: procedure and some applications. Proc. Natl. Acad. Sci. U. S. A. *76*, 4350-4354.

Traxler, P., Furet, P., Mett, H., Buchdunger, E., Meyer, T., and Lydon, N. (1997). Design and synthesis of novel tyrosine kinase inhibitors using a pharmacophore model of the ATP-binding site of the EGF-R. J. Pharm. Belg. *52*, 88-96.

Tsunoda, S., Rodgers, A., Aggeler, R., Wilce, M., Yoshida, M., and Capaldi, R. (2001). Large conformational changes of the ε subunit in the bacterial F_1F_0 ATP synthase provide a ratchet action to regulate this rotary motor enzyme. Proc. Natl. Acad. Sci. *98*, 6560-6564.

Uhlemann, E.M., Pierson, H.E., Fillingame, R.H., and Dmitriev, O.Y. (2012). Cell-free synthesis of membrane subunits of ATP synthase in phospholipid bicelles: NMR shows subunit a fold similar to the protein in the cell membrane. Prot. Sci. *21*, 279-288.

Uhlin, U., Cox, G., and Guss, J. (1997). Crystal structure of the ε subunit of the proton-translocating ATP synthase from *Escherichia coli*. Structure. *5*, 1219-1230.

Valiyaveetil, F., Fillingame, R. (1997). On the Role of Arg-210 and Glu-29 of Subunit *a* in proton Translocation by *Escherichia coli* F_0F_1-ATP synthase. J. Biol. Chem. *272*, 32635-32641.

Valiyaveetil, F., Fillingame, R. (1998). Transmembrane topography of subunit *a* in the *Escherichia coli* F_1F_0 ATP synthase. J. Biol. Chem. *26*, 16241-16247.

Valiyaveetil, F.I., and Fillingame, R.H. (1998). Transmembrane topography of subunit *a* in the *Escherichia coli* F_1F_0 ATP synthase. J. Biol. Chem. *273*, 16241-16247.

Vazquez-Memije, M.E., Rizza, T., Meschini, M.C., Nesti, C., Santorelli, F.M., and Carrozzo, R. (2009). Cellular and functional analysis of four mutations located in the mitochondrial ATPase6 gene. J. Cell. Biochem. *106*, 878-886.

Vik, S.B., and Antonio, B.J. (1994). A mechanism of proton translocation by F_1F_0 ATP synthases suggested by double mutants of the *a* subunit. J. Biol. Chem. *269*, 30364-30369.

Vik, S.B., Lee, D., Curtis, C.E., and Nguyen, L.T. (1990). Mutagenesis of the *a* subunit of the F_1F_0-ATP synthase from *Escherichia coli* in the region of Asn-192. Arch. Biochem. Biophys. *282*, 125-131.

Vik, S.B., Long, J.C., Wada, T., and Zhang, D. (2000). A model for the structure of subunit *a* of the *Escherichia coli* ATP synthase and its role in proton translocation. Biochim. Biophys. Acta *1458*, 457-466.

Vik, S.B., Patterson, A.R., and Antonio, B.J. (1998). Insertion scanning mutagenesis of subunit *a* of the F_1F_0 ATP synthase near His245 and implications on gating of the proton channel. J. Biol. Chem. *273*, 16229-16234.

Vollmar, M., Schlieper, D., Winn, M., Buchner, C., and Groth, G. (2009). Structure of the c_{14} rotor ring of the proton translocating chloroplast ATP synthase. J. Biol. Chem. *284*, 18228-18235.

von Ballmoos, C., Wiedenmann, A., and Dimroth, P. (2009). Essentials for ATP synthesis by

F_1F_0 ATP synthases. Annu. Rev. Biochem. *78*, 649-672.

Vonck, J., von Nidda, T.K., Meier, T., Matthey, U., Mills, D.J., Kuhlbrandt, W., and Dimroth, P. (2002). Molecular architecture of the undecameric rotor of a bacterial Na^+-ATP synthase. J. Mol. Biol. *321*, 307-316.

Wada, T., Long, JC., Zhang, D., Vik, SB. (1999). A novel labeling approact supports the five-transmembrane model of subunit *a* of the *Escherichia coli* ATP synthase. . J. Biol. Chem. *24*, 17353-17357.

Walker, J.E., Saraste, M., and Gay, N.J. (1984). The unc operon. Nucleotide sequence, regulation and structure of ATP-synthase. Biochim. Biophys. Acta *768*, 164-200.

Warschawski, D. (2012). Proteins of known structure determined by solid-state NMR. Available at http://www.drorlist.com/nmr/SPNMR.html, access on October 12, 2012.

Wilkens, S., Borchardt, D., Weber, J., and Senior, A. (2005). Structural characterization of the interaction of the δ and α subunits of the *Escherichia coli* F_1F_0-ATP synthase by NMR spectroscopy. Biochem. *44*, 11786-11794.

Wilkens S., and Capaldi, R. (1998). Solution structure of the ε subunit of F_1 ATPase from *Escherichia coli* and interactions of this subunit with the β subunits in the complex. J. Biol. Chem. *273*, 26645-26651

Wilkens, S., Rodgers, A., Ogilvie, I., and Capaldi, R. (1997). Structure and arrangement of the δ subunit in the *E. coli* ATP synthase (ECF_1F_0). Biophys. Chem. *68*, 95-102

White, S. (2012). Membrane proteins of known structure. Available at http://blanco.biomol.uci.edu/mpstruc/listAll/list. Accessed on October 11, 2012.

White, S.L., Collins, V.R., Wolfe, R., Cleary, M.A., Shanske, S., DiMauro, S., Dahl, H.H., and Thorburn, D.R. (1999). Genetic counseling and prenatal diagnosis for the mitochondrial DNA mutations at nucleotide 8993. Am. J. Hum. Genet. *65*, 474-482.

Wu, B., Chien, E.Y., Mol, C.D., Fenalti, G., Liu, W., Katritch, V., Abagyan, R., Brooun, A., Wells, P., Bi, F.C., Hamel, D.J., Kuhn, P., Handel, T.M., Cherezov, V., and Stevens, R.C. (2010). Structures of the CXCR4 chemokine GPCR with small-molecule and cyclic peptide antagonists. Science. *330*, 1066-1071.

Xing, J., Wang, H., von Ballmoos, C., Dimroth, P., and Oster, G. (2004). Torque generation by the F_0 motor of the sodium ATPase. Biophys. J. *87*, 2148-2163.

Yi, L., Celebi, N., Chen, M., and Dalbey, R.E. (2004). Sec/SRP requirements and energetics of membrane insertion of subunits *a*, *b*, and *c* of the *Escherichia coli* F_1F_0 ATP synthase. J. Biol. Chem. *279*, 39260-39267.

Yi, L., Jiang, F., Chen, M., Cain, B., Bolhuis, A., and Dalbey, R.E. (2003). YidC is strictly required for membrane insertion of subunits *a* and *c* of the F_1F_0 ATP synthase and SecE of the

SecYEG translocase. Biochemistry (Mosc). *42*, 10537-10544.

Yoshida, M., Muneyuki, E., and Hisabori, T. (2001). ATP synthase--a marvellous rotary engine of the cell. Nat. Rev. Mol. Cell Biol. *2*, 669-677.

Yoshida, M., Sone, N., Hirata, H., Kagawa, Y., and Ui, N. (1979). Subunit structure of adenosine triphosphatase. Comparison of the structure in thermophilic bacterium PS3 with those in mitochondria, chloroplasts, and *Escherichia coli.* J. Biol. Chem. *254*, 9525-9533.

Zhang, D., and Vik, S.B. (2003a). Close proximity of a cytoplasmic loop of subunit *a* with *c* subunits of the ATP synthase from *Escherichia coli.* J. Biol. Chem. *278*, 12319-12324.

Zhang, D., and Vik, S.B. (2003b). Helix packing in subunit *a* of the *Escherichia coli* ATP synthase as determined by chemical labeling and proteolysis of the cysteine-substituted protein. Biochemistry (Mosc). *42*, 331-337.

Ziegler, D.M., Linnane, A.W., Green, D.E., Dass, C.M., and Ris, H. (1958). Studies on the electron transport system. XI. Correlation of the morphology and enzymic properties of mitochondrial and sub-mitochondrial particles. Biochim. Biophys. Acta. *28*, 524-538.